1-28-2015

Validation Studies of Single-Phase Natural Circulation Response of the Fluoride salt-cooled High-temperature Reactor (FHR)

Amy Drumm

Amy Drumm
Candidate

Nuclear Engineering
Department

This thesis is approved, and it is acceptable in quality and form for publication:

Approved by the Thesis Committee:

Edward Blandford, Chairperson

Anil Prinja

Vincent Mousseau

VALIDATION STUDIES OF SINGLE-PHASE NATURAL CIRCULATION RESPONSE OF THE FLUORIDE SALT-COOLED HIGH-TEMPERATURE REACTOR (FHR)

by

AMY N. DRUMM

B.S. MECHANICAL ENGINEERING, NEW MEXICO INSTITUTE OF MINING AND TECHNOLOGY, 2012

THESIS

Submitted in Partial Fulfillment of the
Requirements for the Degree of

Master of Science
Nuclear Engineering

The University of New Mexico
Albuquerque, New Mexico

December 2014

ACKNOWLEDGMENTS

This work could not have been completed without the invaluable help of many people both within and outside of the university. I would like to thank my advisor for his guidance, direction and support throughout the research and the writing of this manuscript. I would like to thank my other committee members Dr. Prinja and Dr. Mousseau for their help understanding both the numerical and experimental aspects of my research

I would like to thank Dr. Vijayan and Dr. Borgohain for getting me a copy of the LeBENC code to use in my research. I would especially like to thank Dr. Borgohain for helping me understand how the code works and answering all of my questions while I was becoming familiar with the code.

I would like to thank the many students who helped me complete this research. In particular, I would like to mention Floren, Daniel, and Joel for their help getting experimental data. I would especially like to thank Floren for taking time on the weekend to ensure the experimental data was collected in time to finish my research and Joel for taking the time to trouble shoot certain aspects of the code and to make sure the experiment was done in a way to get validation appropriate data. I would also like to thank Bobbi, Vanessa and Nathan for their help.

Finally, I would like to thank my parents and siblings for their prayers and encouragement throughout my time at UNM.

Validation Studies of Single-Phase Natural Circulation Response of the Fluoride salt-cooled High-temperature Reactor (FHR)

by

Amy N. Drumm

B.S. Mechanical Engineering, New Mexico Institute of Mining and Technology, 2012
M.S., Nuclear Engineering, University of New Mexico, 2014

ABSTRACT

The purpose of this work was to develop and validate a design tool for the transients that are of interest in designing the decay heat removal system for a Fluoride salt-cooled High-temperature Reactor (FHR). The loop of interest operates with a single phase, near ambient pressure molten salt coolant. Most of the codes used for LWR safety and licensing were designed to model more complex heat transfer problems. A single phase, one dimensional, natural circulation code is more suited to validating with simple university experiments. A code designed for lead bismuth eutectic at the Bhabha Atomic Research Centre (BARC) was modified to use it to model the flow in the decay heat removal system in an FHR. The discretization of the governing equations was modified to account for non-uniform mesh spacing and to allow for an explicit (forward Euler), semi-implicit (Crank Nicolson), or fully implicit (backward Euler) solution. The models used to approximate the density integral were also modified to account for a variable mesh scheme.

The code was benchmarked against the original code developed at BARC, tested for parameter sensitivities, and then validated with experimental data. The most sensitive

areas in the code were tested with a simple validation experiment. The experimental data was compared to the computational results to determine how accurately the methods used in the code can model the physical process involved in the transients being studied.

The code was found to model the overall flow and temperature profiles fairly well for the startup, heater step, and loss of heat sink transients involved in an FHR. In general, the code overestimated the flow rate and underestimated the temperatures. Inaccurate modeling of the loss coefficients and parasitic heat loss could be the largest contributing factors these effects.

TABLE OF CONTENTS

LIST OF FIGURES

LIST OF TABLES

Chapter 1 Introduction

A growing population means growing energy needs. One of the cleanest, safest, and most economical ways to meet this need is through nuclear energy. To remain competitive in these areas, new reactors must be designed and prepared for operation. The current design ideas are categorized into different "generations". Designs that are developed enough to be built by 2030 are called Generation III+. New reactor concepts, still early in the design phase are designated as Generation IV and are looking at deployment sometime after the year 2030. The US DOE Nuclear Energy Research Advisory Committee and the Generation IV International Forum issued a roadmap in December 2002 that details the Generation IV designs with the most potential and recommends a plan for the technology development needed for them to become a reality [U.S. DOE, 2002]. In 2003, a new concept combining features of three of the Generation IV designs was created by C. W. Forsberg and P. F. Peterson [Holcomb, 2009]. The new concept was named the fluoride salt-cooled high temperature reactor (FHR) and is described in the next chapter.

For these new reactor concepts to turn into designs that can be licensed and built, research must be done to prove the concepts are valid and safe. In the past, this was done with expensive experiments. Now it is more cost effective to use computer codes to model key physics and certain aspects of the designs. While these codes have advantages over full-scale experiments, they must be very carefully characterized and tested. The numerics in the code must be verified and results validated to show that the code accurately represents the physical phenomena it models. The verification process consists of code verification and solution verification. Code verification is used to check for errors in the code itself, ensuring that the equations were entered and solved correctly. Solution

verification is used to find the numerical error introduced by any discretization techniques and the resulting uncertainties. Once the verification process is complete, the simulation results can be validated. The validation process involves comparing the simulation results to well characterized results from an experiment or analytical solution and a detailed description is given in the next chapter [Oberkampf, 2010].

Computer codes such as RELAP5-3D and TRACE have been used in the safety and licensing of light water reactors (LWRs) and other older reactor designs. The thermal fluids physics and operating conditions involved in the cooling system for an FHR are much simpler than those in LWRs. Consequently, the codes used in the reactor space so far which are designed to model complex heat transfer problems involving two-phase flow, high pressure conditions, and/or three dimensional effects are not suited to use for the FHR design. The single-phase coolant operating at near ambient pressure in an FHR provides an opportunity for benchmarking a simple 1-D single-phase natural circulation code with existing LWR legacy codes. The LeBENC natural circulation code originally developed at the Bhabha Atomic Research Centre (BARC) [Borgohain, 2011] was adapted to be suited for use with the FHR cooling system.

The LeBENC code was rewritten into MATLAB and the adapted code was given the name FLiBeNC after flibe (the working fluid) and natural circulation (the operating conditions) in the FHR cooling system. The fluid energy equation in the LeBENC code was solved explicitly using the first order upwind scheme for the convective term and the central difference scheme for the diffusion term. The solid energy equation for the pipe was also discretized explicitly using the central difference scheme for the diffusion term. The capability to solve both energy equations implicitly or semi implicitly was added to

FLiBeNC. This addition allows the user to set the solution method to explicit (as it was solved in LeBENC), semi-implicit (using the Crank Nicolson method), or fully implicit. The breakdown of how the equations are solved with each method is described in further detail in Section 3.2.4.

The implicitly discretized momentum equation was solved for the flow rate in LeBENC using an iterative guess and check method. Given the appropriate set of simplifying equations, the momentum equation can be written in the form of a quadratic equation when discretized implicitly (or semi implicitly) which means that that it can be solved algebraically using the quadratic formula. Since the solution of a quadratic equation involves taking a square root, the solution could end up with complex values. A formal constraint on the time step size was developed based on the algebraic solution of the momentum equation to avoid getting complex values in the calculation. This constraint ensures that a real solution of the momentum equation can be found. With the previous guess and check method, if the criterion to get a real solution was not satisfied, the code would simply not converge to a solution. Both the algebraic solution to the momentum equation and the time step constraint were added to the FLiBeNC code.

The trapezoidal rule and Simpson's rule were options used in the LeBENC code to approximate the value of the temperature integral in the momentum equation. The implementation of the trapezoidal rule was such that different mesh sizes for different pieces of the loop lead to small errors in the calculation. A more flexible version of the trapezoidal rule was added to FLiBeNC to account for the varying mesh sizes between pieces in the loop. The flow rate in the LeBENC code was solved using the friction factor calculated from the flow rate at the previous time step. Since the friction factor and flow

rate are interdependent, a loop was added in FLiBeNC to solve the friction factor and the flow rate iteratively until a converged solution was found at each time step.

A simplified benchmark problem that had an analytical solution was solved in the code. The benchmark problem was 1D single-phase natural circulation flow at steady state. The Boussinesq approximation was assumed to be valid and thermal resistance, axial diffusion, and heat loss to ambient were ignored. The analytical solution was solved and the same simplified problem was molded in the code. The code was modified slightly to match the assumptions in the benchmark problem so that the code could be verified by comparing the results from the analytical solution and corresponding results from the code.

The original LeBENC code used the upwind and central differencing schemes to discretize the energy equations in time. These methods are designed to be used with a mesh of constant spacing, which is not the case with this code. A similar discretization scheme designed for a variable spacing mesh was implemented via Taylor series expansions. The approach used was based on the descriptions and equations found in Randall [D. A. Randall, 2013].

A sensitivity test matrix was created to determine which parameters the code is most sensitive to. The four areas that were tested were nodalization, geometry, inputs, and numerical methods. Each of these areas had multiple parameters that were varied in the code to test the sensitivity. The test matrix and a description of each test can be found in Chapter 4.

Preliminary runs were completed to inform the experimental set up so that the experiment could be more effective in validating the code. The preliminary results were used to advise the placement of the thermocouples based on the locations in the loop where

the biggest changes to the results occurred. Tests were performed with the experiment and the conditions were modeled in the code as closely as possible. The initial conditions, boundary conditions, and geometry were all measured or calculated from the experiment to use in the code so that the code and experiment were "solving the same problem" which is very important in validation studies. The results from the experiment and the code were compared to test the predictive accuracy of the code.

The secondary side heat transfer coefficient for the heat exchanger was calculated from the experimental values and the heat loss to ambient was calculated for the experimental conditions and included in the code. The material properties and heat transfer characteristics of water were added to the code so the validation experiments could be modeled.

This thesis presents the methods used to determine the predictive accuracy of numerical methods used to model single-phase heat transfer and the results that followed. Chapter 2 covers the background information on the FHR design and a detailed description of what the verification and validation process are. The chapter also includes a section detailing work investigating the heat transfer properties of various salts and the advantages and disadvantages of using each in various parts of the FHR cooing system. Chapter 3 describes the natural circulation code including a background, a detailed description of the code and how it works, a comparison to an analytical solution, and sensitivity studies for multiple parameters. Chapter 4 is a description of the experiment used to validate the code. The loop geometry, testing procedures, and transient test descriptions are included. Chapter 5 gives the simulation and experimental results as well as the results from the

sensitivity studies and additional modeling efforts. Chapter 6 includes a conclusion and identifies possible future work.

References

A. Borgohain, B. K. Jaiswal, N. K. Maheshwari, P. K. Vijayan, D. Saha and R. K. Sinha, "Natural Circulation Studies in a Lead Bismuth Eutectic Loop," *Progress in Nuclear Energy*, **53**, 308-319 (2011).

D. A. Randall, "Chapter 2: Finite-Difference Approximations to Derivatives", An Introduction to Numerical Modeling of the Atmosphere (2013).

D. E. Holcomb. *An Analysis of Testing Requirements for Fluoride Salt-Cooled High Temperature Reactor Components.* ORNL-TM-297, Oak Ridge National Laboratory, November (2009).

U.S. DOE Nuclear Energy Research Advisory Committee and the Generation IV International Forum, *A Technology Roadmap for Generation IV Nuclear Energy Systems*, 1-6 (2002).

W. L. Oberkampf and R. J. Roy. *Verification and Validation in Scientific Computing*. New York: Cambridge UP, 372-420 (2010).

Chapter 2 Background and Theory

2.1 Fluoride salt-cooled High-temperature Reactor (FHR) Background

The Fluoride salt-cooled High-temperature Reactor (FHR) is a Generation IV reactor class that is currently under development under support by the Department of Energy's (DOE) Advanced Reactor Concepts program. The FHR combines elements of existing reactor technologies to improve reactor safety and performance. This is shown visually in Figure 2.1. The FHR reactor class combines the pool configuration and decay heat removal systems used in sodium fast reactors, the TRISO-based fuel used in gas-cooled high temperature reactors, and a fluoride salt coolant used in the molten salt reactor [Holcomb, 2009].

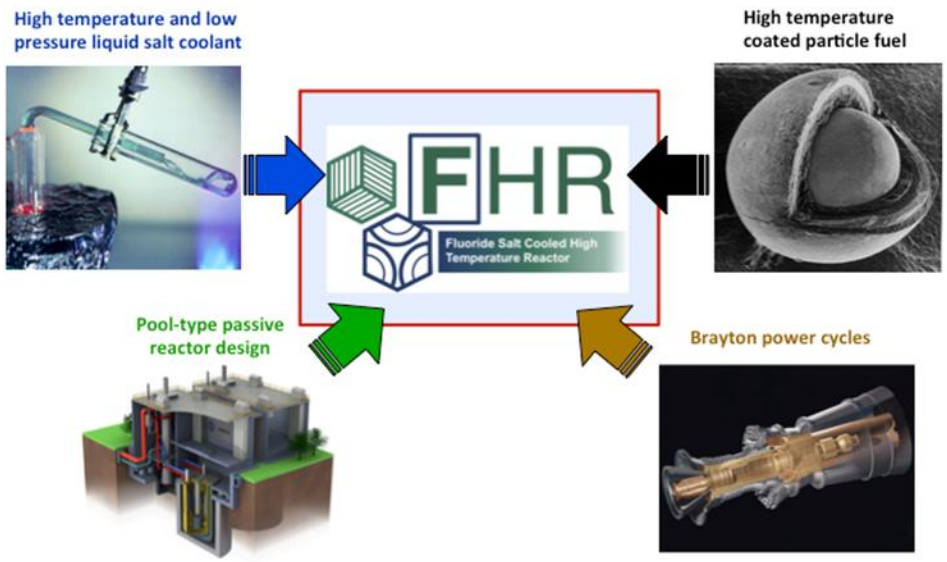

Figure 2.1 FHR Technology Diagram

The origin of the FHR started in 2002 with the Liquid Salt Very High Temperature Reactor (LS-VHTR) which took the Very High Temperature Reactor (VHTR) concept and utilized liquid salt as the primary coolant at near atmospheric pressure. Eventually, the LS-VHTR concept evolved into the Advanced High-Temperature Reactor (AHTR) with a core

outlet temperature low enough that materials already code-certified by the American Society of Mechanical Engineers (ASME) could be used for the pressure boundary. The current FHR conceptual designs are the Pebble Bed FHR (PB-FHR) at UC Berkeley, the Small Modular AHTR (SmAHTR) at ORNL, and a large-scale AHTR concept also at ORNL [T. Allen, et al., 2013b]. These FHR concepts are still early in the pre-conceptual design phase and are still undergoing substantial trade studies for different design options. The combination of existing nuclear technologies in the FHR design allows previous experience from other reactor types to inform the design of an FHR and might also help with FHR licensing in the future [Holcomb, 2013]. The primary decay heat removal system in the FHR design is called a Direct Reactor Auxiliary Cooling System (DRACS). The basic concept for the DRACS was developed for the Experimental Breeder Reactor II and has been used in liquid-metal reactor designs. The DRACS used in the FHR design is similar to previous versions but incorporates a fluidic diode into the design to limit parasitic heat loss from the primary coolant during normal reactor operation [Holcomb, 2009]. The FHR version of the DRACS is shown in Figure 2.2 and is described in more detail below.

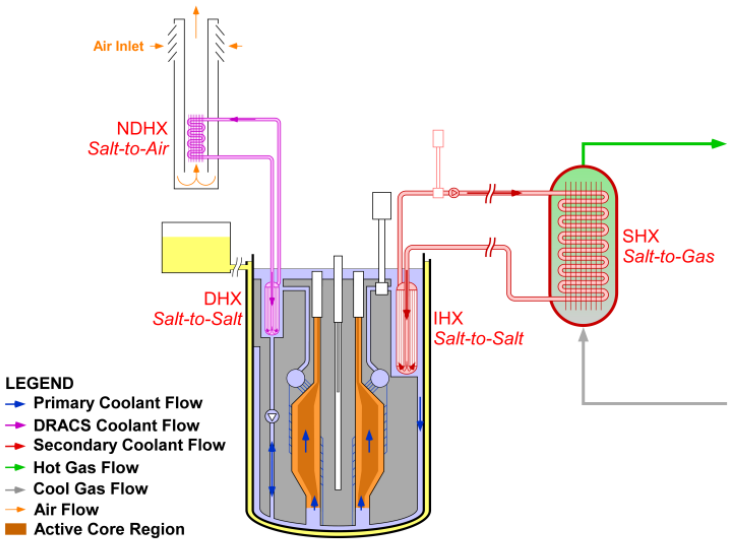

Figure 2.2 FHR Cooling System

Under normal operation, the primary coolant (blue arrow) takes heat from the reactor core and transfers it to the secondary side through the intermediate heat exchanger (IHX). The heat is then transferred to a gas loop through the secondary heat exchanger and power is extracted through a power conversion system (it is important to note that there are a variety of power conversion systems under consideration for the FHR; however, this is not the focus of this work). There is some parasitic heat loss through the DRACS loop during normal operation. The loss is controlled through a fluidic diode in line with the DHX. A fluidic diode has a high flow resistance in one direction, but a low flow resistance in the other direction. The diode is placed so that the flow through the DHX is limited during normal operation but allows enough heat to keep the DRACS loop from freezing. During a loss of forced circulation (LOFC) accident, flow through the DHX is reversed via natural circulation that develops between the core and a set of redundant heat exchangers called DRACS Heat Exchangers (DHX). When the flow reverses, it is less restricted by the fluidic diode thereby allowing the decay heat to be transferred through the DHX into the DRACS

coolant. Heat is ultimately rejected to the outside environment through an additional natural circulation loop. Ambient air is drawn in through the natural draft heat exchangers (NDHX) and rejected out the top of the DRACS stack (see the purple flow path). The NDHX can be designed to include adjustable shutters, which can be utilized to throttle airflow [Holcomb, 2009]. The main coolant loop can be modeled as a natural circulation loop with the core as the heat source and the DHX as the heat sink. A second natural circulation loop can be modeled from the DRACS loop with the DHX as the heat source and the NDHX as the heat sink. The main coolant loop is the one primarily focused on in this thesis.

2.2 Comparison of Heat Transfer Performance of Various Candidate Salts for the FHR

The candidate salts for the FHR are flibe, flinabe, flinak, $MgCl_2$ based, KZrF, KF-ZrF_4, and $NaBF_4$ [T. Allen, et al., 2013b]. The molten salts discussed in this section are flibe, flinak and KCl-$MgCl_2$. These salts were chosen because of their potential for use in the FHR and readily available thermophysical property data.

2.2.1 Heat transfer parameter work for various flow scenarios

For forced convection through a duct or channel, the Blasius equation and definitions of Nu, Re, and Pr were used to determine the heat transfer parameter (HTP) in terms of a fluid's thermophysical properties. The derivation done in Ghajar and Tang [1995] is shown below. The derivation starts with Equation 2.1 as a general expression for Nu as a function of Re and Pr.

$$Nu = C * Re^m * Pr^n \quad 2.1$$

$$Nu = \frac{hD}{k};\ Re = \frac{\rho VD}{\mu};\ Pr = \frac{\mu c_p}{k} \quad 2.2$$

Using Equation 2.2 as the definitions for the Nusselt number, Reynolds number, and Prandtl number, the heat transfer coefficient can be written as Equation 2.3.

$$h = C\frac{k}{D} * \left(\frac{\rho VD}{\mu}\right)^m * \left(\frac{\mu c_p}{k}\right)^n \quad 2.3$$

The variables were collected to get Equation 2.4 below.

$$h = Ck^{1-n}D^{m-1}\rho^m\mu^{n-m}{c_p}^nV^m \quad 2.4$$

Assuming constant geometry and flow velocity for all salts, V and D can be taken out of the equation. The constant C can also be taken out since it depends on flow regime and configuration and would not change for the different salts. This is done by defining an HTP as shown in Equation 2.5

$$HTP = \frac{h * D^{1-m}}{C * V^m} \quad 2.5$$

This simplifies the heat transfer parameter so it is only dependent on the material properties of the salt with exponents as shown in Equation 2.6:

$$HTP = k^{1-n}\rho^m\mu^{n-m}{c_p}^n \quad 2.6$$

Using the values given for m and n in the paper by Ghajar (m = 0.5, n = 0.4 for turbulent flow) and (m = 0.8, n = 0.4 for laminar flow), the HTP becomes Equation 2.7 for laminar flow and 2.8 for turbulent flow.

$$HTP = k^{0.6}\rho^{0.5}\mu^{-0.1}{c_p}^{0.4} \quad 2.7$$

$$HTP = k^{0.6}\rho^{0.8}\mu^{-0.4}{c_p}^{0.4} \quad 2.8$$

The thermophysical properties for each salt were used to get the HTP as a function of temperature. Figure 2.3 below shows this for laminar and turbulent flow through a duct or channel.

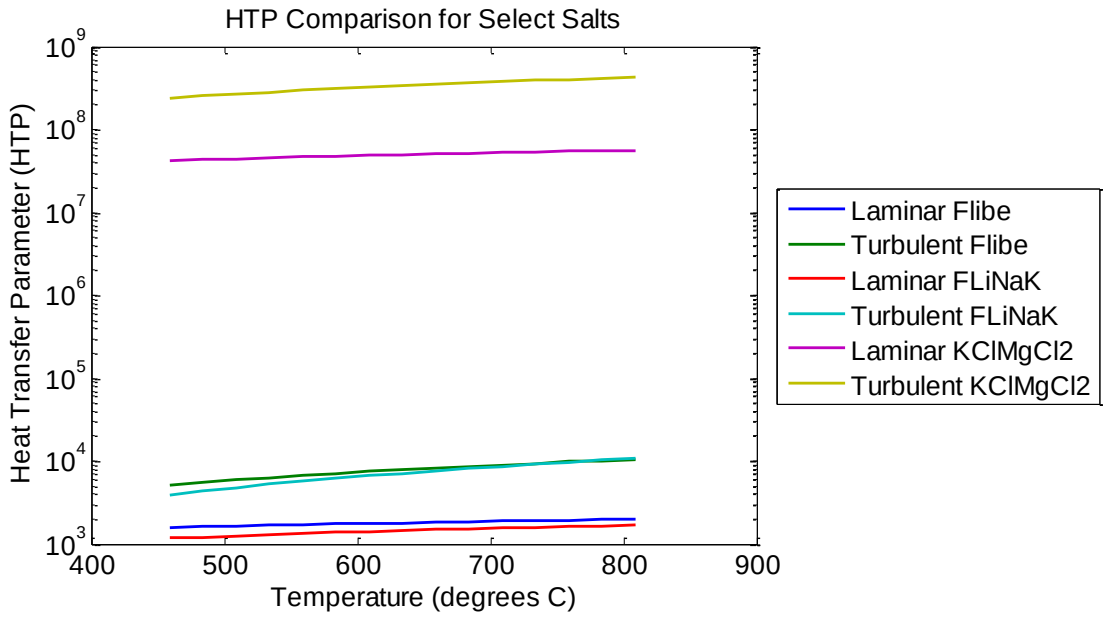

Figure 2.3 HTP for Flow Through a Duct or Channel

The heat transfer characteristics of flow through a pebble bed will be an important phenomenon to study for the PB-FHR design [T. Allen, et al., 2013a]. The Wakao and Kaguei (1982) and Whitaker (1972) heat transfer coefficients for forced convection inside a pebble bed are given as Equations 2.9 and 2.10 respectively.

$$h = \frac{k}{D_p}(2 + 1.1Re^{0.62}Pr^{0.33});\ 5 < Re < 100{,}000 \qquad 2.9$$

$$h = \frac{k}{D_h}\left(0.5Re^{1/2} + 0.2Re^{2/3}\right)Pr^{1/3}\left(\frac{\mu_b}{\mu_s}\right)^{0.14};\ 20 < Re < 10{,}000 \qquad 2.10$$

The corresponding HTPs were developed following the same logic and methodology as before. The HTPs based on the Wakao and Kaguei and Whitaker heat transfer coefficients are Equations 2.11 and 2.12 respectively.

$$HTP = 2k + 1.1\rho^{0.62}\mu^{-0.29}{c_p}^{0.33}k^{0.67} \qquad 2.11$$

$$HTP = \left(0.5\rho^{0.5}\mu^{-0.5+1/3}{c_p}^{1/3}k^{2/3} + 0.2\rho^{2/3}\mu^{-1/3}{c_p}^{1/3}k^{2/3}\right)\left(\frac{\mu_b}{\mu_s}\right)^{0.14} \qquad 2.12$$

Equation 2.11 from the Wakao and Kaguei correlation was used because $\frac{\mu_b}{\mu_s}$ was not found for the salts. Figure 2.4 below shows the HTP for the different salts.

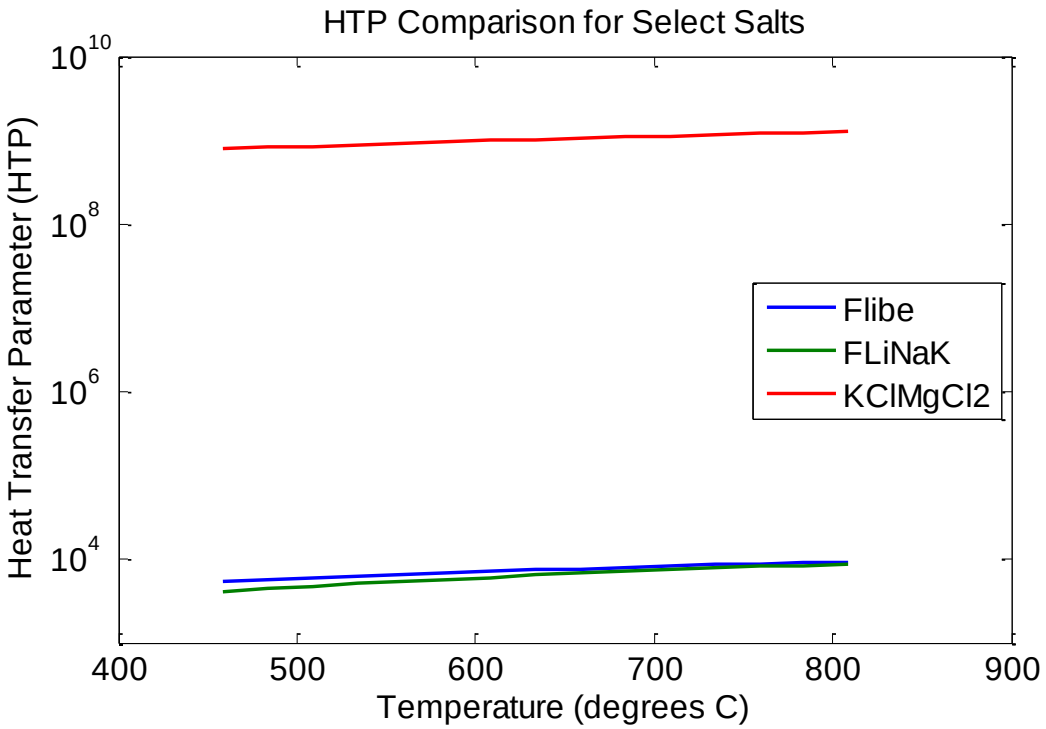

Figure 2.4 HTP for Flow Through a Pebble Bed

The correlations for Nu_L and Ra, for natural convection over a vertical plate are given below as Equations 2.13 and 2.14 respectively.

$$\overline{Nu_L} = 0.68 + \frac{0.67 Ra_L^{\frac{1}{4}}}{\left[1 + \left(\frac{0.492}{Pr}\right)^{\frac{9}{16}}\right]^{4/9}} \qquad 2.13$$

$$Ra = GrPr = \frac{g\beta(T_s - T_\infty)L^3}{\nu\alpha};\ Pr = \frac{\mu c_p}{k}; \qquad 2.14$$

Equations 2.13 and 2.14 were used with the definition for Nusselt number from Equation 2.2 to get the corresponding heat transfer coefficient in the form of Equation 2.15.

$$h = \frac{k}{L}\left(0.68 + \frac{0.67\left(\frac{g\beta(T_s - T_\infty)L^3}{\nu\alpha}\right)_L^{\frac{1}{4}}}{\left[1 + \left(\frac{0.492}{\left(\frac{\mu c_p}{k}\right)}\right)^{\frac{9}{16}}\right]^{4/9}}\right) \qquad 2.15$$

The plate length was assumed to be constant because it does not depend on the material properties of the salt so it was ignored in the HTP which reduces it to Equation 2.16.

$$HTP = k0.68 + k\frac{0.67\left(\frac{\beta(T_s - T_\infty)}{\nu\alpha}\right)^{\frac{1}{4}}_{L}}{\left[1 + \left(\frac{0.492}{\left(\frac{\mu c_p}{k}\right)}\right)^{\frac{9}{16}}\right]^{4/9}} \quad 2.16$$

More properties are needed to compare the salts performance with regards to natural circulation. Specifically, the temperature difference between the surface and the free stream flow, β, and α are needed.

2.2.2 Discussion

The results showed that the HTP for flibe is slightly higher than that of flinak for turbulent flow through a channel, laminar flow through a channel, and forced convection inside a pebble bed. While flibe and flinak have comparable HTPs, $KClMgCl_2$ had a much higher HTP than either of them in all three cases. The difference in HTP for $KClMgCl_2$ versus either of the other two salts was much larger than the difference for any of the salts between laminar and turbulent flow conditions. This shows that the $KClMgCl_2$ salt would be a good candidate where a high HTP is required or desired. This analysis only takes into account the material properties of the salts and does not include other important aspects such as radiation properties.

2.3 Verification and Validation

Thermal-fluids computer codes utilized in reactor design use mathematical models to predict how a physical process will occur and are used to inform designs, satisfy licensing

requirements, or even determine legal liability. As simulations become more important and widely used, they need to have a documented reliability. The processes of code Verification and Validation plus Uncertainty Quantification (V&VUQ) are used to assess this reliability. Verification is the process used to show that the solution to the model is solved correctly by the code, namely, that the numerical algorithm was put into the code without errors and that it produces repeatable results. Verification involves testing the code for iterative, spatial, and temporal convergence and comparing results from the code to a highly accurate solution. This could be an analytical or semi-analytical solution, a numerical solution or some other benchmark solution [Oberkampf, 2010]. In short, verification is the process utilized to ensure that the *math* in the code has been implemented correctly.

Validation differs from verification as it focuses on the *physics* captured in the code and is used to determine how well the model represents real world physical process for the intended application. Validation is achieved by running a very well characterized experiment followed by running the code to solve the exact same problem and then comparing the results. The point of the validation process is to ask exactly the same question of the experiment representing nature and the model to be validated so that when the results are compared, something can be said for how well the model represents nature. This means that the person creating or running the code is the one who wants information from a validation experiment. Not only does the customer differ between a traditional experiment and a validation experiment, but the information gathered differs as well. While traditional experiments are typically run to measure values of a physical process, validation experiments are run to characterize the experiment by measuring the conditions

of the experiment and its surroundings. A controlled environment and repeatability are important in traditional experiments whereas an understanding and careful measurements of the conditions are more important in a validation experiment [Oberkampf, 2010].

Since the validation experiment and code must solve the same problem, information will have to be passed between the computational analyst and the experimentalist. The computational analyst must tell the experimentalist what inputs the model requires and what outputs the model will provide. Inputs required by codes typically consist of the geometry, initial conditions, and boundary conditions. The measurements to be taken from the experiment and compared to the output from the code are sometimes called system response quantities (SRQs) [Oberkampf, 2010]. The computational analyst must communicate to the experimentalist not only what quantities to measure and where to measure them, but also what level of accuracy and sampling rates that are needed to properly test the models in the code. In some cases, the computational analyst might suggest changes to the boundary conditions or initial conditions to better challenge the models in the code. The analyst should be given all of the details necessary to run the code and only those details. This would include the physical modeling parameters, initial conditions, and boundary conditions. It would not include the experimental measurements of the SRQs. The analyst should quantify the errors in the inputs to get the uncertainty of the outputs that are compared with the experimental results. The experimental measurements should be kept from the analyst until the predictive results from the model have been obtained. This is to minimize distortion or misleading results when they are compared [Oberkampf, 2010]. According to Oberkampf and Trucano [Oberkampf, 2008], computational analysts will often change a calibration parameter, reformulate assumptions,

or blame the experimentalist if the data from the experiment does not agree with the results obtained from the code. Oberkampf and Roy [Oberkampf, 2010] go as far as suggesting that the final comparison of the SRQs between the code and the experiment should be done by the experimentalist or a third party, and not the analyst. In comparing the computational and experimental results, it is important to give the uncertainty for both sides. It is also important to compare the same SRQs. This can be difficult as it might be challenging for the models and physical measurement devices to predict or measure the same quantities.

2.3.1 Previous thermal hydraulic codes relevant to the FHR

Many computer codes have been developed to model the thermal hydraulic performance in reactors. Efforts have been made to improve the usefulness of these simulations in predicting reactor phenomena by improving the models used for hydrodynamics and heat transfer as well as the numerical methods used to solve them. Therefore, the best version to use for different cases and scenarios must be determined. This is done by validating the models used in codes for the different applications they are intended to model [T. Allen, et al., 2013a].

Codes used to model thermal hydraulics in reactors vary from simple 1-D models of connected pipes to a complex 3-D CFD simulation capturing spatial effects in individual components. Codes are needed at both ends of this spectrum to fully understand and capture the phenomena in reactor systems. It is not practical to use a full 3-D CFD simulation to model the whole reactor coolant system, but it can be useful to see detail of how heat transfer and fluid mechanics will behave with respect to individual reactor components. The simple 1-D models cannot capture complicated physics such as flow

through a new heat exchanger design, but they capture the overall system phenomena and performance with a reasonable amount of computational resources. Table 2.1 below shows codes that have aspects which are applicable to key FHR phenomena. More information on these codes and their applicability to the FHR can be found in Allen, et al. [2013a]

Table 2.1 Current Modeling Capability for FHR phenomena [T. Allen, et al., 2013a]

Code	High Prandtl Number	Multidimensional Porous Media Flow	Effective Natural Circulation for Passive Decay Heat Removal	Potential for Freezing (Overcooling Transients)	Conduction in Fuel and Structures	Core Bypass Flow	Regulatory Basis
THERMIX		xxx			xxx		
COMMIX		xxx	xxx				
RELAP5-3D	xx	x	xx		x		
VIPRE-01			xxx				x
Computational Fluid Dynamics Codes	x	xx				x	

x: Code has been used but lacks V&V basis.
xx: Code has been used and compared to other codes but lacks validation experimental basis.
xxx: Code has been used and validated for other reactor designs sharing FHR phenomena.

The RELAP5-3D code was used to create a 1-D model of the LS-VHTR with flibe as the primary coolant and showed promising results. RELAP5-3D was initially intended as a modeling tool for LWRs, but recent improvements have allowed for the simulation of new Gen IV designs. The addition of flibe thermophysical properties which were compared to available data allows the code to be used to model thermal-fluids phenomena in the FHR. A few variations in flibe properties implemented in the code were the constant thermal conductivity used by RELAP5-3D and slight variations in the specific heat values

used. These will either need to be fixed or accounted for as errors propagated through the code. RELAP5-3D allows for user added heat transfer and friction loss correlations so pebble bed cores can be modeled, but there is still a substantial amount of validation needed for these correlations. Although RELAP5-3D looks like a promising candidate code for system modeling of the FHR, it lacks the ability to model some key transients such as overcooling and bypass flow and an extensive validation effort needs to be done. Other codes are needed to compare to the results of RELAP5-3D. These other codes would also be potential options for ultimate safety analysis of FHR design [T. Allen, et al., 2013a].

References

A. J. Ghajar and W. Tang, "Methodology for Comparison of Hydraulic and Thermal Performance of Alternative Heat Transfer Fluids in Complex Systems," *Heat Transfer Engineering*, **16**, 60-72 (1995).

D. E. Holcomb. *An Analysis of Testing Requirements for Fluoride Salt-Cooled High Temperature Reactor Components.* ORNL-TM-297, Oak Ridge National Laboratory, November 2009.

D. E. Holcomb. *Fluoride Salt-Cooled High-Temperature Reactor Technology Development and Demonstration Roadmap*. ORNL-TM-401, Oak Ridge National Laboratory, September 2013.

T. Allen, et al., Fluoride Salt-cooled High Temperature Reactor (FHR) Subsystems Definition, Functional Requirement Definition and Licensing Basis Even (LBE) Identification White Paper, Chapter 1, University of California Berkeley, Berkeley (August 2013b)

T. Allen, et al., Fluoride Salt-cooled High Temperature Reactor (FHR) Methods and Experiments Program White Paper, University of California Berkeley, Berkeley (April 2013a)

W. L. Oberkampf and R. J. Roy. *Verification and Validation in Scientific Computing*. New York: Cambridge UP, 2010. 372-420.

W. L. Oberkampf and T. G. Trucano. "Verification and Validation Benchmarks." *Nuclear Engineering and Design* 238.2 (2008): 716-43.

Chapter 3 Natural Circulation Simulation

3.1 Background and Theory

This chapter of the thesis describes the code FLiBeNC which is a modified version of the Lead Bismuth Eutectic Natural Circulation (LeBENC) code. The LeBENC code was adapted at the Bhabha Atomic Research Centre (BARC) from a code named TRANCO originally developed to study the steady state and transient behavior of rectangular natural circulation loops with a constant diameter [Vijayan, 2001]. The modifications allowed for the following:

- the use of non-uniform diameter loops
- the ability to use different primary and secondary working fluids
- the ability to handle trace heating and heat loss from the surface of the pipes
- the capability to model axial conduction through the liquid metal coolant and pipe walls

LeBENC was written in FORTRAN 90 and used to study one-dimensional transient and steady state behaviors of liquid metal in a natural circulation loop. The finite difference code was validated with data from a single-phase natural circulation water loop at BARC.

The code models the flow assuming the fluid properties are constant across the pipe cross section. The Boussinesq approximation is assumed to be valid and the fluid is taken as incompressible. The simplified transport equations for mass, momentum, fluid energy, and solid energy (Equations 3.1 – 3.4 respectively) and the equation for the boundary condition between the fluid and wall (Equation 3.5) are shown below [Ishii, 1982].

$$u_i = \frac{a_0}{a_i} u_r \qquad 3.1$$

$$\rho \frac{du_r}{dt} \sum_i \frac{a_0}{a_i} l_i = \beta g \rho \Delta T l_h - \frac{\rho u_r^2}{2} \sum_i \left(\frac{fl}{d} + K\right)_i \left(\frac{a_0}{a_i}\right)^2 \quad 3.2$$

$$\rho C_p \left\{\frac{\partial T}{\partial t} + u \frac{\partial T}{\partial z}\right\} = \frac{4h}{d}(T_s - T) \quad 3.3$$

$$\rho_s C_{ps} \frac{\partial T_s}{\partial t} - k_s \nabla^2 T_s - \dot{q}_s = 0 \quad 3.4$$

$$-k_s \frac{\partial T_s}{\partial y} = h(T_s - T) \quad 3.5$$

The code models a natural circulation loop with a single heated section (source) and heat exchanger (sink) connected by pipes as defined in the input file. It can model different diameter components as well as surface heat loss through the pipes. Upwind and central difference schemes were used to solve the solid and fluid energy equations explicitly for the wall and fluid temperatures respectively. The momentum equation was solved implicitly for the mass flow rate, which is assumed to be constant throughout the loop [Borgohain, 2011].

Natural circulation is prone to certain types of instabilities due to the small driving force and the significant coupling between the driving force and the flow itself. Some instabilities can be caused by the geometry in both symmetric and asymmetric loops [Vijayan, 2005]. Many codes and experiments have been used to determine the stability ranges of symmetric 1-D single-phase natural circulation with a heat source at the bottom and a heat sink at the top. Less research has been done to test the temperature and flow profiles of a loop that is heated and cooled in opposite vertical legs. The experiment used to validate the numerical code FLiBeNC is heated and cooled in opposite vertical legs, so the studies of instabilities associated with symmetric loops are not as applicable.

Instabilities in single-phase natural circulation have been encountered less often than those in two-phase natural circulation and have therefore been studied less. According to

Vijayan and Nayak [Vijayan, 2005], the first theoretical studies on single-phase natural circulation were done by Welander (1957 and 1976) and Keller (1966). The four types of single-phase instabilities which Vijayan and Nayak [Vijayan, 2005] list are as follows: stability of the rest state, static instabilities associated with multiple steady states, dynamic instabilities, and compound dynamic instabilities. According to Allen, et al. [2013a], each of these instability types must be studied for applicability to the FHR once a compete set of events has been established. The multiple steady states instabilities can occur with the same flow direction or different flow direction. Vijayan and Nayak state that theoretically multiple steady states in the same flow direction could occur in a closed loop with single-phase natural circulation, but it has not been seen experimentally. This possibility arises from the polynomial nature of the momentum equation used to describe the flow.

The instability of multiple steady states with different flow directions cannot be determined from a steady state analysis. The instability would come from the uncertainty of the flow direction during start up or a flow reversal after a transient. Vijayan and Nayak mention instability in asymmetric loops referencing a transient where the flow is started with a horizontal heater and then reversed by adding heat with a vertical heater. They do not provide information on the potential instability of flow started with a vertical heater.

Vijayan, Sharma, and Saha [Vijayan, 2001] studied the potential for single-phase instabilities for various heating and cooling orientations. They report only fining instabilities when the loop was symmetrically heated on the bottom and cooled on the top. Nishihara [1997] however, recorded finding instabilities caused by enthalpy waves carried at the average flow velocity based on a theoretical study and experimental tests.

3.2 Numerical Code – FLiBeNC

The equations in FLiBeNC were modified from their original implementation in LeBENC in order to test various solution methods. The momentum and energy equations were discretized using a θ parameter and the Crank Nicolson method to allow for an explicit, semi-implicit, or fully implicit solution. The energy equations were modified to account for the fact that the mesh spacing is not constant throughout the whole loop. Various methods for finding the Nusselt number and ultimately the internal heat transfer coefficient were also added to be tested in the code. The Boussinesq approximation was made in the LeBENC code, but the material properties are solved at each node based on the nodal temperature in the FLiBeNC code. The buoyancy term was defined in its original form as the density times gravity times the incremental height difference. The trapezoidal rule and Simpson's rule were used to approximate the temperature integral in the simplified buoyancy term in the LeBENC code. These were modified for FLiBeNC to take the variable mesh size into account and used to approximate the density times the height difference for the loop. Material properties for water were implemented so the working fluid in the validation experiment could be modeled in the code. The properties for flibe and Dowtherm A, a simulant fluid, could be added as well. FLiBeNC was written in MATLAB and is described in the sections that follow.

3.2.1 Inputs and SRQs

The inputs for FLiBeNC consist of the boundary conditions, initial conditions, geometry, and material properties. Initially, different values of these inputs were tested to inform the design of the experiment, but the final values in the code are ultimately those

recorded when the validation experiment is run. The boundary conditions needed for the code and the methods used to get the values from the experimental data are detailed below. The measurement techniques used in the experiment are described in chapter 4.

The heat transfer coefficient for the secondary side of the heat exchanger was calculated using data from the validation experiment described in the next chapter. The material properties for water at 198 K and 0.10132 MPa were obtained from the National Institute of Standards and Technology (NIST) [Secretary of Commerce, 2011] and used in the calculations. The material properties, mass flow rate, dimensions, and temperature for the secondary side of the heat exchanger are given in Table 3.1 below.

Table 3.1 Secondary Side Heat Exchanger Properties

D_i	0.0254	Inner diameter (m)
D_o	0.0404	Outer diameter (m)
L_{hx}	0.6096	Heat exchanger length (m)
ρ	998.97	Water density (kg/m^3)
Cp	4187.6	Water specific heat (J/kg-K)
k	0.59094	Water thermal conductivity (W/m-K)
μ	0.0011124	Water dynamic viscosity (Pa-s)
T_s	288	Secondary side temperature (K)
$\dot{m}$	3 or 6	Secondary side mass flow rate (gal/min)

The Reynolds number was calculated to be Equation 3.8 using the definitions of the flow area and hydraulic diameter given in Equations 3.6 and 3.7.

$$A_{flow} = \frac{\pi D_o^2}{4} - \frac{\pi D_i^2}{4} = \frac{\pi}{4}(D_o^2 - D_i^2) \tag{3.6}$$

$$D_h = \frac{4A_{flow}}{P} = \frac{4\frac{\pi}{4}(D_o^2 - D_i^2)}{\pi(D_o + D_i)} = \frac{(D_o - D_i)(D_o + D_i)}{(D_o + D_i)} = (D_o - D_i) \tag{3.7}$$

$$Re = \frac{\dot{m}D_h}{A_{flow}\mu} = \frac{\dot{m}(D_o - D_i)}{\frac{\pi}{4}(D_o^2 - D_i^2)\mu} = \frac{4\dot{m}(D_o - D_i)}{\pi(D_o - D_i)(D_o + D_i)\mu} = \frac{4\dot{m}}{\pi(D_o + D_i)\mu} \tag{3.8}$$

The mass flow rate was converted to kg/s and used to calculate the Reynolds number. The flow was turbulent, so the Gnielinski correlation [Hallquist, 2011] was used to find the Nusselt number. The correlation is valid for a Prandtl number between 0.5 and 1000 and for a Reynolds number between 3,000 and 5E6. The values for both are well within the ranges, so this correlation is applicable. The Darcy friction factor (Equation 3.9) was calculated for use in the Gnielinski correlation (Equation 3.10).

$$f_{Darcy} = \frac{0.25}{\left\{log_{10}\left[\frac{\varepsilon}{3.7D_h} + \frac{5.74}{Re^{0.9}}\right]\right\}^2} \quad 3.9$$

$$Nu_{Gnielinski} = \frac{(f/8)(Re - 1000)Pr}{1 + 12.7(f/8)^{0.5}\left(Pr^{2/3} - 1\right)} \quad 3.10$$

Equations 3.11 through 3.13 were used to calculate the heat transfer coefficient and heat removed by the heat exchanger. The fluid temperature is assumed to be 60°C for the calculation of heat removed.

$$h = Nu * \frac{k}{D_h} \quad 3.11$$

$$A_{surface} = \pi D_i L_{hx} \quad 3.12$$

$$Q = h * A_{surface} * (T_w - T_s) \quad 3.13$$

Table 3.2 below shows the results of the calculations for the secondary side heat transfer coefficient.

Table 3.2 Secondary Side Heat Transfer Coefficient Results

	for 3 gal/min flow	for 6 gal/min flow	Units
flow rate	0.189	0.378	(kg/s)
Re	3289	6578	(-)
Darcy friction factor	0.043	0.035	(-)
Nusselt number	25.9	55.2	(-)
heat transfer coefficient	1021.7	2176.0	W/m^2-K
heat removed	2237	4763	W

For the heated section, the actual power level from the experiment is put into the code to ensure that the code and the experiment are solving the same problem. For each of the piping sections, the ambient air temperature and the heat transfer coefficient for heat lost to ambient are measured in the experiment and put into the code.

The heat lost to the ambient air with no insulation was estimated. The radiation heat losses were found to be negligible compared to the natural convection heat losses. The natural convection heat losses were estimated using the Grashoff, Prandlt, and Raleigh numbers found for the ambient air around the loop given by Equations 2.14 and 3.15.

$$Gr = \frac{g\beta(T_w - T_{out})D^3}{\nu^2} \quad 3.14$$

$$Ra = Gr \cdot Pr \quad 3.15$$

The values used in the calculations are shown in the Table 3.3.

Table 3.3 Parameters for Air at 40°C

g	9.81	m/s^2
β	3.2E-3	K^{-1}
D	0.0255	m
ν	1.7E-5	m^2/s
Pr	0.711	-

Various Nusselt number correlations were used to get an idea of what the heat transfer coefficient should be. The Nusselt number for horizontal pipes and another correlation were tested and are shown as Equation 3.16 and 3.17 respectively.

$$Nu_{horiz} = 0.125 * Ra^{0.333} \quad 3.16$$

$$Nu = \frac{0.707 * Gr^{0.25} * 0.75 * Pr^{0.5}}{(0.609 + 1.221 * Pr^{0.5} + 1.238 * Pr)^{0.25}} \quad 3.17$$

The heat transfer coefficient ranged along the loop from about 5 – 10 W/m^2-K, so these are the values tested in the code.

The initial conditions needed by the models in the code are the fluid and wall temperatures for each piece and the flow rate in the loop. These were measured using thermocouples and a flow meter respectively. The SRQs were the flow rate and temperatures of the fluid and wall. The measurements were taken at certain time intervals during operation of the loop to ensure a useful comparison to the results from the code. The location of the thermocouples is described in chapter 4.

The loss coefficients for the tees and the ball valves were obtained from Rennels [2012]. The edges inside the tees are sharp which means their *r/d* value is zero. This was used to find the loss factor for flow to and from the branch. Flow was assumed to be zero in the 3rd leg of the tee. The *k* value for run to branch was 1.2 and the value for branch to run was 1.1. The flow through just the run has very little loss with a *k* value of 0.05 to account for slight effect of the brief change in diameter. The ball valve has a constant inner diameter and the k value was found to be 0.02.

There are tees on each corner of the loop. The vertical and horizontal components of the tees are modeled in separate pieces to account for the orientation. The loss coefficients for the tees at the corners of the loop were split between the two pieces that model it. For the rest of the pieces, the k value for each of the components was added to get the total loss coefficient for each piece. The high uncertainties associated with loss coefficient values are discussed in the conclusion as a potentially significant source of error. Methods for reducing the effect of the uncertainty on the results are discussed as potential future work.

The primary fluid modeled in the loop was water. The fluid properties used in the code were density in kg/m^3, thermal conductivity in W/m-K, dynamic viscosity in Pa-s, and specific heat in J/kg-K shown as Equations 3.18 through 3.21 respectively. The

temperature dependent properties for water were found by interpolating data for water at 0.10132 MPa obtained from NIST [Secretary of Commerce, 2011]. The units are K for temperature, kg/m^3 for density, W/m-K for thermal conductivity, Pa-s for viscosity, and J/kg-K for specific heat.

$$\rho = -0.00353 * T^2 + 1.85 * T + 757.95 \quad 3.18$$

$$k = -9.57 * 10^{-6} * T^2 + 7.38 * 10^{-3} * t - 0.741 \quad 3.19$$

$$\mu = 1.847 * 10^{-7} * T^2 - 1.32 * 10^{-4} * T + 0.0239 \quad 3.20$$

$$Cp = 2.786 * 10^{-6} * T^4 - 0.00374 * T^3 + 1.8876 * T^2 - 424 * T + 39910 \quad 3.21$$

The geometry of a natural circulation loop is put into the code by means of an input text file. The loop is separated into a number of *pieces* based on the physical connections in the loop. For example, different diameter pipes, a heated section, or a heat exchanger would each be their own separate piece.

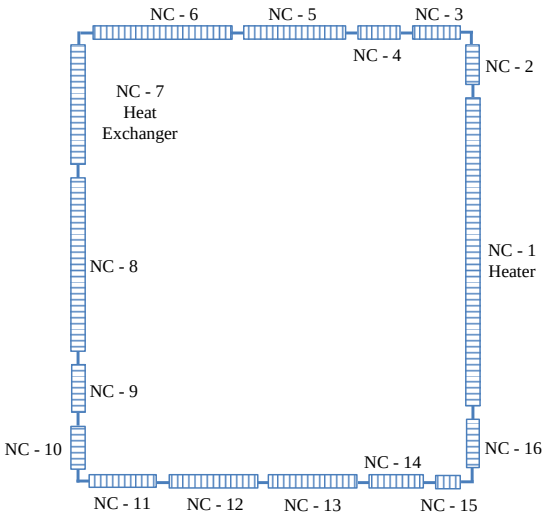

Figure 3.1 Nodalization of Heat Transfer Loop

The length, diameter, orientation, number of nodes, initial fluid and wall temperatures, designation (heater, heat exchanger or pipe), minor loss coefficient, thickness, power, heat transfer coefficient, and ambient temperature for each piece are detailed in the input file. Each piece is broken up evenly into the number of *nodes*

specified in the input file for it. The values of each parameter listed for the piece are assigned to each of the nodes in that piece. An example of the nodalization for the experimental loop is shown in Figure 3.1.

3.2.2 Analytical benchmark verification for steady state

A benchmark run involving a simple, rectangular loop with a constant diameter was performed to compare results from the code to an analytical solution. Water was used as both the primary and secondary fluids. Figure 3.2 shows a schematic of the geometry used for the benchmark test. The analytical solution was derived based on an analytical solution previously compared with LeBENC. This allowed for a comparison with LeBENC results as well as the analytical results. The derivation of the analytical solution is detailed in the following section.

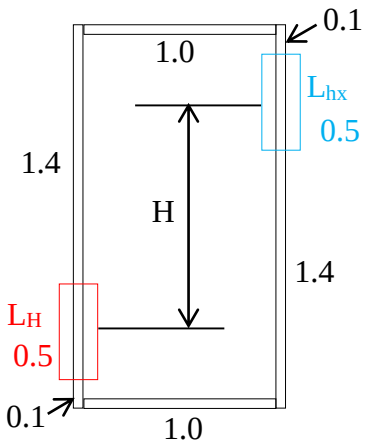

Figure 3.2 Benchmark Test Geometry

The assumptions for the analytical solution are listed below.

- Heat loss through pipes is negligible everywhere except the heat exchanger
- No axial thermal diffusion in the fluid or the pipes

- No radial thermal resistance in the pipe
- The loop is at steady state
- The Boussinesq approximation is valid

The input parameters and properties used in the benchmark test are shown in Table 3.4.

Table 3.4 Properties Used in Benchmark Test

Properties		
D_i	0.02	Inner diameter (m)
D_o	0.022	Outer diameter (m)
L_{hx}	0.5	Heat exchanger length (m)
L_h	0.5	Heater length (m)
L_{total}	6	Total loop length (m)
H	1.3	Centerline elevation difference (m)
Q_H	50(100)	Heater power (W)
ρ_0	1000	Water density (kg/m^3)
Cp	4200	Water specific heat (J/kg-K)
k	0.61	Water thermal conductivity (W/m-K)
β	0.0005	Water thermal expansion (K^{-1})
μ	0.001	Water dynamic viscosity (Pa-s)
g	9.81	Gravity (m/s^2)
k_{loss}	2	Loss coefficient
T_s	30	Secondary side temperature (°C)
h_o	250	Heat exchanger heat transfer coefficient (W/m^2-K)
Nu	3.66	Nusselt number for constant wall temperature

The steady state flow rate is solved analytically from the simplified momentum equation. The momentum equation for 1-D incompressible flow neglecting viscous dissipation and assuming the Bousinessq approximation to be valid is given below as Equation 3.22.

$$\sum_{j=1}^{N} \frac{\Delta x_j}{A_{in,j}} \frac{dW}{dt} = -\sum_{j=1}^{N} \left(\frac{\frac{f_j \Delta x_j}{D_{i,j}} + k_{loss,j}}{2\rho_0 A_{in,j}^2} \right) W^2 + \rho_0 g \beta \int T dz \qquad 3.22$$

The last term is the temperature integral and can be approximated using Equation 3.23.

$$\int Tdz = \int_{z=0}^{H} T_{hl}dz + \int_{z=H}^{0} T_{cl}dz = H(T_{hl} - T_{cl}) \quad 3.23$$

Using the advection equation, the temperature integral can be written in terms of the centerline elevation difference, H; the heater power, Q_H; the flow rate, W; and the specific heat, Cp as is shown in Equation 3.24.

$$Q_H = WCp(T_{hl} - T_{cl}) \rightarrow \int Tdz = \frac{HQ_H}{WCp} \quad 3.24$$

Substituting for the temperature integral and solving for the steady state flow rate gives Equation 3.25.

$$W = \left[\frac{2g\beta\rho_0^2 A_{in}^2 HQ_H}{\left(\frac{fL_{total}}{D_i} + k_{loss}\right)Cp}\right]^{1/3} \quad 3.25$$

The Darcy friction factor, f, depends on the Reynolds number (Equation 3.26) which depends on the flow rate (Equation 3.27), so an iterative approach is required.

$$Re = \frac{4W}{\pi\mu D_i} \quad 3.26$$

The flow regime is laminar, so the friction factor can be solved using the equation below.

$$f = \frac{64}{Re} \quad 3.27$$

A new flow rate value was found and the process was repeated until a converged solution was obtained. The final values for the flow rate, friction factor, and Reynolds number for a heater power of 50W and 100W are shown in Table 3.5.

Table 3.5 Friction Factor, Flow Rate, and Reynold Number for 50 W and 100W

Q_H (W)	f	W	Re
50	0.15	0.00689	439
100	0.10	0.00966	615

The heat balance equations at the heater and heat exchanger are solved for the steady state hot and cold leg temperatures. The heat balance at the heated section reduces down to the advection equation, which is shown below and solved for the hot leg temperature. This is shown in Equation 3.28.

$$Q_H = W * Cp * \Delta T_H = W * Cp * (T_{hl} - T_{cl}) \rightarrow T_{hl} = T_{cl} + \frac{Q_H}{W * Cp} \quad 3.28$$

The rate at which the heat leaves through the heat exchanger depends on the overall heat transfer coefficient, LMDT, and heat transfer area. The secondary side of the heat exchanger is assumed to stay at a constant temperature from inlet to outlet. The expression for overall heat loss is given as Equation 3.29 below with the log mean temperature difference equation at constant temperature and the heat transfer coefficient assuming no thermal resistance in the axial direction of the pipe.

$$Q_{hx} = (UA) * \Delta T_{lm}; where\ UA = \frac{\pi * L_{hx}}{\frac{1}{D_i h_i} + \frac{1}{D_o h_o}}\ and\ \Delta T_{lm} = \frac{T_{cl} - T_{hl}}{ln\frac{T_{cl} - T_s}{T_{hl} - T_s}} \quad 3.29$$

The outside heat transfer coefficient, h_o, was a specified input and the internal heat transfer coefficient, h_i, was solved using the Nusselt number for internal laminar flow with constant temperature given below as Equation 3.30.

$$h_i = \frac{Nu * k}{D_i} = 111.63 \frac{W}{m^2 - K} \quad 3.30$$

The product (UA) was found to be 2.4944 W/K. The only remaining unknown quantities in the heat balance for the heater and the heat exchanger are the hot and cold leg temperatures. Rearranging the heat balance equation for the heater gives an expression for the difference between the cold and hot leg temperatures, which can be substituted into the heat balance equation for the heat exchanger. The heat balance equation at the heat exchanger can then be written with hot and cold leg temperatures on one side and known

quantities on the other. These forms of the heat balance equations at the heater and heat exchanger are given as Equations 3.31 and 3.32 respectively.

$$Q_H = W * Cp * \Delta T_H = W * Cp * (T_{hl} - T_{cl}) \rightarrow (T_{cl} - T_{hl}) = -\frac{Q_H}{(W * Cp)} \quad 3.31$$

$$Q_{hx} = (UA) * \frac{-Q_H/(W * Cp)}{ln\frac{T_{cl} - T_s}{T_{hl} - T_s}} \rightarrow ln\frac{T_{cl} - T_s}{T_{hl} - T_s} = -(UA) * \frac{Q_H/(W * Cp)}{Q_{hx}} \quad 3.32$$

Since there is assumed to be no heat loss through the pipes, the heat added by the heater, Q_H, and the heat removed by the heat exchanger, Q_{hx}, are equal and can be canceled in Equation 3.32. The LMTD is given in Equation 3.33 and used in solving Equation 3.32 for the cold leg temperature. This result is given as Equation 3.34. Equation 3.31 was solved for the hot leg temperature and written as Equation 3.35.

$$ln\frac{T_{cl} - T_s}{T_{hl} - T_s} = -\frac{(UA)}{W * Cp} \rightarrow \frac{T_{cl} - T_s}{T_{hl} - T_s} = e^{-\frac{(UA)}{W*Cp}} \quad 3.33$$

$$\rightarrow T_{cl} = T_s + (T_{hl} - T_s)e^{-\frac{(UA)}{W*Cp}} \quad 3.34$$

$$\rightarrow T_{hl} = T_{cl} + \frac{Q_H}{W * Cp} \quad 3.35$$

An iterative solution was found for the hot and cold leg temperatures from the heat balance equations for a heater power of 50 W and 100 W. Table 3.6 shows the results for the steady state temperatures and flow rate from the analytical solution described above and the analytical solution performed at BARC to compare with LeBENC.

Table 3.6 Analytical Results and Comparison

	Cold Leg Temp		Hot Leg Temp		Flow Rate	
Power	50W	100W	50W	100W	50W	100W
New analytical	49.19	68.87	50.92	71.33	0.00689	0.00966
BARC analytical	48.15	66.6	49.9	69.1	0.00689	N/A
Percent difference	2.16	3.41	2.04	3.23	0	N/A

The benchmark test was run with the FLiBeNC code to compare to the analytical solution. The same explicit discretization used in LeBENC was used in the benchmark runs in FLiBeNC for a more similar comparison. The code was run with a heater power of 50 W to steady state and then the heater power was increased to 100 W and allowed to continue to run until the new steady state is reached. The transient temperatures and flow rate were recorded, but only the steady state values could be compared to the analytical solution. The temperatures along the loop were solved for both the inline heating case and the resistive heating case. The inline heating case was solved to match the solution method used in LeBENC and the resistive heating case was solved to more closely match the validation experiment. The steady state solution is the same for both cases. Figures 3.3 and 3.4 below show the transient temperatures and flow rate for inline heating starting at 50 W and increasing to 100 W after 40000 seconds.

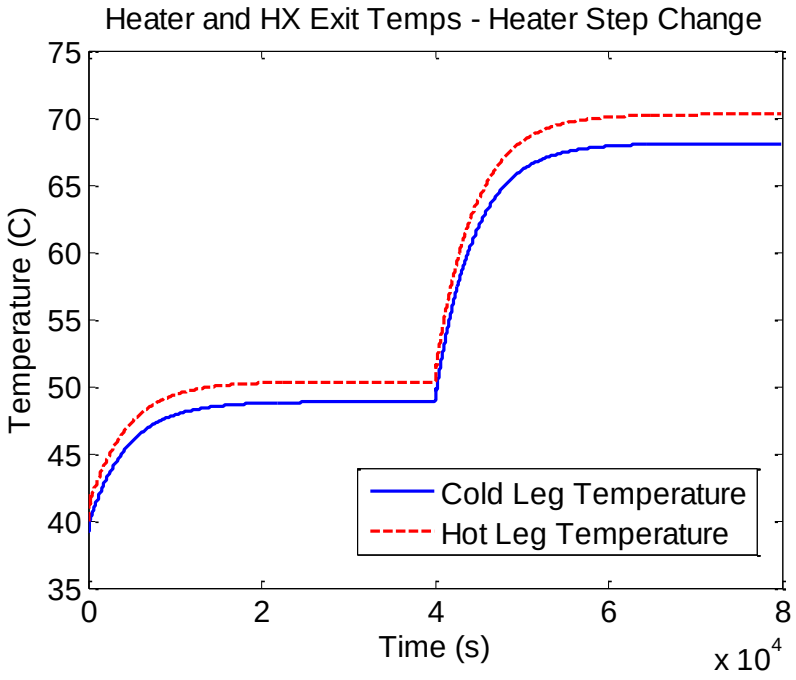

Figure 3.3 Cold leg and Hot leg temperatures for 50W to 100W

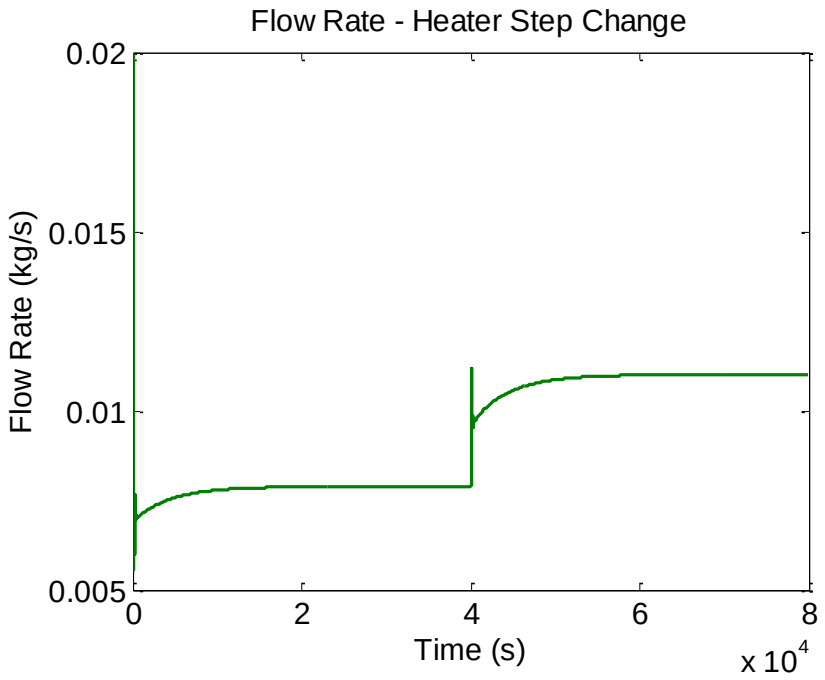

Figure 3.4 Flow rate for 50W to 100W

Table 3.7 shows the results for the steady state temperatures and flow rate from the FLiBeNC and LeBENC codes. The values for the LeBENC results are from a document put together by researchers at BARC, for comparing their analytical solution to LeBENC. The last row shows the difference between the two codes' solutions.

Table 3.7 Code Results From Analytical Study

	Cold Leg Temp		Hot Leg Temp		Flow Rate	
Power	50W	100W	50W	100W	50W	100W
FLiBeNC	48.85	68.09	50.36	70.26	0.00788	0.0110
LeBENC	48.45	67.4	49.8	69.45	N/A	N/A
Percent difference	0.8255934	1.02374	1.1245	1.16631	N/A	N/A

3.2.3 Equations and assumptions with validity or suitability arguments

FLiBeNC models a single-phase one-dimensional natural circulation loop with incompressible flow neglecting viscous dissipation. The one-dimensional single-phase model matches the validation experiment much more closely than the current LWR codes. For incompressible flow, the one-dimensional mass conservation equation reduces down

to a mass flow rate that is independent of position around in the loop. The fluid and solid energy equations in terms of heat balance are given below as Equations 3.36 and 3.37 respectively.

$$\frac{\rho Cp\pi LD_{in}^2}{4}\frac{\partial T_f}{\partial t} = \frac{k\pi LD_{in}^2}{4}\frac{\partial^2 T_f}{\partial x^2} - \pi LD_{in}h_{in}\left(T_f - T_w\right) - \dot{m}CpL\frac{\partial T_f}{\partial x} \tag{3.36}$$

$$\rho_w Cp_w \frac{\pi L(D_o^2 - D_{in}^2)}{4}\frac{\partial T_w}{\partial t} = k_w \frac{\pi L(D_o^2 - D_{in}^2)}{4}\frac{\partial^2 T_w}{\partial x^2} + \pi LD_{in}h_{in}\left(T_f - T_w\right) + \pi LD_o h_{out}\left(T_{out} - T_w\right) + Q_{heater} \tag{3.37}$$

The term on the LHS of each equation is the heat capacity term with the different cross sectional areas of each defined in terms of diameters. The first term on the RHS of each equation is the conduction term, which accounts for conduction in the axial direction. The second term in each of the equations is the heat transferred between the fluid and the wall expressed in terms of the heat transfer coefficient. The two terms are the same except the sign is reversed. The last term in Equation 3.36 is the advection term. The third term on the RHS of Equation 3.37 is the heat lost to the ambient air expressed in terms of an overall heat transfer coefficient. The last term in Equation 3.37 is the source term in watts per second from the resistive heating. Equations 3.36 and 3.37 were solved for the change in temperature with respect to time given as Equations 3.38 and 3.39 respectively. These equations are the final forms that were discretized and implemented into the code.

$$\frac{\partial T_f}{\partial t} = \alpha\frac{\partial^2 T_f}{\partial x^2} - \frac{4\dot{m}}{\rho\pi D_{in}^2}\frac{\partial T_f}{\partial x} + \frac{4h_{in}\left(T_w - T_f\right)}{\rho CpD_{in}} \tag{3.38}$$

$$\frac{\partial T_w}{\partial t} = \alpha_w \frac{\partial^2 T_w}{\partial x^2} + \frac{4h_{out}(T_{out} - T_w)}{\rho_w Cp_w} \frac{D_o}{(D_o^2 - D_{in}^2)} + \frac{4h_{in}(T_f - T_w)}{\rho_w Cp_w} \frac{D_{in}}{(D_o^2 - D_{in}^2)} + \frac{4Q_{heater}}{\rho_w Cp_w \pi L (D_o^2 - D_{in}^2)} \quad 3.39$$

The momentum equation given earlier as Equation 3.2 was rewritten in terms of the mass flow rate and modified to write the buoyancy term using the local density and defined as Equation 3.40 below.

$$\sum_{j=1}^{N} \frac{\Delta x_j}{A_{in,j}} \frac{dW}{dt} = -\left(\frac{W^2}{2}\right) \sum_{j=1}^{N} \left(\frac{f_j \Delta x_j}{D_{in,j}} + k_j\right) \frac{1}{\rho_j A_{in,j}^2} + g \sum_{j=1}^{N} \rho_j \Delta z_j \quad 3.40$$

This can be rewritten into Equation 3.41 below where C_1 is the inertial term, C_2 is the losses term, and C_3 is the buoyancy driven term.

$$C_1 \frac{dW}{dt} = -C_2 W^2 + C_3$$

$$Where,\ C_1 = \sum_{j=1}^{N} \frac{\Delta x_j}{A_{in,j}};\ C_2 = \sum_{j=1}^{N} \left(\frac{f_j \Delta x_j}{D_{in,j}} + k_j\right) \frac{1}{2\rho_j A_{in,j}^2};\ and\ C_3 = g \sum_{j=1}^{N} \rho_j \Delta z_j \quad 3.41$$

The momentum equation takes the buoyancy force and subtracts the friction and form losses to get the net driving pressure. This means that if the flow reverses, the friction term will be acting in the other direction. This was taken into account in the code by multiplying the losses term by the sign of the flow rate.

3.2.4 Numerical discretization of governing equations

In the original LeBENC code, the momentum equation was discretized implicitly and solved iteratively every time step until a converged solution was found. In the FLiBeNC code, it was re-discretized via the Crank Nicolson method to allow for an explicit, semi-implicit, or fully implicit solution. The semi and fully implicit versions were written in the

form of a quadratic equation which allowed the required time step for stability to be determined and the solution to be solved for directly every time step. If the explicit method is used, the solution is solved for directly in terms of known quantities. The losses term must be in the opposite direction of flow, so a variable ϖ representing the sign of the flow rate is used. The discretized momentum equation is developed in the section below in terms of the same coefficients C_1, C_2, and C_3 described above. Equation 3.42 is the momentum equation with the ϖ term included to represent direction of the friction force depending on the direction of flow.

$$C_1 \frac{dW}{dt} = -C_2 \varpi W^2 + C_3 \rightarrow \frac{dW}{dt} = -\frac{C_2}{C_1} \varpi W^2 + \frac{C_3}{C_1}$$

$$Where,\ C_1 = \sum_{j=1}^{N} \frac{\Delta x_j}{A_{in,j}};\ C_2 = \sum_{j=1}^{N} \left(\frac{f_j \Delta x_j}{D_{in,j}} + k_j \right) \frac{1}{2\rho_j A_{in,j}^2};\ and\ C_3 = g \sum_{j=1}^{N} \rho_j \Delta z_j \qquad 3.42$$

The equation is discretized into Equation 3.43 using the parameter θ so that the equation is explicit, semi implicit, or fully implicit when θ is 0, 1/2, or 1 respectively. The parameters C_2 and C_3 are functions of time, but the values from the new time step are used for simplicity.

$$\frac{W^{n+1} - W^n}{\Delta t} = \frac{\theta}{C_1} \left[-C_2 \varpi (W^{n+1})^2 + C_3 \right] + \frac{1-\theta}{C_1} \left[-C_2 \varpi (W^n)^2 + C_3 \right] \qquad 3.43$$

The explicit version of Equation 3.43 where θ equals zero is relatively straight forward to solve because it is only a function of known quantities from the previous time step. It is given as Equation 3.44 below.

$$W^{n+1} = W^n - \frac{C_2 \Delta t \varpi}{C_1} (W^n)^2 + \frac{C_3 \Delta t}{C_1} \qquad 3.44$$

For the semi-implicit and fully implicit versions, Equation 3.43 is written in terms of a quadratic given in Equations 3.55 and 3.56.

$$C_2\frac{\theta\Delta t}{C_1}\varpi(W^{n+1})^2 + W^{n+1} - W^n - C_3\frac{\theta\Delta t}{C_1} + C_2\frac{(1-\theta)\Delta t}{C_1}\varpi(W^n)^2 - C_3\frac{(1-\theta)\Delta t}{C_1} = 0 \quad 3.55$$

$$a(W^{n+1})^2 + bW^{n+1} + c = 0$$

$$where\ a = C_2\frac{\theta\Delta t}{C_1}\varpi;\ b = 1;\ and\ c = -W^n - C_3\frac{\theta\Delta t}{C_1} + C_2\frac{(1-\theta)\Delta t}{C_1}\varpi(W^n)^2 - C_3\frac{(1-\theta)\Delta t}{C_1} \quad 3.56$$

The flow rate value at the new time step can then be written in the following form as Equation 3.57.

$$W^{n+1} = \frac{-b \pm \sqrt{b^2 - 4ac}}{2a} \quad 3.57$$

To determine whether to add or subtract the determinant, the signs of possible solutions are explored. If the determinant is assumed to be subtracted so that the flow rate equation is of this form $W^{n+1} = \frac{-b-\sqrt{b^2-4ac}}{2a}$, then the flow will reverse signs every time step. This can be seen by noting that the terms *b* and *c* are always positive and the sign of *a* is the same as the sign of the flow rate from the previous time step. This means that if *a* is negative, the flow rate at the new time step would be positive and if *a* is positive, then the flow rate at the new time step would be negative. Looking at the other option of adding the determinant shows that the flow rate at the new time step could be either direction regardless of the direction in the previous time step. This is seen by taking $W^{n+1} = \frac{-b+\sqrt{b^2-4ac}}{2a}$ and realizing that since *a* is the only potential negative value, the overall calculation can end up positive or negative depending of the magnitude of the parameters *a*, *b*, and *c*. So, the equation used in the code is Equation 3.58.

$$W^{n+1} = \frac{-b + \sqrt{b^2 - 4ac}}{2a} \quad 3.58$$

For the flow rate calculation, W^{n+1} to be real, the discriminant must be greater than or equal to zero. Solving this gives Equation 3.59 below that leads to a quadratic equation in the time step.

$$1^2 - 4C_2\frac{\theta\Delta t}{C_1}\varpi\left[-W^n - C_3\frac{\theta\Delta t}{C_1} + C_2\frac{(1-\theta)\Delta t}{C_1}\varpi(W^n)^2 - C_3\frac{(1-\theta)\Delta t}{C_1}\right] \geq 0 \qquad 3.59$$

This can be reduced to the quadratic equation in the form $E(\Delta t)^2 + F\Delta t + G \geq 0$ where E, F, and G are constants defined below.

$$E = 4C_2\frac{\theta}{C_1}\varpi\left[-C_3\frac{\theta}{C_1} + C_2\frac{(1-\theta)}{C_1}\varpi(W^n)^2 - C_3\frac{(1-\theta)}{C_1}\right]$$

$$F = (4C_2\frac{\theta}{C_1}\varpi W^n;\ G = 1$$

To ensure that the flow rate calculation results in a real value, the inequality $E(\Delta t)^2 + F\Delta t + G \geq 0$ must be true. This means the time step requirement depends on the coefficients E and F since G is always one. If they exist, the zeros of the equation are solved for using the quadratic formula. Then, the ranges of Δt values that result in a real solution for the flow rate are determined. This is shown in Equation 3.60.

$$zero_1 = \frac{-F + \sqrt{F^2 - 4EG}}{2E}\ and\ zero_2 = \frac{-F - \sqrt{F^2 - 4EG}}{2E} \qquad 3.60$$

If E is positive and two zeros exist, than any value of Δt that is not between the zeros will result in a real solution for the flow rate. If E is positive and fewer than two zeros exist, than any value of Δt will result in a real solution for the flow rate. If E is negative and two zeros exist, than any value of Δt that is between the zeros will result in a real solution for the flow rate. If E is negative and fewer than two zeros exist, than there is no value of Δt that will result in a real solution for the flow rate. This is summed up in the expressions below.

If $E < 0$ then $\frac{-F+\sqrt{F^2-4EG}}{2E} \leq \Delta t \leq \frac{-F-\sqrt{F^2-4EG}}{2E}$ for wn to be real

If $E > 0$ then $\Delta t \leq \frac{-F-\sqrt{F^2-4EG}}{2E}$ or $\Delta t \geq \frac{-F+\sqrt{F^2-4EG}}{2E}$ for wn to be real

If the zeros do not exist, then the flow rate will always be real for E > 0 and never be real for $E < 0$. If $E = 0$ then the time step depends only on F which is shown below in Equation 3.61.

$$F\Delta t + 1 \geq 0 \rightarrow \Delta t \geq \frac{-1}{F} \tag{3.61}$$

The energy equations were both discretized in time using the same θ parameter to allow for explicit, semi-implicit, or implicit solutions still using material property values from the new time step. Again, if θ is set equal to 0, 1/2, or 1, then the solution is explicit, semi-implicit, or impact respectively. The discretization in space was done assuming a constant mesh in the original LeBENC code. This is not the case because of the way the mesh is created. For the FLiBeNC code, a discretization scheme allowing for varying mesh spacing was found following the format in Randall [2013]. The equations from this paper are described below starting with the generalized form of a finite difference approximation of a first order derivative shown in Equation 3.62.

$$\frac{\partial T}{\partial x} \cong \sum_{k=-\infty}^{\infty} b_{j,k} T\left(x_{j+k}\right) \tag{3.62}$$

The coefficient $b_{j,k}$ is a function of space to allow the grid spacing to vary. Equation 3.63 shows a Taylor series expansion done for a variable mesh.

$$T\left(x_{j+k}\right) = T(x,t) + \left(x_{j+k} - x_j\right)\frac{\partial T}{\partial x} + \frac{\left(x_{j+k} - x_j\right)^2}{2!}\frac{\partial^2 T}{\partial x^2} + \frac{\left(x_{j+k} - x_j\right)^3}{3!}\frac{\partial^3 T}{\partial x^3} \ldots \tag{3.63}$$

Substituting Equation 3.63 into Equation 3.62 gives Equation 3.64.

$$\frac{\partial T}{\partial x} \cong \sum_{k=-\infty}^{\infty} b_{j,k}\left[T(x,t) + \left(x_{j+k} - x_j\right)\frac{\partial T}{\partial x} + \frac{\left(x_{j+k}-x_j\right)^2}{2!}\frac{\partial^2 T}{\partial x^2} + \frac{\left(x_{j+k}-x_j\right)^3}{3!}\frac{\partial^3 T}{\partial x^3} \ldots\right] \tag{3.64}$$

The accuracy depends on how many terms are used and the smoothness of the solution. The general form for accuracy of at least nth order is given in Equation 3.65

$$\sum_{k=-\infty}^{\infty} b_k \left(x_{j+k} - x_j\right)^m = \delta_{m,1} \text{ for all j, and for } 0 \le \text{m} \le \text{n} \qquad 3.65$$

This equation for accuracy gives a way to determine the coefficients b_k. Following a similar approach, the second derivate approximation can be written as Equation 3.66 and 3.67.

$$\frac{\partial^2 T}{\partial x^2} \cong \sum_{k=-\infty}^{\infty} c_{j,k} T\left(x_{j+k}\right) \qquad 3.66$$

$$\frac{\partial^2 T}{\partial x^2} \cong \sum_{k=-\infty}^{\infty} c_{j,k} \left[T(x,t) + \left(x_{j+k} - x_j\right) \frac{\partial T}{\partial x} + \frac{\left(x_{j+k} - x_j\right)^2}{2!} \frac{\partial^2 T}{\partial x^2} + \frac{\left(x_{j+k} - x_j\right)^3}{3!} \frac{\partial^3 T}{\partial x^3} \ldots \right] \qquad 3.67$$

The accuracy requirements are given by Equation 3.68.

$$\sum_{k=-\infty}^{\infty} c_{j,k} \left(x_{j+k} - x_j\right)^m = (2!)\delta_{m,2} \text{ for all j, and for } 0 \le \text{m} \le \text{n+1} \qquad 3.68$$

Again, the accuracy equation is used to determine the coefficients $c_{j,k}$. For first order accuracy, the equation for the first derivative boils down to the same equation that is used for a constant mesh because only two points are used for each calculation. The derivation of this for the advection term in the fluid energy equation for forward (Equations 3.69 through 3.72) or reverse (Equations 3.73 through 3.75) flow is shown below. From Equation 3.64 using the points at j and j -1 for the forward direction and the points j and j+1 for the reverse direction, the approximation can be written as Equations 3.69 and 3.72. Using Equation 3.65, expressions for the b coefficients can be written as Equations 3.70 and 3.73 for first order accuracy. Equations 3.71 and 3.74 show the results of solving for

the coefficients and Equations 3.72 and 3.75 show the final result for the forward and reverse flow profiles.

$$\frac{\partial T}{\partial x}_{forward} = b_{j,0}T_j^n + b_{j,-1}T_{j-1}^n \quad 3.69$$

$$b_{j,0} + b_{j,-1} = 0 \; and \; b_{j,-1}\left(x_{j-1} - x_j\right) = 1 \quad 3.70$$

$$b_{j,-1} = \frac{1}{\left(x_{j-1} - x_j\right)}; and \; b_{j,0} = \frac{-1}{\left(x_{j-1} - x_j\right)} \quad 3.71$$

$$\frac{\partial T}{\partial x}_{forward} = \frac{1}{\left(x_j - x_{j-1}\right)}T_j^n + \frac{-1}{\left(x_j - x_{j-1}\right)}T_{j-1}^n \quad 3.72$$

$$\frac{\partial T}{\partial x}_{reverse} = b_{j,1}T_{j+1}^n + b_{j,0}T_j^n \quad 3.73$$

$$b_{j,0} = \frac{-1}{\left(x_{j+1} - x_j\right)} \; and \; b_{j,1} = \frac{1}{\left(x_{j+1} - x_j\right)} \quad 3.74$$

$$\frac{\partial T}{\partial x}_{reverse} = \frac{1}{\left(x_{j+1} - x_j\right)}T_{j+1}^n + \frac{-1}{\left(x_{j+1} - x_j\right)}T_j^n \quad 3.75$$

The mesh spacing at node j is defined to be $\Delta x_j = x_{j+1} - x_j$ and similarly the spacing at node $j-1$ is defined to be $\Delta x_{j-1} = x_j - x_{j-1}$. These definitions were substituted into Equations 3.72 and 3.75 and simplified into equations 3.76 and 3.77 below.

$$\frac{\partial T}{\partial x}_{forward} = \frac{1}{\Delta x_{j-1}}T_j^n + \frac{-1}{\Delta x_{j-1}}T_{j-1}^n = \frac{T_j^n - T_{j-1}^n}{\Delta x_{j-1}} \quad 3.76$$

$$\frac{\partial T}{\partial x}_{backward} = \frac{1}{\Delta x_j}T_{j+1}^n + \frac{-1}{\Delta x_j}T_j^n = \frac{T_{j+1}^n - T_j^n}{\Delta x_j} \quad 3.77$$

The diffusion term in both the fluid and solid energy equations has a second order derivative in space. The method outlined for the discretization of a second order derivative outlined previously was used to approximate the diffusion derivative to first order

accuracy. Equation 3.68 for the second order accuracy leads to Equation 3.78 for first order accuracy.

$$\sum_{k=-\infty}^{\infty} c_{j,k} = 0; \quad \sum_{k=-\infty}^{\infty} c_{j,k}\left(x_{j+k} - x_j\right) = 0; \quad \sum_{k=-\infty}^{\infty} c_{j,k}\left(x_{j+k} - x_j\right)^2 = 2! \tag{3.78}$$

The points j, $j-1$, and $j+1$ were used which reduces the Equation 3.78 into the set of Equations 3.79 through 3. 81 that can be solved for $c_{j,-1}, c_{j,0}$, and $c_{j,1}$.

$$c_{j,-1} + c_{j,0} + c_{j,1} = 0; \tag{3.79}$$

$$-c_{j,-1}\left(x_j - x_{j-1}\right) + c_{j,1}\left(x_{j+1} - x_j\right) = 0; \tag{3.80}$$

$$c_{j,-1}\left(x_j - x_{j-1}\right)^2 + c_{j,1}\left(x_{j+1} - x_j\right)^2 = 2!; \tag{3.81}$$

Solving these equations gives $c_{j,-1}, c_{j,0}$, and $c_{j,1}$ as Equations 3.82 through 3.84 in terms of the delta x values as defined before.

$$c_{j,-1} = \frac{2}{\left(\Delta x_{j-1}\right)^2 + \left(\Delta x_{j-1}\right)\left(\Delta x_j\right)} \tag{3.82}$$

$$c_{j,1} = \frac{2}{\left(\Delta x_j\right)^2 + \left(\Delta x_{j-1}\right)\left(\Delta x_j\right)} \tag{3.83}$$

$$c_{j,0} == -\frac{2}{\left(\Delta x_{j-1}\right)\left(\Delta x_j\right)} \tag{3.84}$$

This diffusion derivative is defined in terms of Equation 3.85 below.

$$\frac{\partial^2 T}{\partial x^2} = \frac{2}{\left(\Delta x_{j-1}\right)^2 + \Delta x_{j-1}\Delta x_j} T_{j-1} - \frac{2}{\Delta x_{j-1}\Delta x_j} T_j + \frac{2}{\left(\Delta x_j\right)^2 + \Delta x_{j-1}\Delta x_j} T_{j+1} \tag{3.85}$$

The fluid and wall energy equations discretized in time using the θ parameter and space using the variable mesh discretization are given as Equations 3.86 and 3.87 respectively. The fluid energy equation is shown with the advective term discretized for positive or negative flow.

$$\frac{T_j^{n+1}-T_j^n}{\Delta t}=\theta\left[\alpha\left(\frac{2}{\left(\Delta x_{j-1}\right)^2+\Delta x_{j-1}\Delta x_j}T_{j-1}^{n+1}-\frac{2}{\Delta x_{j-1}\Delta x_j}T_j^{n+1}+\frac{2}{\left(\Delta x_j\right)^2+\Delta x_{j-1}\Delta x_j}T_{j+1}^{n+1}\right)+Advective^{n+1}-\frac{4h_{in,j}T_j^{n+1}}{D_{in,j}\rho_0 Cp}+\frac{4h_{in,j}T_{w,j}^{n+1}}{D_{in,j}\rho_0 Cp}\right]+(1-\theta)\left[\alpha\left(\frac{2}{\left(\Delta x_{j-1}\right)^2+\Delta x_{j-1}\Delta x_j}T_{j-1}^{n}-\frac{2}{\Delta x_{j-1}\Delta x_j}T_j^{n}+\frac{2}{\left(\Delta x_j\right)^2+\Delta x_{j-1}\Delta x_j}T_{j+1}^{n}\right)+Advective^{n}-\frac{4h_{in,j}T_j^{n}}{D_{in,j}\rho_0 Cp}+\frac{4h_{in,j}T_{w,j}^{n}}{D_{in,j}\rho_0 Cp}\right] \quad 3.86$$

$$W>0: Advective=-\frac{W}{\rho_0 A_{in,j}}\left(\frac{T_j-T_{j-1}}{\Delta x_{j-1}}\right) \text{ and } W<0: Advective=-\frac{W}{\rho_0 A_{in,j}}\left(\frac{T_{j+1}-j}{\Delta x_j}\right)$$

$$\frac{T_{w,j}^{n+1}-T_{w,j}^n}{\Delta t}=\theta\left[\alpha_w\left(\frac{2}{\left(\Delta x_{j-1}\right)^2+\Delta x_{j-1}\Delta x_j}T_{w,j-1}^{n+1}-\frac{2}{\Delta x_{j-1}\Delta x_j}T_{w,j}^{n+1}+\frac{2}{\left(\Delta x_j\right)^2+\Delta x_{j-1}\Delta x_j}T_{w,j+1}^{n+1}\right)-\frac{4h_{in,j}T_{w,j}^{n+1}}{\rho_w Cp_w}\left(\frac{D_{in,j}}{D_{o,j}^2-D_{in,j}^2}\right)+\frac{4h_{in,j}T_j^{n+1}}{\rho_w Cp_w}\left(\frac{D_{in,j}}{D_{o,j}^2-D_{in,j}^2}\right)-\frac{4h_o T_{w,j}^{n+1}}{\rho_w Cp_w}\left(\frac{D_{in,j}}{D_{o,j}^2-D_{in,j}^2}\right)+\frac{4h_o T_o}{\rho_w Cp_w}\left(\frac{D_{in,j}}{D_{o,j}^2-D_{in,j}^2}\right)+\frac{4Q_{heater}/L}{\rho_w Cp_w\left(D_{o,j}^2-D_{in,j}^2\right)}\right]+(1-\theta)\left[\alpha_w\left(\frac{2}{\left(\Delta x_{j-1}\right)^2+\Delta x_{j-1}\Delta x_j}T_{w,j-1}^{n}-\frac{2}{\Delta x_{j-1}\Delta x_j}T_{w,j}^{n}+\frac{2}{\left(\Delta x_j\right)^2+\Delta x_{j-1}\Delta x_j}T_{w,j+1}^{n}\right)-\frac{4h_{in,j}T_{w,j}^{n}}{\rho_w Cp_w}\left(\frac{D_{in,j}}{D_{o,j}^2-D_{in,j}^2}\right)+\frac{4h_{in,j}T_j^{n}}{\rho_w Cp_w}\left(\frac{D_{in,j}}{D_{o,j}^2-D_{in,j}^2}\right)-\frac{4h_o T_{w,j}^{n}}{\rho_w Cp_w}\left(\frac{D_{in,j}}{D_{o,j}^2-D_{in,j}^2}\right)+\frac{4h_o T_o}{\rho_w Cp_w}\left(\frac{D_{in,j}}{D_{o,j}^2-D_{in,j}^2}\right)+\frac{4Q_{heater}/L}{\rho_w Cp_w\left(D_{o,j}^2-D_{in,j}^2\right)}\right] \quad 3.87$$

The discretization of the energy equations is first order accurate in space and explicit, semi implicit, or fully implicit in time.

3.2.5 Solution method

First, the initial conditions, boundary conditions, wall material properties, and solution parameters are read in from a user supplied text file. If the equations solved are explicit, then the solution procedure is completed once for each time step so the new values can be found based on known quantities from the last time step. If the equations to be solved are implicit or semi implicit, then a convergence criteria is added so the equations are solved until a converged solution is reached. Either way, the same general solution method applies. For each time step iteration, the following steps are taken:

1. The fluid material properties are found based on the fluid temperature.
2. If the energy equations are discretized explicitly, the minimum of the required wall and fluid time step is found and set as the new time step value.
3. The wall conduction equation is solved for the wall temperature at each node.
4. The fluid energy equation is solved for the fluid temperature at each node.
5. The density integral in the momentum equation is approximated.
6. The momentum equation is solved for the mass flow rate. The time step is reset if it is outside the bounds of stability for the implicit or semi implicit cases.
7. The heat transfer coefficient is calculated based on the flow characteristics.
8. The time is increased by one time step and the process repeats until a user specified maximum is reached.

3.3 Sensitivity studies

The code was tested to see what parameters the solution was sensitive to. These parameters were categorized into a test matrix with four main categories: nodalization,

geometry, inputs, and numerical methods. The parameters are numbered under their corresponding subcategory and are referenced by the Roman numeral of the main category, the letter of the subcategory, and the number of the parameter. The test matrix is shown below.

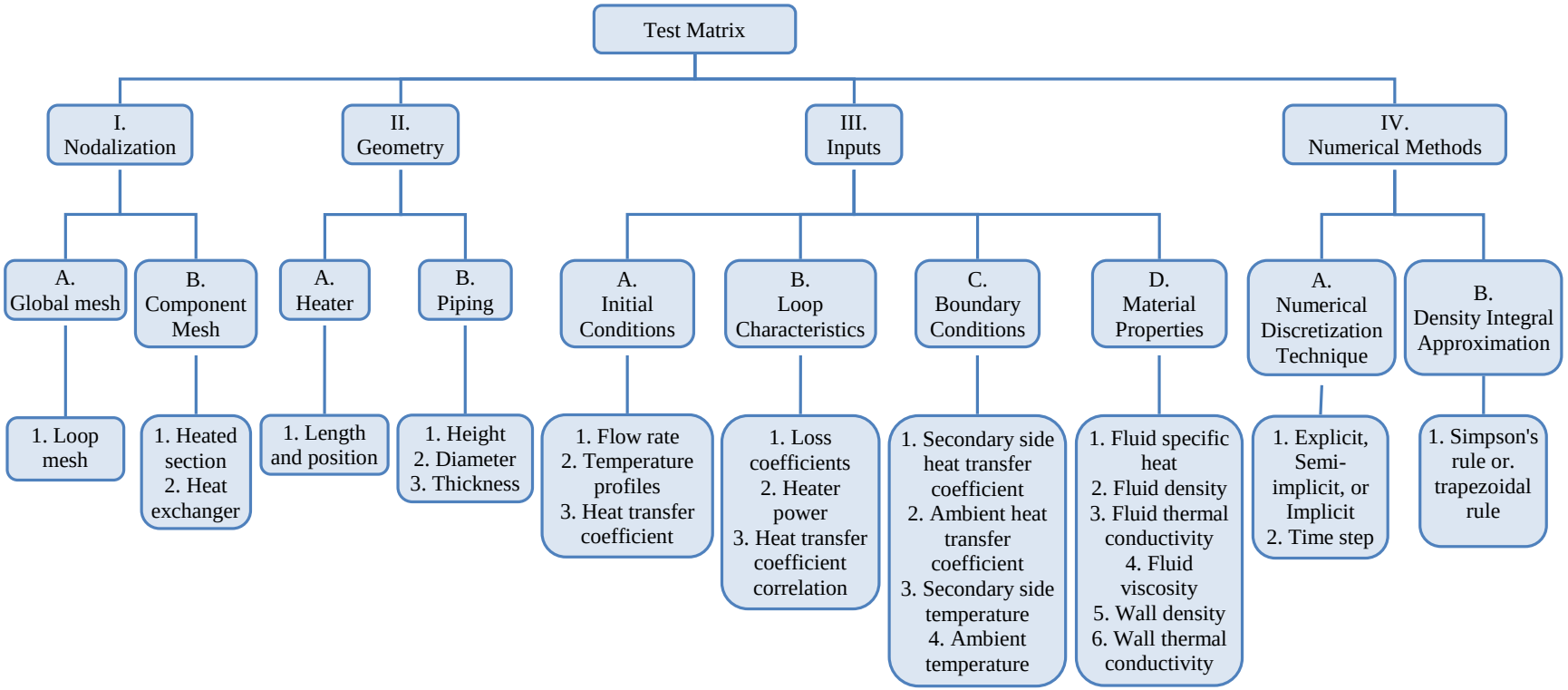

Figure 3.5 Sensitivity Test Matrix

For most of the studies, only one parameter was changed and the others were held constant. In a few of the studies, two closely related parameters were changed together. Most of the tests involved running the nominal case and two variations of the parameter of interest. The results of the studies are presented in Chapter 5. The geometry, parameters, and mesh used in the nominal case are described below.

The geometry for the nominal case was based on rough measurements of the experimental validation loop. The runs that were done to compare to the experimental data had more precise measurements. The nuts, fittings, and tubes were all lumped together into piping sections with an averaged diameter. The orientation of each piece was given a number corresponding to the direction of flow through that piece. The designations for positive vertical, negative vertical, positive horizontal, and negative horizontal were 1, 2, 3, and 4 respectively. The length, thickness, and orientation of each piece for the sensitivity studies are listed in Table 3.8. For the nominal mesh, the number of nodes for each piece was determined based on having a delta x smaller than 10 cm. The smallest even number of nodes (with a minimum of 2) that met this was used for the mesh. This method resulted in atypical values for node spacing, but gave the most consistent spacing around the loop without having an unrealistically fine mesh. The number of nodes for each piece had to be even so that Simpson's rule could be used to approximate the temperature integral and are listed in Table 3.8. The loss coefficients for the tees and the ball valves were obtained from Rennels [2012] as described in Section 3.2.1. The values obtained for each piece are listed Table 3.8.

Table 3.8 Sensitivity Test Geometry, Mesh, and Loss Factors for the Nominal Case

Piece	Length (m)	Thickness (m)	Orientation	# of Nodes	Loss Factor, K
1 Heater	2.34	0.00225	1	24	0
2 Pipe	0.073	0.0075	1	2	0.6
3 Pipe	0.094	0.0075	4	2	0.6
4 Pipe	0.03	0.044	4	2	0
5 Pipe	0.502	0.00422	4	6	0.6
6 Pipe	0.073	0.0075	2	2	0.55
7 HX	0.594	0.00225	2	6	0
8 Pipe	1.644	0.00323	2	18	0.15
9 Pipe	0.083	0.02050	2	2	0.02
10 Pipe	0.092	0..00642	2	2	0.6
11 Pipe	0.192	0.00425	3	2	0.6
12 Pipe	0.083	0.0205	3	2	0.02
13 Pipe	0.2125	0.00628	3	4	0.05
14 Pipe	0.03	0.044	3	2	0
15 Pipe	0.1085	0.0068	3	2	0.55
16 Pipe	0.073	0.0075	1	2	0.55

The heat transfer coefficient in the vertical pipes was modeled using the equations for Grashoff number, Raleigh number, and Nusselt number shown below [Totala, 2013].

$$\mathrm{Gr} = \frac{\beta g D_{in}^3 (T_w - T_f)\rho^2}{\mu^2}$$

$$\mathrm{Ra} = \mathrm{Gr} \cdot \mathrm{Pr}$$

$$\mathrm{Nu} = 0.59\mathrm{Ra}^{0.25}$$

For flow through the horizontal pipes, the Nusselt number correlation used depended on the values of the Reynolds number and the Prandtl number. For laminar flow, a value of 3.657 was used for the Nusselt number. The Dittus Boelter correlation (Equation 3.88) was used to find the Nusselt number whenever it gave a higher value than the one used for laminar flow.

$$Nu = 0.023 * Re^{0.8} Pr^{0.4} \qquad 3.88$$

The combinations of the Reynolds number and Prandtl number which resulted in a value higher than 3.657 from the Dittus Boelter correlation were found using Equation 3.89.

$$0.023 * Re^{0.8} Pr^{0.4} > 3.657 \qquad 3.89$$

If the constraint given by Equation 3.89 was met, the Dittus Boelter correlation was used. Otherwise, a value of 3.657 was used for the Nusselt number. The other parameters used in the sensitivity studies are given in Table 3.9. The fluid properties are temperature dependent where the temperature is in Kelvin.

Table 3.9 Sensitivity Studies Parameters for the Nominal Case

Parameters used	Value(s) and units
Initial flow rate	1E-16 kg/s
Initial fluid and wall temperatures	23℃
Heater power	1 kW for startup and 1.5 kW for heater step
Inner diameter	0.021 m
Secondary side heat transfer coefficient	1021.7 W/m^2-K
Ambient heat transfer coefficient	5 W/m^2-K
Secondary side temperature	15℃
Ambient temperature	23℃
Fluid specific heat	2.786E-6*T^4-3.74E-3*T^3+18876*T^2-424*T+39910 J/kg-K
Fluid density	-3.53E-3*T^2+1.85*T+757.95 kg/m^3
Fluid thermal conductivity	-9.57E-6*T^2+7.38E-3*T-0.741 W/m-K
Fluid viscosity	1.847E-7*T^2-1.32E-4*T+2.39E-2 Pa-s
Wall specific heat	525 J/kg-K
Wall density	7800 kg/m^3
Wall thermal conductivity	16.2 W/m-K
Initial heat transfer coefficient	100 W/m^2-K
Numerical discretization technique	Semi-implicit Crank Nicolson
Time step	0.5 seconds
Density integral approximation	Simpson's rule

The startup, heater step, and Loss of Heat Sink (LOHS) transients were studied for parameter sensitivity. The runs for the heater step and LOHS transients were first run to

steady state from startup, and then the appropriate parameter was changed. Unless otherwise specified the transients were performed as follows:

- For the startup transient, the flow was initially set to 1E-16 kg/s and then the simulation ran for 5,000 seconds at a heater power of 1 kW to reach steady state.
- For the heater step after startup, the heater power was stepped up to 1.5 kW and then continued for another 5,000 seconds to reach the new steady state.
- For the LOHS after startup, the secondary heat transfer coefficient was set to zero and then continued for another 5,000 seconds to reach the new steady state.

The code cannot model a flow rate of zero, so the initial flow rate was set to 1E-16 for the startup transient. The details of each parameter study are in the sections that follow.

3.3.1 Nodalization

3.3.1.1 Global mesh

The heater step and LOHS transients were run for the global mesh sensitivity studies. For each test there are three different runs each with a different mesh. For the first mesh, the number of nodes for each piece was set to 2 which is the minimum value for Simpson's rule to work. The second mesh had the nominal number of nodes and the third mesh had three times the number of nodes in the nominal case. These tests compare the nominal mesh to a mesh that is coarser and one that is finer for the heater step and LOHS transients as described in Table 3.10.

Table 3.10 Global Mesh Refinement Test Matrix

I.A.1. Global Mesh Refinement Test Matrix			
		Mesh	Transient
Test 1	Case 1	2 nodes per piece	Heater step
	Case 2	nominal	
	Case 3	3*nominal	
Test 2	Case 1	2 nodes per piece	LOHS
	Case 2	nominal	
	Case 3	3*nominal	

3.3.1.2 Component mesh

There are two different component mesh parameters: the heated section mesh and the heat exchanger mesh. For both parameters, the section of interest (heater or heat exchanger) is broken up into three sections: beginning, middle, and end. For the heated section, the length and number of nodes are varied for each of the three sections. The heat exchanger section is too short for it to make sense to change the length of the refined section, so only the number of nodes per section is varied. For the heated section tests, the heat input is split among the three sections with equal heat flux. The tests for the heated section mesh are the heater step transient and the tests for the heat exchanger mesh are the LOHS transient. Tables 3.11 and 3.12 below show the details for the tests.

Table 3.11 Heated Section Nodalization Test Matrix

I.B.1. Heated Section Nodalization Test Matrix							
Heater Segment		Beginning		Middle		End	
		Length (m)	Nodes	Length (m)	Nodes	Length (m)	Nodes
Test 1	Case 1	0.39	4	1.56	16	0.39	4
	Case 2	0.39	8	1.56	16	0.39	8
	Case 3	0.39	16	1.56	16	0.39	16
Test 2	Case 1	0.39	16	1.56	8	0.39	16
	Case 2	0.39	16	1.56	16	0.39	16
	Case 3	0.39	16	1.56	32	0.39	16
Test 3	Case 1	0.195	4	1.95	20	0.195	4
	Case 2	0.39	8	1.56	16	0.39	8
	Case 3	0.78	16	0.78	8	0.78	16

Table 3.12 Heat Exchanger Nodalization Test Matrix

I.B.2. Heat Exchanger Section Nodalization Test Matrix LOHS							
HX Segment		Beginning		Middle		End	
		Length (m)	Nodes	Length (m)	Nodes	Length (m)	Nodes
Test 1	Case 1	0.099	2	0.396	4	0.099	2
	Case 2	0.099	4	0.396	4	0.099	4
	Case 3	0.099	8	0.396	4	0.099	8
Test 2	Case 1	0.099	4	0.396	4	0.099	4
	Case 2	0.099	4	0.396	8	0.099	4
	Case 3	0.099	4	0.396	16	0.099	4

Figure 3.6 shows a visual representation of where the mesh is refined for each test for the heater and heat exchanger.

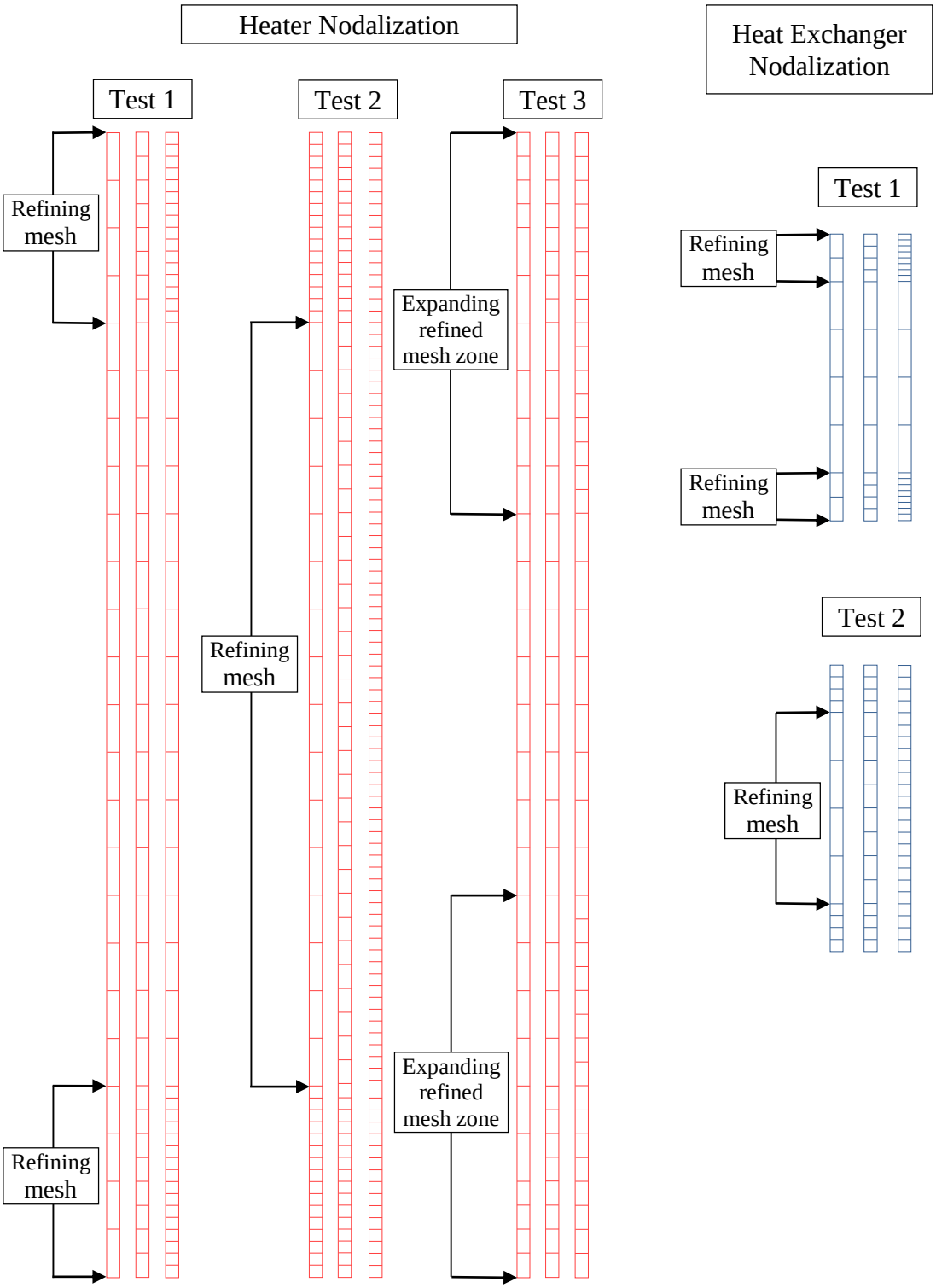

Figure 3.6 Local Mesh Refinement

3.3.2 Geometry

The geometry of the loop is relatively easy to change in the code, but some changes are more difficult to make in the experimental loop. The resistive heating method makes it easier to make certain changes in which section of pipe gets heated. The electrical leads can be moved up and down to shrink the heated section and move it up and down within certain limits. These changes to the heated section are studies in the first subsection of the geometry tests.

3.3.2.1 Heater

The heated section was divided up into three sections with the middle one heated. The length of each section was varied to resize and move the heated section up or down. The node spacing was held constant for all of the cases. Table 3.13 below details the different configurations that were tested. The transient used for these studies was the heater step from 1 kW to 1.5 kW.

Table 3.13 Heated Section Length and Position Test Matrix

II.A.1. Heated Section Length and Position Test Matrix							
		Pipe		Heated		Pipe	
		Length	Nodes	Length	Nodes	Length	Nodes
Test 1	Case 1	0	0	2.34	24	0	0
	Case 2	0.39	4	1.56	16	0.39	4
	Case 3	0.78	8	0.78	8	0.78	8
Test 2	Case 1	0.78	8	1.56	16	0	0
	Case 2	0.39	4	1.56	16	0.39	4
	Case 3	0	0	1.56	16	0.78	8
Test 3	Case 1	0	0	1.56	16	0.78	8
	Case 2	0	0	1.95	20	0.39	4
	Case 3	0	0	2.34	24	0	0
Test 4	Case 1	0.78	8	1.56	16	0	0
	Case 2	0.39	4	1.95	20	0	0
	Case 3	0	0	2.34	24	0	0

Figure 3.7 below shows a visual representation of the different configurations of the heater for each test. The red portions are where the section is heated and the black sections are where there is just pipe.

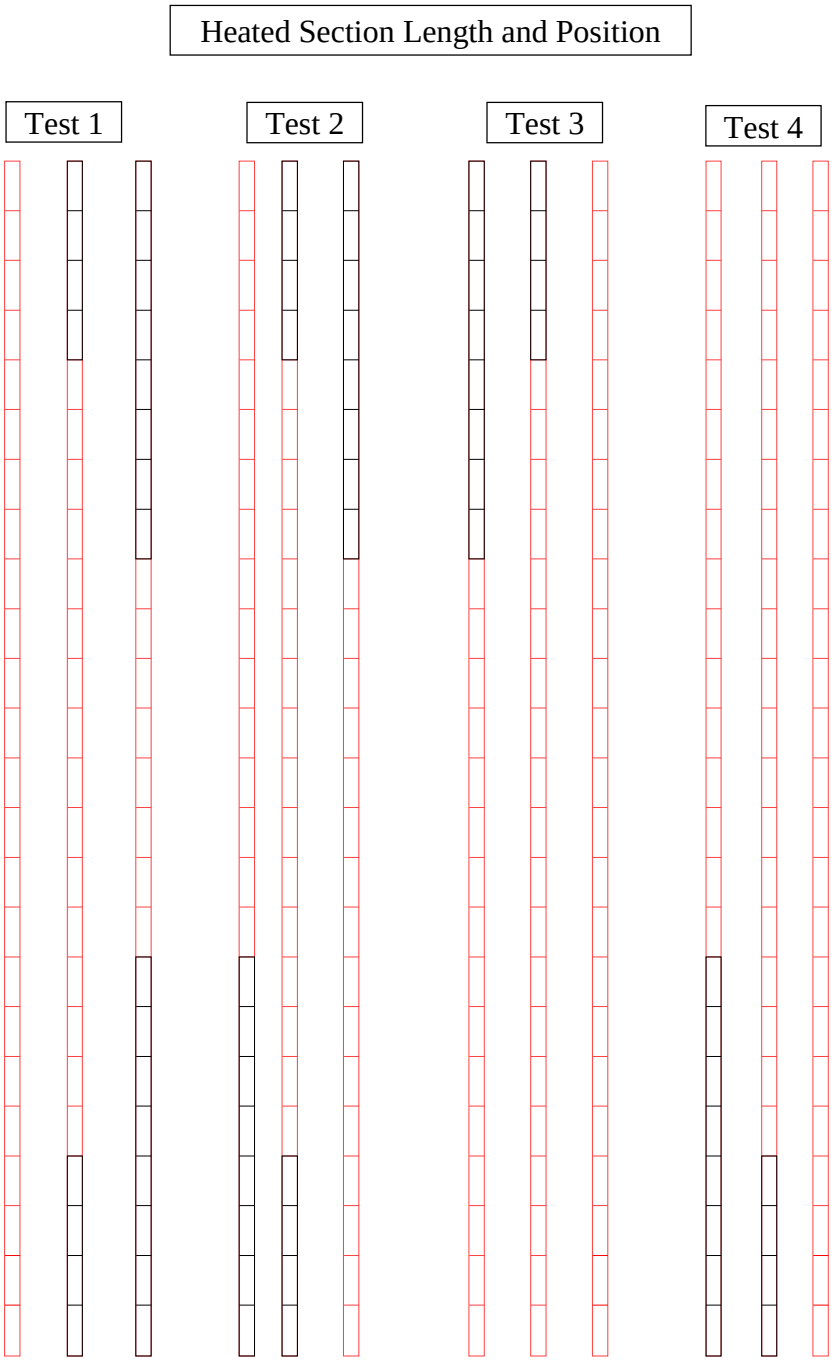

Figure 3.7 Heated Section Length and Position Drawing

3.3.2.2 Piping

For this study, the loop height, diameter, and thickness were varied. The values used were some multiple or fraction of the values used in the nominal case, so that is how they are described in Tables 3.14, 3.15, and 3.16 below. The heater step and LOHS transients were run for each of the varied parameters.

Table 3.14 Loop Height Test Matrix

II.B.1 Loop Height Test Matrix			
		Height	Transient
Test 1	Case 1	nominal	Heat Step
	Case 2	4 times nominal	Heat Step
	Case 3	8 times nominal	Heat Step
Test 2	Case 1	nominal	LOHS
	Case 2	4 times nominal	LOHS
	Case 3	8 times nominal	LOHS

Table 3.15 Loop Diameter Test Matrix

II.B.2 Loop Diameter Test Matrix			
		Diameter	Transient
Test 1	Case 1	1/2 nominal	Heat Step
	Case 2	nominal	Heat Step
	Case 3	2 times nominal	Heat Step
Test 2	Case 1	1/2 nominal	LOHS
	Case 2	nominal	LOHS
	Case 3	2 times nominal	LOHS

Table 3.16 Loop Thickness Test Matrix

II.B.3 Loop Thickness Test Matrix			
		Thickness	Transient
Test 1	Case 1	1/2 nominal	Heat Step
	Case 2	nominal	Heat Step
	Case 3	2 times nominal	Heat Step
Test 2	Case 1	1/2 nominal	LOHS
	Case 2	nominal	LOHS
	Case 3	2 times nominal	LOHS

3.3.3 Inputs

3.3.3.1 Initial conditions

The initial flow rate, temperature profiles, and heat transfer coefficient were varied in the initial conditions studies. Only the startup transient was studied for the sensitivity studies of the initial conditions.

The initial flow rate was varied to see what impact it had on the SRQs. The first case was run with the nominal value of 1E-16 kg/s. The second case used 0.01 kg/s because that is approximately the flow rate the pump can start flow in the natural circulation loop with the given setup. For the last case, a value of 0.1 kg/s was used to see how the code would respond to a higher initial flow. Table 3.17 lists the cases for the initial flow rate test.

Table 3.17 Initial Flow Rate Test Matrix

III.A.1 Initial Flow Rate Test Matrix		
		Flow rate (kg/s)
Test 1	Case 1	1E-16
	Case 2	0.01
	Case 3	0.1

The initial temperature studies tested both the initial fluid temperature and the initial wall temperature. For the first three tests, varied temperatures were given values of 16, 23, and 30 for cases 1, 2, and 3 respectively. For the first test, both the fluid and wall temperatures were changed from the nominal value. For the second test just the fluid temperatures were changed and for the third test just the wall temperatures were changed. The last test varied both temperatures much higher than nominal to see how the code would respond to a high initial temperature with no initial flow. The values used for all of the tests are detailed in Table 3.18.

Table 3.18 Initial Temperature Profile Test Matrix

III.A.2 Initial Temperature Profile Test Matrix			
		Wall temperature	Fluid temperature
Test 1	Case 1	16	16
	Case 2	23	23
	Case 3	30	30
Test 2	Case 1	23	16
	Case 2	23	23
	Case 3	23	30
Test 3	Case 1	16	23
	Case 2	23	23
	Case 3	30	23
Test 4	Case 1	23	23
	Case 2	60	60
	Case 3	80	80

The heat transfer coefficient is calculated in the code at each time step based on the Nusselt number, thermal conductivity of the fluid, and the inner diameter of the pipe. For the first iteration, however, an initial value is set. This initial value was tested to see if it had any impact on the solution. The values were chosen with a wide range to determine if the parameter has any effect on the SRQs. The test is summarized in Table 3.19 below.

Table 3.19 Initial HTC Test Matrix

III.A.3 Initial HTC Test Matrix		
		Heat transfer coefficient
Test 1	Case 1	0
	Case 2	1E5
	Case 3	1E10

3.3.3.2 Loop characteristics

The sensitivity of the code to the loss coefficients was tested. For the first case, the loss coefficients used were doubled from the nominal value for each piece. The second case was run with the nominal values. For the third case the loss coefficients for all of the pieces were added up (4.89 m) and divided by the number of pieces (16) to get an average

value (0.305625 m). Each piece was given this average value for the third case. Each of these cases was run for the heater step and LOHS transients as shown in Table 3.20.

Table 3.20 Loss Coefficients Test Matrix

III.B.1 Loss Coefficients Test Matrix			
		Loss coefficients	Transient
Test 1	Case 1	doubled	Heat Step
	Case 2	nominal	Heat Step
	Case 3	averaged	Heat Step
Test 2	Case 1	doubled	LOHS
	Case 2	nominal	LOHS
	Case 3	averaged	LOHS

The heater power for the loop was varied for the heater step and LOHS transients. For the first three tests, the heater step transient was studied varying the initial power, stepped-up power, or both for tests1, 2, and 3 respectively. The initial power was varied for the LOHS transient in the last test. Table 3.21 below shows this and lists the power levels used.

Table 3.21 Heater Power Test Matrix

III.B.2 Heater Power Test Matrix				
		Initial power	Stepped-up power	Transient
Test 1	Case 1	700	1500	Heat Step
	Case 2	1000	1500	Heat Step
	Case 3	1300	1500	Heat Step
Test 2	Case 1	700	1000	Heat Step
	Case 2	700	1500	Heat Step
	Case 3	700	2000	Heat Step
Test 3	Case 1	700	1000	Heat Step
	Case 2	1000	1500	Heat Step
	Case 3	1300	2000	Heat Step
Test 4	Case 1	700	N/A	LOHS
	Case 2	1000	N/A	LOHS
	Case 3	1300	N/A	LOHS

Three different equations to calculate the Nusselt number in the horizontal sections were tested. The first case used the Dittus Boelter correlation as described for the nominal parameters run. The second case used the Gnielinski correlation as described next. For laminar flow with Re < 886.652, the friction factor was found using Equation 3.90. For flows Re > 886.652, the friction factor was found using Equation 3.91, a correlation based on the explicit first Petukhov equation [M. Hallquist, 2011]. The Reynolds number of 886.652 was chosen to avoid a discontinuity in the calculation of the friction factor. A value of 3.657 was used for the Nu for laminar flow. The Gnielinski correlation [M. Hallquist, 2011], Equation 3.92, was used whenever it would result in a value above 3.657 to avoid discontinuity in the Nu calculation.

$$f = \frac{64}{Re} \tag{3.90}$$

$$f = (0.79 \ln Re - 1.64)^{-2} \tag{3.91}$$

$$Nu = \frac{(f/8)(Re - 1000)Pr}{1 + 12.7(f/8)^{0.5}(Pr^{2/3} - 1)} \tag{3.92}$$

The third case used the Churchill correlation [S. W. Churchill, 1977]. The friction factor was calculated using Equation 3.93 for Re < 7 and by Equation 3.94 for Re > 7. The Nusselt number was found using Equation 3.95 for all ranges of Re and Pr.

$$f = \frac{8}{Re} \tag{3.93}$$

$$f = \left(\frac{1}{\left[\left(\frac{8}{Re} \right)^{10} + \left(\frac{Re}{36500} \right)^{20} \right]^{1/2}} + \left(2.21 \, ln \frac{Re}{7} \right)^{10} \right)^{-1/5} \tag{3.94}$$

$$Nu = \left[4.364^{10} + \left[\frac{e^{(2200 - Re)/365}}{4.364^2} + \left(\frac{1}{6.3 + \frac{0.079 Re * f^{\frac{1}{2}} * Pr}{(1 + Pr^{4/5})^{5/6}}} \right)^2 \right]^5 \right]^{1/10} \tag{3.95}$$

The heater step and LOHS transients were studied and the correlation used in each case is summarized in Table 3.22 below.

Table 3.22 Heat Transfer Coefficient Correlation Test Matrix

III.B.3 Heat Transfer Coefficient Correlation Test Matrix			
		Correlation	Transient
Test 1	Case 1	Dittus Boelter	Heat Step
	Case 2	Gnielinski	Heat Step
	Case 3	Churchill	Heat Step
Test 2	Case 1	Dittus Boelter	LOHS
	Case 2	Gnielinski	LOHS
	Case 3	Churchill	LOHS

3.3.3.3 Boundary conditions

The secondary side heat transfer coefficient was varied and tested for the heater step and LOHS transients. The first case used a value of 60 to model only conduction heat transfer on the secondary side. The second case used a value of 580, and the third case used the nominal value of 1021.7. The values and transients are summarized in Table 3.23.

Table 3.23 Secondary Side Heat Transfer Coefficient Test Matrix

III.C.1 Secondary Side Heat Transfer Coefficient Test Matrix			
		Secondary side HTC	Transient
Test 1	Case 1	60	Heat Step
	Case 2	580	Heat Step
	Case 3	1021.7	Heat Step
Test 2	Case 1	60	LOHS
	Case 2	580	LOHS
	Case 3	1021.7	LOHS

For the sensitivity tests, the ambient heat transfer coefficient was tested at 10 (twice the nominal value), 5 (the nominal value), and at zero (no parasitic heat losses). The heater step and LOHS transients were run to test the sensitivity. The tests are described in Table 3.24.

Table 3.24 Ambient Heat Transfer Coefficient Test Matrix

III.C.2 Ambient Heat Transfer Coefficient Test Matrix			
		Ambient HTC	Transient
Test 1	Case 1	10	Heat Step
	Case 2	5	Heat Step
	Case 3	0	Heat Step
Test 2	Case 1	10	LOHS
	Case 2	5	LOHS
	Case 3	0	LOHS

The secondary side temperature was tested for 10℃ above the nominal value and 20℃ above the nominal value as detailed in Table 3.25.

Table 3.25 Secondary Side Temperature Test Matrix

III.C.3 Secondary Side Temperature Test Matrix			
		Temperature	Transient
Test 1	Case 1	15	Heat Step
	Case 2	25	Heat Step
	Case 3	35	Heat Step
Test 2	Case 1	15	LOHS
	Case 2	25	LOHS
	Case 3	35	LOHS

Variations in the ambient temperature were tested for any impact they might have on the SRQs by ranging from 0 to the nominal value of 23 to 100 as shown in Table 3.26.

Table 3.26 Ambient Temperature Test Matrix

III.C.4 Ambient Temperature Test Matrix			
		Ambient HTC	Transient
Test 1	Case 1	0	Heat Step
	Case 2	23	Heat Step
	Case 3	100	Heat Step
Test 2	Case 1	0	LOHS
	Case 2	23	LOHS
	Case 3	100	LOHS

3.3.3.4 Material properties

The material properties for the fluid and the wall were tested. The fluid properties are not constant values, so the value calculated was multiplied by some percentage to get the desired variation. The ranges tested for each property were based on the amount of variation in the fluid property value data for Flibe, because the properties for water are well characterized. Each property was varied according to the variation in the values. All of the fluid properties were also varied by worst overall variation, +/-30%, so that the effect of each property could be compared for the same variation.

The specific heat for flibe only varied by 1-2%, so a variation of +/- 5% was tested to account for this slight variation. This test and the test for +/-30% to compare to the other fluid properties are shown in Table 3.27.

Table 3.27 Fluid Specific Heat Test Matrix

III.D.1.a. Fluid Specific Heat Test Matrix			
		Cp	Transient
Test 1	Case 1	95%	Heat step
	Case 2	100%	Heat step
	Case 3	105%	Heat step
Test 2	Case 1	70%	Heat step
	Case 2	100%	Heat step
	Case 3	130%	Heat step
Test 3	Case 1	95%	LOHS
	Case 2	100%	LOHS
	Case 3	105%	LOHS
Test 4	Case 1	70%	LOHS
	Case 2	100%	LOHS
	Case 3	130%	LOHS

The density of flibe varies around 15%, so a range of +/- 20% was tested along with the +/-30% to be compared to the other properties. Table 3.28 shows all of these tests.

Table 3.28 Fluid Density Test Matrix

III.D.1.b. Fluid Density Test Matrix			
		ρ	Transient
Test 1	Case 1	80%	Heat step
	Case 2	100%	Heat step
	Case 3	120%	Heat step
Test 2	Case 1	70%	Heat step
	Case 2	100%	Heat step
	Case 3	130%	Heat step
Test 3	Case 1	80%	LOHS
	Case 2	100%	LOHS
	Case 3	120%	LOHS
Test 4	Case 1	70%	LOHS
	Case 2	100%	LOHS
	Case 3	130%	LOHS

The thermal conductivity of flibe varied with a wide range of 30%, so the variation tested was +/-30% as is shown in Table 3.29.

Table 3.29 Fluid Thermal Conductivity Test Matrix

III.D.1.c. Fluid Thermal Conductivity Test Matrix			
		k	Transient
Test 1	Case 1	70%	Heat step
	Case 2	100%	Heat step
	Case 3	130%	Heat step
Test 2	Case 1	70%	LOHS
	Case 2	100%	LOHS
	Case 3	130%	LOHS

The viscosity of flibe varied by less than 1%, so a range of +/-5% was tested along with the +/-30% variation to compare to the other properties. Table 3.30 lists the tests.

Table 3.30 Fluid Dynamic Viscosity Test Matrix

III.D.1.d. Fluid Dynamic Viscosity Test Matrix			
		μ	Transient
Test 1	Case 1	95%	Heat step
	Case 2	100%	Heat step
	Case 3	105%	Heat step
Test 2	Case 1	70%	Heat step
	Case 2	100%	Heat step
	Case 3	130%	Heat step
Test 3	Case 1	95%	LOHS
	Case 2	100%	LOHS
	Case 3	105%	LOHS
Test 4	Case 1	70%	LOHS
	Case 2	100%	LOHS
	Case 3	130%	LOHS

The density and specific heat of the wall only appear in the code when they are multiplied together, the product of the values was varied in this study. The density and specific heat of stainless steel vary by less 1% and ~7% respectively. A range of +/- 10% for the product was tested as is shown in Table 3.31.

Table 3.31 Wall Specific Heat and Density Test Matrix

III.D.2.a Wall Specific Heat and Density Test Matrix			
		ρ_w*cp_w	transient
Test 1	Case 1	90%	Heat step
	Case 2	7800*525	Heat step
	Case 3	110%	Heat step
Test 2	Case 1	90%	LOHS
	Case 2	7800*525	LOHS
	Case 3	110%	LOHS

The thermal conductivity of stainless steel varies by ~5-10%, so a range of +/-10% was used in the study as is shown in Table 3.32.

Table 3.32 Wall Thermal Conductivity Test Matrix

III.D.2.b Wall Thermal Conductivity Test Matrix			
		k_w	transient
Test 1	Case 1	90%	Heat step
	Case 2	16.2	Heat step
	Case 3	110%	Heat step
Test 2	Case 1	90%	LOHS
	Case 2	16.2	LOHS
	Case 3	110%	LOHS

3.3.4 Numerical Methods

3.3.4.1 Numerical discretization technique

The θ parameter was varied in this sensitivity study to see if solving the momentum and energy equations explicitly, semi-implicitly, or fully implicitly had an effect on the solution. The time step was set to 0.1 seconds for all of these tests to ensure stability of the explicit solution and a useful comparison among the three cases. The heater step and LOHS transients were each tested as is shown in Table 3.33.

Table 3.33 Crank Nicolson Discretization Parameter Test Matrix

IV.A.1. Crank Nicolson Discretization Parameter Test Matrix			
		θ	Transient
Test 1	Case 1	0	Heat step
	Case 2	1/2	Heat step
	Case 3	1	Heat step
Test 2	Case 1	0	LOHS
	Case 2	1/2	LOHS
	Case 3	1	LOHS

The time step was varied for the semi-implicit and fully implicit methods. For the explicit case (θ = 0) the time step was restricted to <0.15 seconds for stability. This means any variation in the time step would have to be smaller than 0.15 seconds and would not impact the solution. For the semi-implicit (θ = 1/2) and fully implicit (θ = 1)

cases, the time step was only restricted by the quadratic form of the momentum equation. The time step values tested for the semi-implicit case were 1, 10, and 18 for the heater step transient and 1, 5, and 10 for the LOHS transient to test a wide range while still maintaining stability with respect to the momentum equation. The fully implicit case was tested using values of 1, 10, and 18 seconds for both transients. The tests are detailed in Table 3.34.

Table 3.34 Time Step Test Matrix

IV.A.2 Time Step Test Matrix				
		θ	Time step	Transient
Test 1	Case 1	1/2	1	Heat Step
	Case 2	1/2	10	Heat Step
	Case 3	1/2	18	Heat Step
Test 2	Case 1	1	1	Heat Step
	Case 2	1	10	Heat Step
	Case 3	1	18	Heat Step
Test 3	Case 1	1/2	1	LOHS
	Case 2	1/2	5	LOHS
	Case 3	1/2	10	LOHS
Test 4	Case 1	1	1	LOHS
	Case 2	1	10	LOHS
	Case 3	1	18	LOHS

3.3.4.2 Density integral approximation

The density integral in the momentum equation can be approximated using the trapezoidal rule or Simpson's rule. The two methods were compared with the heater step and LOHS transients as described in Table 3.35 below.

Table 3.35 Density Integral Approximation Test Matrix

IV.B.1. Density Integral Approximation Test Matrix			
		Method	Transient
Test 1	Case 1	Simpson's	Heat step
	Case 2	Trapezoidal	Heat step
Test 2	Case 1	Simpson's	LOHS
	Case 2	Trapezoidal	LOHS

References

A. Borgohain, B. K. Jaiswal, N. K. Maheshwari, P. K. Vijayan, D. Saha and R. K. Sinha, "Natural Circulation Studies in a Lead Bismuth Eutectic Loop," *Progress in Nuclear Energy*, **53**, 308-319 (2011).

D. A. Randall, "Chapter 2: Finite-Difference Approximations to Derivatives", An Introduction to Numerical Modeling of the Atmosphere (2013).

D. C. Rennels, and Hobart M. Hudson. *Pipe Flow: A Practical and Comprehensive Guide*. Hoboken, N.J: John Wiley & Sons, 2012. Internet resource.

M. Hallquist. "Heat Transfer and Pressure Drop Characteristics of Smooth Tubes at A constant Heat Flux in the Transitional Flow Regime," University of Pretoria (2011).

M. Ishii and I. Kataoka. "Scaling Criteria for LWR's Under Single-Phase and Two-Phase Natural Circulation." *Proceedings of the NRC/ANS Meeting on Basic Thermal Hydraulic Mechanisms in LWR Analysis*, September 14-15, 1982, Bethesda, MD.

N.B. Totala, M.V. Shimpi, N.L. Shete, and V.S. Bhopate, "Natural Convection Characteristicsin Vertical Cylinder," Research Inventy: International Journal Of Engineering And Science, 3, 8, 27-31 (2013).

P. K. Vijayan and A. K. Nayak, "Annex 7: Introduction to Instabilities in Natural Circulation Systems". *IAEA TECDOC 1474: Natural Circulation in Water Cooled Nuclear Power Plants Phenomena, models, and methodology for system reliability assessments* pg 173-201, (2005).

P. K. Vijayan, V. K. Bhojwani, M. H. Bade, M. Sharma, A. K. Nayak, D. Saha and R. K. Sinha, "Investigations on the effect of heater and heat exchanger orientation on the steady state, transient and stability behavior of single-phase natural circulation in a rectangular loop". *BARC internal report:* E/034, (2001).

S. W. Churchill. "Comprehensive Correlating Equations For Heat, Mass, and Momentum Transfer in Fully Developed Flow in Smooth Tubes," Industrial and Engineering Chemistry Fundamentals, **16**, 1, 109-116 (1977).

T. Allen, et al., Fluoride Salt-cooled High Temperature Reactor (FHR) Methods and Experiments Program White Paper, University of California Berkeley, Berkeley (April 2013a)

T. Nishihara, "Oscillatory Instability of a Single-Phase Natural Circulation Loop" Proceedings of the Eighth International Topical Meeting on Nuclear Reactor Thermal-Hydraulics, **2**, (839-847)Kyoto, Japan (1997)

U.S. Secretary of Commerce. "Isobaric Properties for Water – Fluid Data." *NIST Chemistry WebBook* (2011).

Chapter 4 Validation Experiment

4.1 Geometry

The experiment used to validate the FLiBeNC code is a rectangular natural circulation loop resistively heated along one vertical side and cooled via a heat exchanger on the other. The resistive heating is accomplished through the use of a power supply connected to the LabVIEW program so that the desired power level can be set electronically. The heat exchanger is a concurrent flow single tube in tube type with a secondary side flow of chilled water.

4.1.1 Experimental loop description

The loop is approximately 97 inches tall and 25 inches wide. It is made mostly out of stainless steel tubing with stainless steel piping sections before and after the flow meter to account for a slight change in internal diameter between the loop and the flow meter. The heated section spans almost the total height of the loop and the heat exchanger is 2 feet tall at the top of other the vertical section. Flanges are used in the horizontal sections to electrically isolate the rest of the loop from the heated section. A flow meter is on the vertical section below the heat exchanger.

4.1.2 Thermocouple information and placement

There are five inline T-type factory calibrated thermocouples on the primary side of the loop. The inline thermocouples are factory calibrated by lot, so the calibration is based on the first and last thermocouple in each lot at the factory. The first four inline thermocouples are each located at the inlet and outlet of the heated section and the heat exchanger. The

thermocouple at the outlet of the heat exchanger is 22 inches before the flow meter. The fifth thermocouple is 22 inches after the flow meter. There are two inline flow meters on the secondary flow side: one at inlet of the heat exchanger and one at the outlet.

There are 57 surface T-type thermocouples on the loop. They are model 5TC-TT-T-30 from Omega. The calibration of these thermocouples was done using the CL1000A calibrator from Omega. The general placement was informed by preliminary runs of the code focusing on the areas of the loop where the surface temperature was sensitive to input variations. The detailed placement of the surface thermocouples was dependent on where the nodes were in the code so that the experiment and code were measuring the surface temperatures at the same locations along the loop. Since the nodalization in the code is done by piece, the measurement to each thermocouple was from the beginning of the corresponding piece. This has an advantage to measuring from one point on the loop, because any measurement error does not propagate from piece to piece. The code discretizes each piece by defining the first node at the beginning of the piece and then subsequent nodes at intervals of the dx for that piece. Based on this, the thermocouples were placed at locations some multiple of dx from the beginning of the piece. The thermocouples that would correspond to the first node of a piece were placed as close to the beginning of that piece as possible. More details about the exact thermocouple locations can be found in Appendix A.

4.1.3 Flow rate measurements

The flow meter is on the cold side of the loop under the heat exchanger. The accuracy of the flow meter is +/- 0.5% of the measured value for flows between 0.5 and 20 m/s and

is +/-2.5 mm/s for flows less than 0.5 m/s. The flow measurements are recorded in LabView in m^3/hr.

4.2 Experimental Procedure and Measurement Techniques

4.2.1 Boundary conditions measurements

The ambient air temperature was measured by three thermocouples near the loop. Horizontally, they were all in the middle of the loop. Vertically, the first one was half way down the heat exchanger which is 14 inches from the top of the loop, the second one was in the center, and the third one was 14 inches from the bottom of the loop. A fourth thermocouple was placed outside the loop to measure the air temperature in the lab. The values from the thermocouples were used to estimate the ambient temperature for each piece in the loop.

The power level of the power supply is recorded in LabView for all but the first few experimental runs. The recording was not set correctly, so an approximate value of what was set in the program is listed for those runs.

4.2.2 Initial conditions measurements

The initial conditions are measured with the same instruments that the SRQs are measured with and recorded in LabView. The initial temperatures are measured with the thermocouples and the initial flow rate is measured by the flow meter.

4.2.3 SRQ measurement technique

The readings from the thermocouples and flow meter are recorded in LabVIEW every half second for most of the experimental runs. The time at which each measurement is taken is recorded with the data.

4.3 Transient Studies

The sections below detail the parameters that were varied and how the runs were performed. The transient scenarios that were studied varied depending on the parameter of interest. In general the heater step change, gradual heater change, LOHS, and start up transients were studied where applicable. A baseline case was run as a base to compare other runs to. Unless otherwise specified, all of the runs were done with approximately the nominal parameter values except for the parameter of interest. The initial flow rate was slowed by closing a valve in the loop for most of the runs. Some flow remained, but the value was recorded by the flow meter. The loop was cooled down to approximately ambient temperatures before each run unless the initial temperature was being specifically tested. The heater power used for most of the runs was approximately a 1kW for startup and approximately 1.5kW for a heat step. The heater power was varied for some of the runs to avoid boiling in the loop. The chiller flow rate was set to approximately 3 gallons per minute unless otherwise noted. The actual value of the secondary side flow rate was not recorded in lab view and was instead read from a meter on the chiller. Because of this, the recorded secondary side flow rate values are not exact. The temperature of the water going through the secondary side of the heat exchanger was measured using the same type of bulk thermocouples used in the primary loop and the values were recorded using LabView for each run. The secondary side temperature was kept at approximately 15°C

unless otherwise specified. Each of the experimental tests was run twice and the results are presented in Chapter 5.

4.3.1 Length and position of heated section

The heated section of the loop is a stainless steel tube with electric leads at either end which generate heat resistively in the tube wall. The length of the heated section was varied in loop by moving one or both of the heater leads along the section. For the nominal case, the leads were at the bottom and top ends of the heated section. Two runs were completed varying the heater position. For the first test, the bottom lead was moved up 30.5 inches from its original location and the top lead was left at the top end. For this test, the loop was run at a power level of approximately 1kW to steady state and then the power level was increased to approximately 1.5kW. The loop continued to run at 1.5kW until a new steady state was reached. For the second test, the top lead was moved down 30.5 inches and the bottom lead was in its original position at the bottom end of the tube. For this test, the loop was run at approximately 1kW until steady state was reached.

4.3.2 Secondary side heat transfer coefficient

Two experimental tests were done to model changes in the secondary side heat transfer coefficient. This was done by varying the flow rate of the secondary side in the heat exchanger. For the first test, the secondary flow rate was set to 1 gallon per minute and run at approximately 700W to steady state. For the second test, the secondary flow was shut off and the loop was run at approximately 700W until the fluid temperature at the exit

of the heated section reached approximately 85°C. The experiment was stopped at the fluid temperature of 85°C to avoid getting boiling temperatures in the loop.

4.3.3 Initial loop temperature

The loop was heated to ~75°C using the pump and heater. The pump and heater were turned off and flow was stopped with a valve. Quickly, the power was turned to approximately 1kW and the chiller was turned on at the nominal 3 gallons per minute. The loop was run this way until steady state was reached.

4.3.4 Initial flow rate

The pump was used to start flow in the forward direction in the natural circulation section of the loop. Quickly, the pump was shut off, the valves were switched (without obstructing flow) and the heater and chiller were turned on. The power was at 1kW and the loop was run until the flow settled out.

4.3.5 LOHS

The loop was run to steady state at 700 W with baseline parameters and then the chiller was shut off. The first time this transient was tested, the run was stopped once the fluid temperature at the exit of the heater reached about 80°C. This was done to avoid boiling. The second run was tested until the fluid temperature of the heater reached around 100°C.

Chapter 5 Results

5.1 Sensitivity Study Results

The flow rate and key temperatures were plotted with respect to time, so the effect of the parameter on key SRQs could be compared. The fluid and wall temperatures at the last node of the heater and heat exchanger sections were plotted. The key for each plot shows which line corresponds to each case from the tables given in the sensitivity sections in Chapter 3.

5.1.1 Nodalization

5.1.1.1 Global mesh

The study of the global mesh for the heater step transient showed that the very course mesh with 2 nodes per piece resulted in different flow and temperature profiles than the nominal and fine meshes. The values for the flow rate and temperatures were slightly different for the nominal and fine meshes, but the trends were the same. The course mesh model drastically underestimates the temperature values for the startup, heater step and LOHS transients. The heater step transient resulted in a profile similar to the startup profile for flow and temperature. The wall temperatures followed the same trend as the fluid temperatures. The flow rate drops much more significantly after the LOHS with the nominal and fine mesh than it does with the course mesh, so plots of the flow rate and fluid temperatures for this transient are below. The plots for the heater step are omitted because the trends matched those in the startup profile which can be seen in the plots from the LOHS transient.

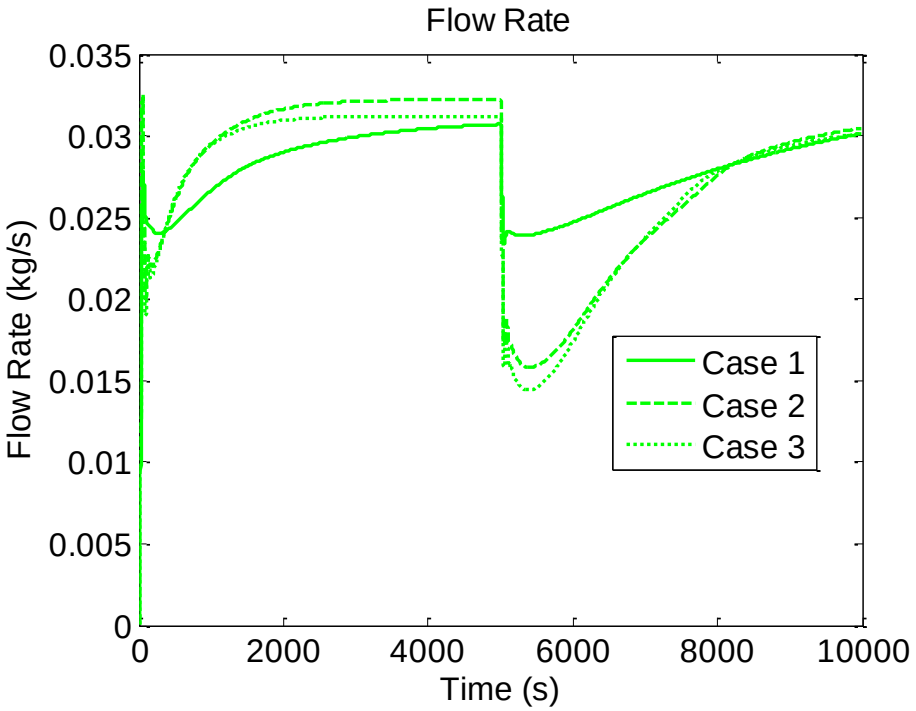

Figure 5.1 Flow Rate from LOHS Global Mesh Study

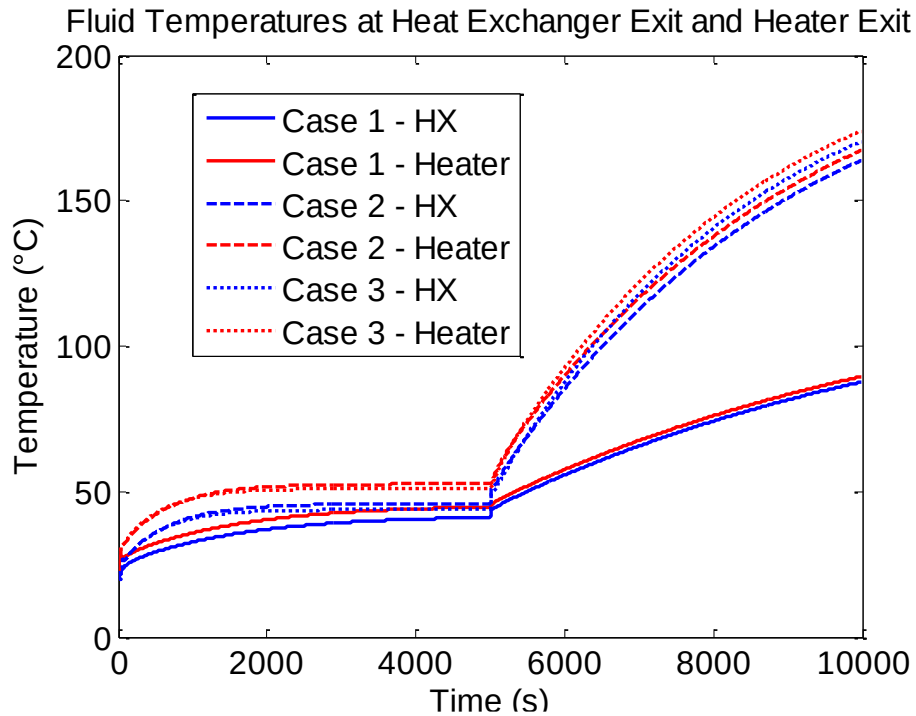

Figure 5.2 Fluid Temperatures from LOHS Global Mesh Study

Although the same amount of heat was added for each of the runs shown in Figure 5.2, the temperatures are drastically different for the course mesh.

5.1.1.2 Component mesh

The heated section nodalization tests showed that the temperatures and flow rate do vary slightly when the mesh is refined at different points in the heated section. The first test showed that the temperatures and flow rate get slightly lower as the mesh at both ends of the heated section is refined. The second test showed that refining the mesh in the center of the heated section increases the temperatures and flow rate which is the opposite effect from refining the mesh at the edges. Based on the third nodalization test, expanding the refinement area at the edges causes the temperatures and flow rate to decrease slightly. These tests show that having a higher concentration of the nodes in the heated section at the edges causes the temperatures and the flow rate to be slightly lower. Plots for these tests can be found in Appendix A. Neither the flow rate, nor the temperatures were affected by varying the mesh in the heat exchanger.

5.1.2 Geometry

5.1.2.1 Heater

The studies of the geometry (length and position) of the heater showed that the biggest impact is on the wall temperature at the heater. The first study showed that the wall temperature increased for a smaller heated section. This result is expected since the heat flux at the heater would be higher for a smaller heated section at the same power level. The wall temperatures are shown in the figure below. A short discussion of the effect on the fluid temperatures and flow rate can be found in Appendix A.

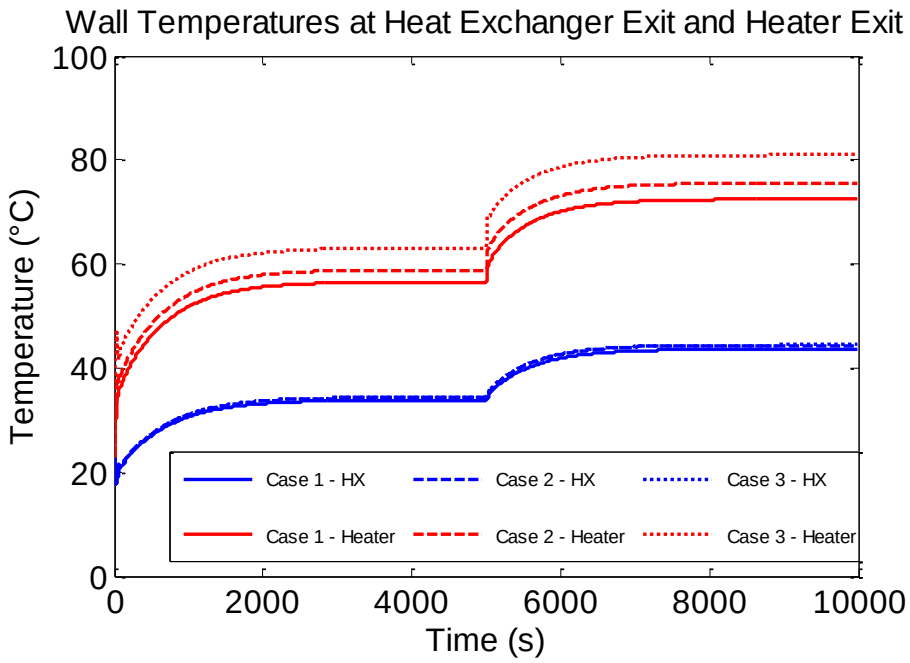

Figure 5.3 Wall Temperatures from the first Heater Geometry Study

The second heater geometry study showed that moving the heated section vertically had a very significant impact on the flow rate, some impact on the fluid temperature at the heater, and little impact on the wall temperatures. As the heated section was moved down, the flow rate increased dramatically and the temperatures at the heater were somewhat decreased. The flow rate and fluid temperature profiles for the second heater geometry study are shown below. A description of the effect on the wall temperatures for this study can be found in Appendix A.

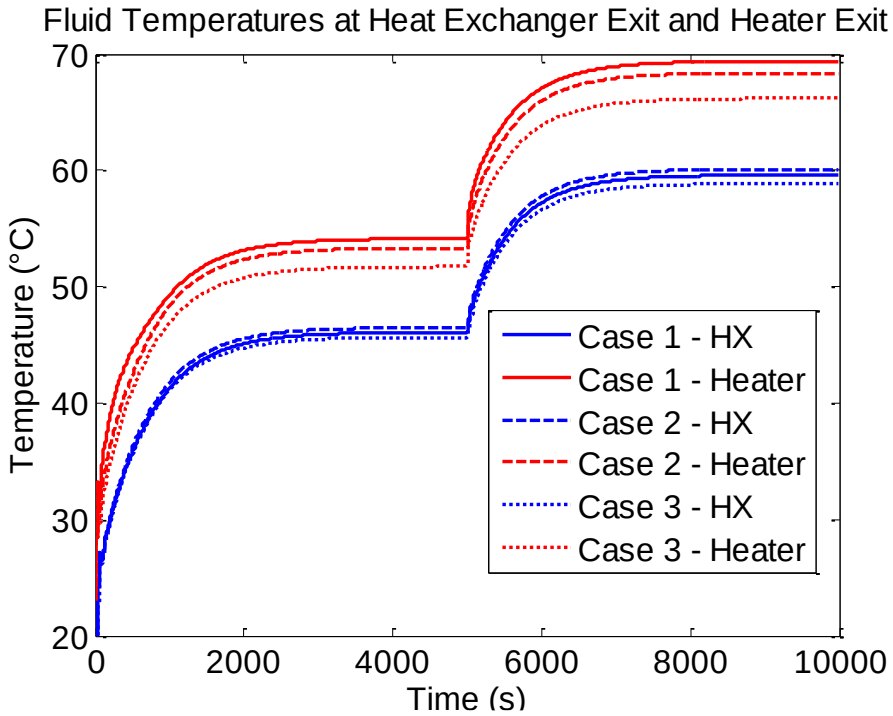

Figure 5.4 Fluid Temperatures from the second Heater Geometry Study

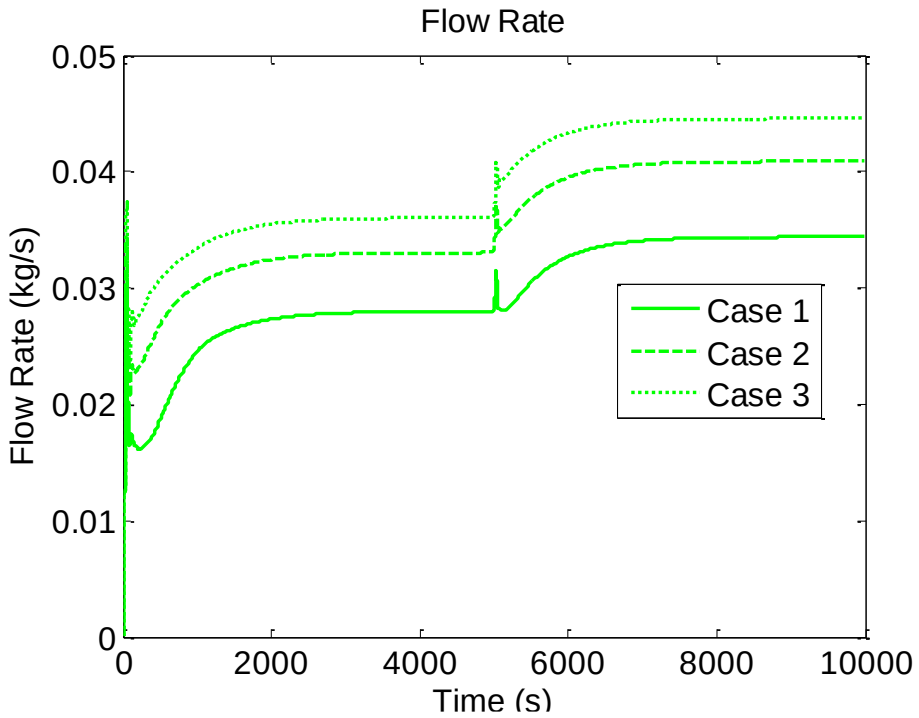

Figure 5.5 Flow Rate from the second Heater Geometry Study

It is evident from the third heater geometry test that increasing the height of a heater at the bottom of the vertical section decreases the flow rate significantly. There was not a significant change in the temperature profile, so a short discussion can be found in Appendix A. A plot of the flow rate is below.

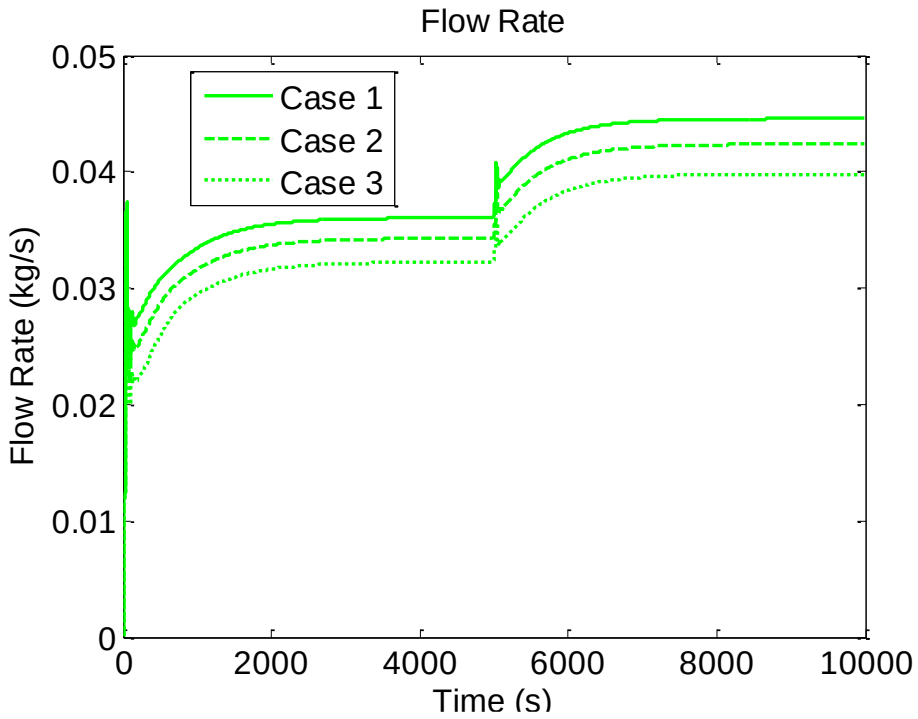

Figure 5.6 Flow Rate from the third Heater Geometry Study

The fourth heater geometry study showed that increasing the length of the heated section positioned at the top of the vertical section had an impact on the temperatures and especially on the flow rate. As the length of the heater was increased, the flow rate increased and the temperatures decreased. A plot of the flow rate is presented below and plots of the temperatures can be found in Appendix A.

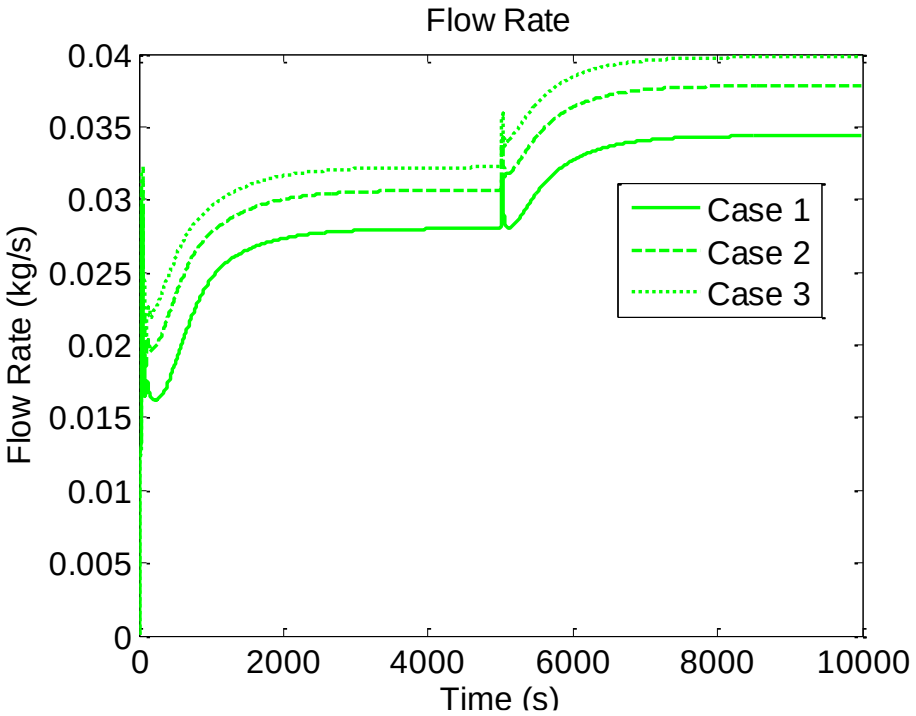

Figure 5.7 Flow Rate from the fourth Heater Geometry Study

5.1.2.2 Piping

The height of the loop did not have a significant impact on the startup or heater step transients. At the very end of the LOHS transient, the taller loops had fluid temperatures about 2°C higher and wall temperatures about 3°C higher than the loop with the nominal height. Increasing the height of the loop decreased the value of the flow rate after the LOHS transient. A plot showing this is can be found in Appendix A.

Increasing the diameter of the piping in the loop drastically decreased the fluid and wall temperatures and increased the flow rate for all of the transients. The fluid and wall temperature profiles were very similar, so only the fluid temperatures and flow rate are shown below. A few plots showing detail of key locations can be found in Appendix A.

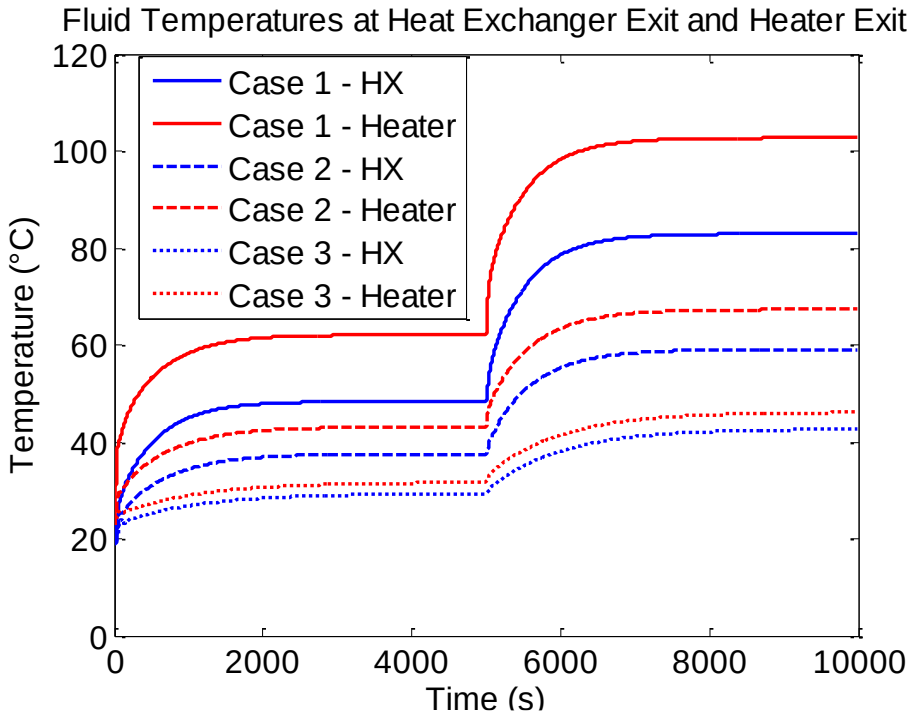

Figure 5.8 Fluid Temperatures for Heat Step from the Loop Diameter Study

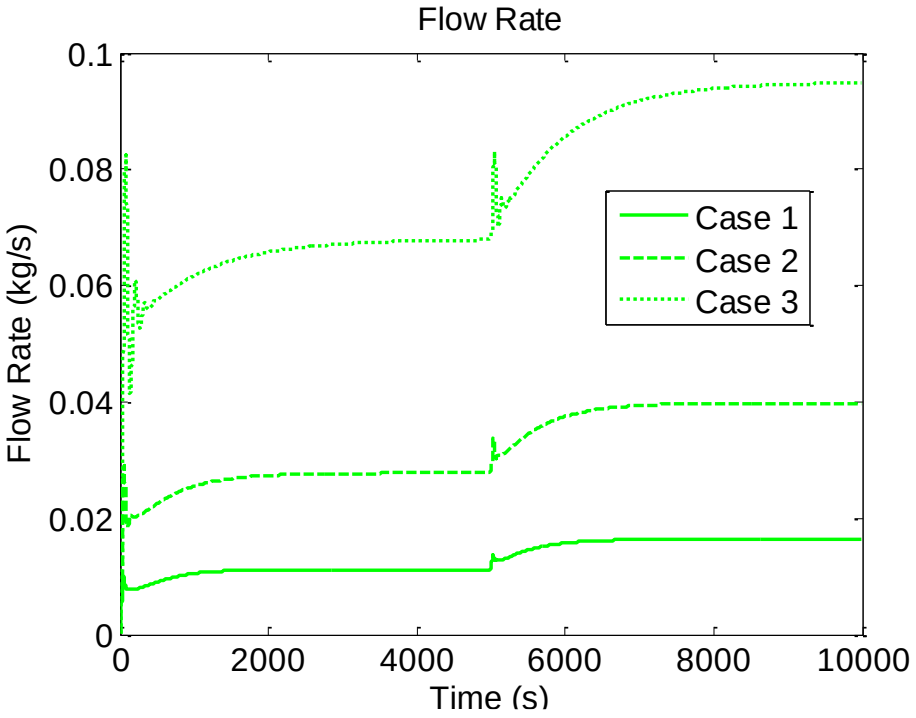

Figure 5.9 Flow Rate for Heat Step from the Loop Diameter Study

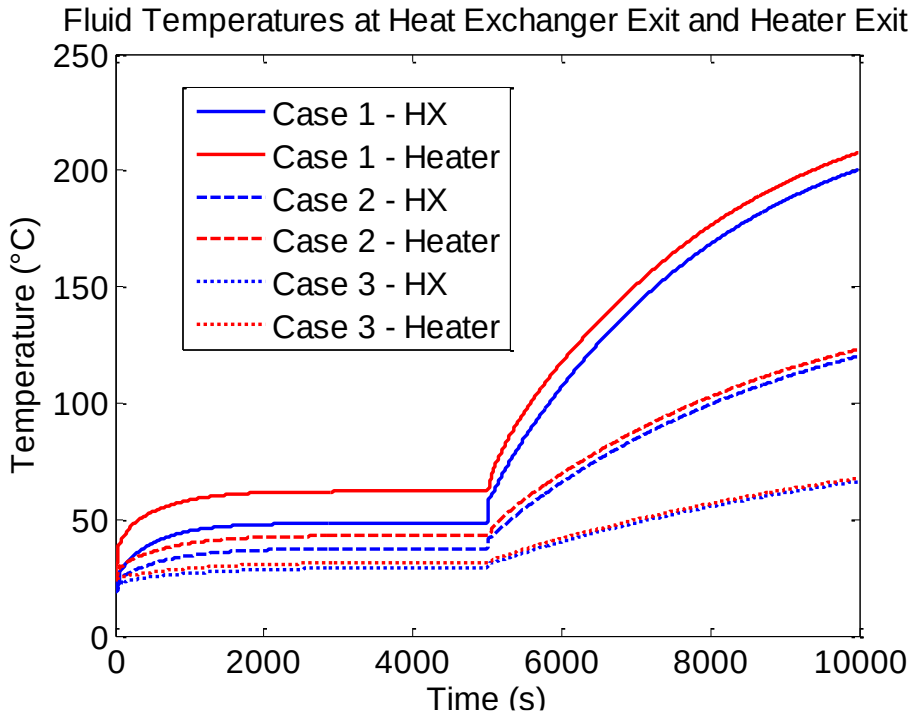

Figure 5.10 Fluid Temperatures for LOHS from the Loop Diameter Study

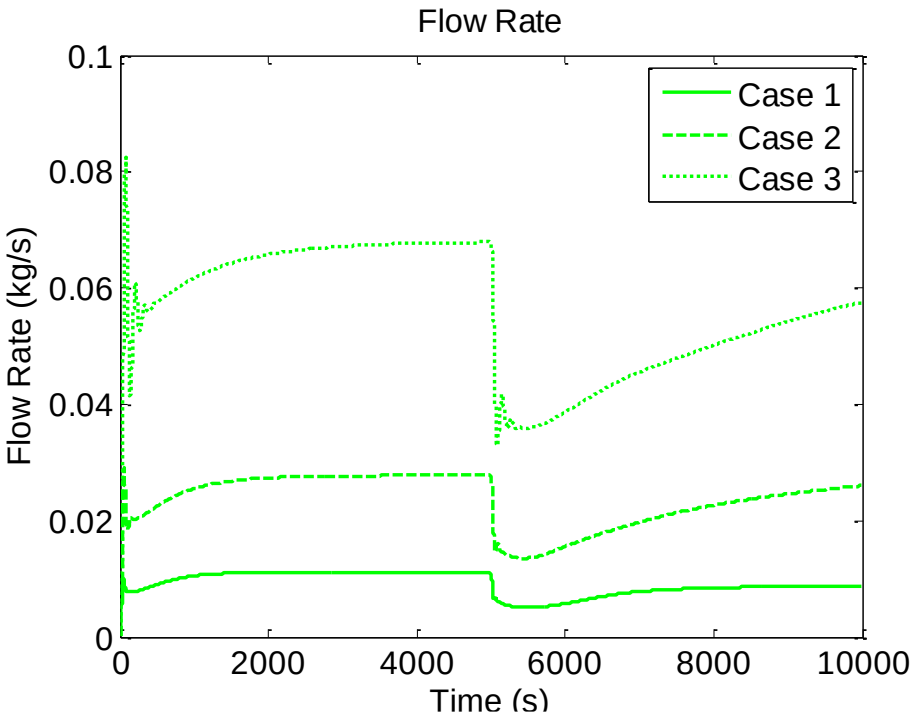

Figure 5.11 Flow Rate for LOHS from the Loop Diameter Study

The thickness of the pipes has a significant effect on the temperature and flow rate profiles for the startup, heater step, and LOHS transients. The thicker pipes had resulted in lower temperatures and a lower flow rate. Plots showing this for both the heater step and LOHS transients are below. Since the fluid and wall temperatures profiles were very similar, only the fluid temperatures are shown.

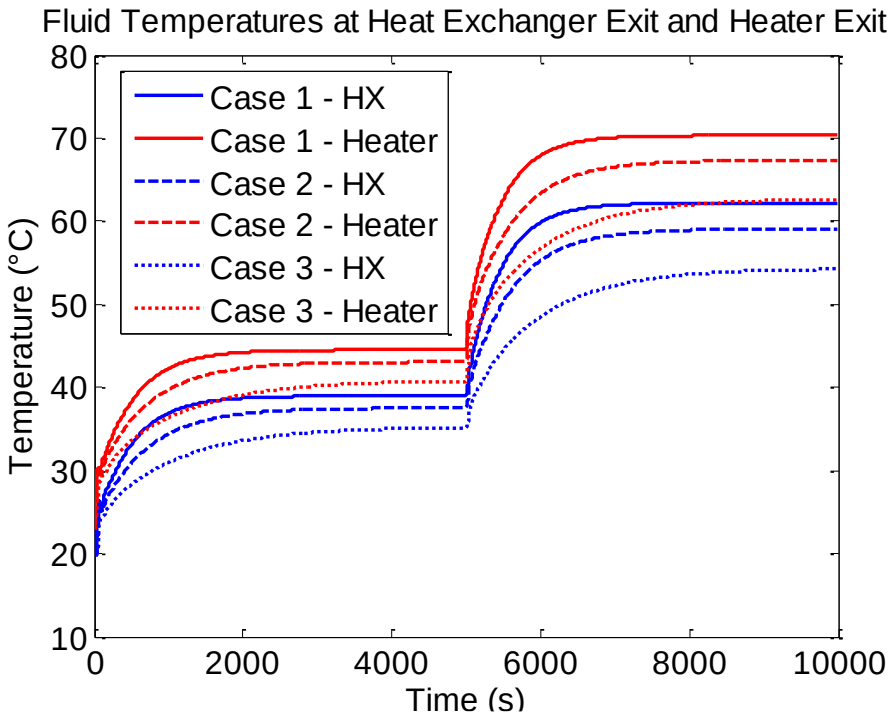

Figure 5.12 Fluid Temperatures for Heater Step from the Pipe Thickness Study

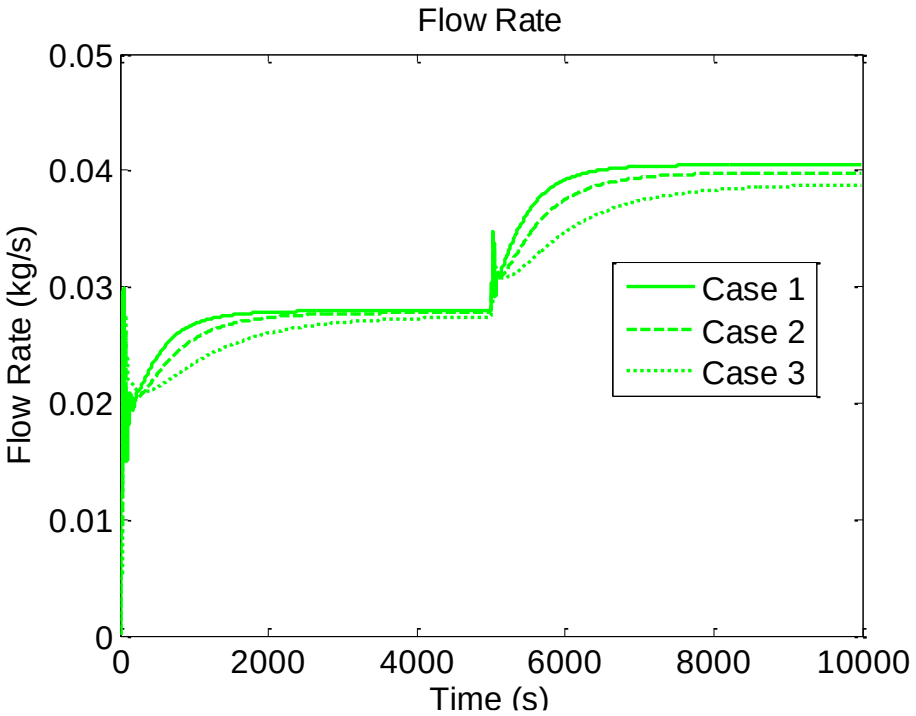

Figure 5.13 Flow Rate for Heater Step from the Pipe Thickness Study

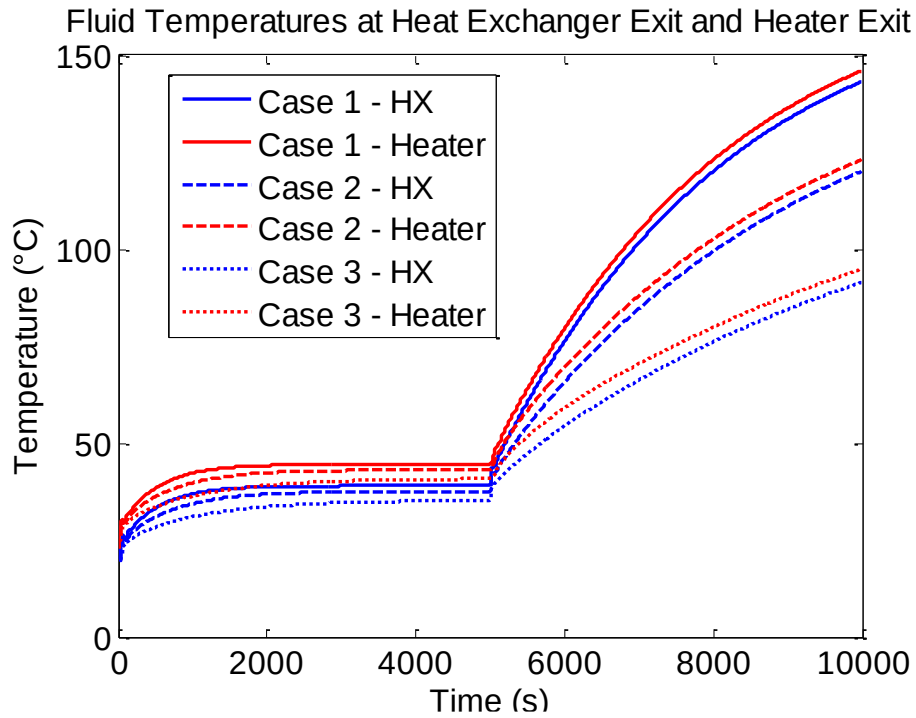

Figure 5.14 Fluid Temperatures for a LOHS from the Pipe Thickness Study

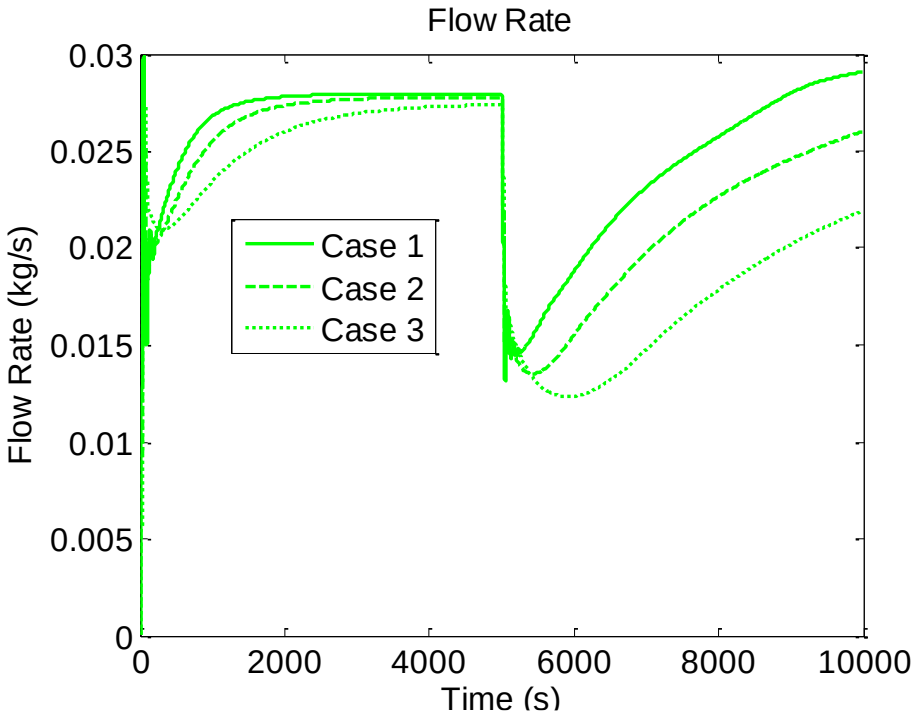

Figure 5.15 Flow Rate for a LOHS from the Pipe Thickness Study

5.1.3 Inputs

5.1.3.1 Initial conditions

There was very little effect from the initial flow rate or initial heat transfer coefficient studies. The first three initial temperature profile tests varied the temperatures 7° below and above the nominal conditions. The initial temperatures did have an effect on the solution, but these three tests gave very similar results. The wall and fluid temperature profiles were also very similar. Plots showing the fluid temperatures and flow rate from the first test below. A detailed plot of the flow rate for the startup transient can be found in Appendix A.

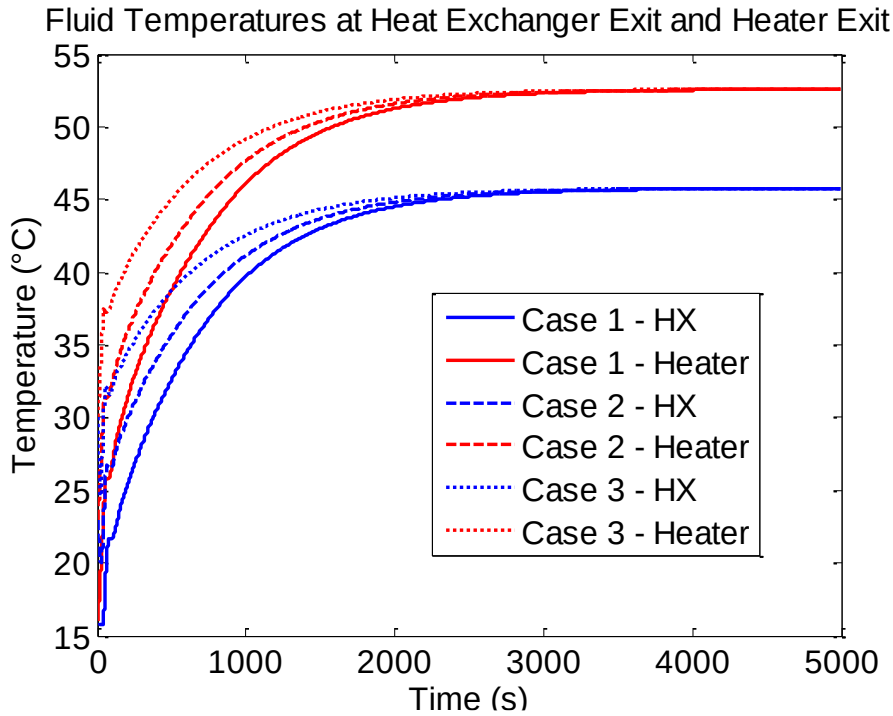

Figure 5.16 Fluid Temperatures from the first Initial Temperature Profile Study

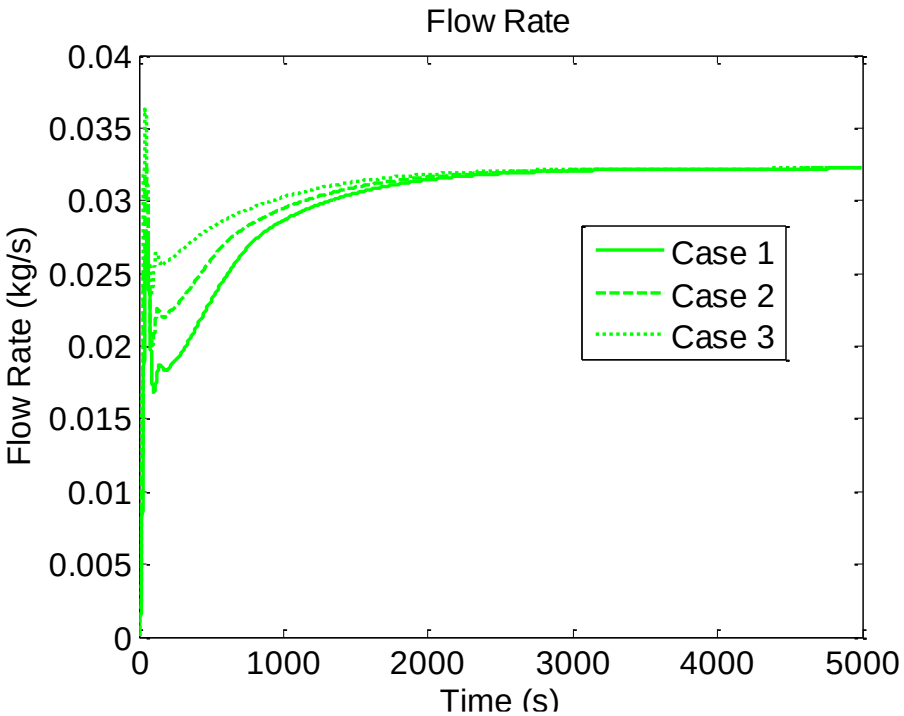

Figure 5.17 Flow Rate from the first Initial Temperature Profile Study

The fourth initial temperature profile test included a temperature value below steady state, a temperature close to the value at steady state, and a temperature value above steady state. The results showed that the flow rate follows the same pattern as the temperatures. For the high initial temperatures the flow rate jumps up quickly and then comes back down to steady state. For the low initial temperature, the flow rate increases slowly to steady state and for the temperature that started at approximately the steady state value, the flow rate oscillated, and then settles into a steady state. These effects can be seen in the plots below. A detailed plot of the flow rate from startup can be found in Appendix A.

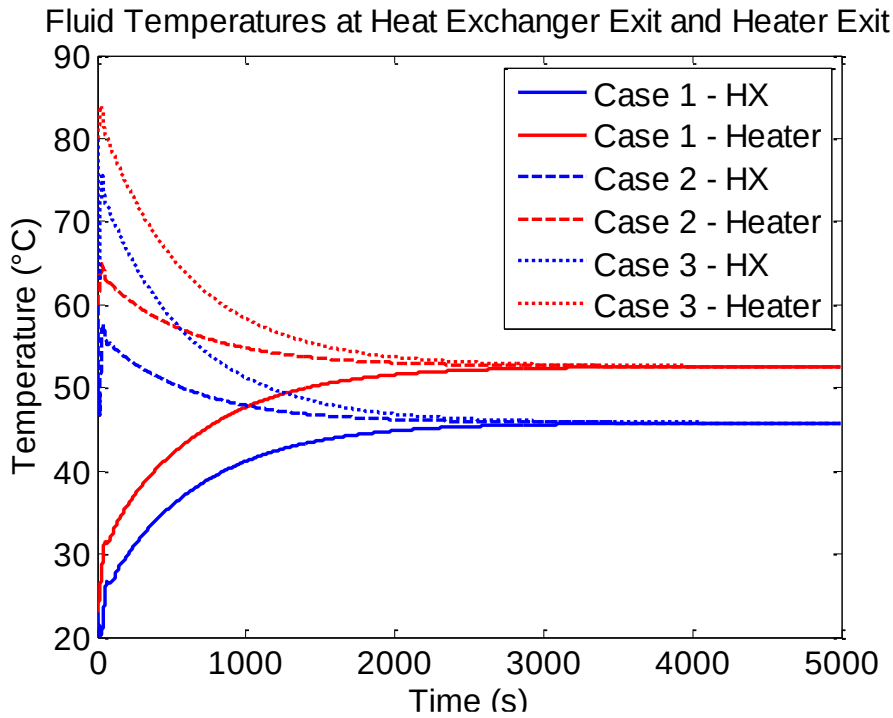

Figure 5.18 Fluid Temperatures for the fourth Initial Temperature Profile Study

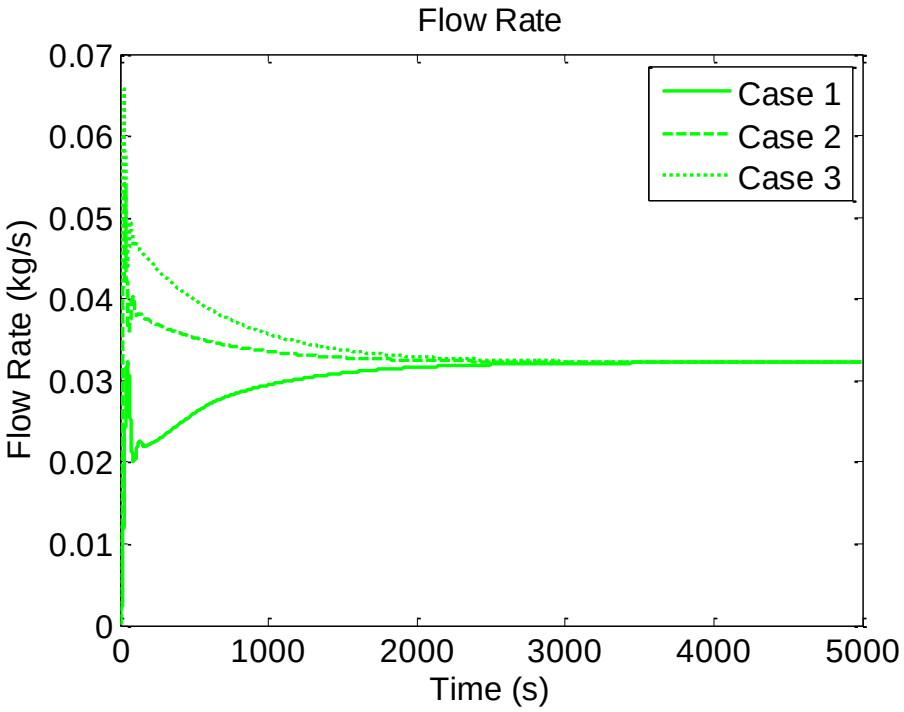

Figure 5.19 Flow Rate for fourth Initial Temperature Profile Study

5.1.3.2 Loop characteristics

The loss coefficient sensitivity tests showed that the temperatures are relatively insensitive to changes in the loss coefficients. The flow rate was sensitive to the total loss coefficient value for the loop, but insensitive to where in the loop the loss coefficients are applied. The flow profile for the heater step transient is below. The profiles for case 1 and case 3 were essentially the same, so the line for case three is black rather than green so that they are both visible on the plot. The flow profile for the LOHS transient can be found in Appendix A.

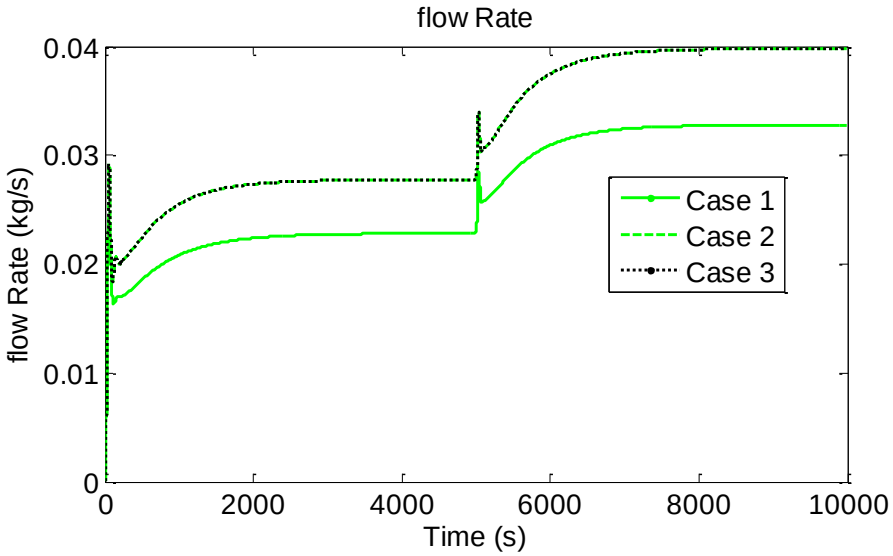

Figure 5.20 Flow Rate for a Heater Step from the Loss Coefficients Study

The heater power tests showed that the flow rate and temperatures were higher for higher power levels. The plots showing the whole startup and heat step transient are in Appendix A. The wall temperature profiles are not shown because they were very similar to the fluid temperature profiles. The oscillation in the flow rate at the beginning of a transient is higher for higher power levels, and the flow rate drops lower from the LOHS for lower heater powers. These can be seen in the plots below.

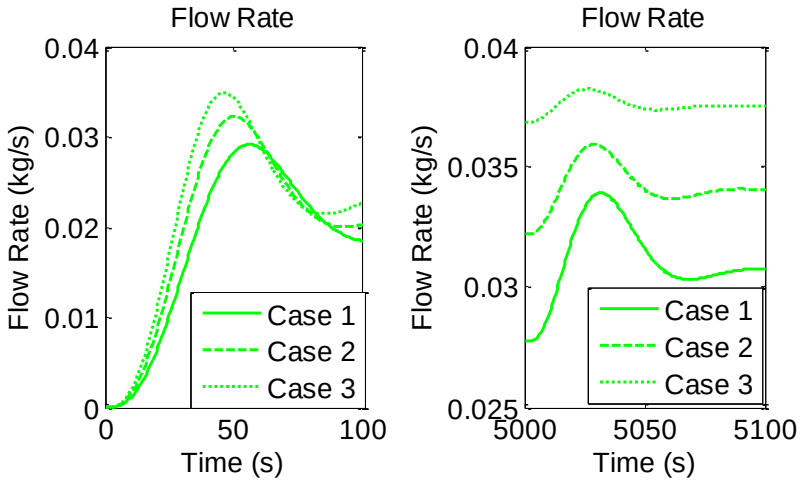

Figure 5.21 Flow rate for the first 100 seconds of the startup and heat step transients for the first Heater Power Study

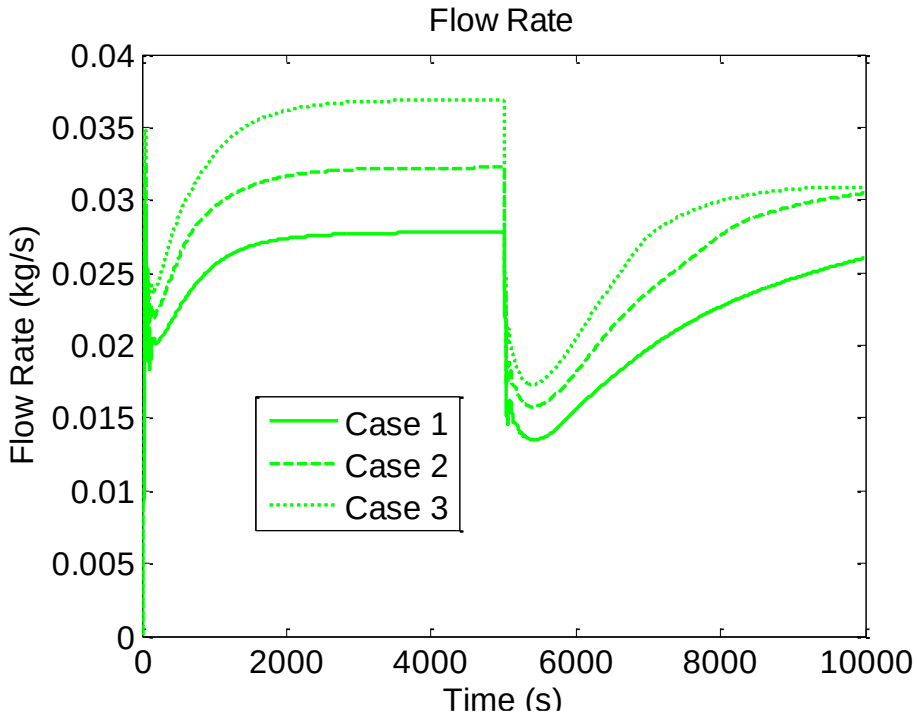

Figure 5.22 Flow rate for the LOHS transient from the fourth Heater Power Study

The heat transfer coefficient used for the horizontal pipes did not impact the solution at all.

5.1.3.3 Boundary conditions

The secondary side heat transfer coefficient significantly affected the solution for all of the transients. The smaller the secondary side heat transfer coefficient resulted in higher temperatures and a lower flow rate. The runs where the heat transfer coefficient assumed only conduction heat transfer on the secondary side had the largest impact. Plots showing this for each transient are below. The wall temperature profiles are very similar to the fluid temperature profiles, so they are not shown.

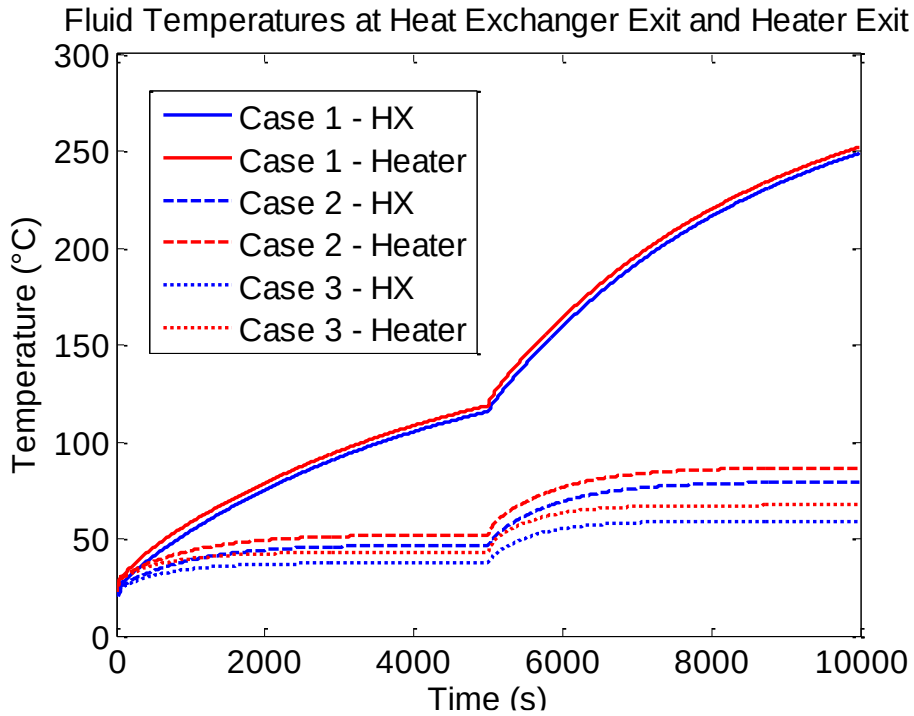

Figure 5.23 Fluid Temperatures for the heater step transient secondary side HTC Study

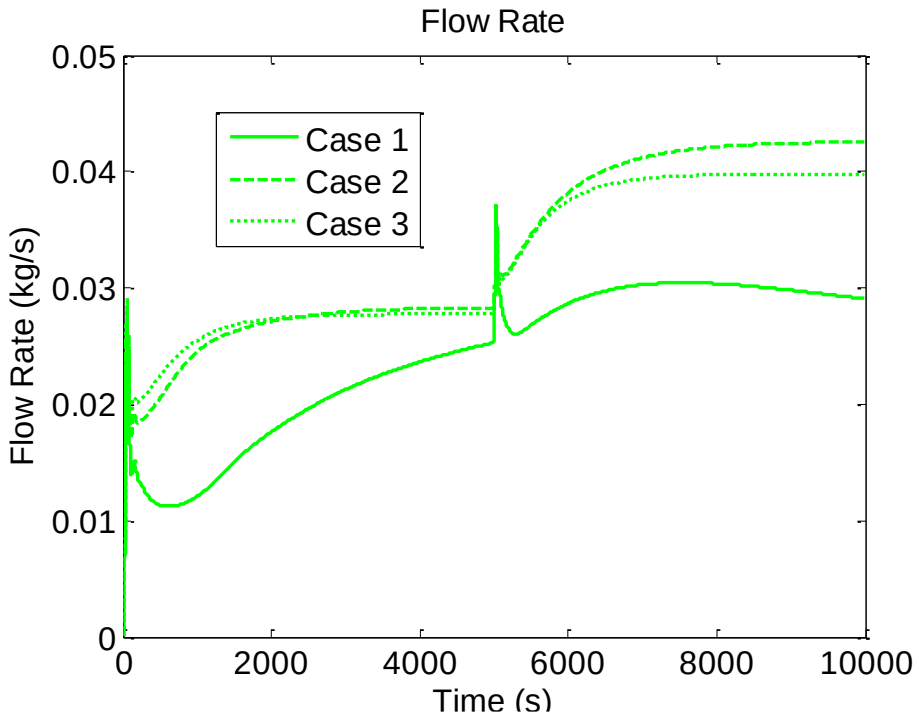

Figure 5.24 Flow Rate for the heater step transient from the secondary side HTC Study

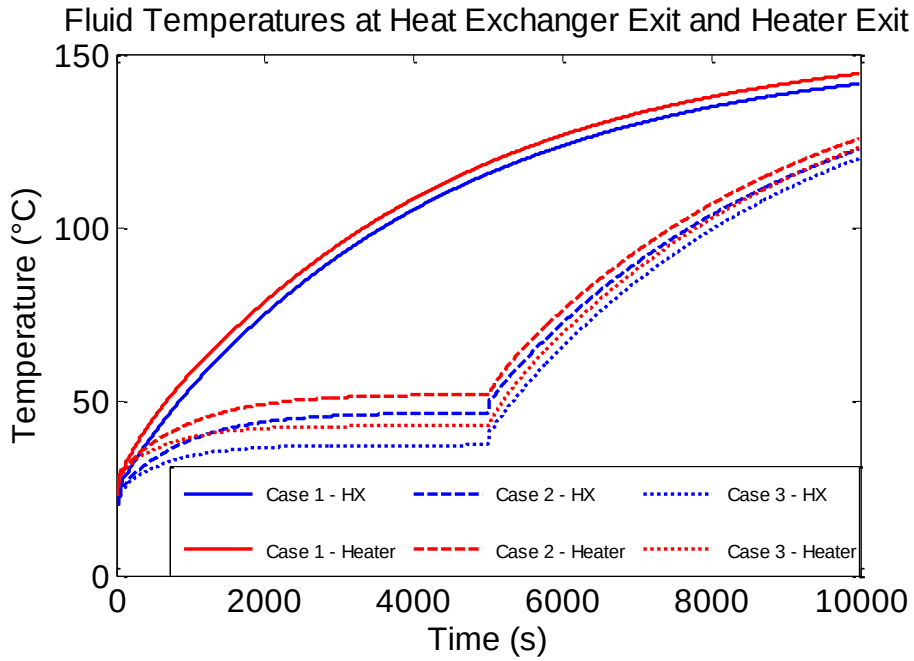

Figure 5.25 Fluid Temperatures for the LOHS transient from the secondary side HTC Study

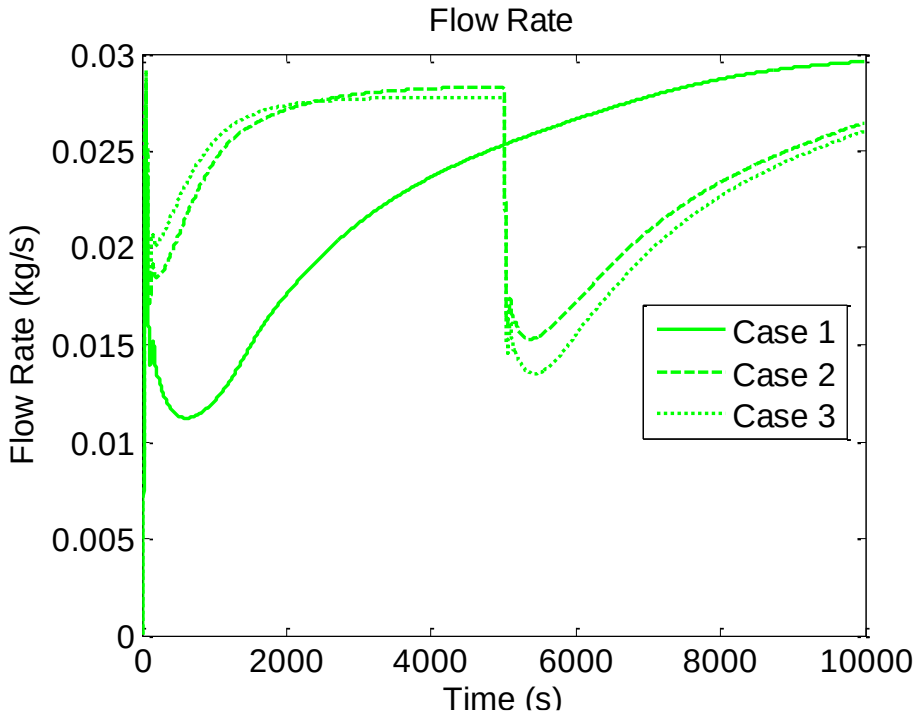

Figure 5.26 Flow Rate for the LOHS transient from the secondary side HTC Study

The heat transfer coefficient used to model the heat loss was varied and found to have an effect on the solution. A higher ambient heat transfer coefficient resulted in lower temperatures, but a higher flow rate. Plots showing this can be found in Appendix A.

Variations in the secondary side temperature changed the solution. When the secondary side temperature is increased, the loop temperatures are higher and the flow rate is higher. The higher flow rate is surprising, because the buoyance force should be lower from the higher secondary side temperature. The plots below show these trends.

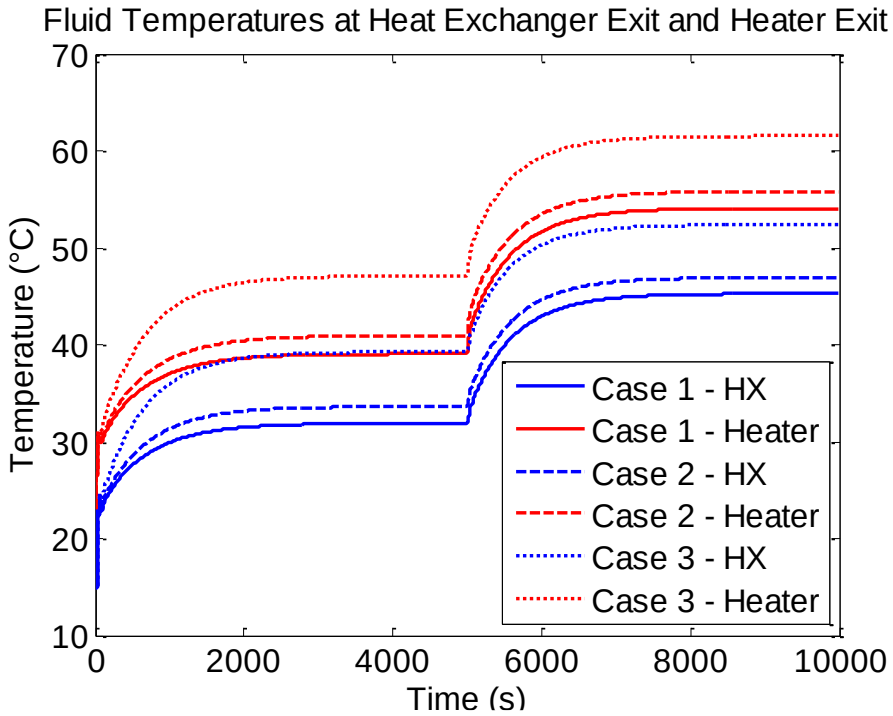

Figure 5.27 Fluid Temperatures for a heater step from the secondary side temperature Study

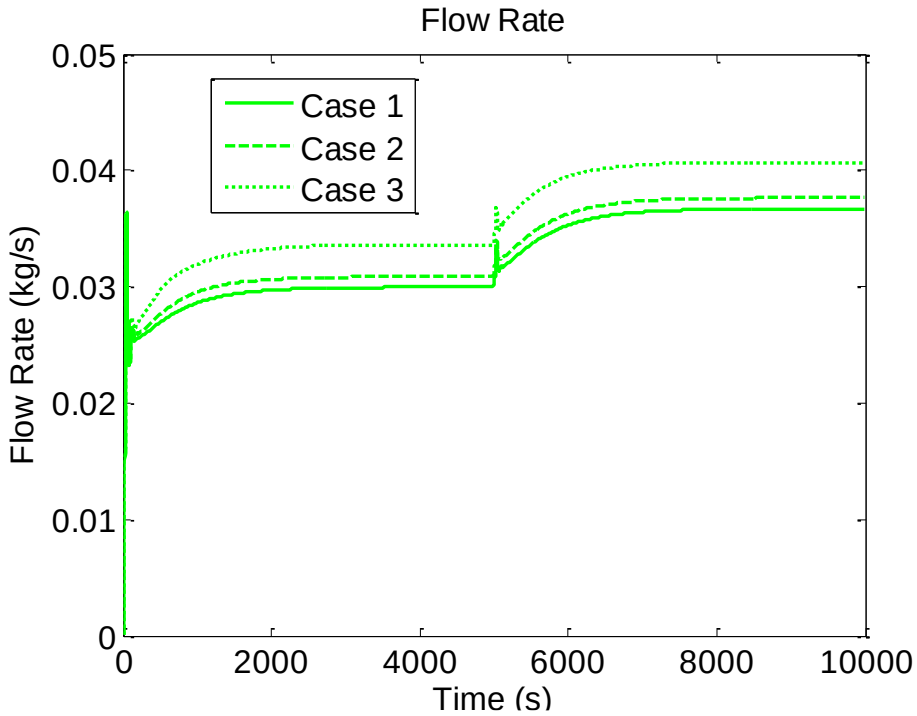

Figure 5.28 Flow Rate for a heater step from the secondary side temperature Study

The ambient temperature was found to have an effect on the temperature and flow rate values. The hotter ambient temperature resulted in hotter loop temperatures and a higher flow rate. A hotter ambient temperature would lead to less losses from the loop, so it makes sense that the flow rate would be higher for higher ambient temperatures. The plots showing the results of the study can be found in Appendix A.

5.1.3.4 Material properties

The specific heat, density, thermal conductivity, and viscosity were tested to determine the solution's sensitivity to each of them. The solution was insensitive to the thermal conductivity and viscosity. The specific heat had a small impact on the solution when varied within the range of data available for the specific heat of flibe. It had a much larger impact on the solution when varied by 30%. Artificially increasing the specific heat resulted in a slightly lower flow rate. The density had a large impact on the hot side

temperatures and flow rate, but not the cold side temperatures. The plots showing the variation of density in the range available for flibe are given below.

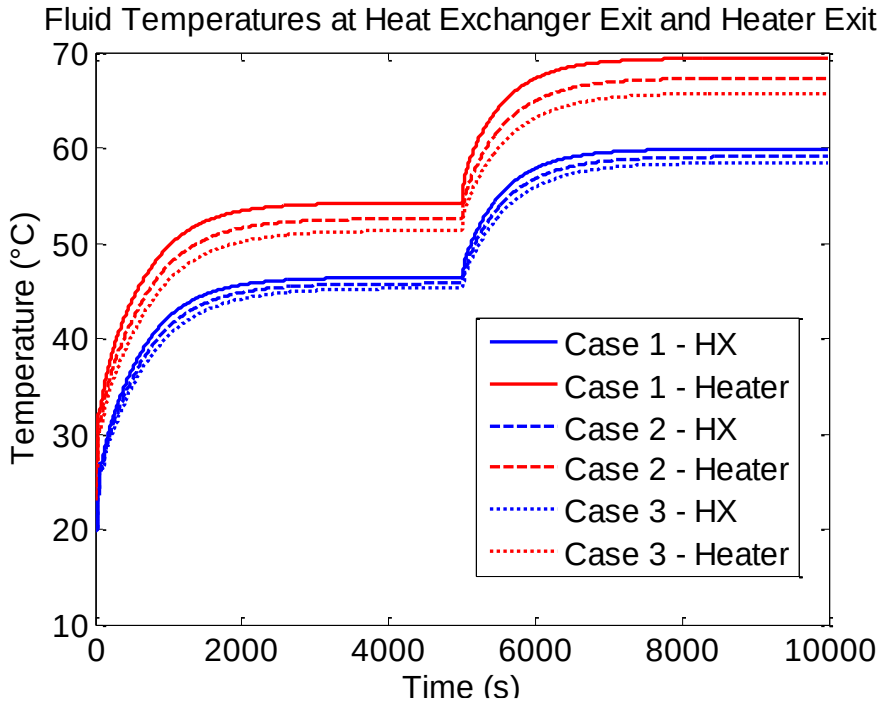

Figure 5.29 Fluid Temperatures for a heater step from the first fluid density Study

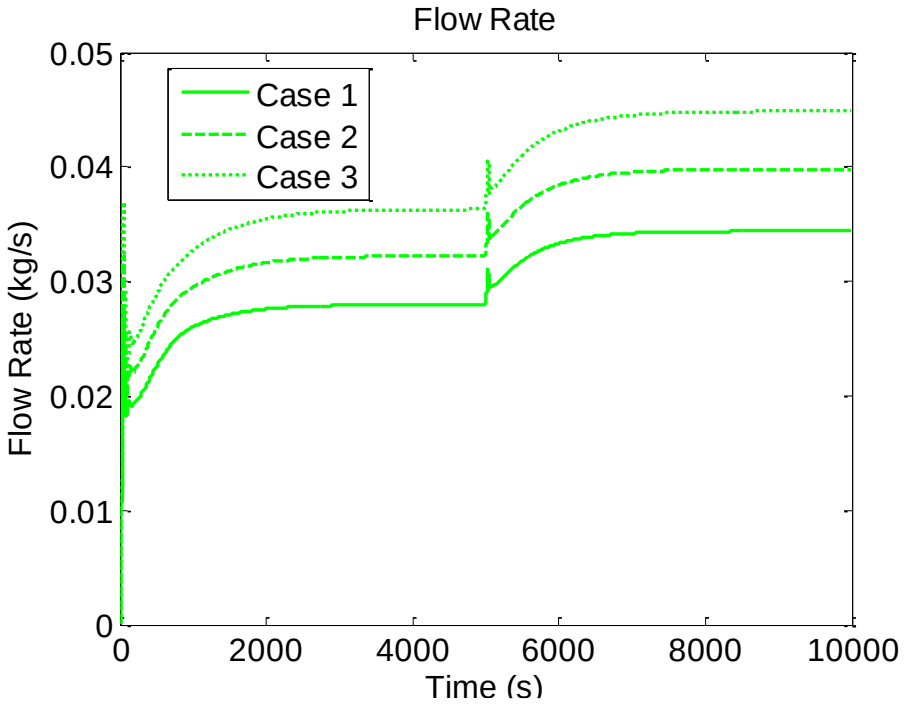

Figure 5.30 Flow Rate for a heater step from the first fluid density Study

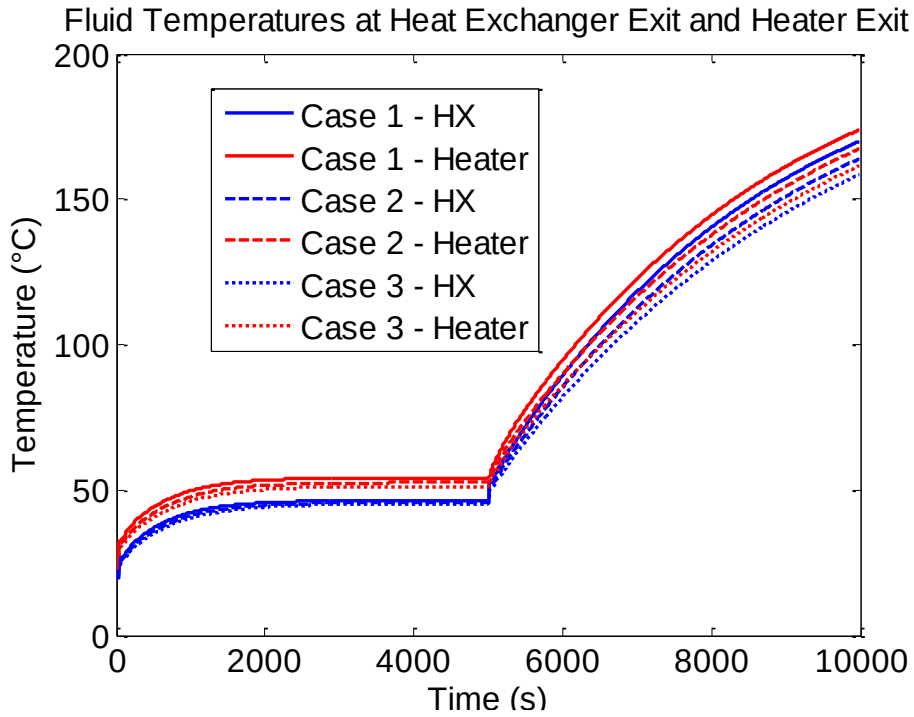

Figure 5.31 Fluid Temperatures for a LOHS from the third fluid density Study

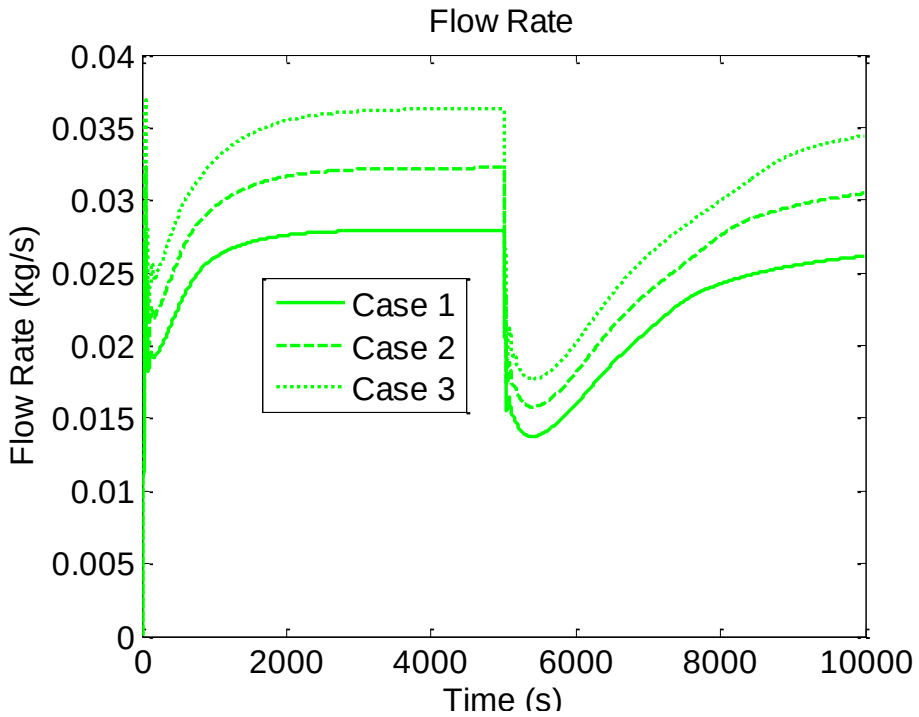

Figure 5.32 Flow Rate for a LOHS from the third fluid density Study

The studies of the wall material properties showed very little effect on the solution.

5.1.4 Numerical Methods

5.1.4.1 Numerical discretization technique

The explicit, semi-implicit, and fully implicit cases all gave the same results for the temperature and flow profiles.

The time step studies showed some interesting results. The profiles of the flow rate and temperatures look relatively similar from using different time steps. However, the larger time step results in a solution that is less smooth. The overall flow and temperature profiles can be found in Appendix A. The plots below show detailed areas of the solution.

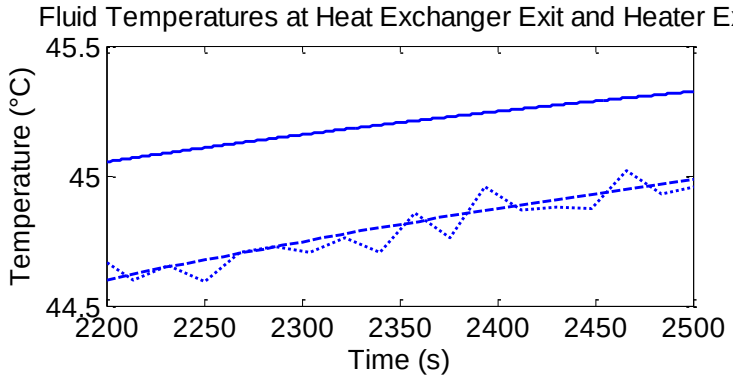

Figure 5.33 Heat Exchanger Exit Fluid Temperature (2200s to 2500s) from first Time Step Study

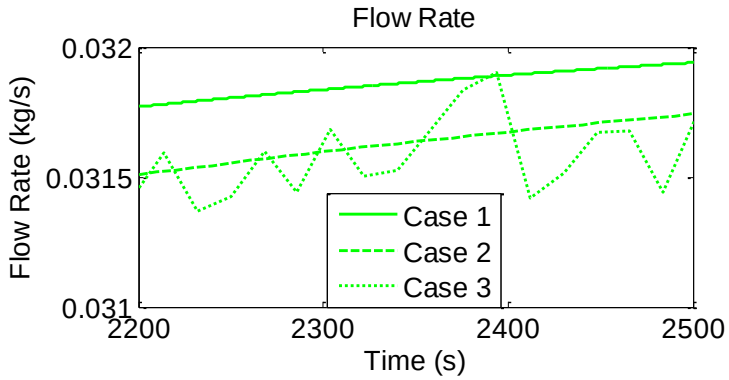

Figure 5.34 Flow rate (2200s to 2500s) of the first Time Step Study

The second time step study showed that varying the time step affects the solution of the temperatures and flow rate profiles. The steady state values are not significantly different, but the transient values do vary. Plots showing this can be found in Appendix A.

The results from the third and fourth time step studies showed that the time step has an impact on the result of the LOHS study. The results from the fourth study are more pronounced. The plots showing the results from the fourth study are below.

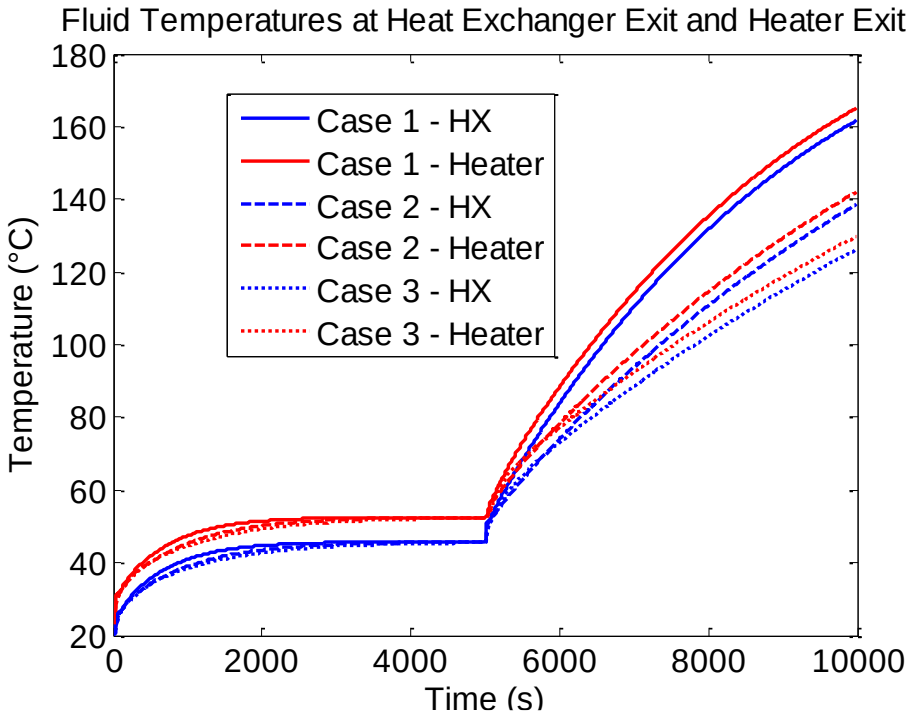

Figure 5.35 Fluid Temperatures for the fourth Time Step Study

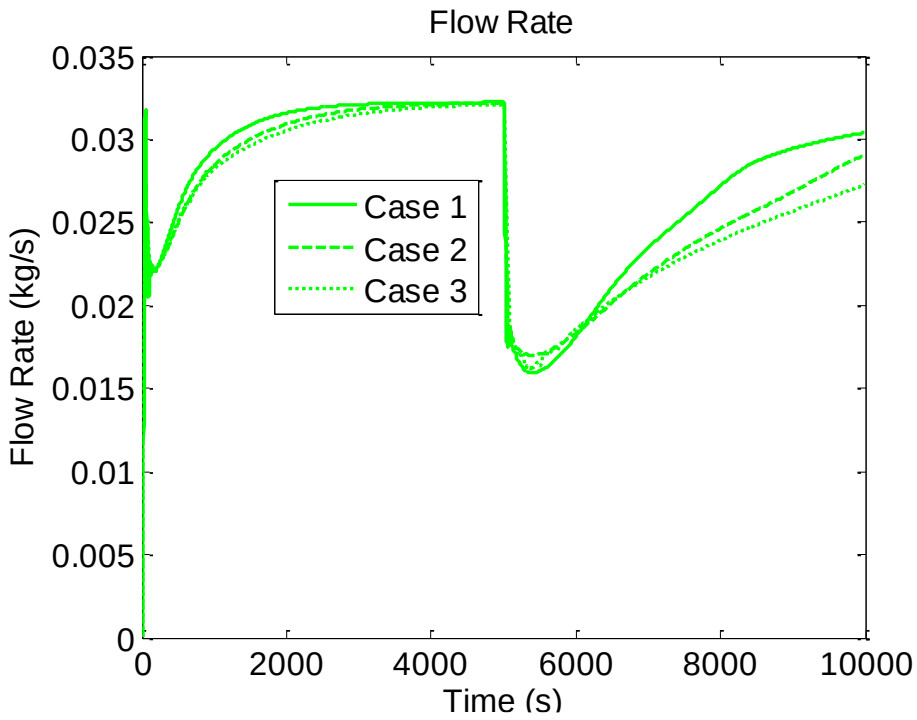

Figure 5.36 Flow Rate for the fourth Time Step Study

5.1.4.2 Density integral approximation

The method used to approximate the density integral had no effect on the solution.

5.2 Experimental Results

The results from the first baseline run are presented here. The rest of the experimental data can be found in Appendix B. The experimental data is compared to the model results in the next section, so it can be seen there as well. Figure 5.37 below shows the flow rate for the first baseline test.

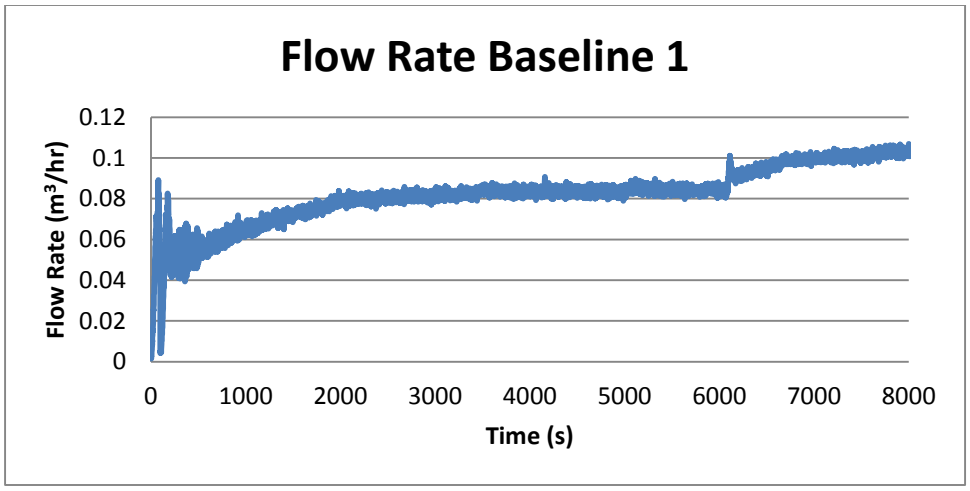

Figure 5.37 Flow Rate from 1st Experimental Baseline Test

The fluid temperatures for the first baseline test are shown in Figure 5.38 below. The temperature drops somewhat between the exit of the heat exchanger and entrance of the heater due to heat losses in the loop.

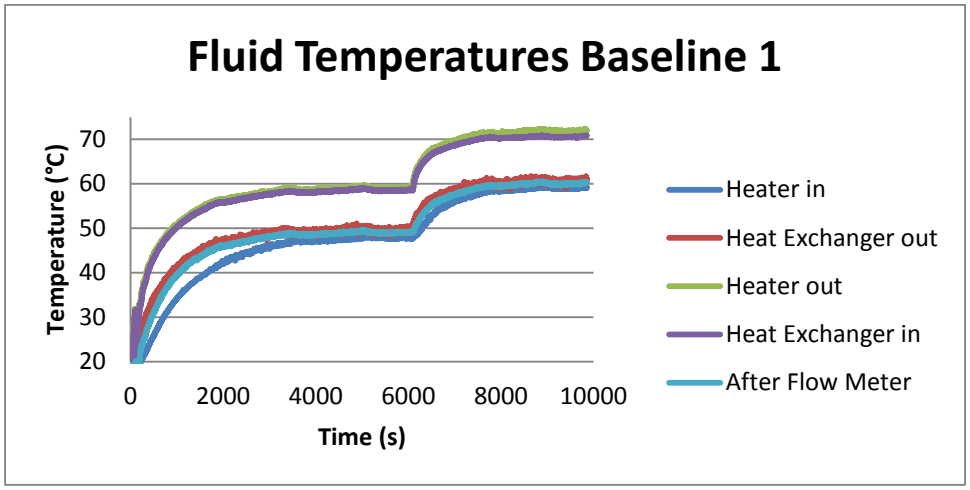

Figure 5.38 Fluid Temperatures from 1st Experimental Baseline Test

There were 15 thermocouples recording the temperature of the heated section. Five of them are presented in Figure 5.39 to show the temperature distribution along the section.

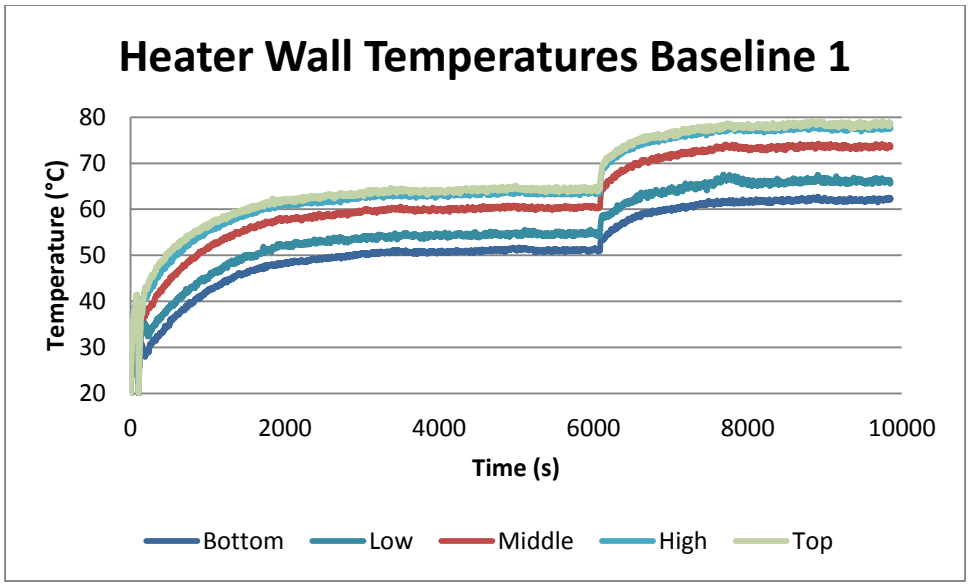

Figure 5.39 Heater Wall Temperatures from 1st Experimental Baseline Test

The temperatures from the first baseline test for the hot and cold leg sections are shown in Figure 5.40 below.

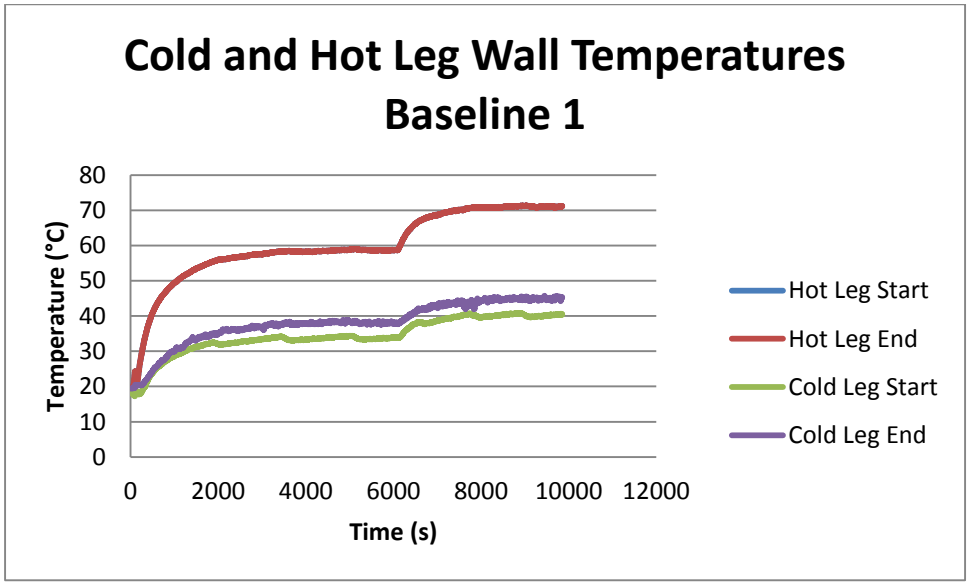

Figure 5.40 Key Wall Temperatures from 1st Experimental Baseline Test

5.3 Simulation Results for Transient Studies

The initial conditions, boundary conditions, and geometry were taken from the experimental runs and put into FLiBeNC files for a validation study to compare the results from the experiment with results from the code. The comparisons for each experimental run are given in this section. The results from the second experimental run of each study is only presented where there was a difference in the results.

First, the results from the baseline tests were compared. The flow rate from the first baseline test was over estimated by the code, but the experimental and computational results both showed oscillations at the beginning of startup and a spike in the flow rate value when the heater power was stepped. This can be seen in Figure 5.41 below.

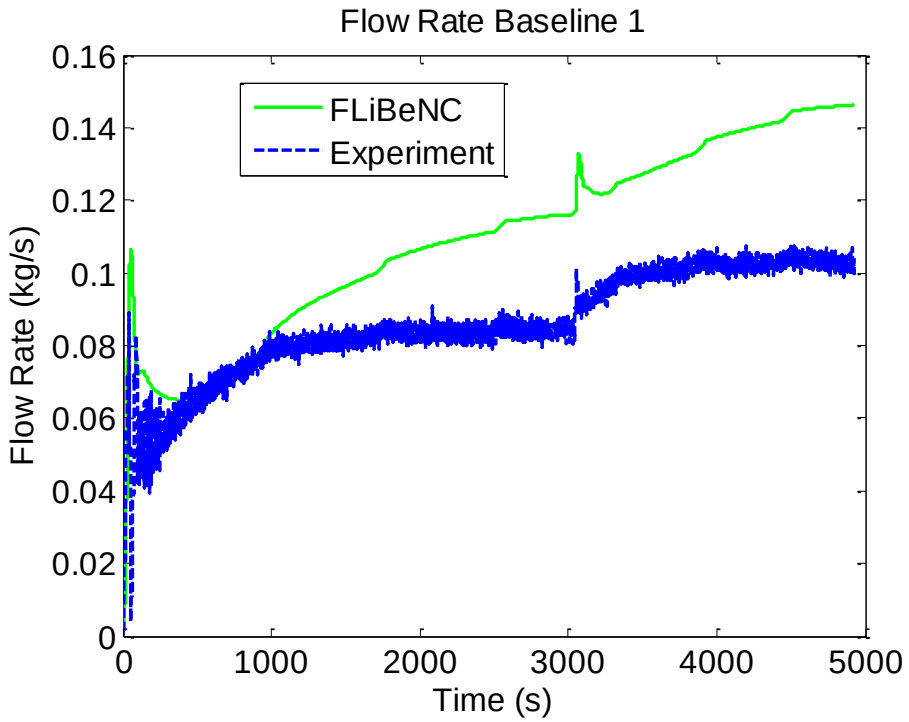

Figure 5.41 Flow Rates from the 1st Baseline Test

For the first baseline run, FLiBeNC underestimated the time to get to steady state. FLiBeNC also gave temperature profiles that were less steep than the ones from the

experiment. The model also somewhat over predicts the temperature values. This can be seen in Figure 5.42 below.

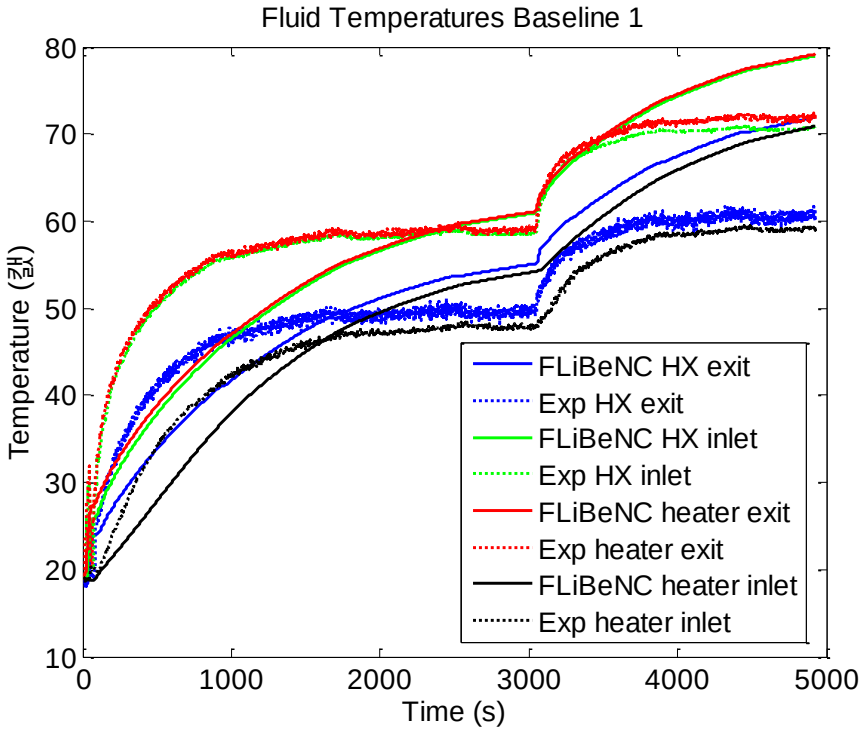

Figure 5.42 Fluid Temperatures from the 1st Baseline Test

The code results in wall temperature profiles that are much closer together than the experiment does. Another interesting point is that the experiment showed that the wall temperature at the heater inlet is hotter than at the heat exchanger inlet, but the coded modeled the heater inlet as slightly colder than the heat exchanger inlet. This can be seen in Figure 5.43 below.

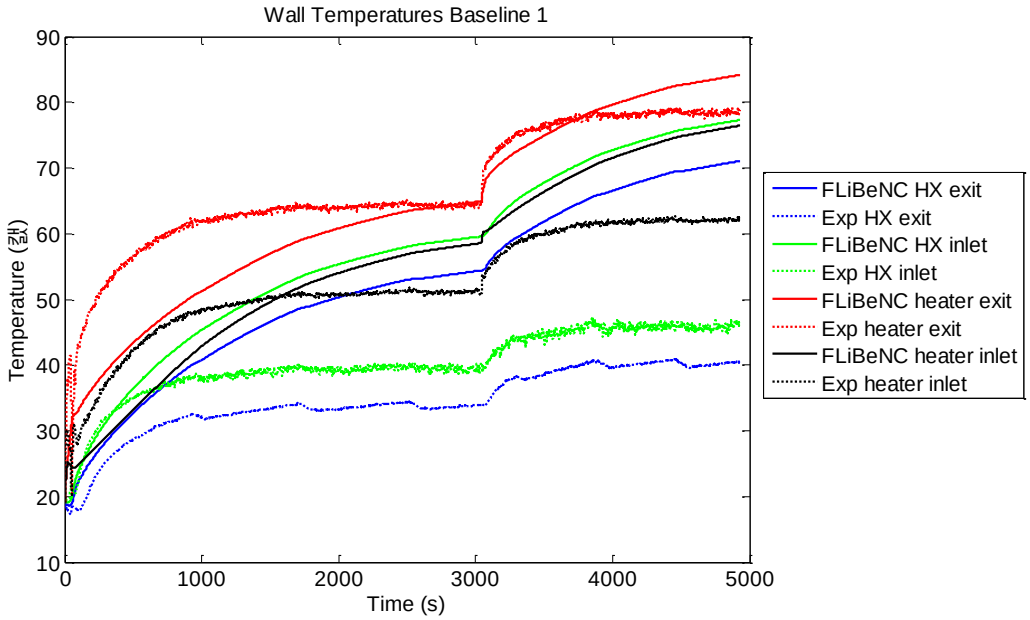

Figure 5.43 Wall Temperatures from the 1st Baseline Test

A comparison of the second baseline test showed that the code still overestimates the flow rate, but initial startup values predicted by the code are higher than they were for the first baseline test as shown in Figure 5.44 below.

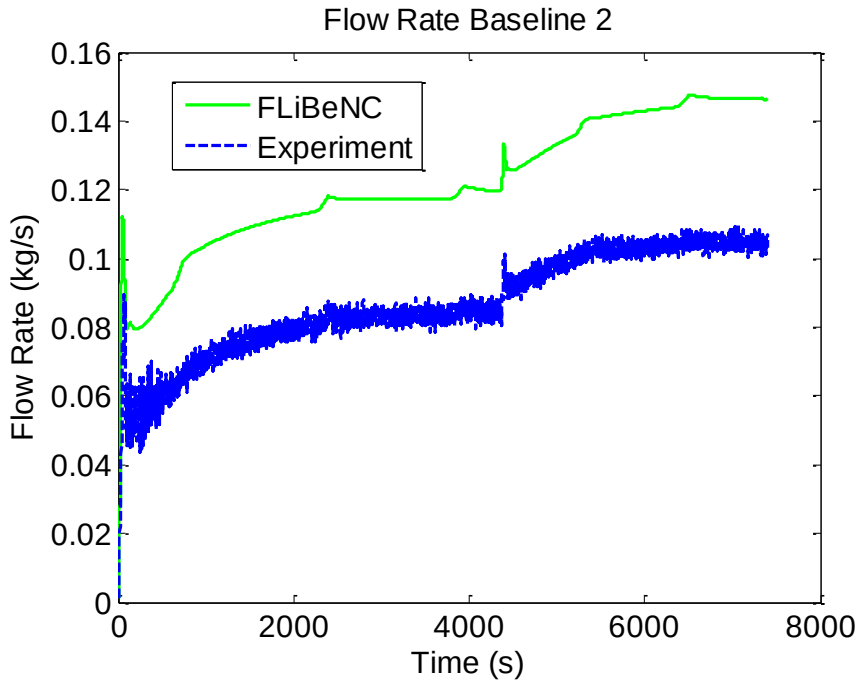

Figure 5.44 Flow Rates from the 2nd Baseline Test

The fluid temperatures predicted by the code followed the trends of the experiment much more closely for the second baseline test; however, the code underestimates all of the fluid temperatures. This can be seen in Figure 5.45 below.

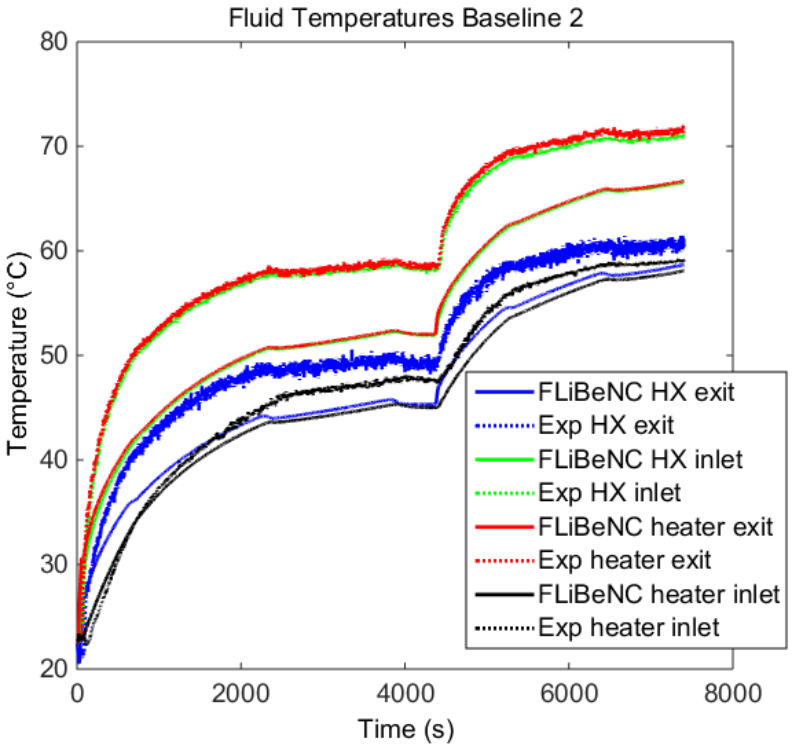

Figure 5.45 Fluid Temperatures from the 2nd Baseline Test

The wall temperatures from the code match the shape of the real temperature profiles from the experiment more closely for the second baseline test, but the code still drastically under predicts the temperature differences across the loop. Figure 5.46 below shows this.

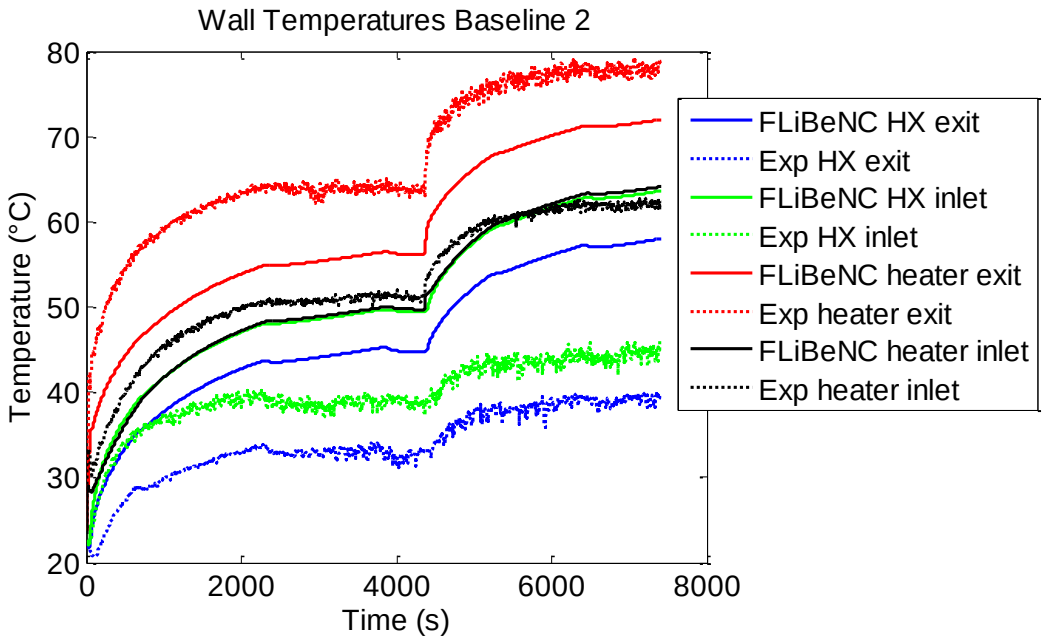

Figure 5.46 Wall Temperatures from the 2nd Baseline Test

The code over-predicted the flow rate for the first high heater test. The plot is shown below in Figure 5.47.

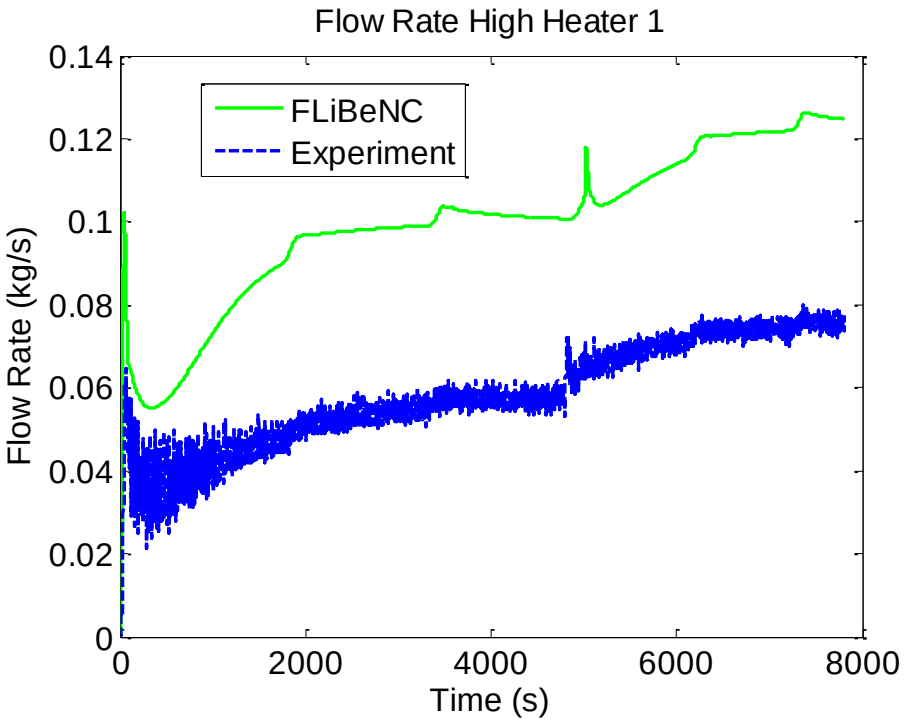

Figure 5.47 Flow Rates from the 1st High Heater Test

The code under-predicted the fluid temperatures in the hot leg, but matched relatively well to the heat exchanger exit temperature from the experiment. The code underestimated the heat loss on the cold side. The plot is shown in Figure 5.48 below.

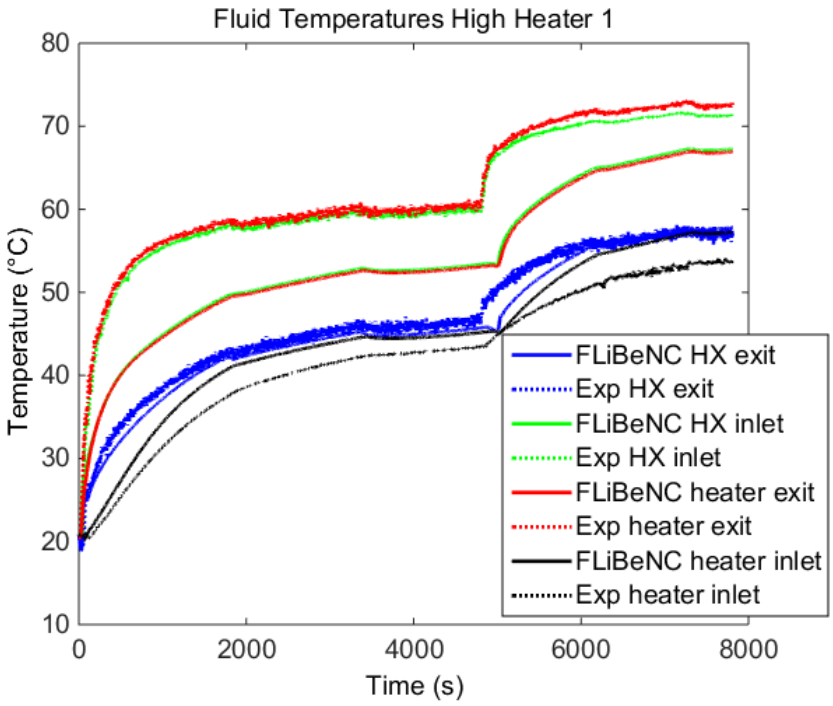

Figure 5.48 Fluid Temperatures from the 1st High Heater Test

The code underestimated the range of the wall temperatures as is shown in Figure 5.49 below. The Figure also shows the temperature at the inlet of the heat exchanger starts out hotter than the temperature at the inlet of the heater, but this changes after about 2000 seconds.

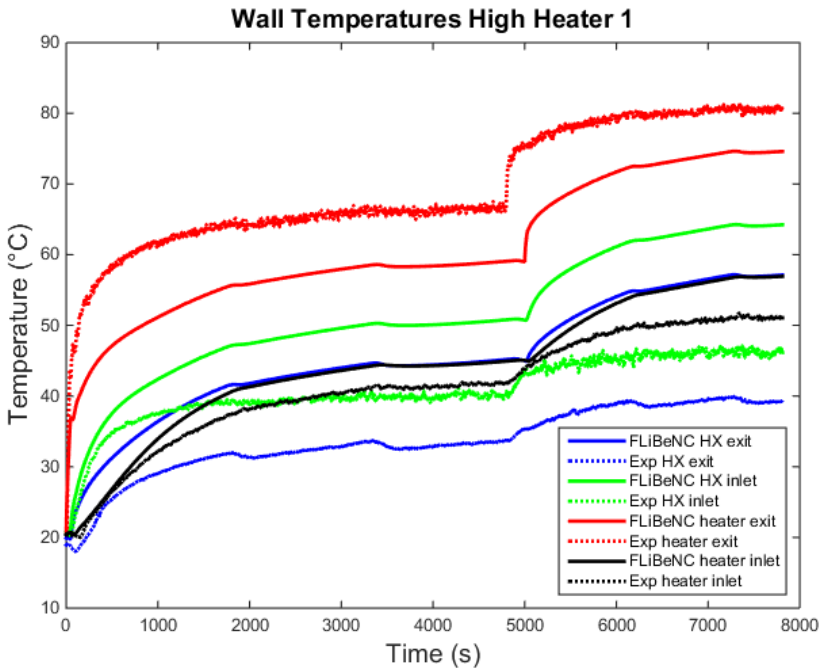

Figure 5.49 Wall Temperatures from the 1st High Heater Test

The only major difference in the results for the second test were in the wall temperatures. The plot is presented below in Figure 5.50. This wall temperature profile does not show the same behavior of the temperature at the inlet of the heater getting hotter than the temperature at the inlet of the heat exchanger.

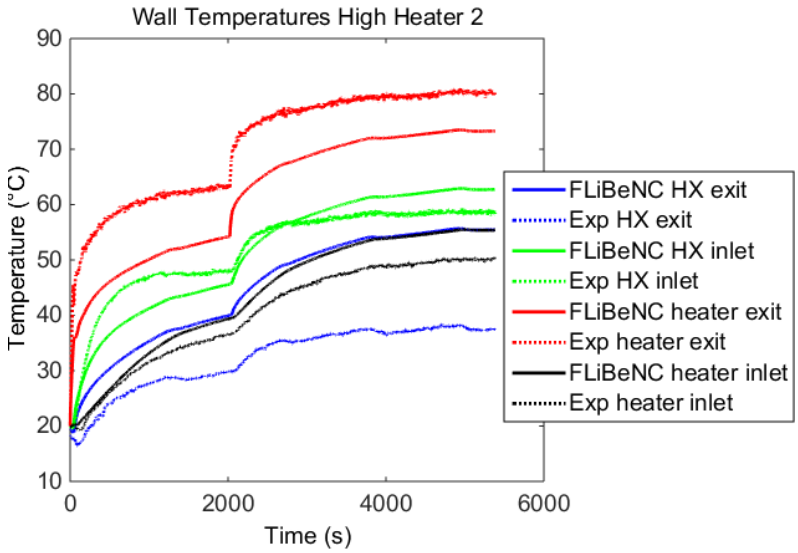

Figure 5.50 Wall Temperatures from the 2nd High Heater Test

In the first low heater test, the results showed that the flow rate in the code is, again, an overestimation and the spread of temperatures is underestimated. This can be seen in Figures 5.51, 5.52, and 5.53 below.

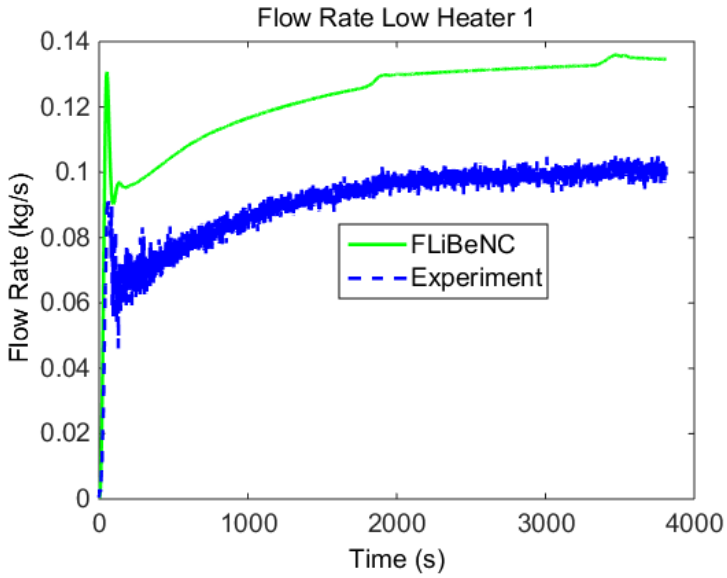

Figure 5.51 Flow Rates from the 1st Low Heater Test

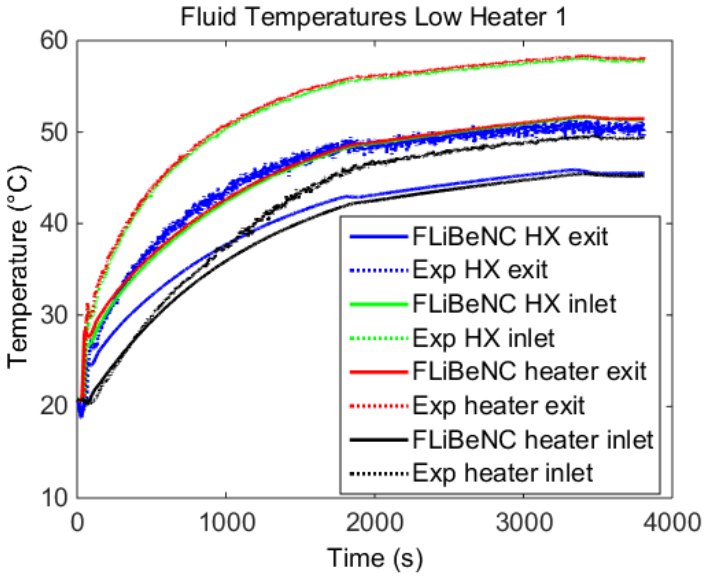

Figure 5.52 Fluid Temperatures from the 1st Low Heater Test

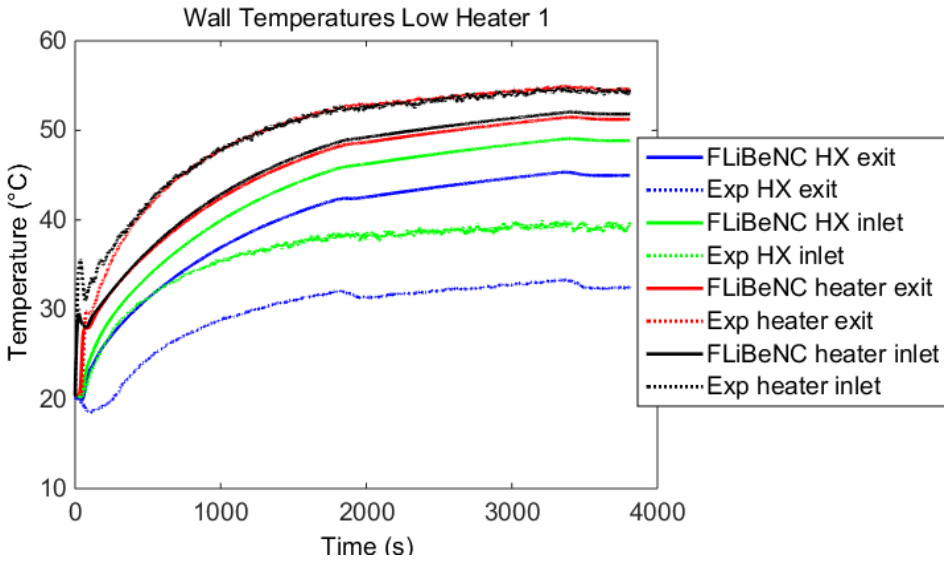

Figure 5.53 Wall Temperatures from the 1st Low Heater Test

The profiles from the second test of the low heater showed the same results, so they are not listed again. Results from the test with secondary flow at 1 gpm are shown below in Figures 5.54, 5.55, and 5.56. This time, the model underestimates the flow rate for most of the transient. The initial spike is in both the results from both the model and the experiment, but the agreement for the rest of the transient is not as good. The model overestimates the value of all of the temperatures and the amount of time it should take to reach steady state.

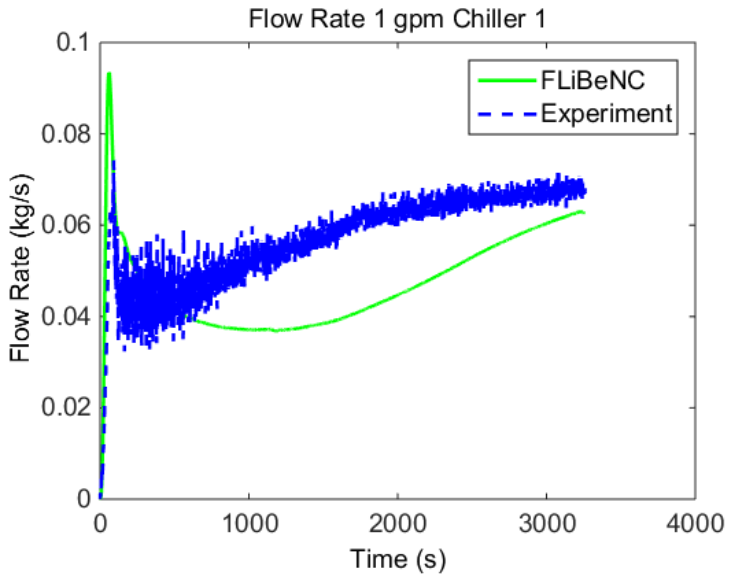

Figure 5.54 Flow Rates from the 1st 1 gpm Chiller Test

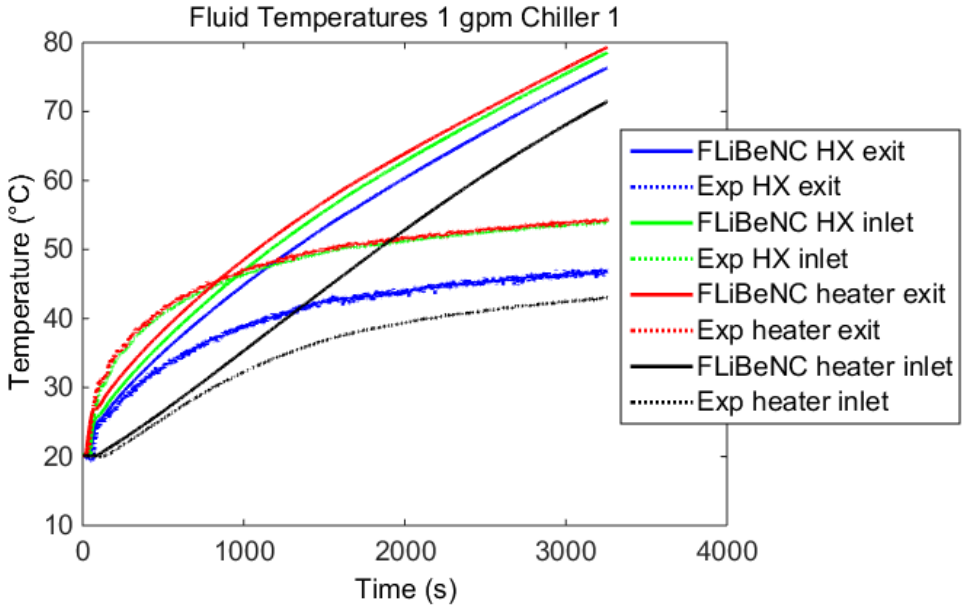

Figure 5.55 Fluid Temperatures from the 1st 1 gpm Chiller Test

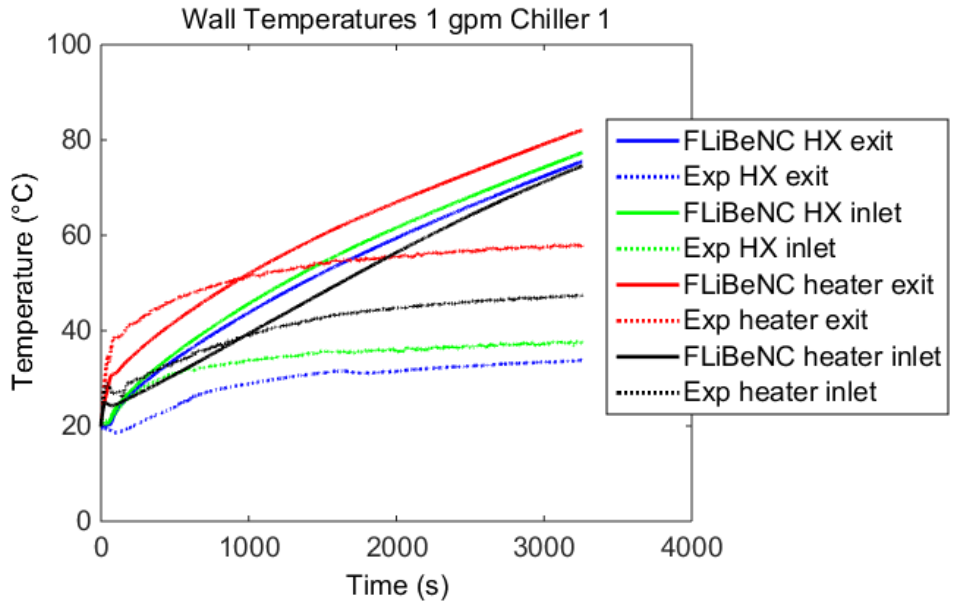

Figure 5.56 Wall Temperatures from the 1st 1 gpm Chiller Test

The second test with the chiller at 1 gpm ran for a longer amount of time, so the flow rate plot shows that the experiment and code start to get closer to the same value towards the end of the transient. The temperature profiles did not vary greatly, so only the flow rate from the second test is presented in Figure 5.57 below.

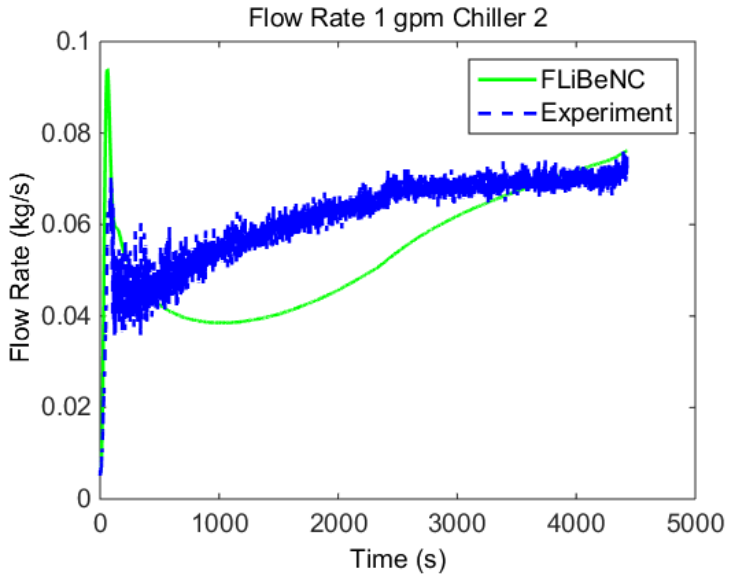

Figure 5.57 Flow Rates from the 2nd 1 gpm Chiller Test

The results from the test with no secondary flow are presented in Figures 5.58, 5.59, and 5.60. The code did a better job modeling this transient except for the heat lost in the cold leg from the experiment. Again, the code modeled the time to approach steady state as longer than the experiment showed based on the curve of the temperature profiles.

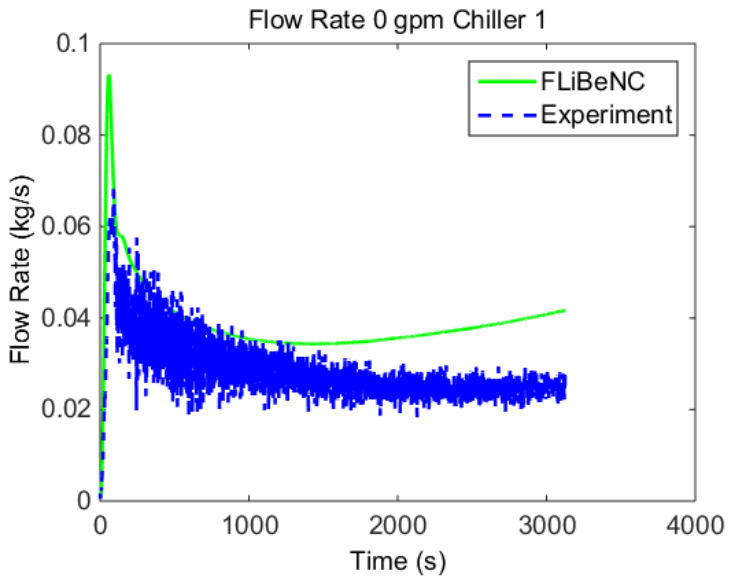

Figure 5.58 Flow Rates from the 1st 0 gpm Chiller Test

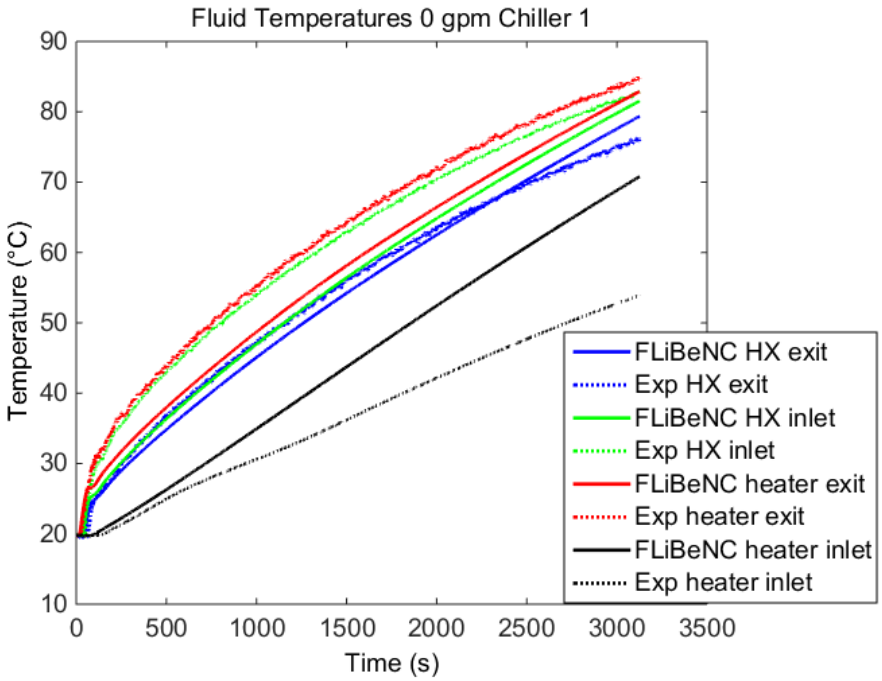

Figure 5.59 Fluid Temperatures from the 1st 0 gpm Chiller Test

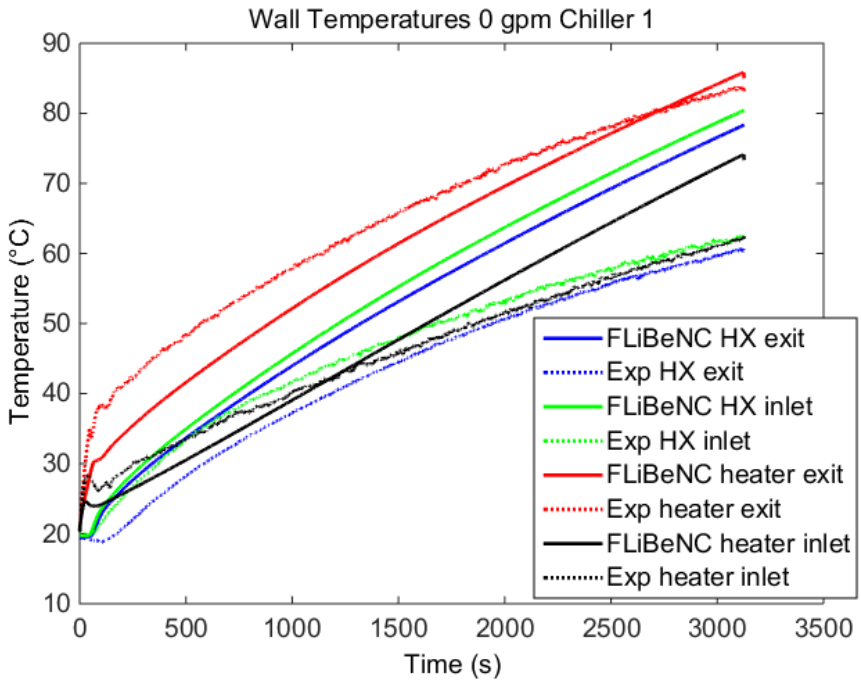

Figure 5.60 Wall Temperatures from the 1st 0 gpm Chiller Test

None of the results from the second run differed significantly, so they are not presented. The results from the initial temperature runs are displayed in Figures 5.61, 5.62, and 5.63. The model over estimates the flow rate and underestimates the temperature difference across the loop. Some of the peaks at the beginning of the transient have similar profiles in the results from the cod and the experiment.

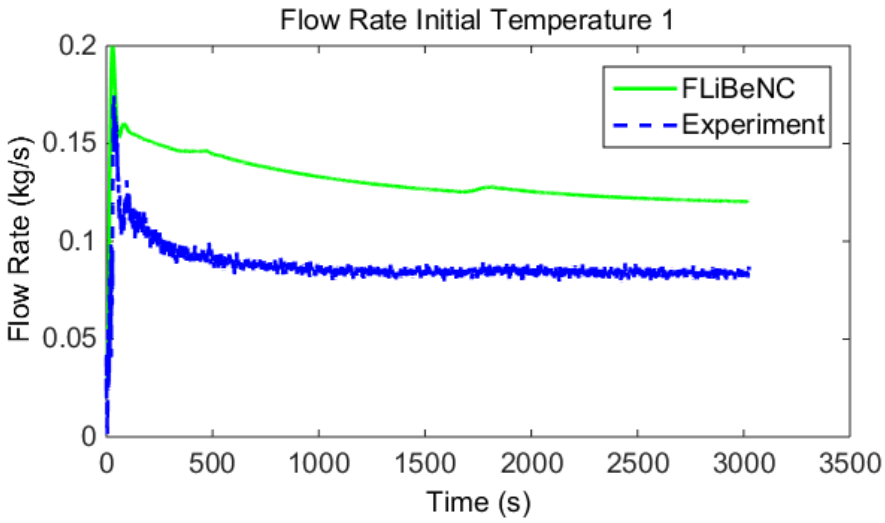

Figure 5.61 Flow Rates from the 1st Initial Temperature Test

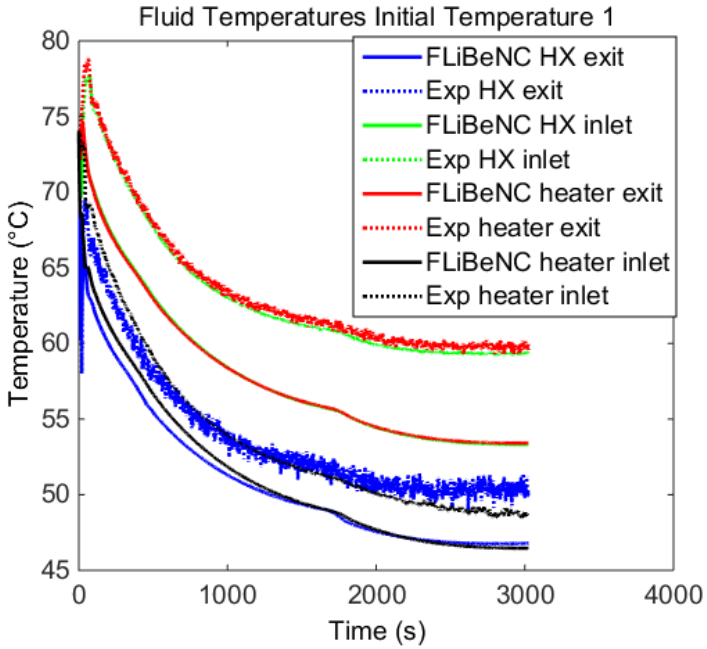

Figure 5.62 Fluid Temperatures from the 1st Initial Temperature Test

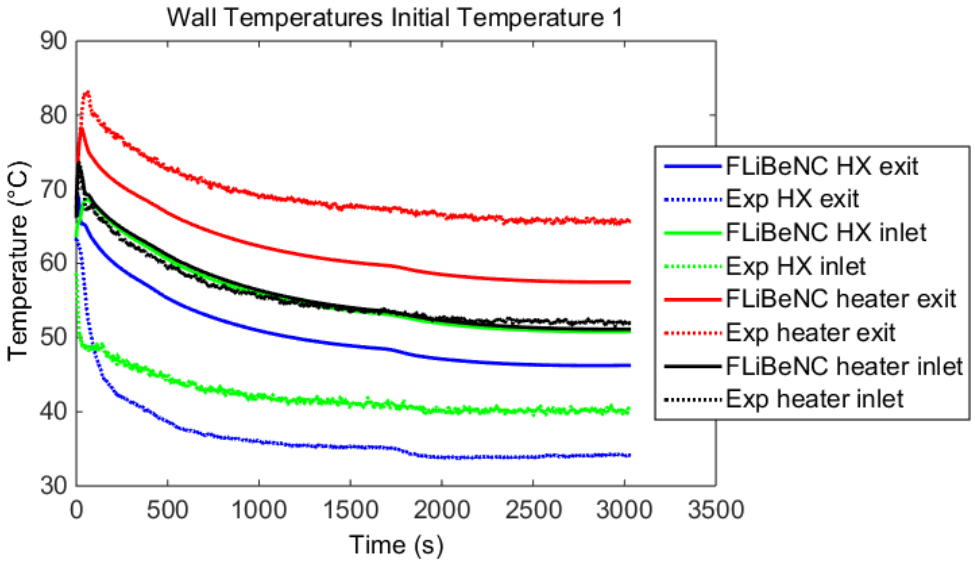

Figure 5.63 Wall Temperatures from the 1st Initial Temperature Test

The results from the second run of the initial temperature test were not significantly different than those from the first run. Results from the first initial flow rate study are presented in Figures 5.64, 5.65, and 5.66. The code modeled the flow rate higher than the experimental data shows, but the oscillatory behavior in the beginning looks very similar. The temperatures from the model underestimate the temperature drop across the loop.

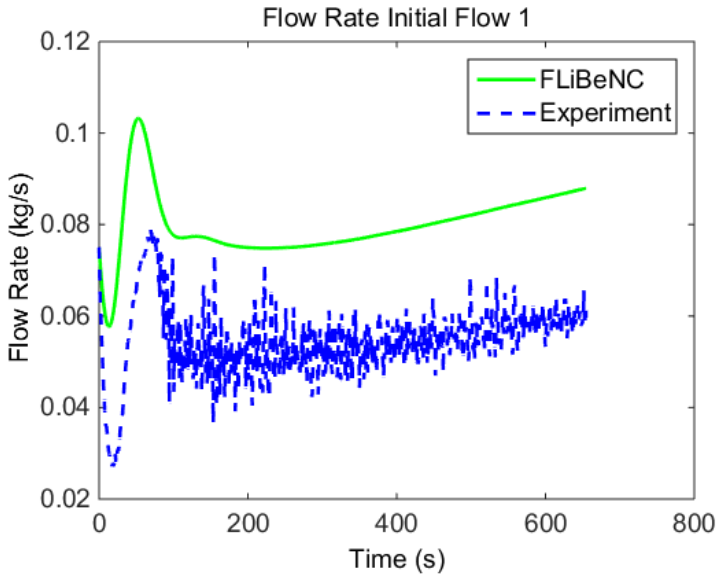

Figure 5.64 Flow Rates from the 1st Initial Flow Test

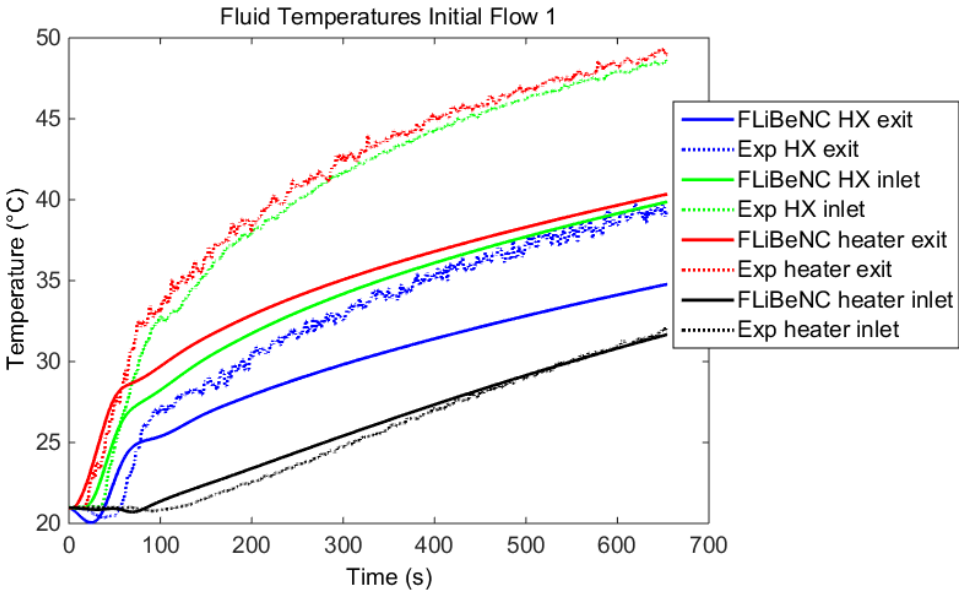

Figure 5.65 Fluid Temperatures from the 1st Initial Flow Test

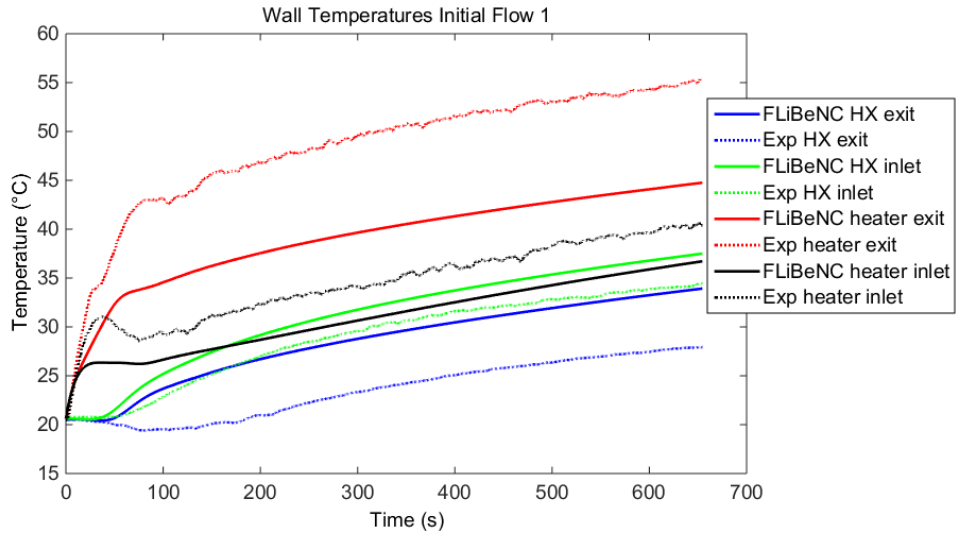

Figure 5.66 Wall Temperatures from the 1st Initial Flow Test

The second run with an initial flow rate was run longer than the first run, so the results from the second run are presented in Figures 5.67, 5.68, and 5.69 below to show the longer profile.

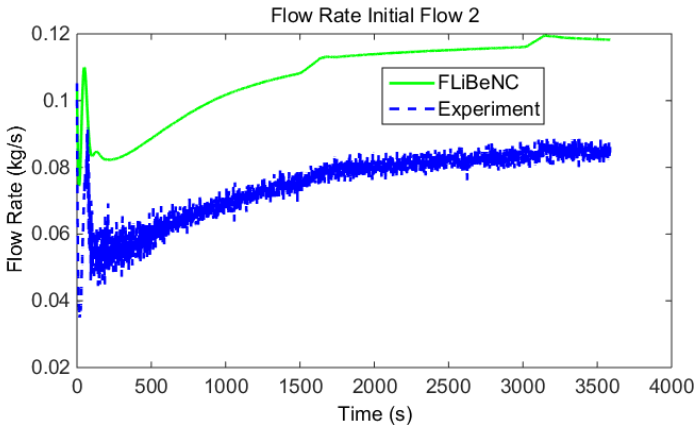

Figure 5.67 Flow Rates from the 2nd Initial Flow Test

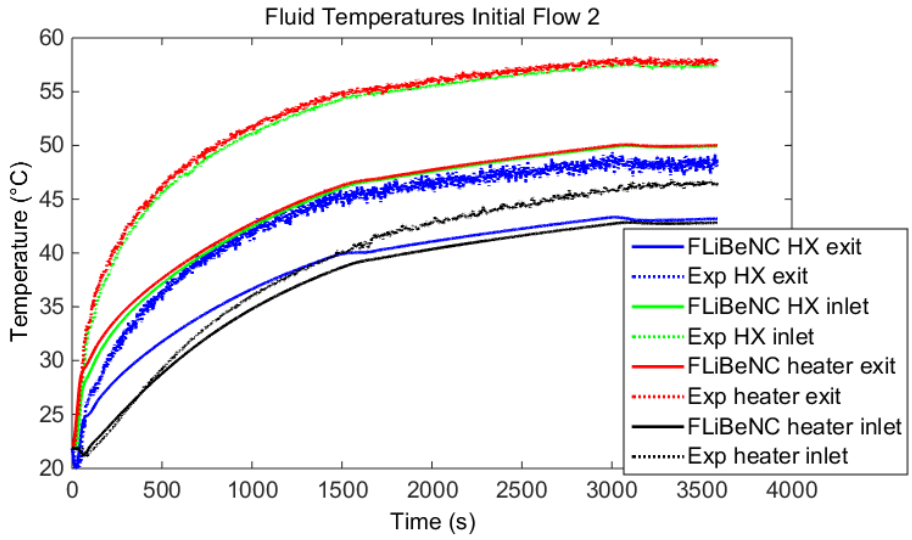

Figure 5.68 Fluid Temperatures from the 2nd Initial Flow Test

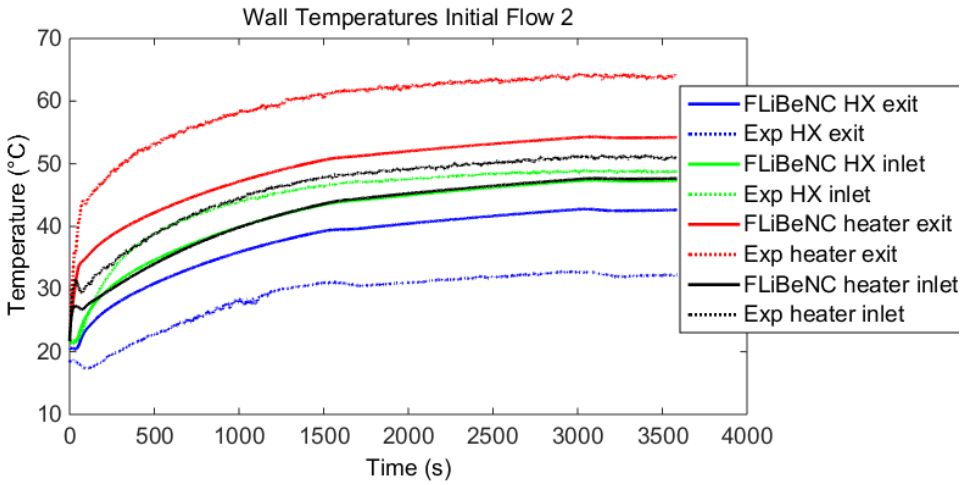

Figure 5.69 Wall Temperatures from the 2nd Initial Flow Test

The results from the LOHS study are presented in Figures 5.70, 5.71, and 5.72. The code over predicts the flow rate, but less so after the LOHS transient starts. The results from the code under estimate the values of the fluid temperatures and the range of the wall temperatures.

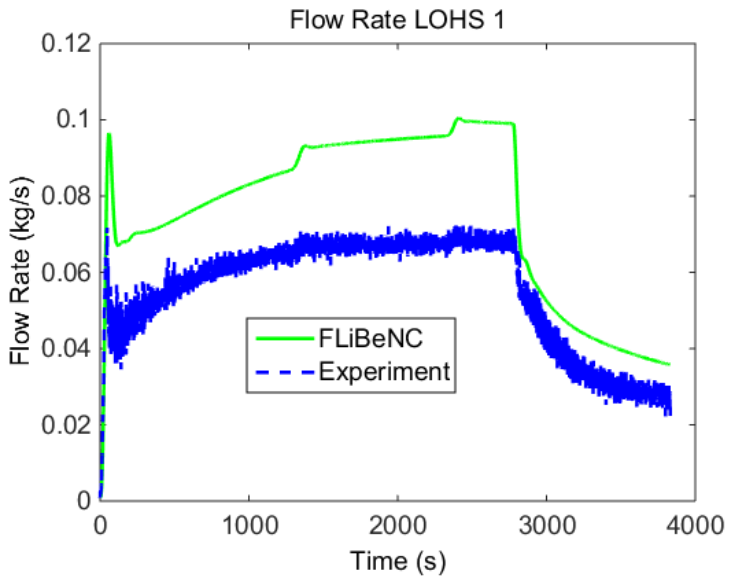

Figure 5.70 Flow Rates from the 1st LOHS Test

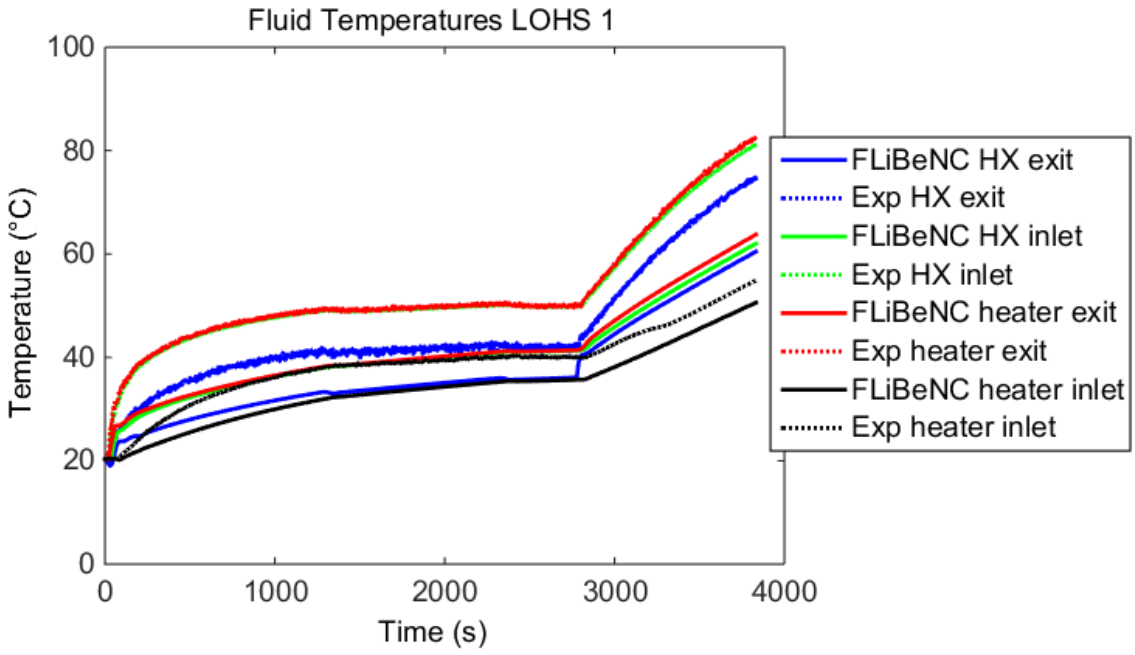

Figure 5.71 Fluid Temperatures from the 1st LOHS Test

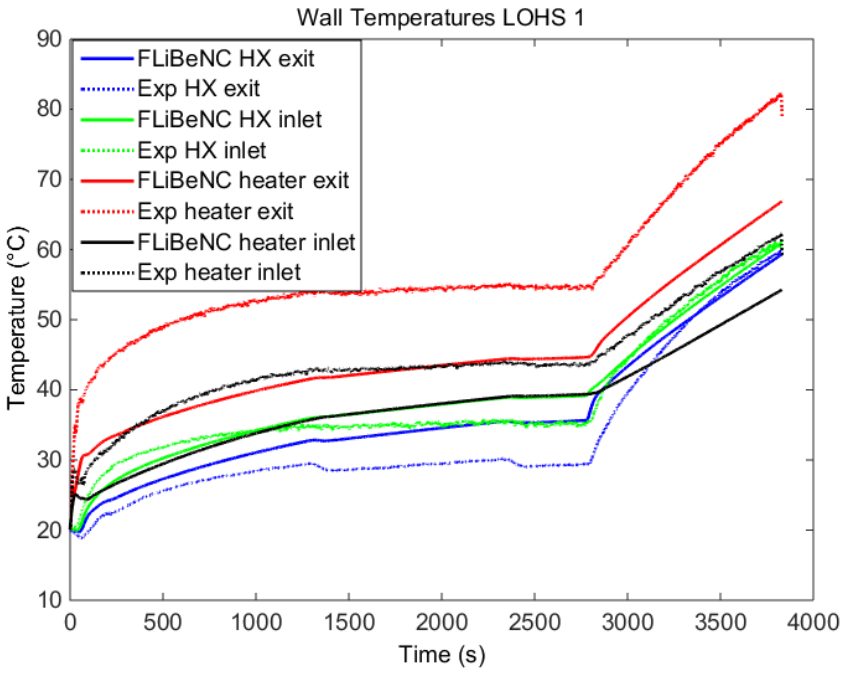

Figure 5.72 Wall Temperatures from the 1st LOHS Test

The second run was longer and the results differed somewhat from the first run, so the results are presented in Figures 5.73, 5.74, and 5.75.

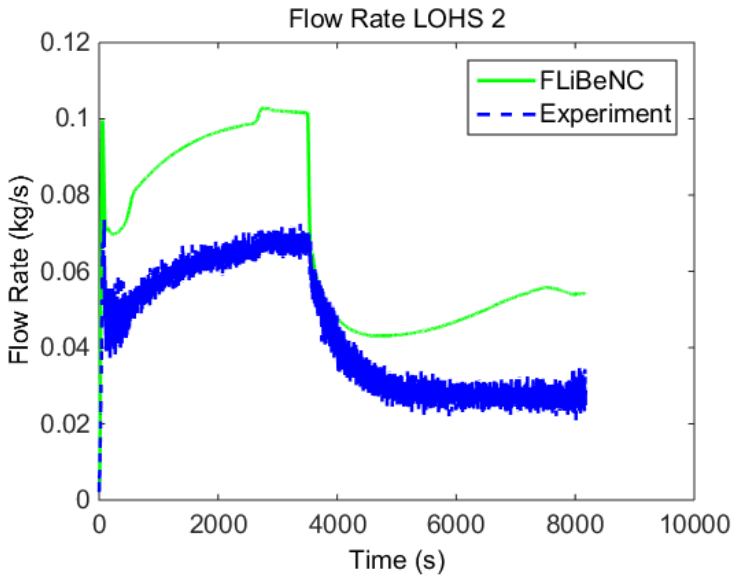

Figure 5.73 Flow Rates from the 2nd LOHS Test

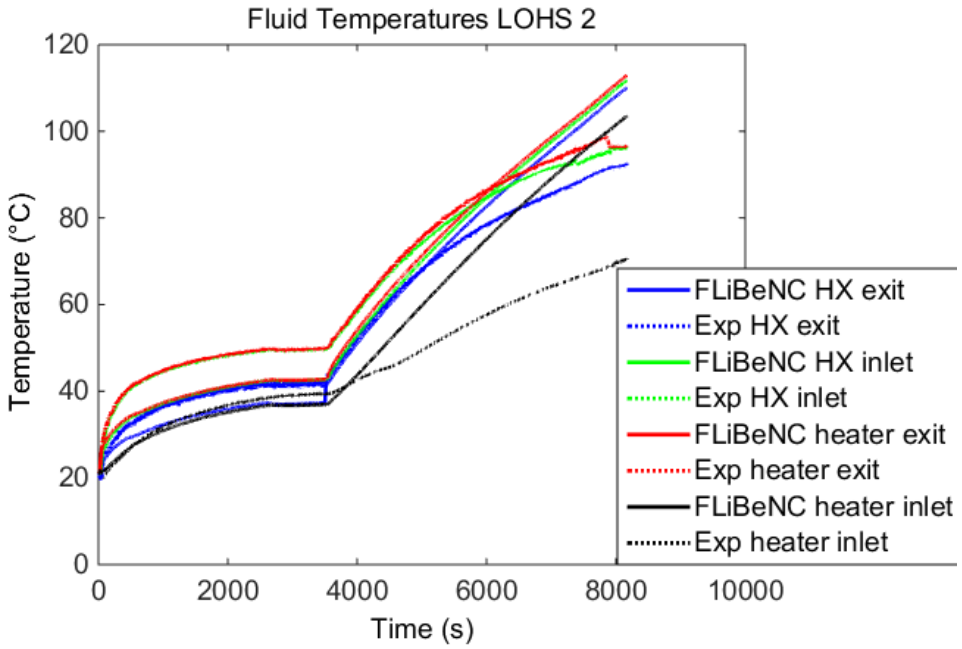

Figure 5.74 Fluid Temperatures from the 2nd LOHS Test

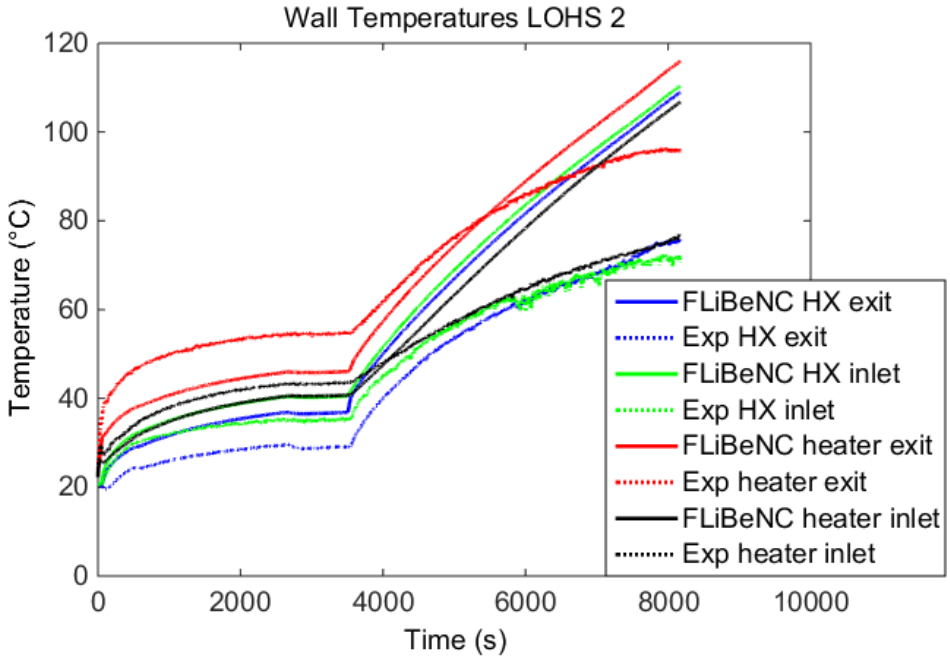

Figure 5.75 Wall Temperatures from the 2nd LOHS Test

Chapter 6 Conclusions and Future Work

Based on the results presented in the previous chapter, FLiBeNC has been shown to capture the temperature and flow profiles for some key transients of interest in the FHR. In general, FLiBeNC overestimated the values of the flow rate and underestimated the values or range of the temperatures in the loop. There are a few primary sources of error that could be contributing to the differences between the experimental and computational results.

The loss coefficients used in FLiBeNC were rough estimations from a table of published values. While this can give a nice starting point, the values have a high uncertainty especially for natural circulation flows. One method for reducing the error caused by this uncertainty is to tune the overall value of the losses in the loop so that the steady state results from the code match those found by the experiment. The preliminary sensitivity study for the loss coefficients that the distribution of the loss coefficients has very little effect on the solution, so an average value could be used for each piece. Future work in this area could be done to verify that the use of average loss coefficient values is acceptable and to tune the values by matching the steady state solutions.

Another potential source of error that could be contributing to the overestimation of the flow rate and underestimation of the temperatures is the heat loss to ambient modeled in the code. Typically experimental validation loops are insulated to minimize the amount of parasitic heat loss, but the loop used in this study was not insulated. A rough calculation was performed to estimate the losses throughout the loop based on the properties of the air surrounding it. This does not factor in the heat lost due to the extra piping connected to the bottom of the loop to allow for forced flow. In the future, the heat lost through various

piping components could be better defined by using the experimental fluid temperature data. This would not work to approximate the heat lost at the heated section, but would improve the calculation of the heat losses in the unheated sections.

The sensitivity studies performed were used to determine which parameters have a significant impact on the solution. The initial conditions studies from the inputs group showed that the initial temperatures had an effect on the startup transient profile, but none of the initial conditions had any effect on the steady state solution. This empirical evidence leads to the conclusion that the steady state solution is unique. Further tests could be done to verify this in the future.

Different geometry configurations of the heater and piping were tested. The results from varying the heater length and position showed that the flow rate is higher for geometries with a larger height difference between the center of the heat exchanger and heater. This usually also resulted in lower fluid temperatures. Increasing the height of the loop was found to have very little effect on the solution. The diameter of the piping, however, mattered considerably. The larger diameter pipes resulted in a higher flow rate and therefore lower fluid temperatures. This result makes sense as the friction would be decreased by an increase pipe diameter. Increasing the thickness of the pipes resulted in a lower flow rate and lower temperatures.

Unsurprisingly, increasing the power level increased the flow rate and temperatures in the loop. The heat transfer coefficient correlation for the horizontal pipes was found to have little effect on the solution. This is encouraging since the correlations and their accuracy for transition flow are not well characterized.

All of the boundary conditions tested were found to have an effect on the solution. This reiterates the importance of a well characterized heat transfer coefficient for heat losses along the loop. The ambient and secondary side temperatures are important to represent accurately as well. The study of the secondary side temperature showed that the flow rate is higher for higher secondary side temperatures. This result is surprising and should be studied further in future studies. The fluid density was the only material property found to have a significant impact on the solution. This is unsurprising as the fluid density drives the buoyance force.

The tests of the numerical parameters gave some interesting results. The solution method (explicit, semi-implicit, or fully implicit) was found to have very little effect on the solution at a small time step. The overall profiles of the startup and heat step transients were very similar for various time steps. A larger time step did, however, result in a more jagged solution. The time step had an impact on the LOHS transient with a more pronounced effect with the fully implicit solution method. Despite any variations in the transient profiles, the steady state values were very similar for the different time steps. This is encouraging as it suggests that the numerical noise (overestimation or underestimation of the solution) at each time step is small enough to converge on the same steady state solution for various time steps. The density integral approximation method did not significantly impact the solution, so the time step used must have been small enough that Simpson's rule and Trapezoidal rule give a very similar result.

The sensitivity studies performed serve as a first step towards a full understanding of the parameter sensitivities in the code. Further work is needed to determine the rate of change in the solution for each parameter. The current study only tested the sensitivity of

varying one parameter at a time. Sensitivities from parameter interactions will need to be studied as this work progresses.

The experimental results showed that the wall temperatures at the heat exchanger exit were the coldest and the wall temperatures at the exit of the heater were the hottest. Most of the runs showed that the wall temperatures at the inlet of the heat exchanger were colder than those at the inlet of the heater, but two of the runs showed different results. The first run with the chiller at 0 gpm and the second run with the high heater showed that the wall temperatures at the heater inlet were colder than those at the heat exchanger inlet. More experimental runs will need to be done in the future to determine if this was because of the parameter being tested, or a result of variation in experimental data.

Appendix A - Extra Sensitivity Study Details

For each of the three heater nodalization tests, the wall temperatures followed the same trend as the fluid temperatures, so only plots for the fluid temperatures and flow rate are produced below for each test.

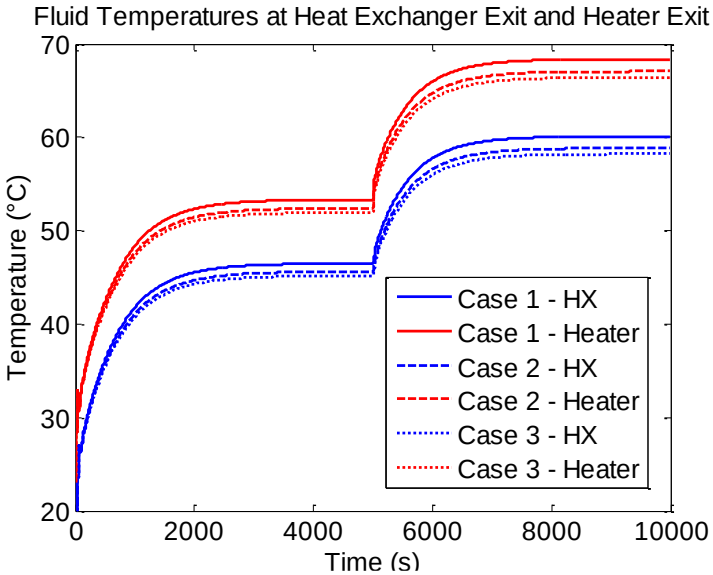

Figure A.1 Fluid Temperatures from the first heater nodalization Study

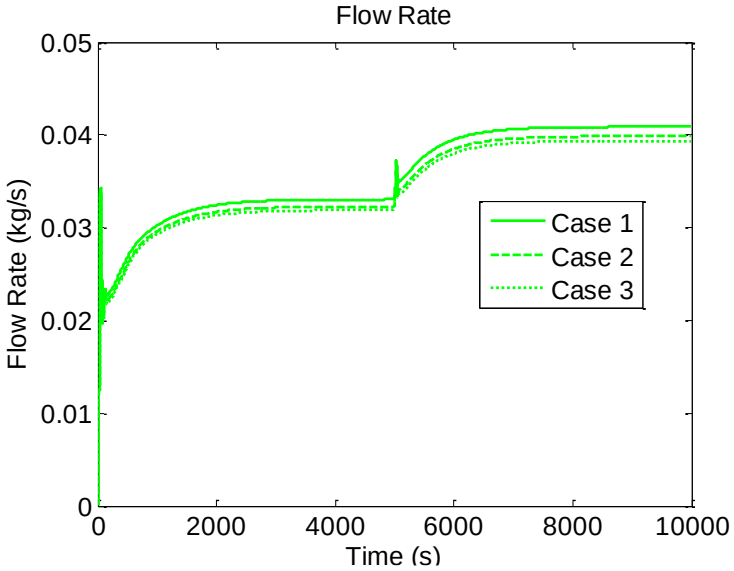

Figure A.2 Flow Rate from the first heater nodalization Study

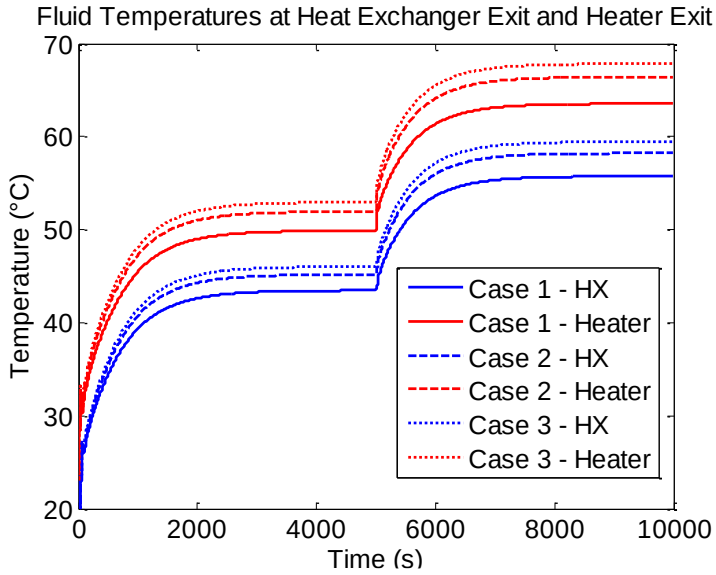

Figure A.3 Fluid Temperatures from the second heater nodalization Study

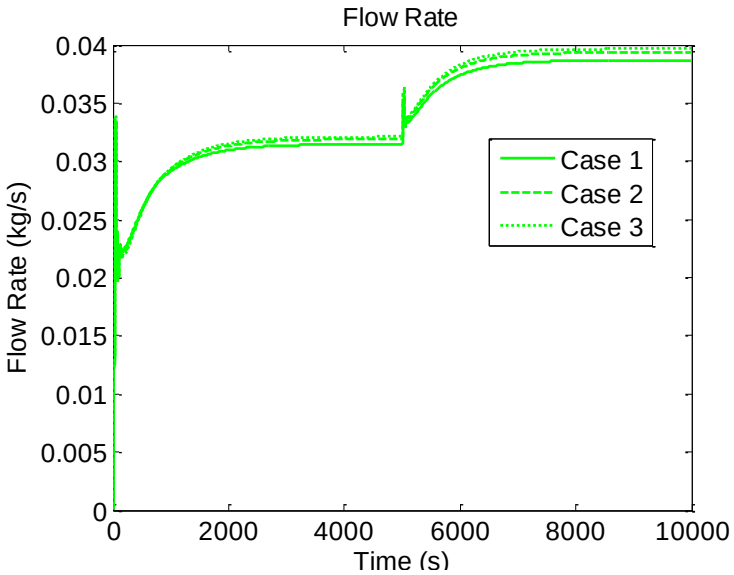

Figure A.4 Flow Rate from the second heater nodalization Study

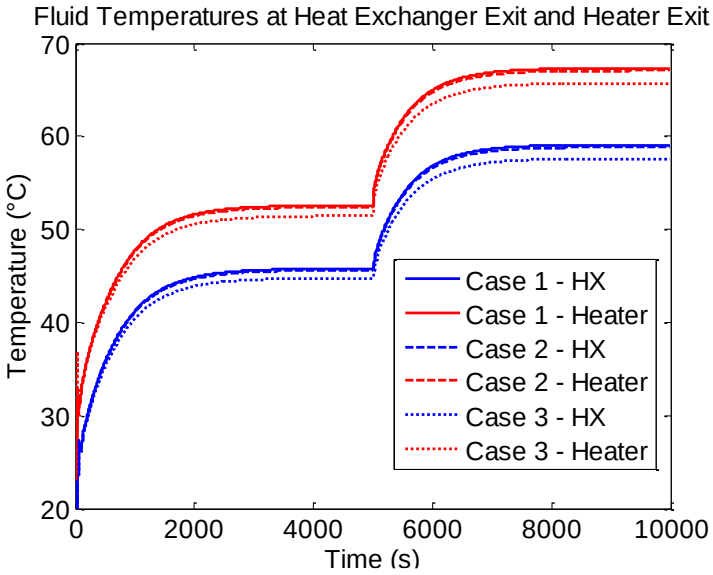

Figure A.5 Fluid Temperatures from the third heater nodalization Study

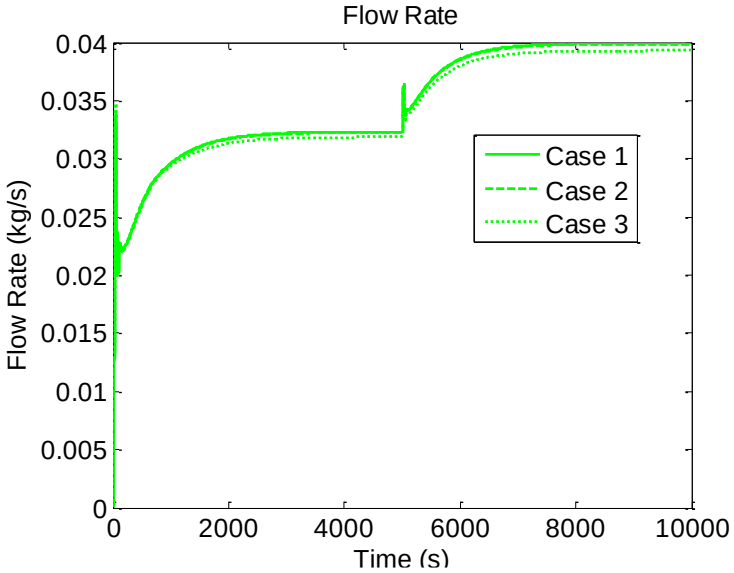

Figure A.6 Flow Rate from the third heater nodalization Study

The first heater location test of shrinking the heated section caused slightly higher temperatures and a slightly higher flow rate. The profiles for the medium and short heated sections (cases 2 and 3) showed very little change. For the second heater geometry study, the wall temperature at the heater exit varied slightly. As the heated section was moved down, the temperature decreased slightly. The wall temperatures at the heat exchanger exit

were not affected by moving the heated section. Test three showed that the fluid and wall temperatures were both relatively unaffected by increasing the height of the heater at the bottom of the vertical section. As the heated section was increased, the wall temperature at the heater decreased slightly and the fluid temperature at the heater increased slightly. The fourth test showed that increasing the length of the heater from the top of the vertical section decreased the fluid and wall temperatures at the heater. Plots showing this are below.

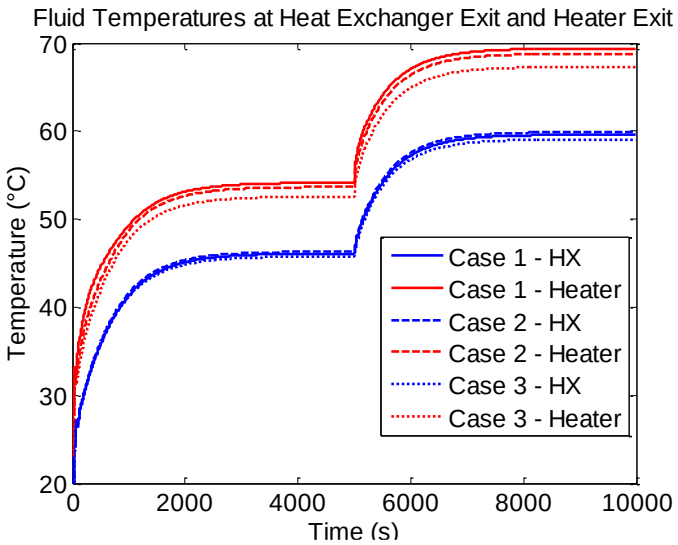

Figure A.7 Fluid Temperatures from the fourth Heater Geometry Study

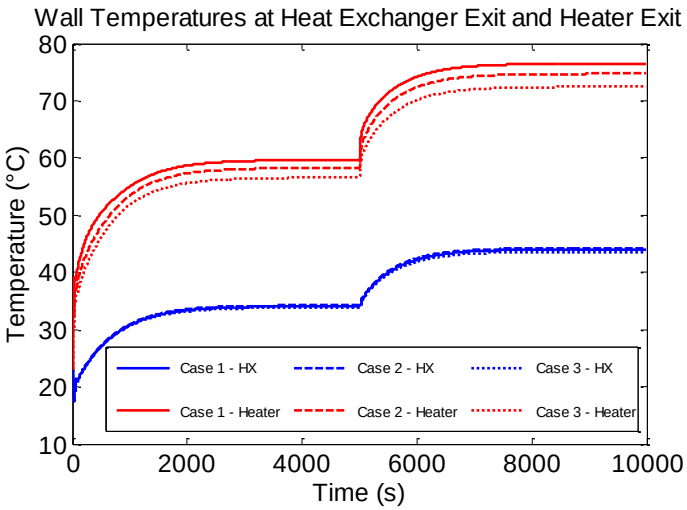

Figure A.8 Wall Temperatures from the fourth Heater Geometry Study

The flow rate for the LOHS transient for differing loops heights is shown below.

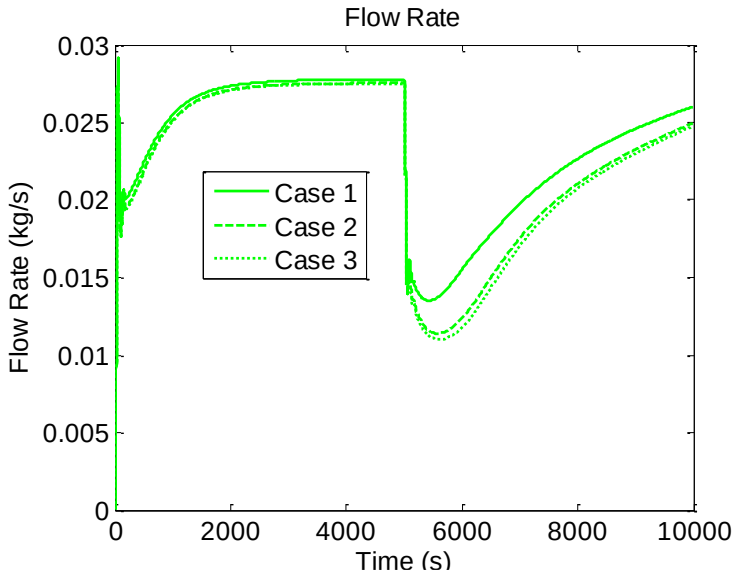

Figure A.9 Flow Rate from the LOHS Loop Height Study

The heater step study showed that the fluid temperatures are relatively unaffected for startup, but they are slightly higher after the heater step for an increased vertical height. The wall temperatures and flow rate were relatively unaffected by a change in height for the heater step transient. The fluid and wall temperatures were relatively unaffected by the loop height for the LOHS study.

The first 500 seconds of the flow rate for the first and fourth initial temperature studies is shown in the plots below.

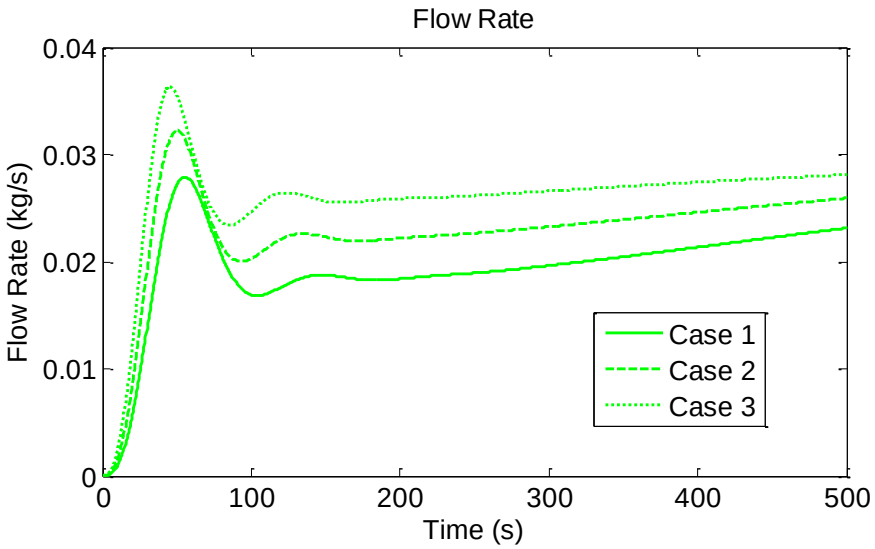

Figure A.10 Flow Rate for the first 500 seconds from the first Initial Temperature Profile Study

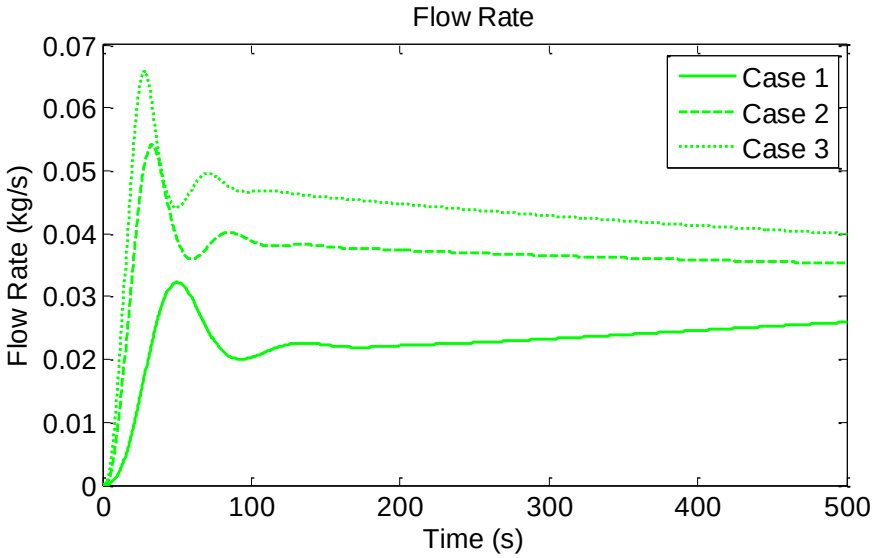

Figure A.11 Flow Rate for the first 500 seconds from the fourth Initial Temperature Profile Study

The flow profile for the LOHS transient from the loss coefficients study is shown below.

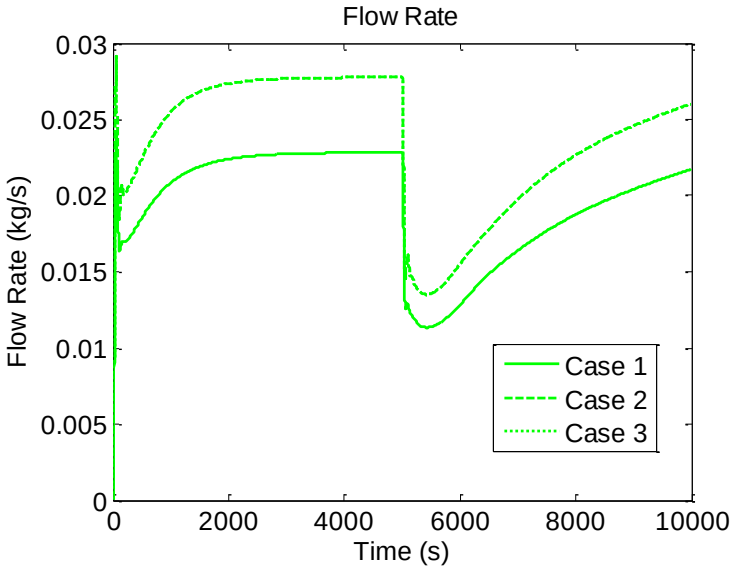

Figure A.12 Flow Rate for a LOHS from the Loss Coefficients Study

The heater power tests resulted in vary characteristic overall profiles. The ones for the fluid temperatures and flow rate are shown in the figures below.

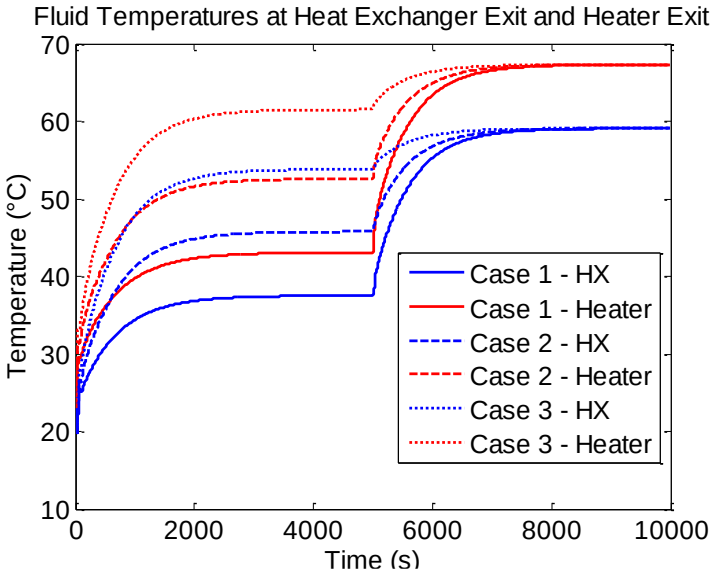

Figure A.13 Fluid Temperatures for the first heater power Study

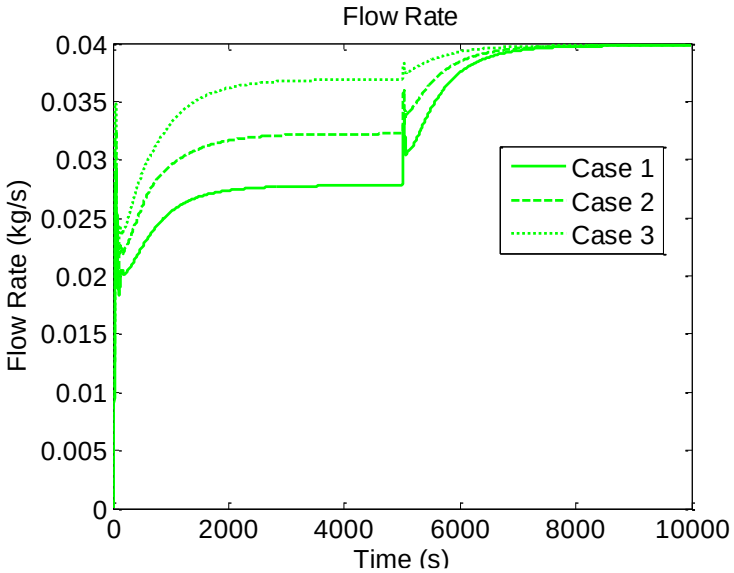

Figure A.14 Flow Rate for the first heater power Study

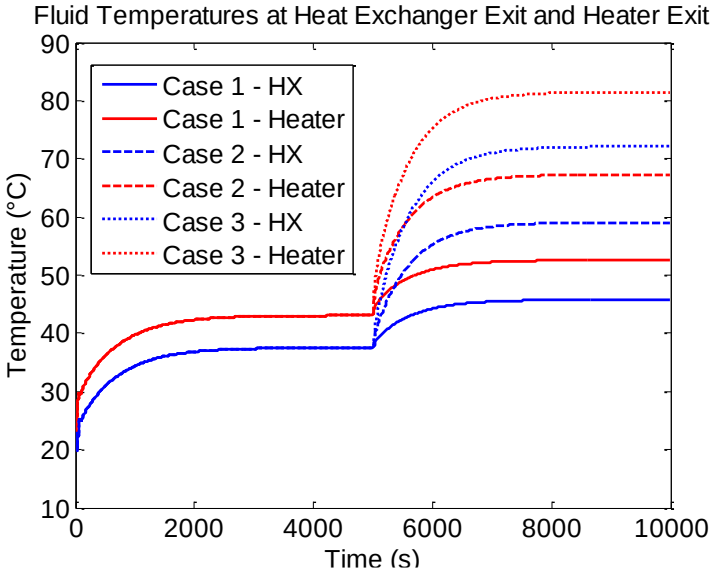

Figure A.15 Fluid Temperatures for the second heater power Study

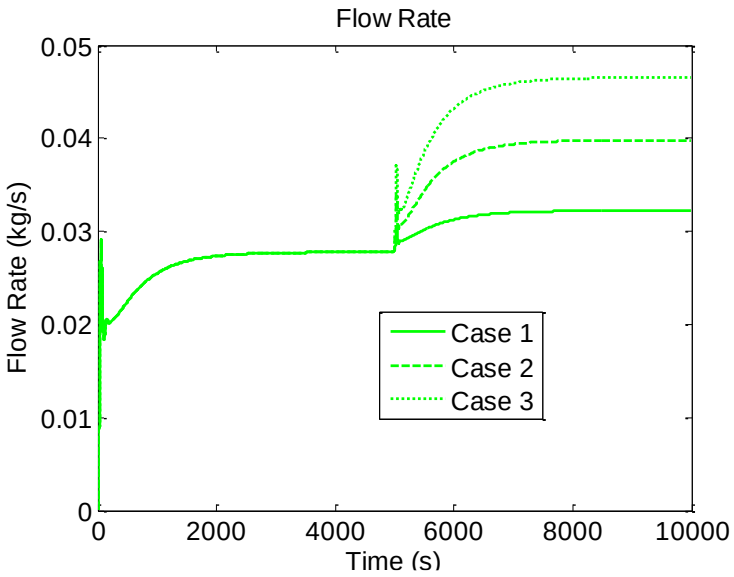

Figure A.16 Flow Rate for the second heater power Study

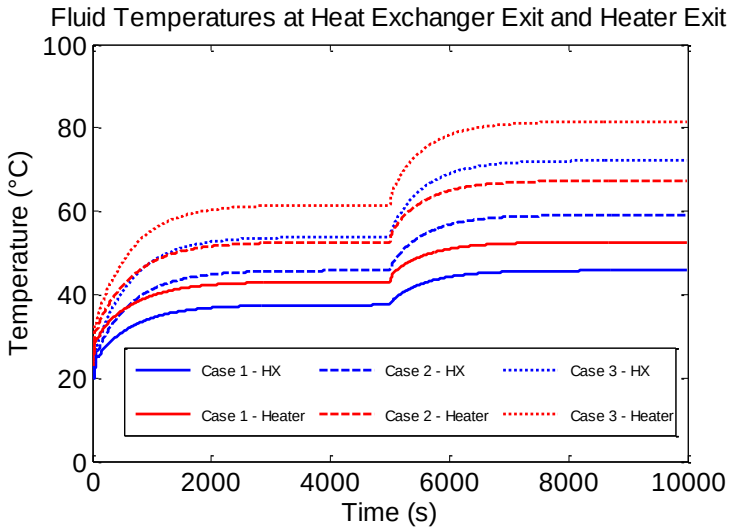

Figure A.17 Fluid Temperatures for the third heater power Study

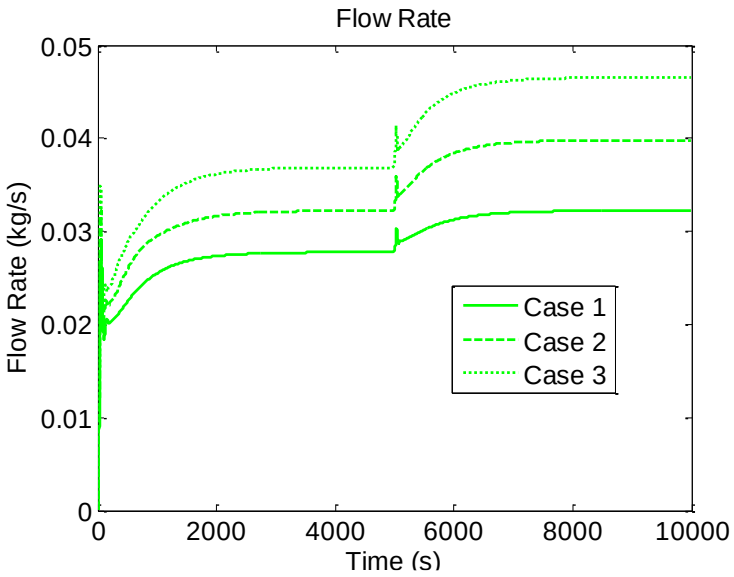

Figure A.18 Flow Rate for the third heater power Study

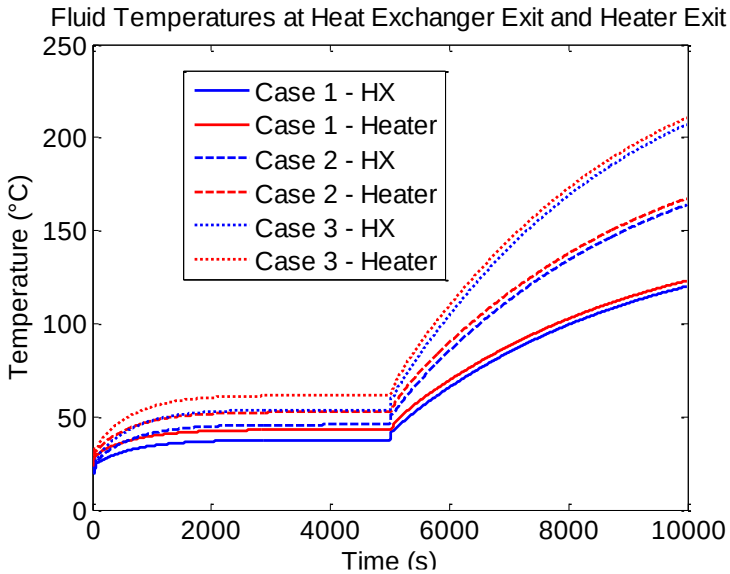

Figure A.19 Fluid Temperatures for the fourth heater power Study

Plots showing the fluid temperature and flow profiles from the ambient HTC studies are shown below. The wall temperature profiles were similar to the fluid temperature profiles, so they are not shown.

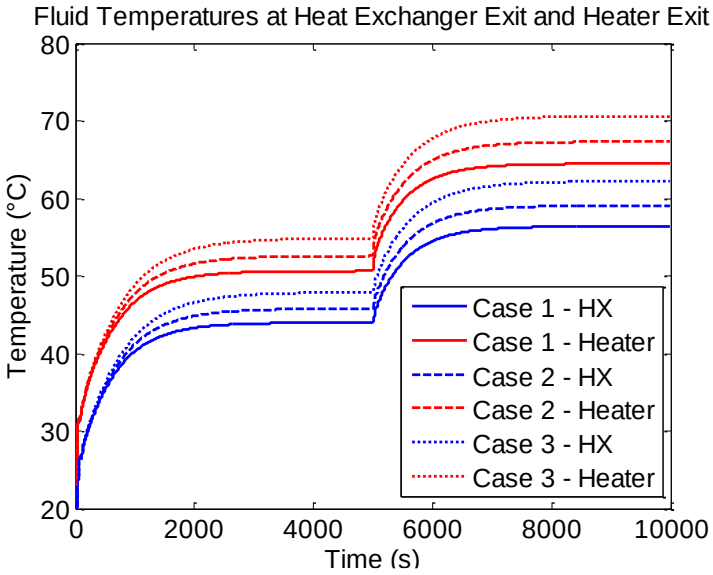

Figure A.20 Fluid Temperatures for the heat step transient from the ambient HTC Study

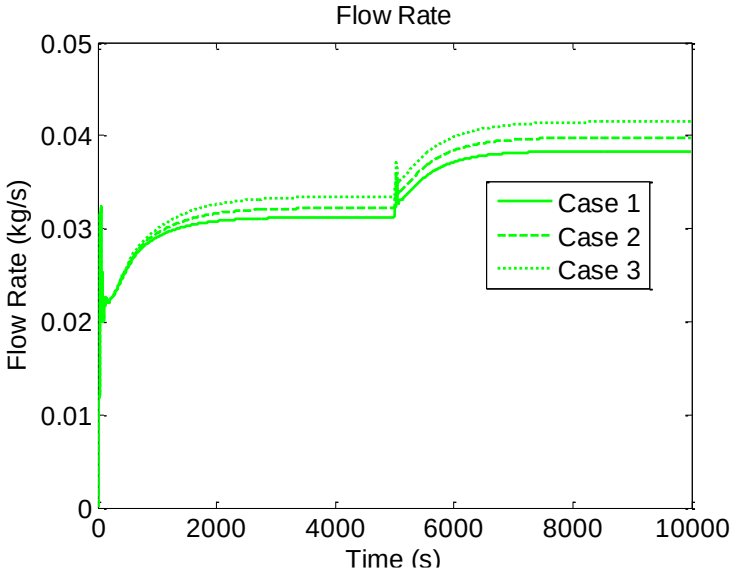

Figure A.21 Flow Rate for the heat step transient from the ambient HTC Study

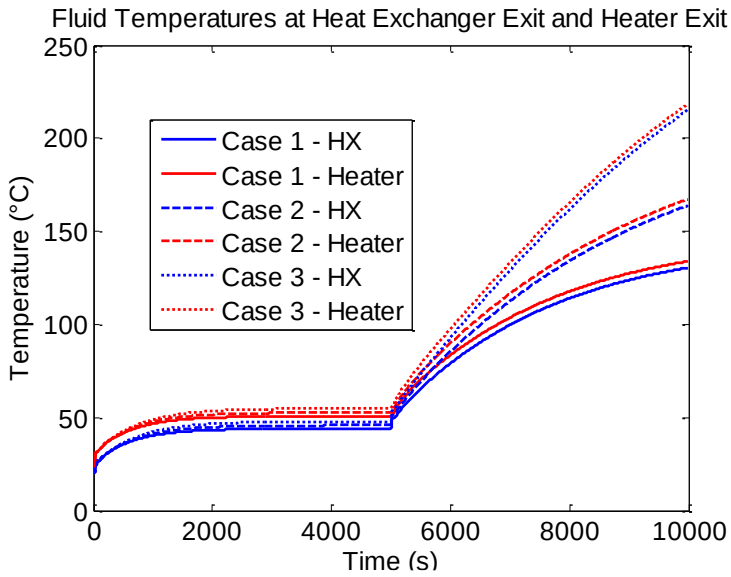

Figure A.22 Fluid Temperatures for the LOHS transient from the ambient HTC Study

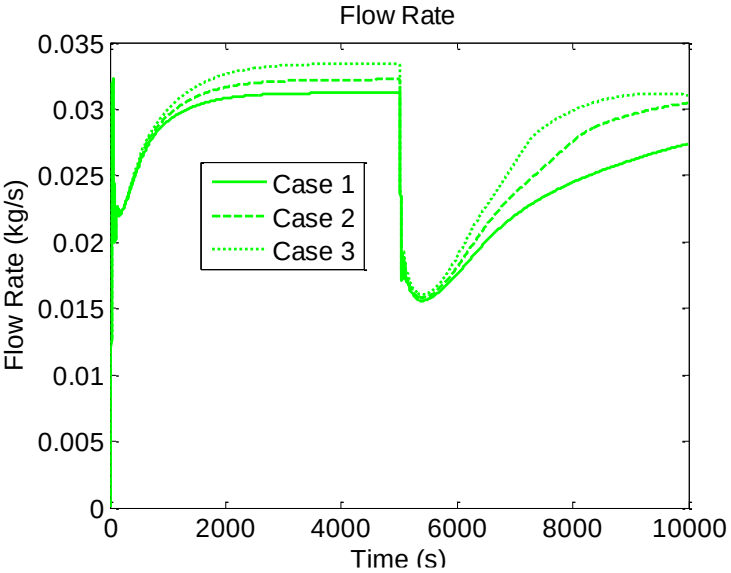

Figure A.23 Flow Rate for the LOHS transient from the ambient HTC Study

Plots showing the results of the ambient temperature study are shown below. The wall temperature plots were omitted because the profiles were similar to the ones in the fluid temperatures.

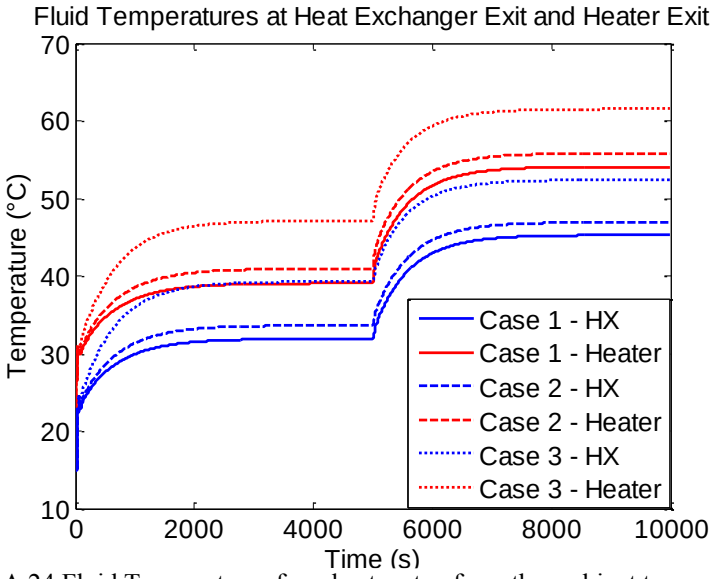

Figure A.24 Fluid Temperatures for a heater step from the ambient temperature Study

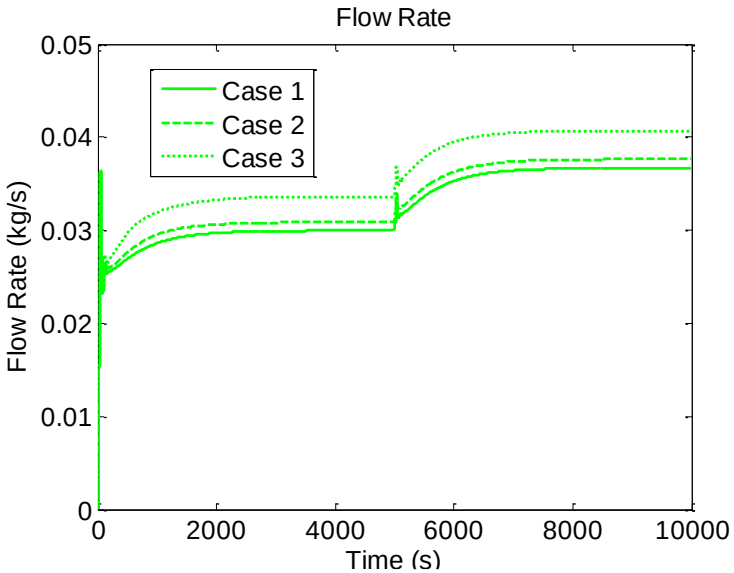

Figure A.25 Flow Rate for a heater step from the ambient temperature Study

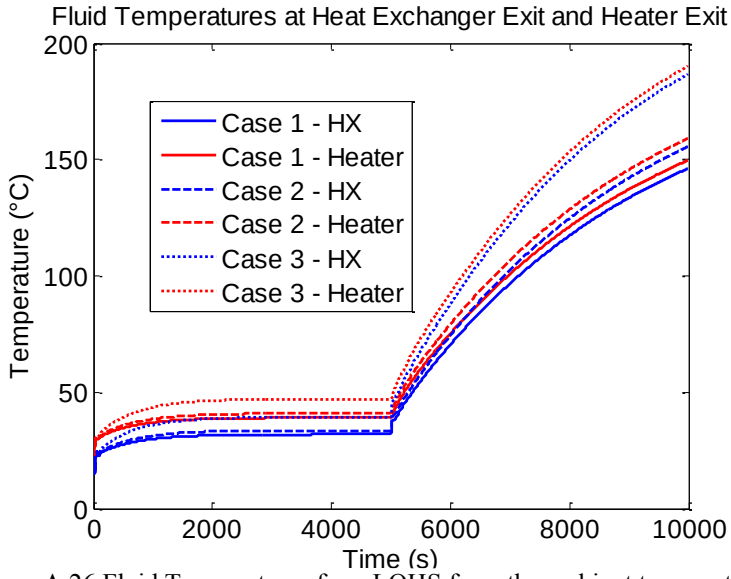

Figure A.26 Fluid Temperatures for a LOHS from the ambient temperature Study

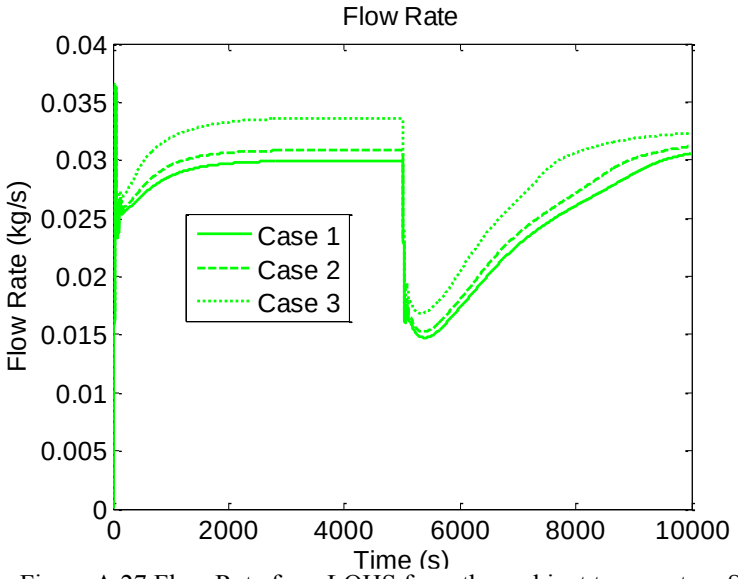

Figure A.27 Flow Rate for a LOHS from the ambient temperature Study

The plots showing the temperatures and flow rate from the first time step study are below.

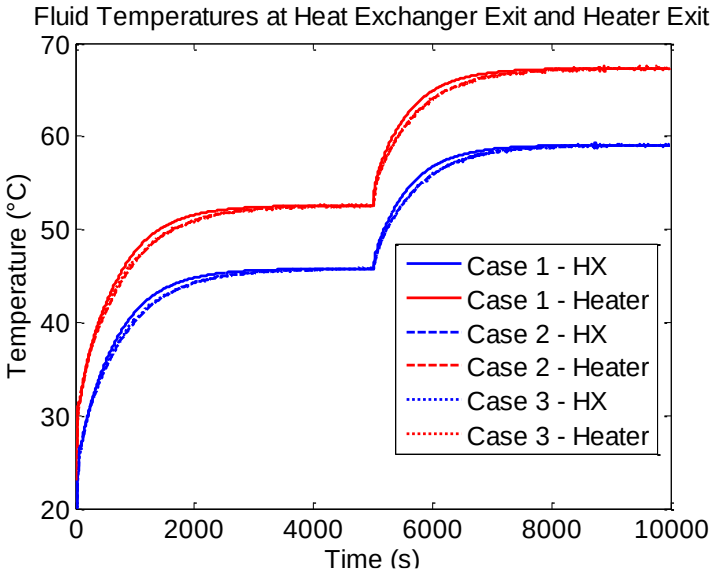

Figure A.28 Fluid Temperatures for a the first time step Study

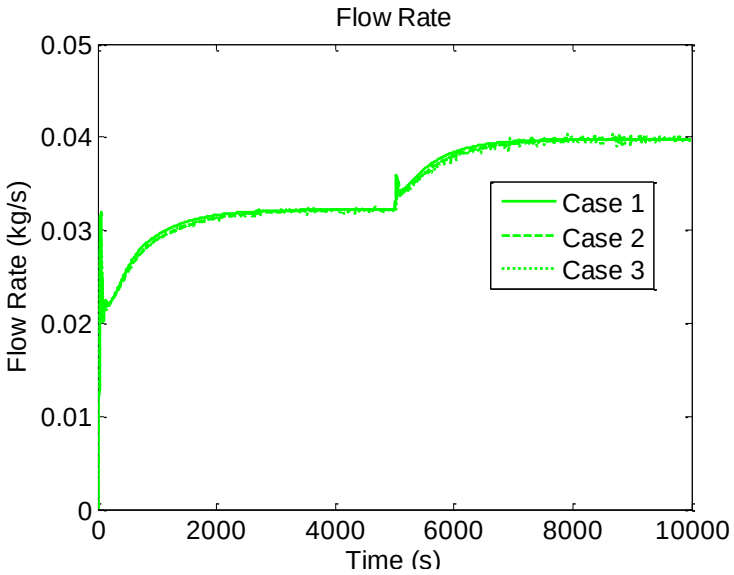

Figure A.29 Flow Rate for a the first time step Study

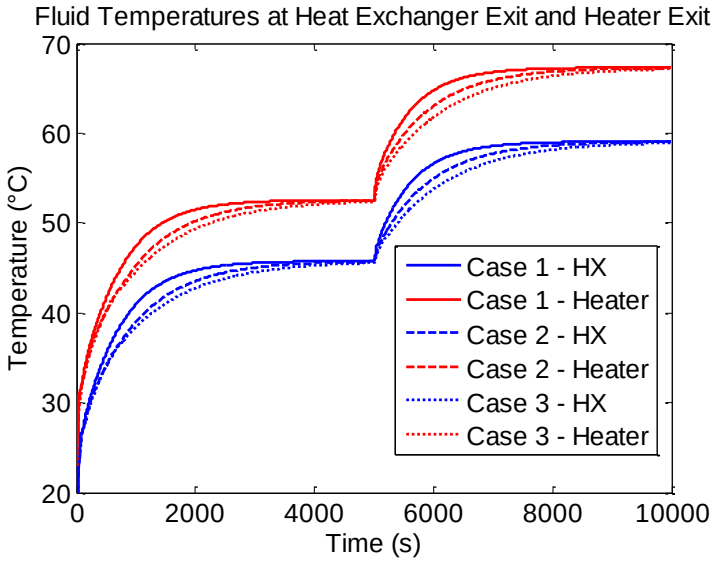

Figure A.30 Fluid Temperatures for the second Time Step Study

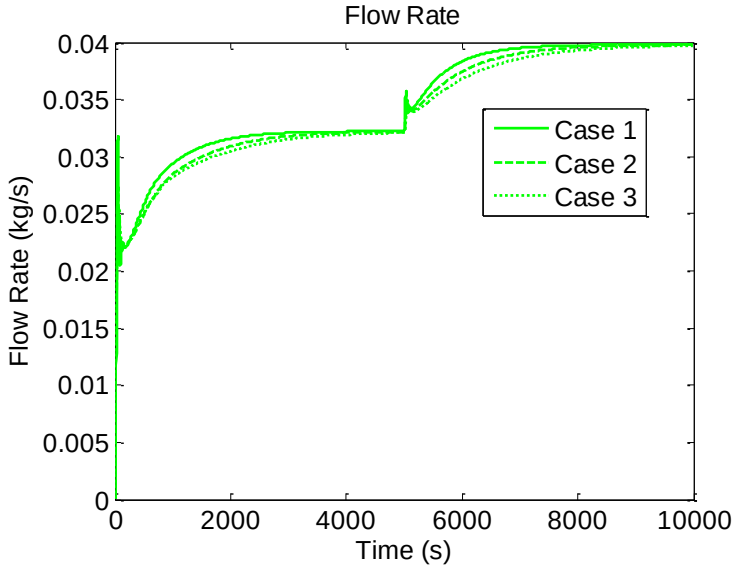

Figure A.31 Flow Rate for the second Time Step Study

Appendix B - Plots of Experimental Results

The data for the second baseline test is presented here. The figure below shows the flow rate for the second baseline test.

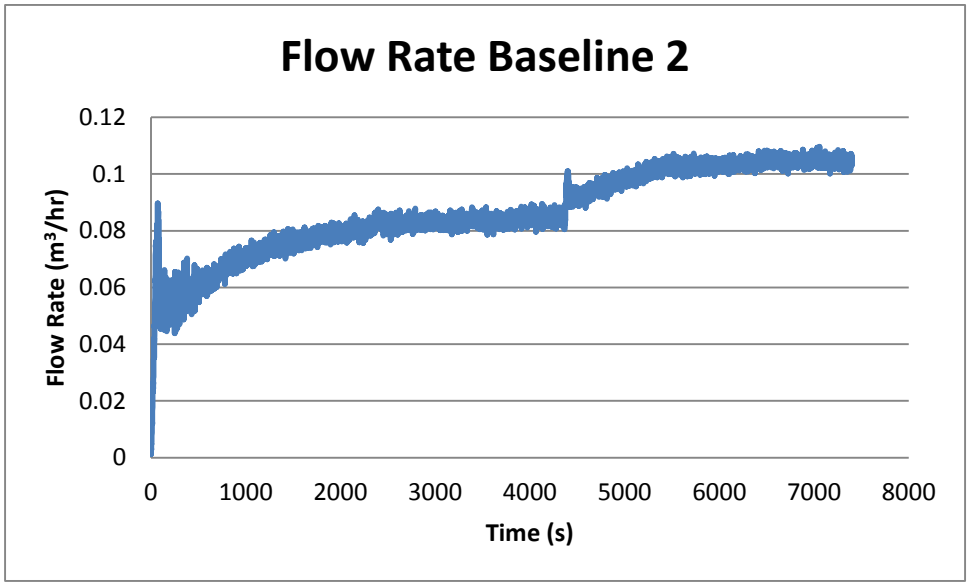

Figure B.1 Flow Rate from the 2nd Baseline Test

The figure below shows the fluid temperatures for the second baseline test.

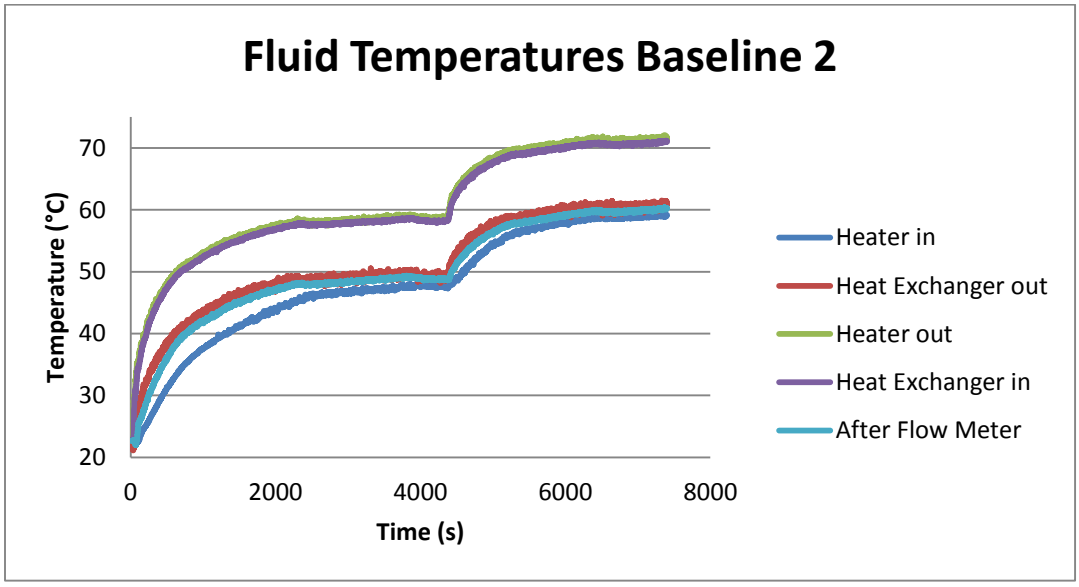

Figure B.2 Fluid Temperatures from the 2nd Baseline Test

Five of the wall temperatures at the heater are shown below.

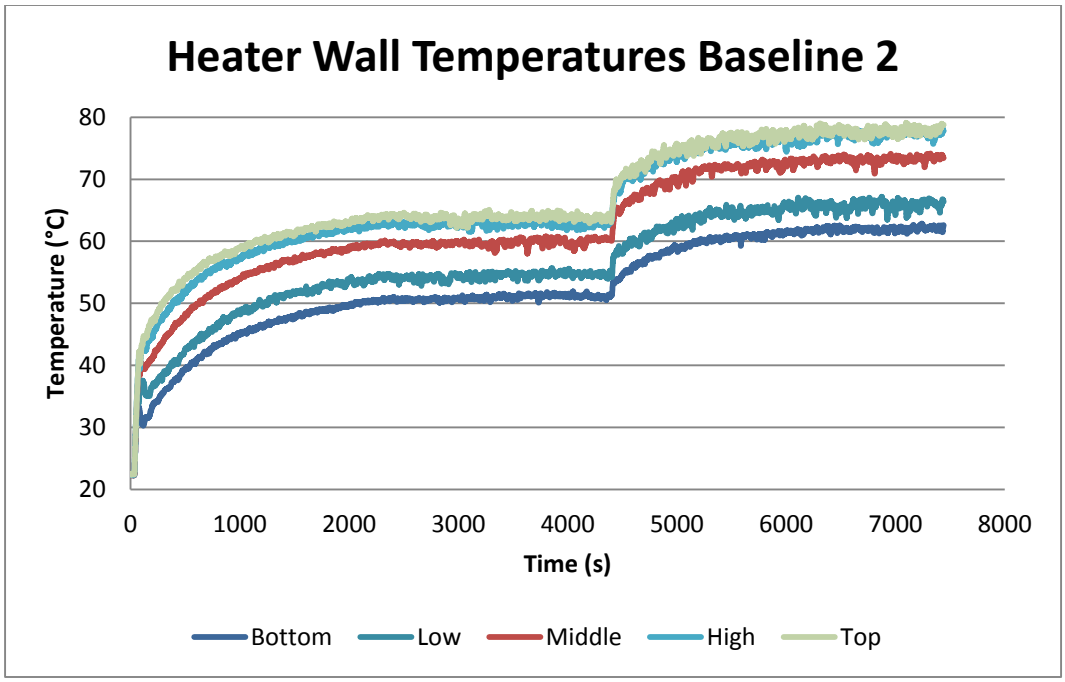

Figure B.3 Heater Wall Temperatures from the 2nd Baseline Test

The wall temperatures at the beginning and end of the hot and cold legs are shown in the figure below. The plot shows that the heat lost in the hot leg was negligible. While the heat lost from the cold leg is less than the heat removed by the chiller, it is a nontrivial amount.

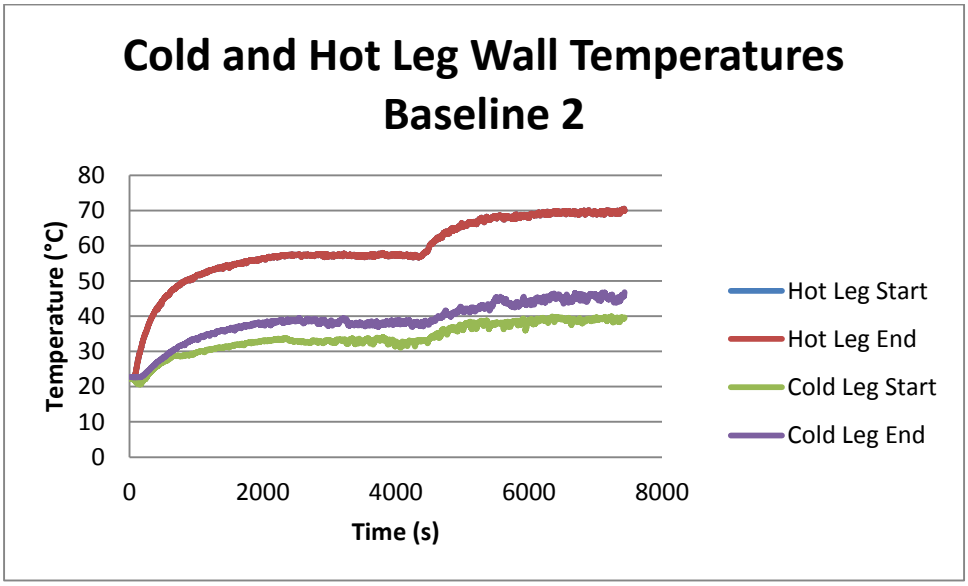

Figure B.4 Key Wall Temperatures from the 2nd Baseline Test

The length and position of the heated section was tested with two different runs. For the first test, the bottom heater lead was moved up (high heater) and for the second test, the top heater lead was moved down (low heater). The data from these runs is presented below.

The flow rate from the first run of the higher heater test is shown below.

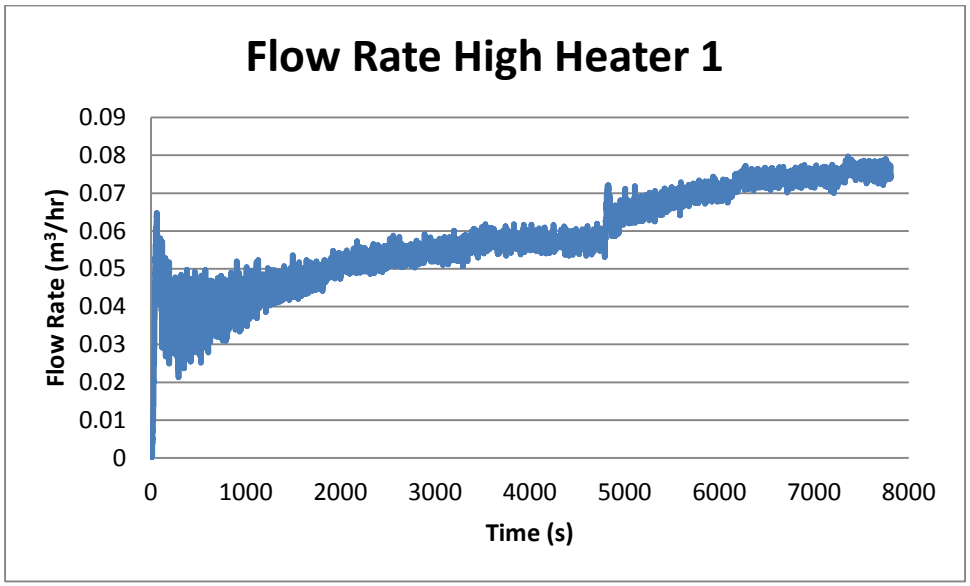

Figure B.5 Flow Rate from the 1st High Heater Test

The fluid temperatures for the first higher heater test are shown in the plot below.

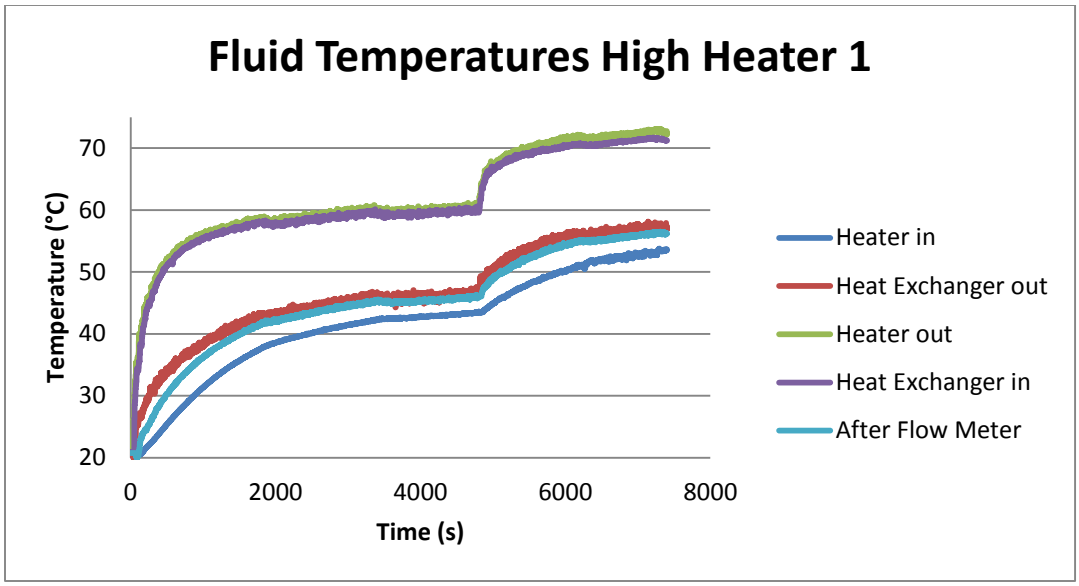

Figure B.6 Fluid Temperatures from the 1st High Heater Test

The wall temperatures on the heated section for the first run of the higher heater test are plotted below.

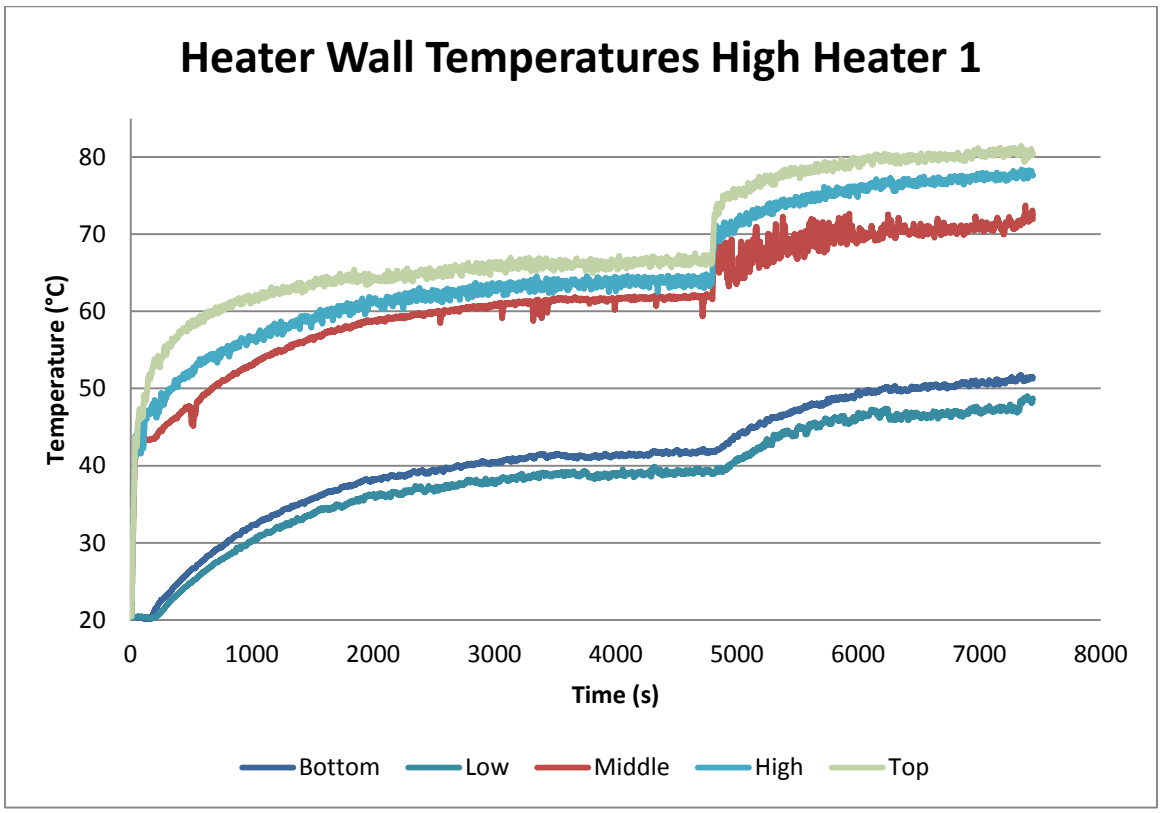

Figure B.7 Heater Wall Temperatures from the 1st High Heater Test

The temperatures for the hot and cold legs in the loop for the first run of the higher heater test are shown below.

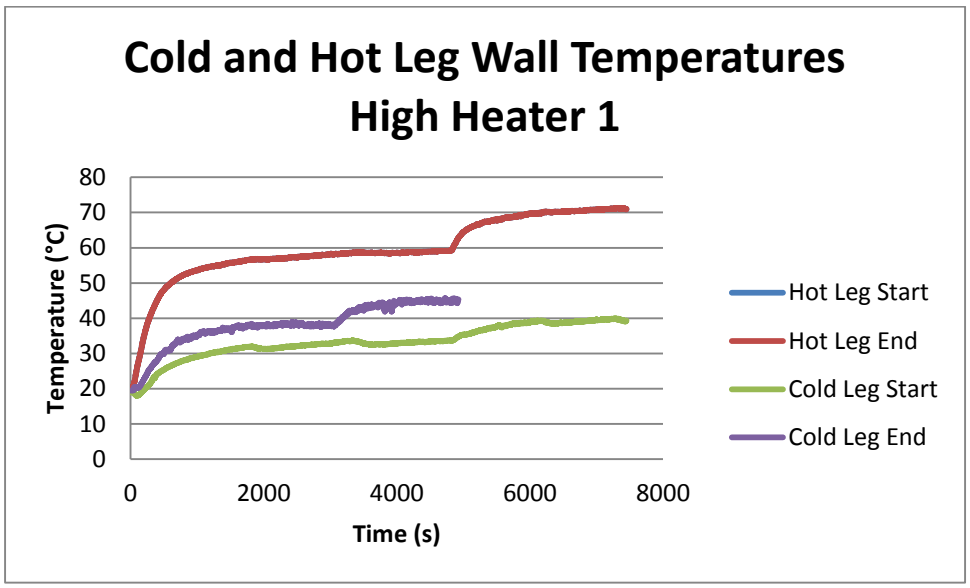

Figure B.8 Key Wall Temperatures from the 1st High Heater Test

The flow rate for the second run of the higher heater test is shown below.

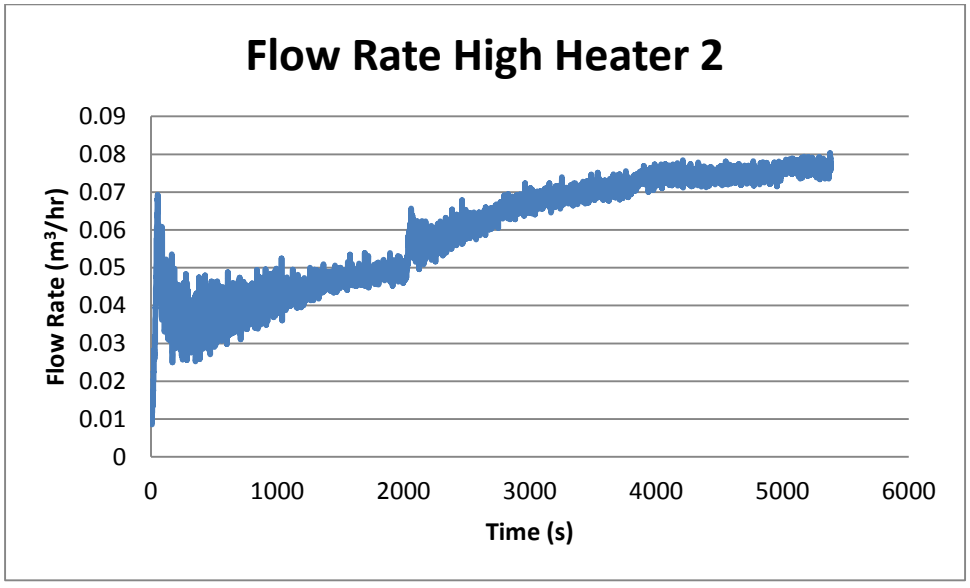

Figure B.9 Flow Rate from the 2nd High Heater Test

The fluid temperatures for the second run of the higher heater test are plotted below.

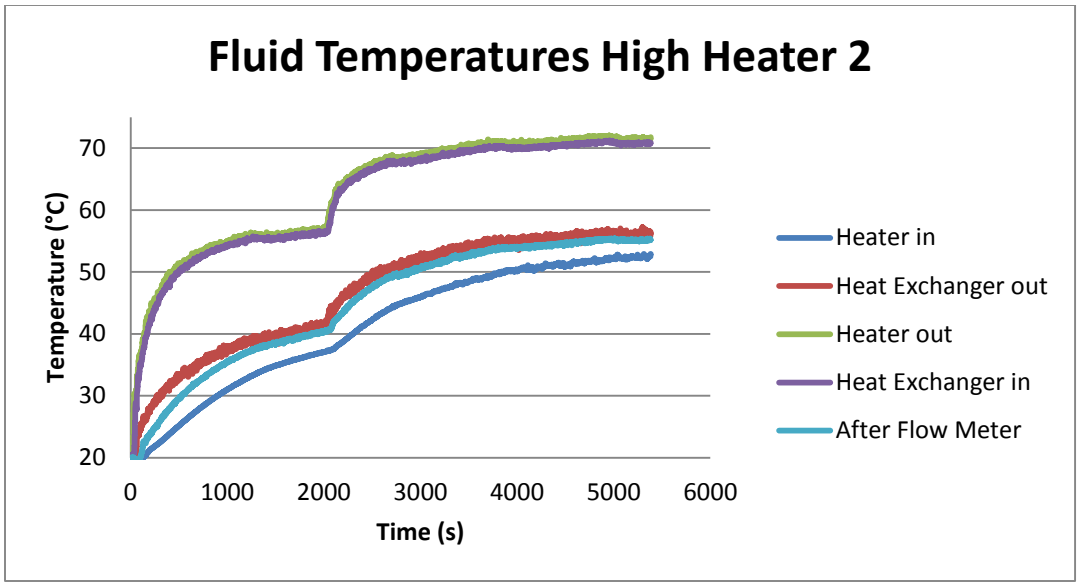

Figure B.10 Fluid Temperatures from the 2nd High Heater Test

The wall temperatures for the second run of the higher heater test are plotted below.

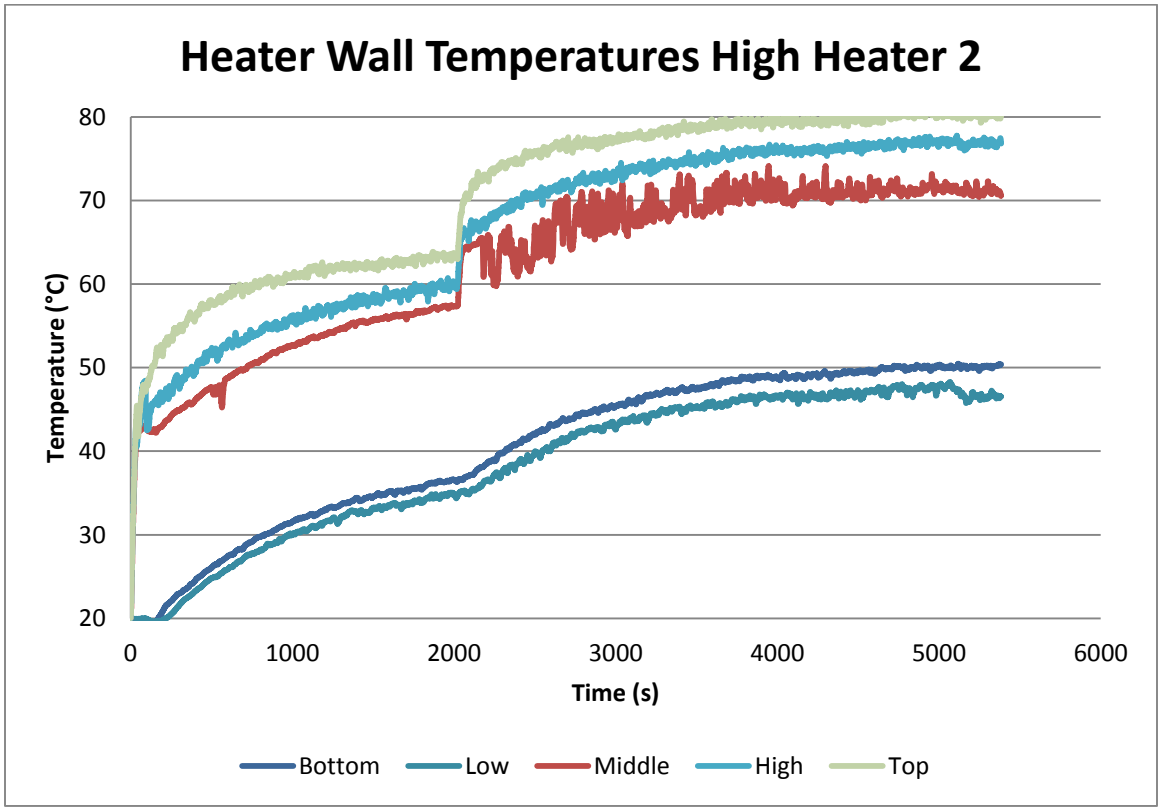

Figure B.11 Heater Wall Temperatures from the 2nd High Heater Test

A plot showing the cold and hot leg temperatures for the second run of the higher heater test is below.

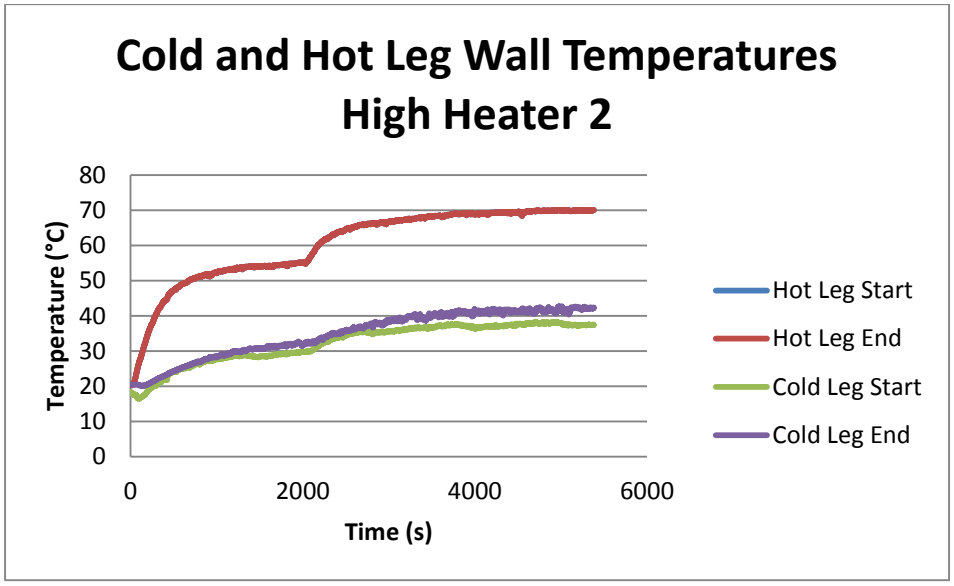

Figure B.12 Key Wall Temperatures from the 2nd High Heater Test

A plot showing the flow rate for the first low heater test is below.

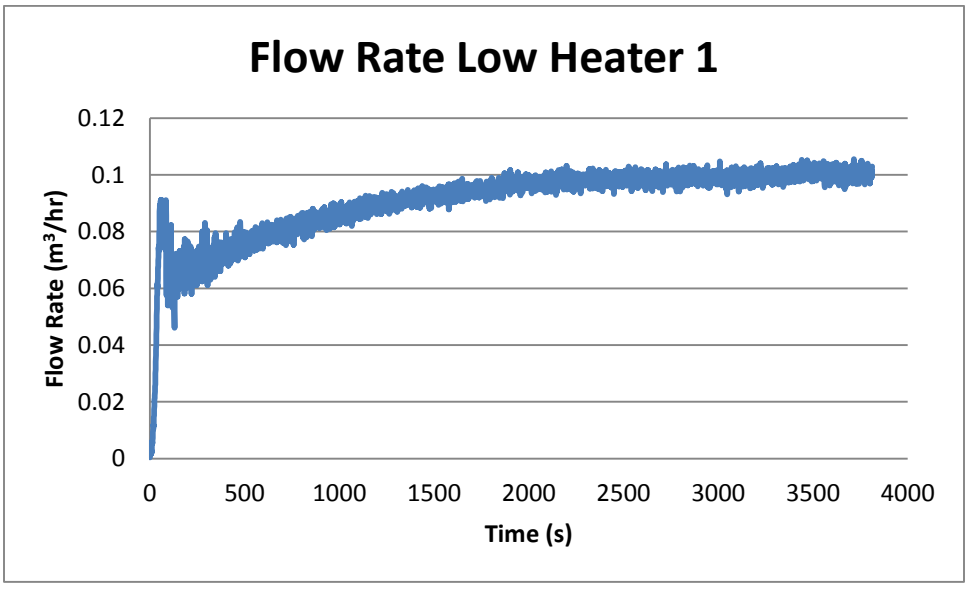

Figure B.13 Flow Rate from the 1st Low Heater Test

The fluid temperatures for the first low heater test are shown below.

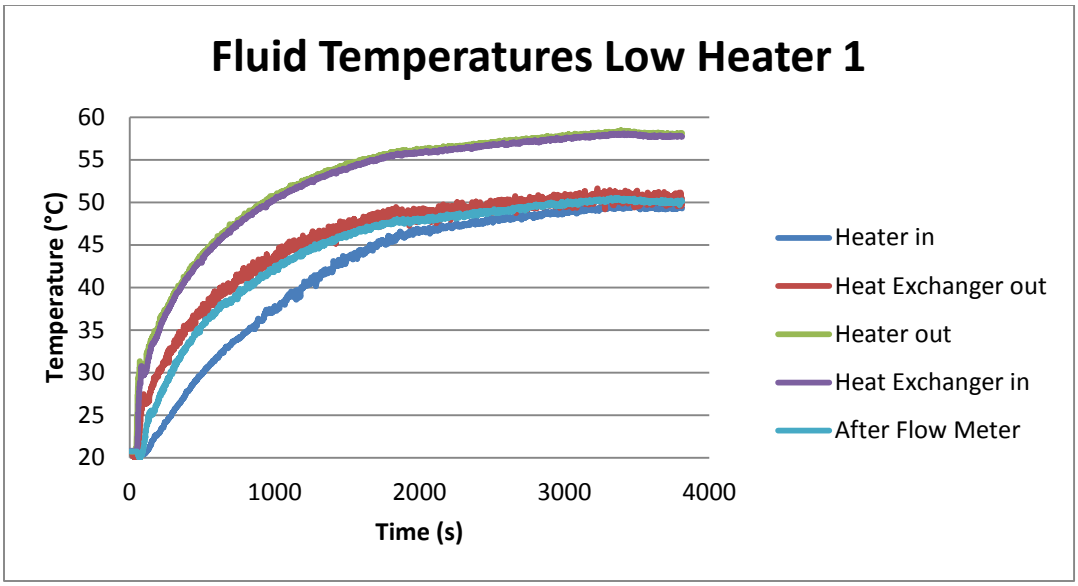

Figure B.14 Fluid Temperatures from the 1st Low Heater Test

The plot below shows the wall temperatures at the heated section for the first low heater test.

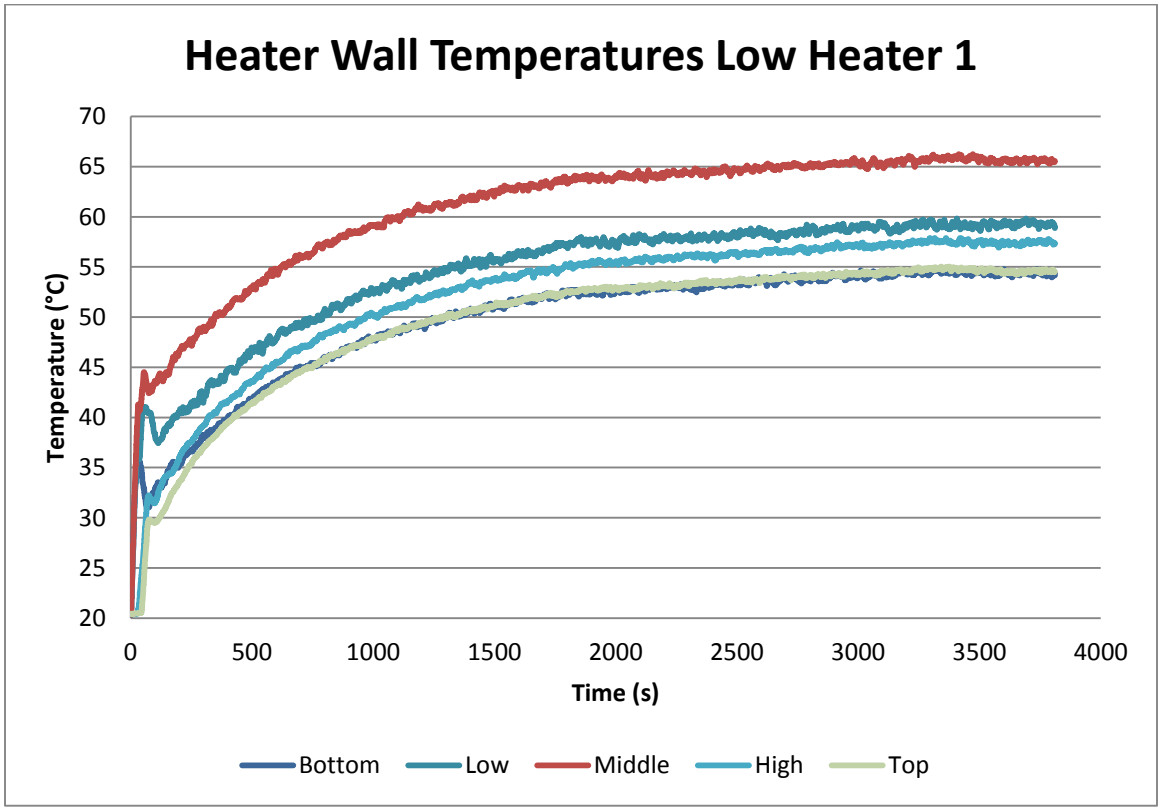

Figure B.15 Heater Wall Temperatures from the 1st Low Heater Test

The cold and hot leg temperatures from the first low heater test are shown in the plot below.

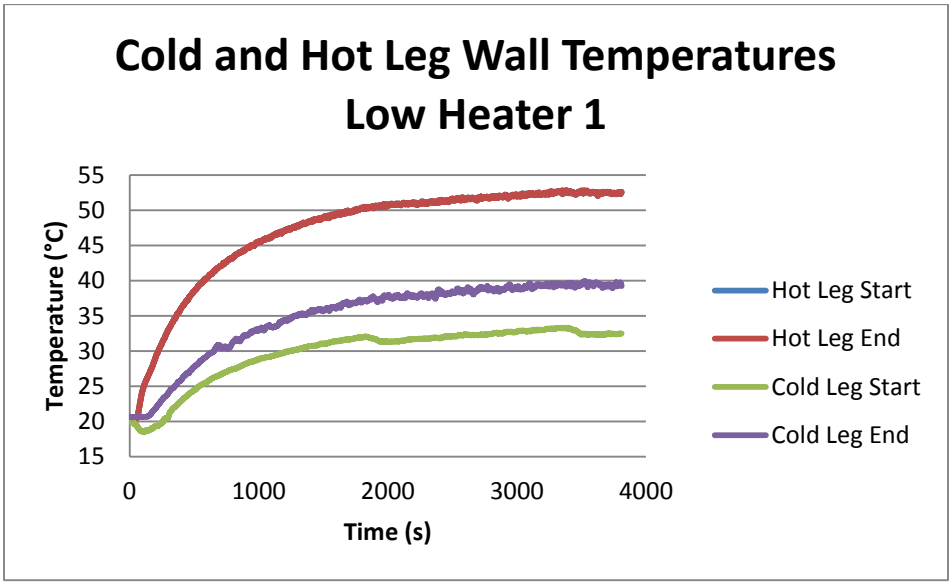

Figure B.16 Key Wall Temperatures from the 1st Low Heater Test

The second test for the low heater resulted in the flow rate profile shown in the plot below.

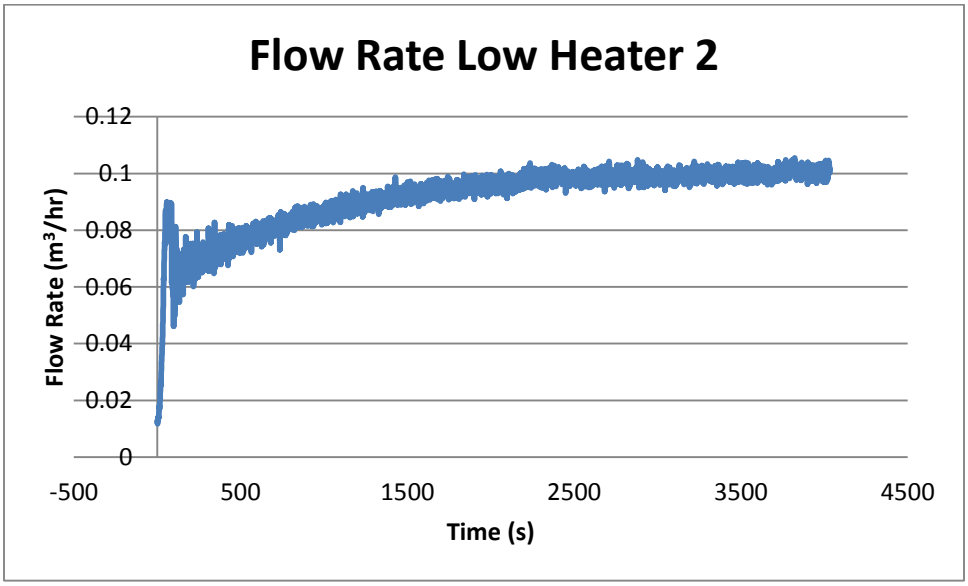

Figure B.17 Flow Rate from the 2nd Low Heater Test

The fluid temperatures for the second low heater test are shown in the plot below.

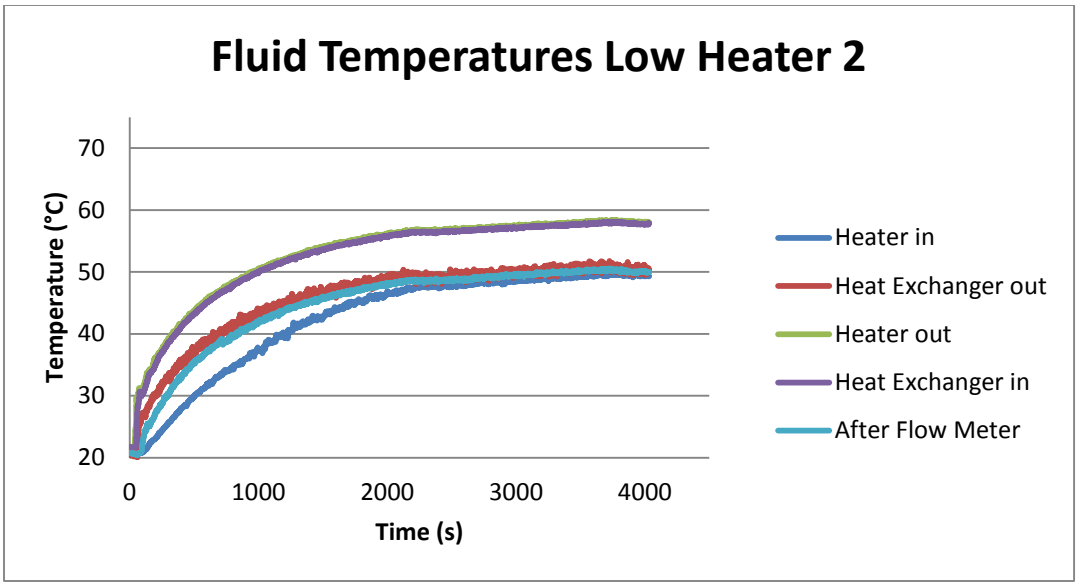

Figure B.18 Fluid Temperatures from the 2nd Low Heater Test

The temperatures at the wall of the heated section for the low heater run are shown below.

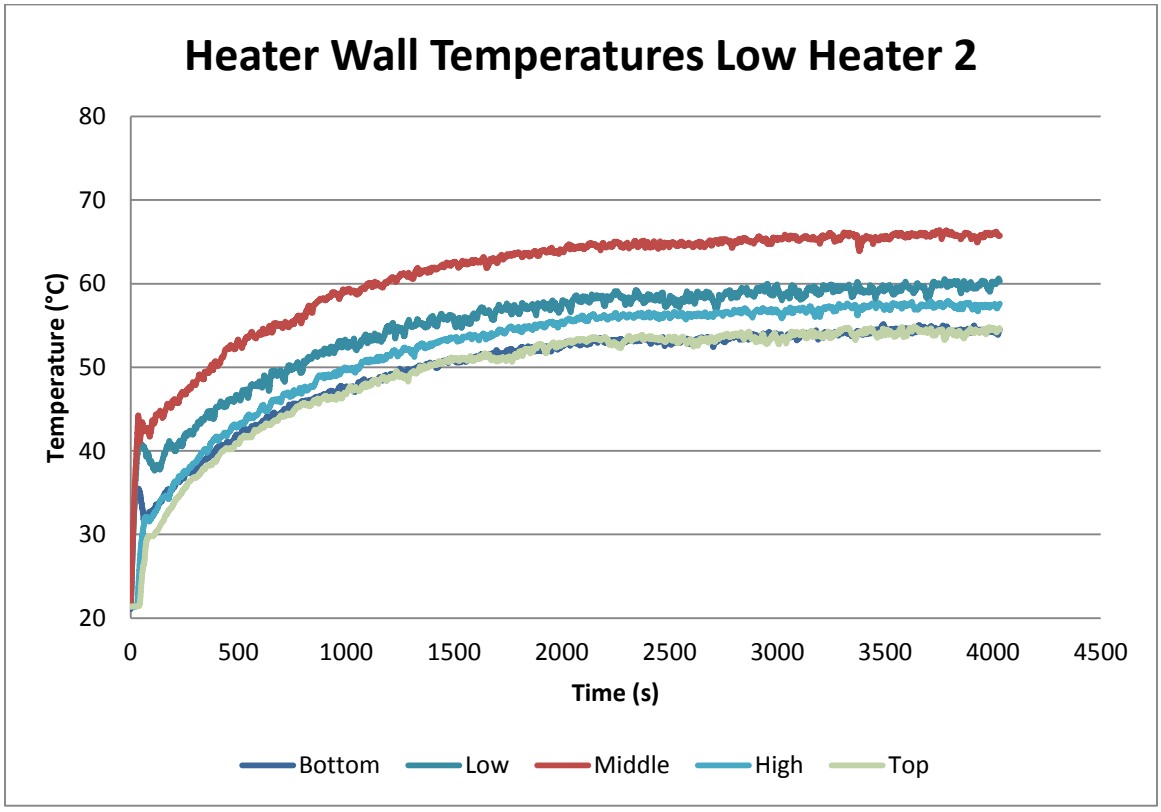

Figure B.19 Heater Wall Temperatures from the 2nd Low Heater Test

The plot below shows the temperatures at the hot and cold leg for the second low heater test.

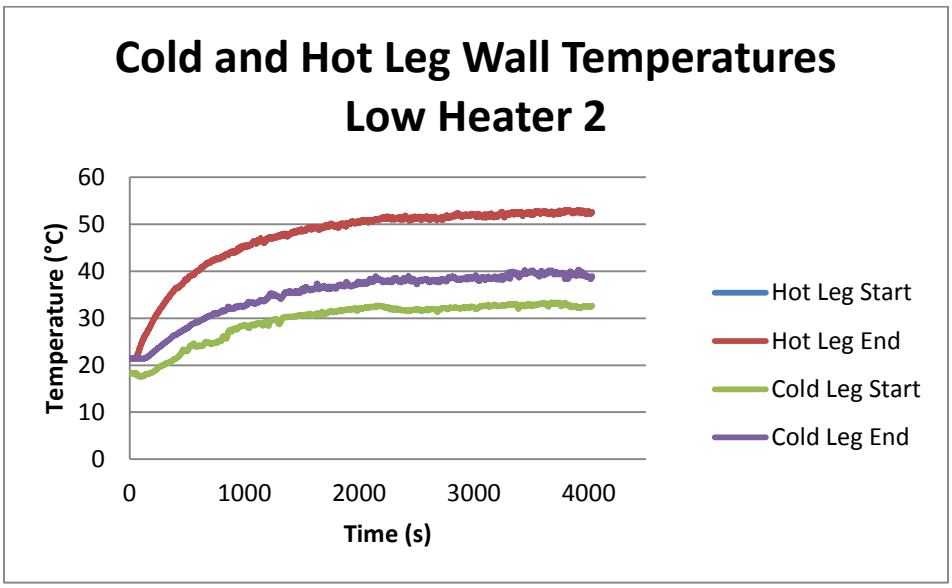

Figure B.20 Key Wall Temperatures from the 2nd Low Heater Test

The secondary side heat transfer coefficient was tested by running two tests each at 1 gpm and at 0 gpm. The results from these tests are shown below.

The flow rate for the primary side of the loop was plotted for the first run with the chiller at 1 gpm. This plot is shown below.

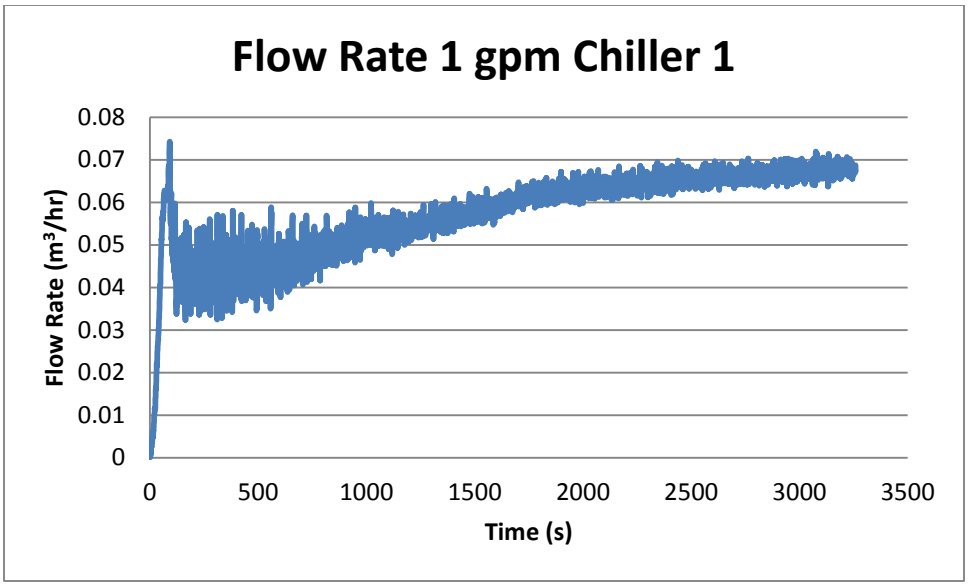

Figure B.21 Flow Rate from the 1st 1 gpm Chiller Test

The fluid temperatures from the first run with the chiller at 1gpm are plotted below.

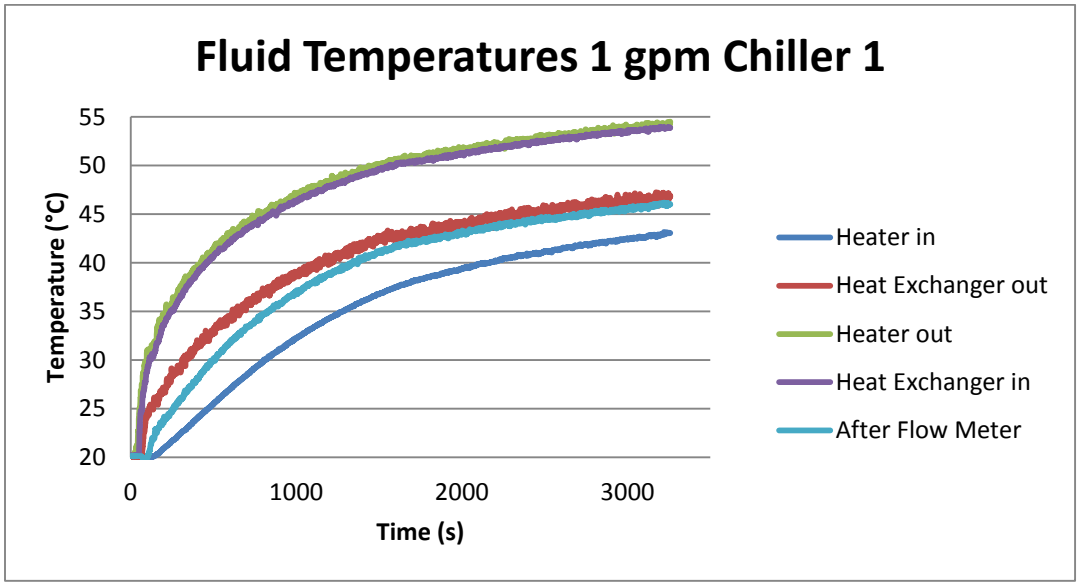

Figure B.22 Fluid Temperatures from the 1st 1 gpm Chiller Test

The wall temperatures at the heated section for the first test at 1 gpm are shown on the plot below.

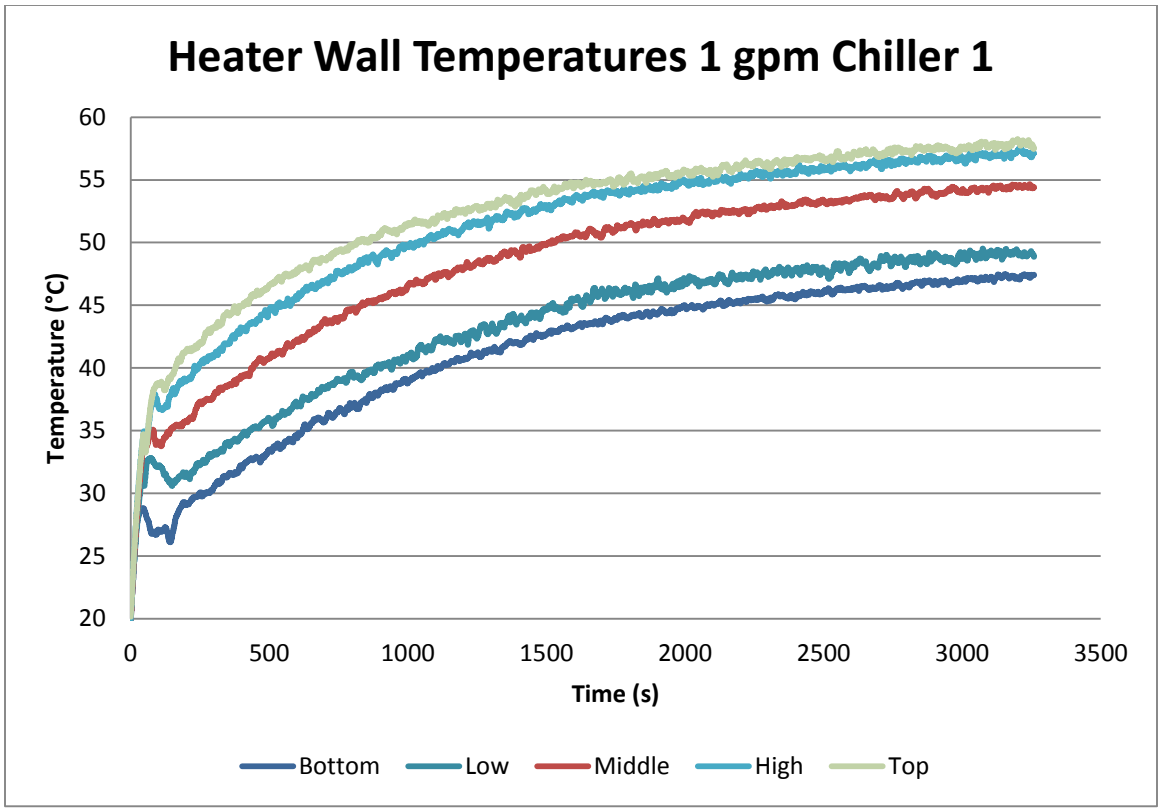

Figure B.23 Heater Wall Temperatures from the 1st 1 gpm Chiller Test

The wall temperatures for the hot and cold legs of the loop from the first test with the chiller at 1 gpm are plotted below.

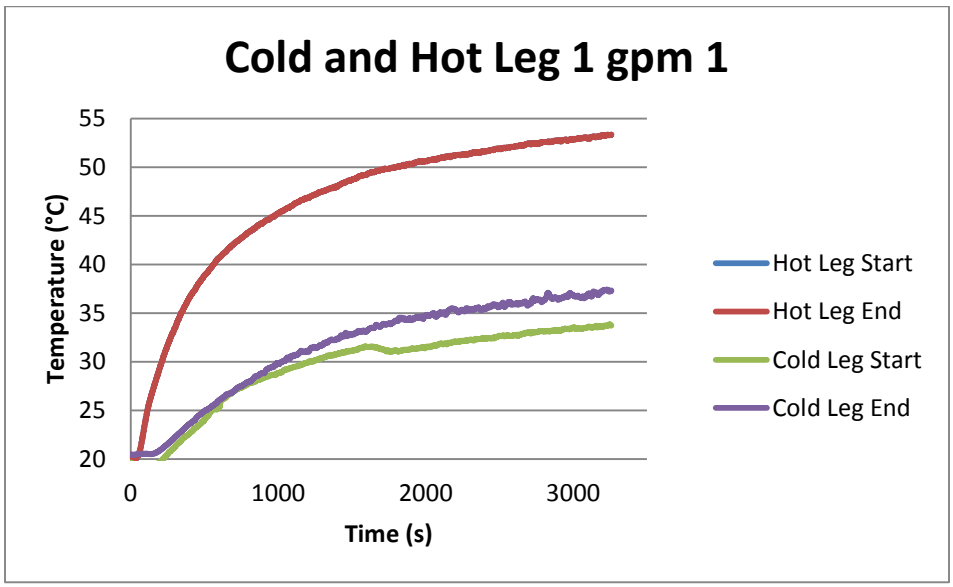

Figure B.24 Key Wall Temperatures from the 1st 1 gpm Chiller Test

The second test with the chiller at 1 gpm resulted in the flow rate plotted below.

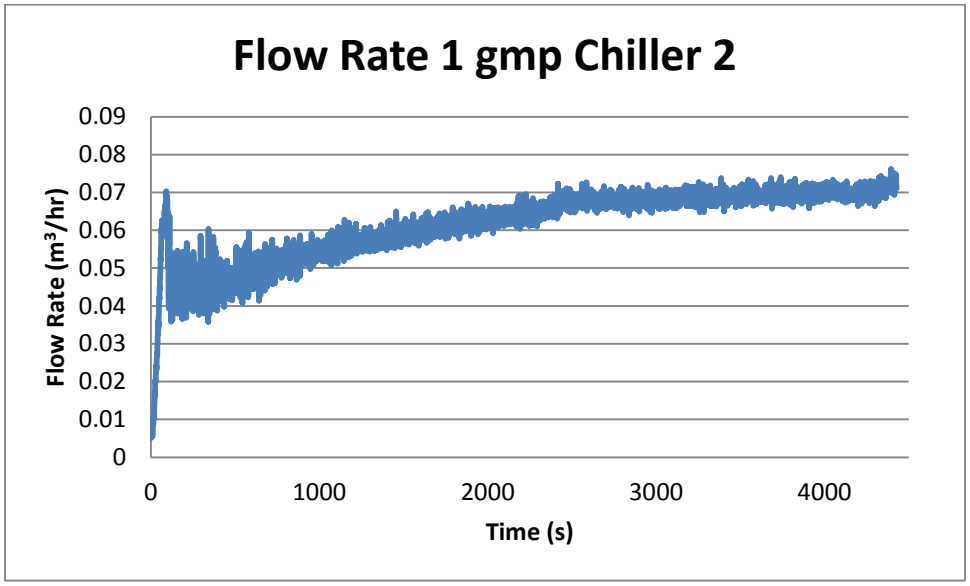

Figure B.25 Flow Rate from the 2nd 1 gpm Chiller Test

The fluid temperatures from the second run with the chiller at 1gpm are shown in the figure below.

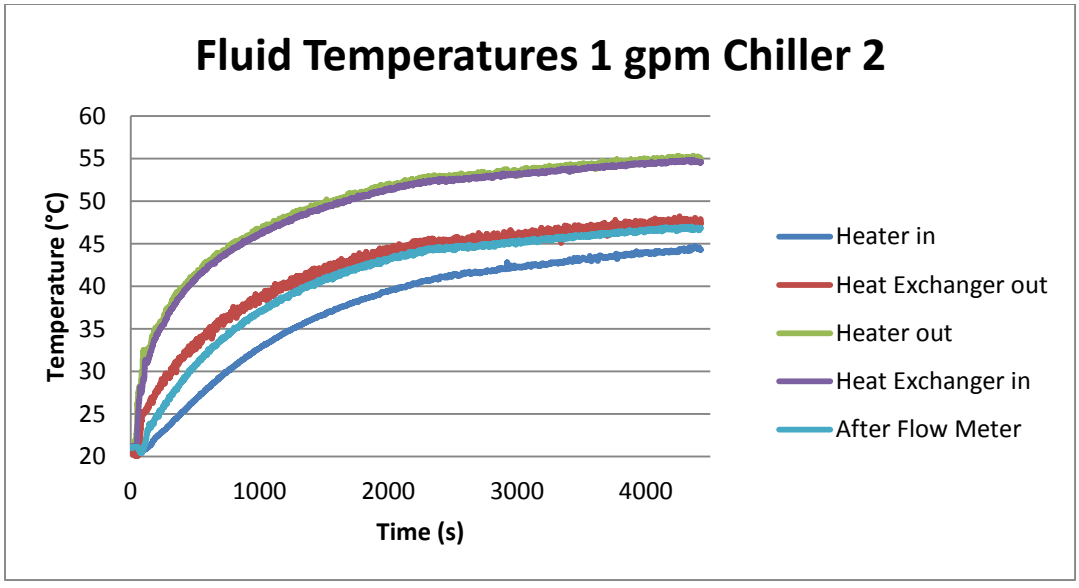

Figure B.26 Fluid Temperatures from the 2nd 1 gpm Chiller Test

The wall temperatures at the heated section from the second test with the chiller at 1 gpm are below.

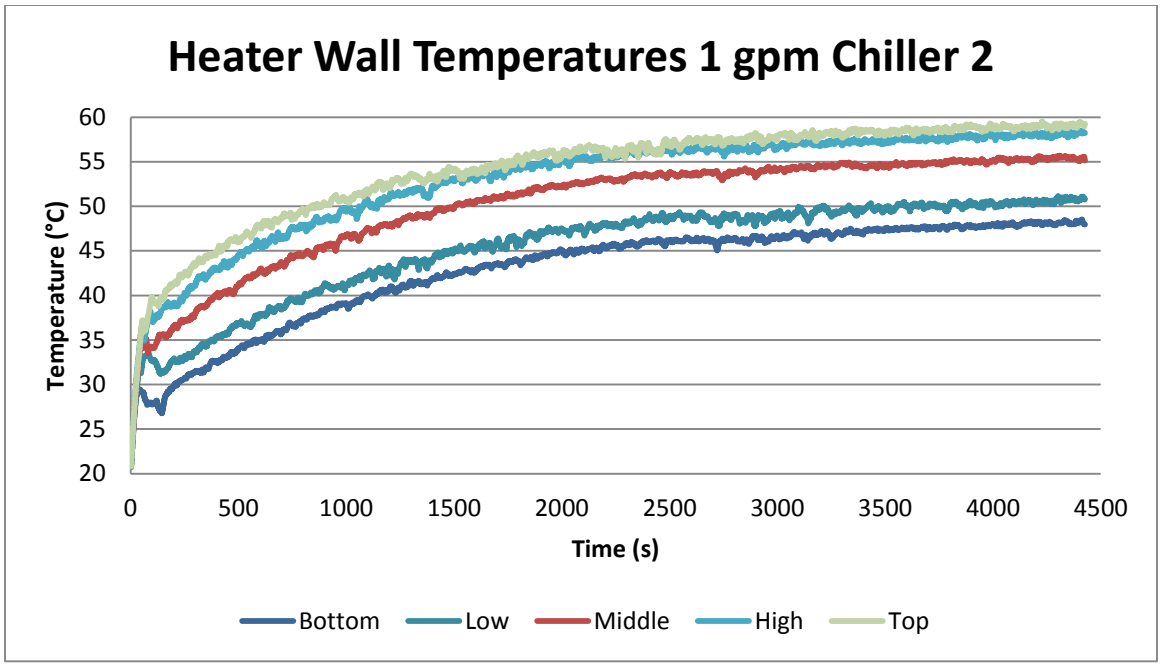

Figure B.27 Heater Wall Temperatures from the 2nd 1 gpm Chiller Test

The temperatures at the hot and cold legs of the loop for the second run with the chiller at 1gpm are shown on the plot below.

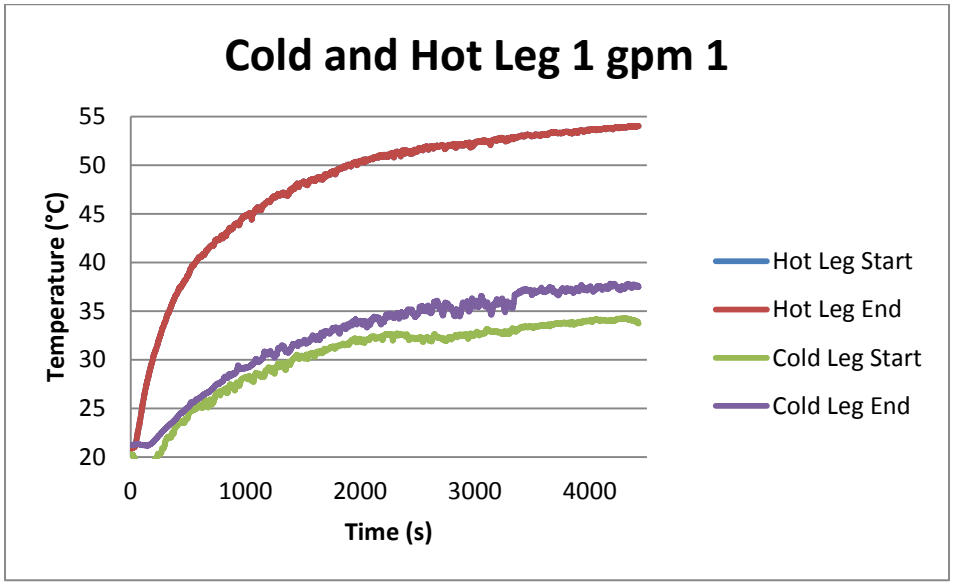

Figure B.28 Key Wall Temperatures from the 2nd 1 gpm Chiller Test

The plots from both tests with the chiller at 0 gpm (off) are shown below.

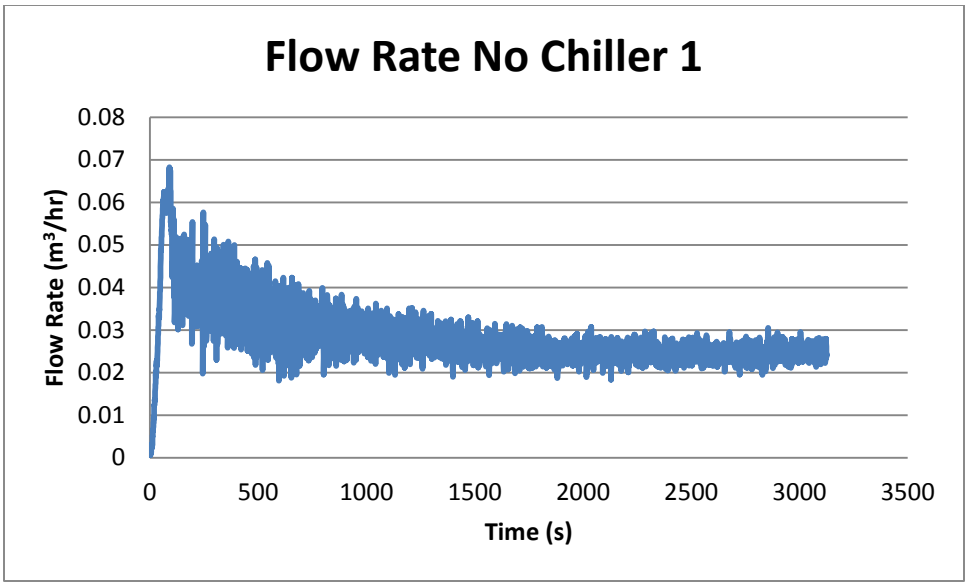

Figure B.29 Flow Rate from the 1st 0 gpm Chiller Test

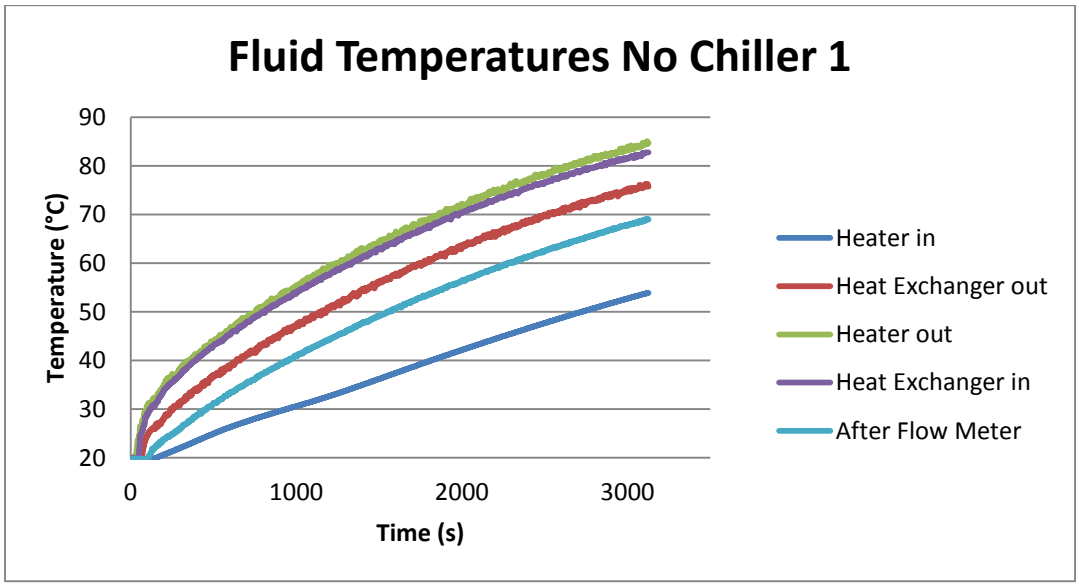

Figure B.30 Fluid Temperatures from the 1st 0 gpm Chiller Test

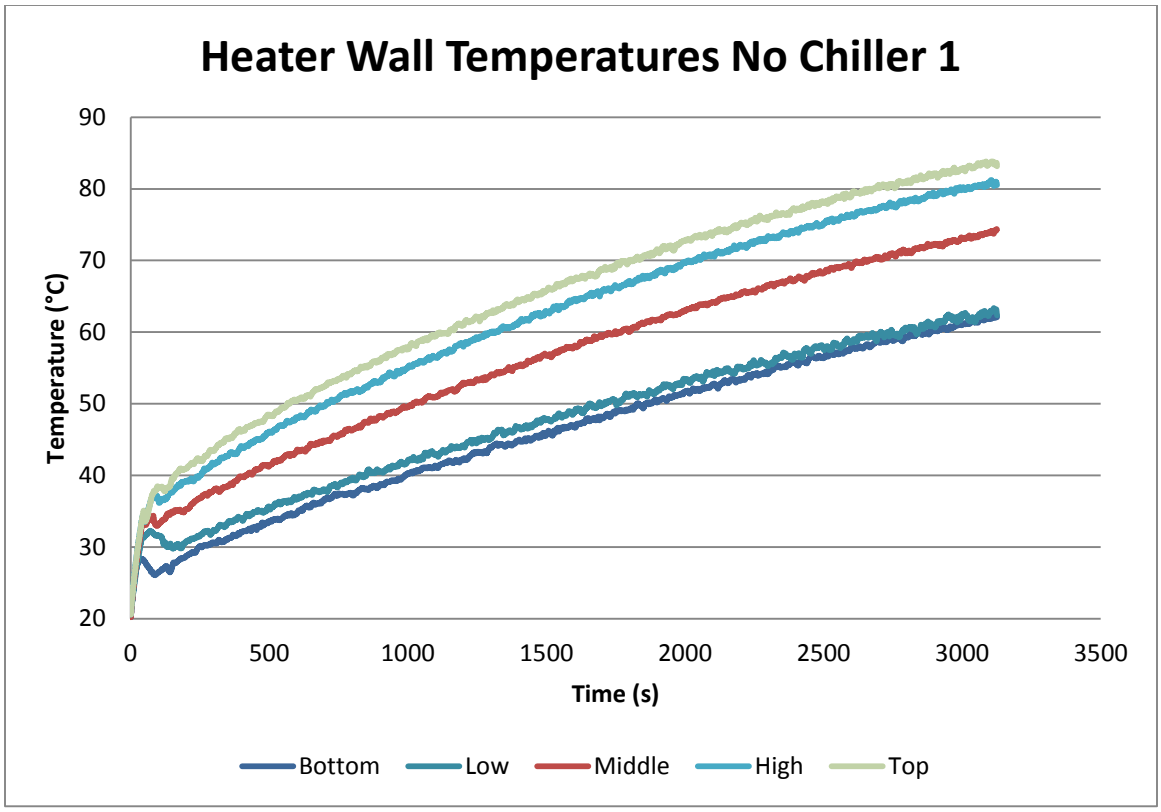

Figure B.31 Heater Wall Temperatures from the 1st 0 gpm Chiller Test

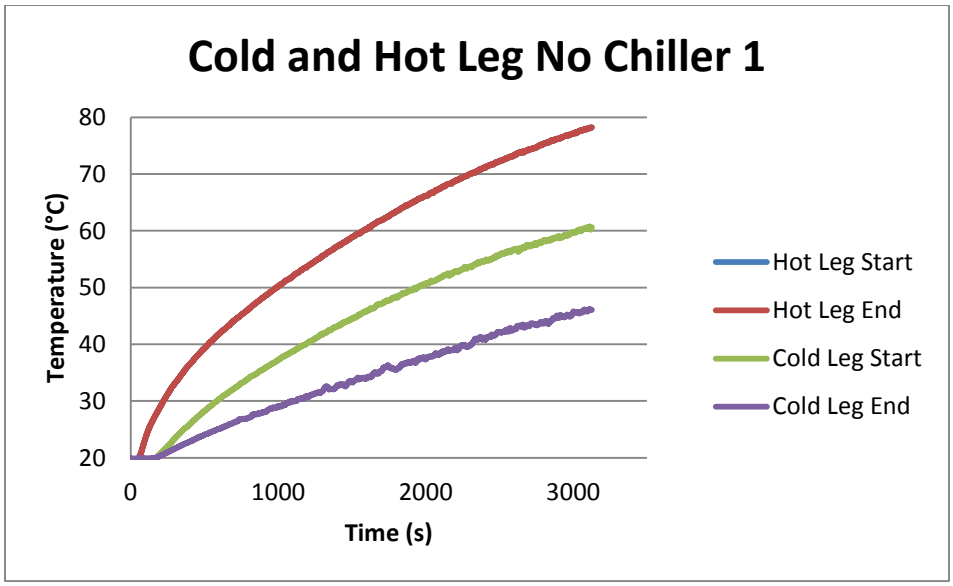

Figure B.32 Key Wall Temperatures from the 1st 0 gpm Chiller Test

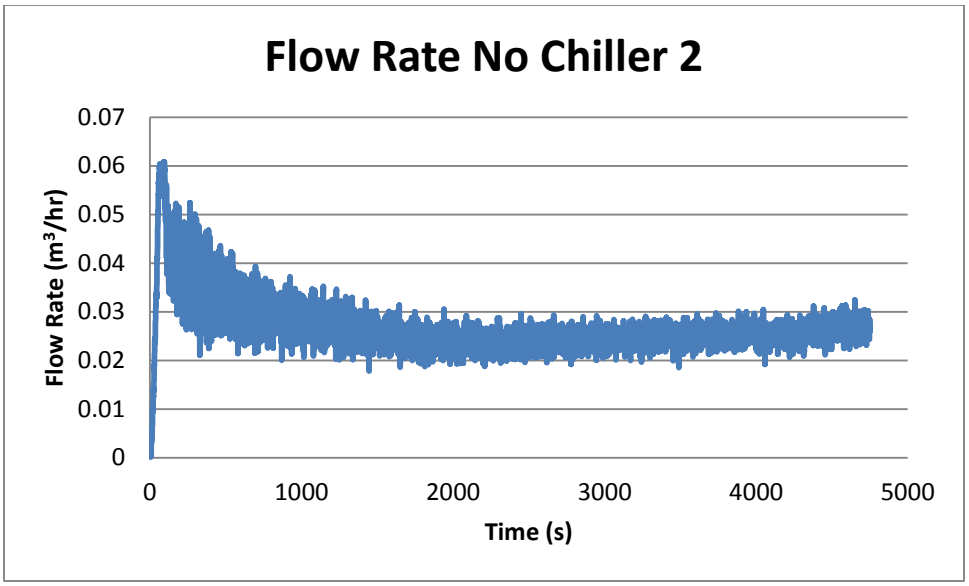

Figure B.33 Flow Rate from the 2nd 0 gpm Chiller Test

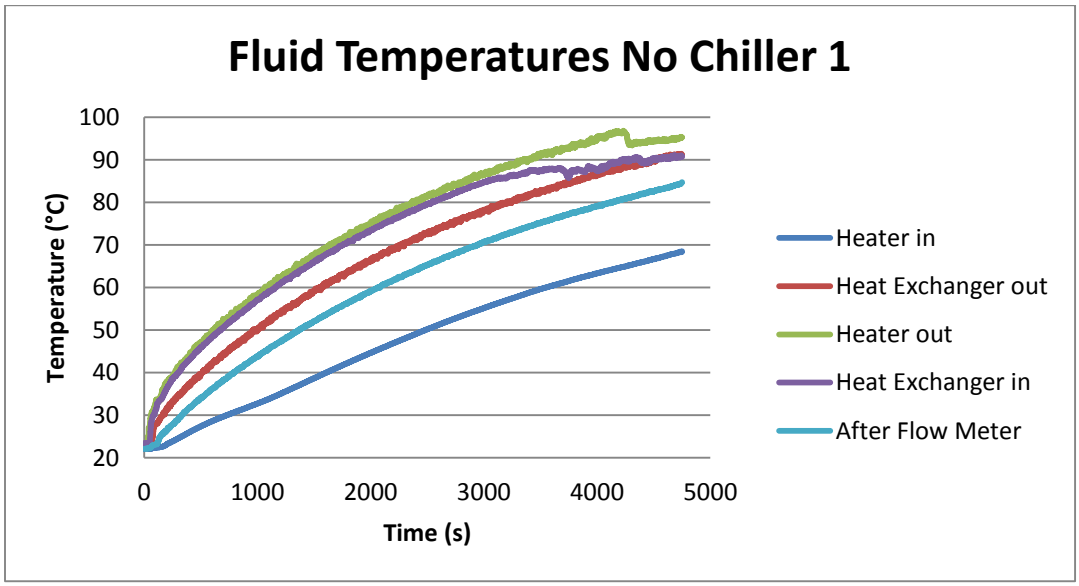

Figure B.34 Fluid Temperatures from the 2nd 0 gpm Chiller Test

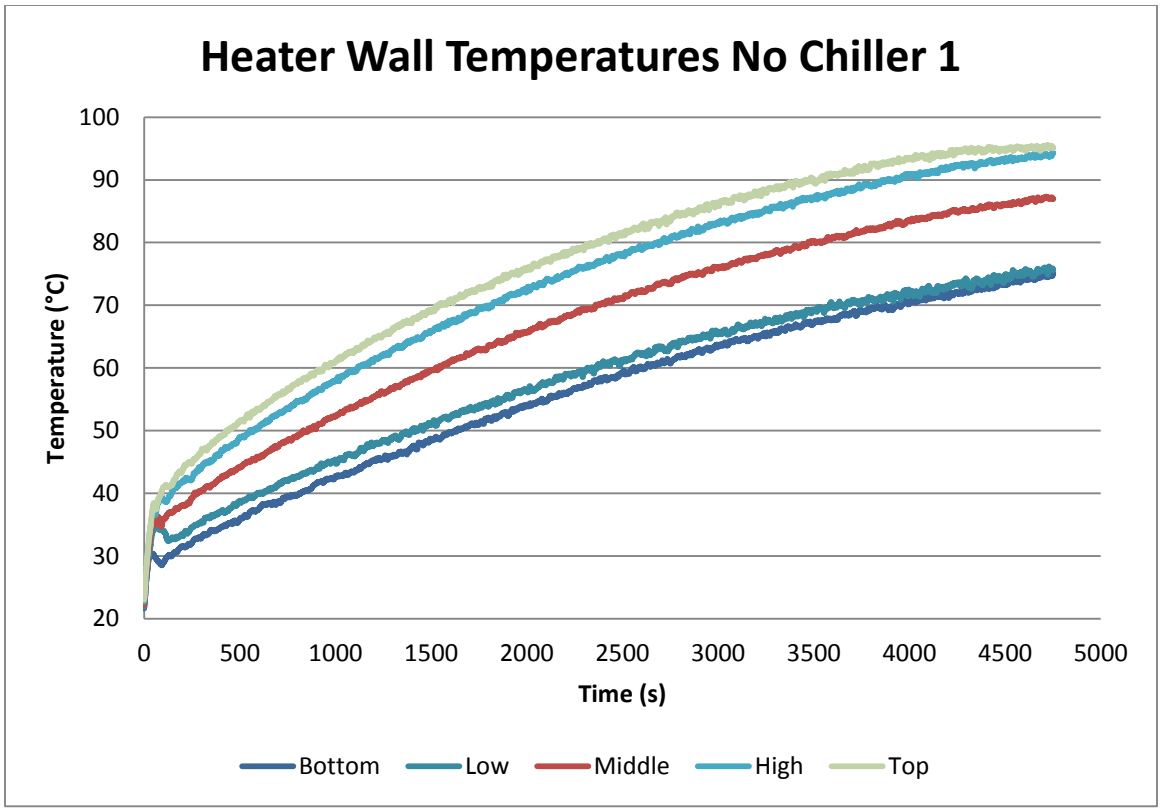

Figure B.35 Heater Wall Temperatures from the 2nd 0 gpm Chiller Test

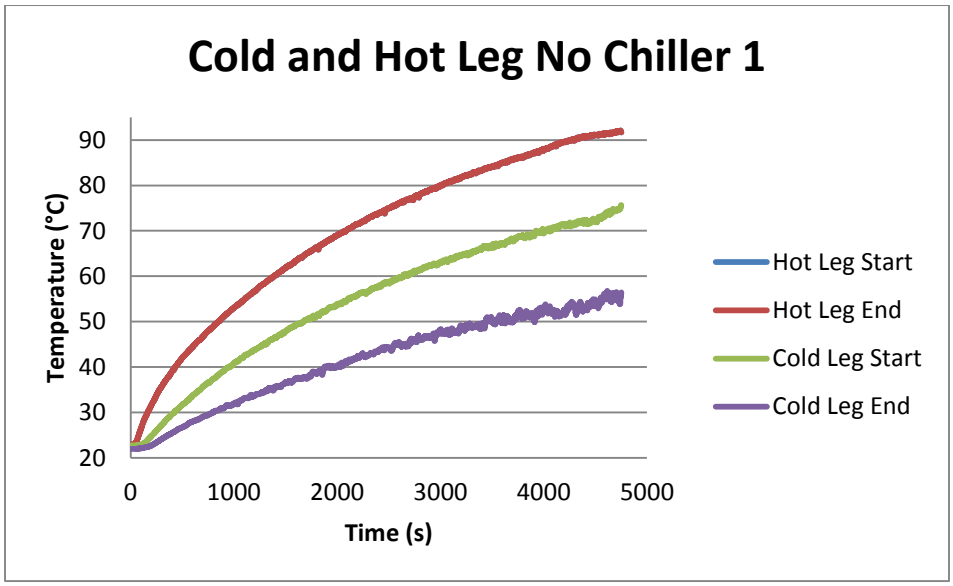

Figure B.36 Key Wall Temperatures from the 2nd 0 gpm Chiller Test

The initial temperature of the loop was increased to approximately 75°C which is above the steady state value (for the 1kW power used). The plots from both of the runs for this transient are shown below.

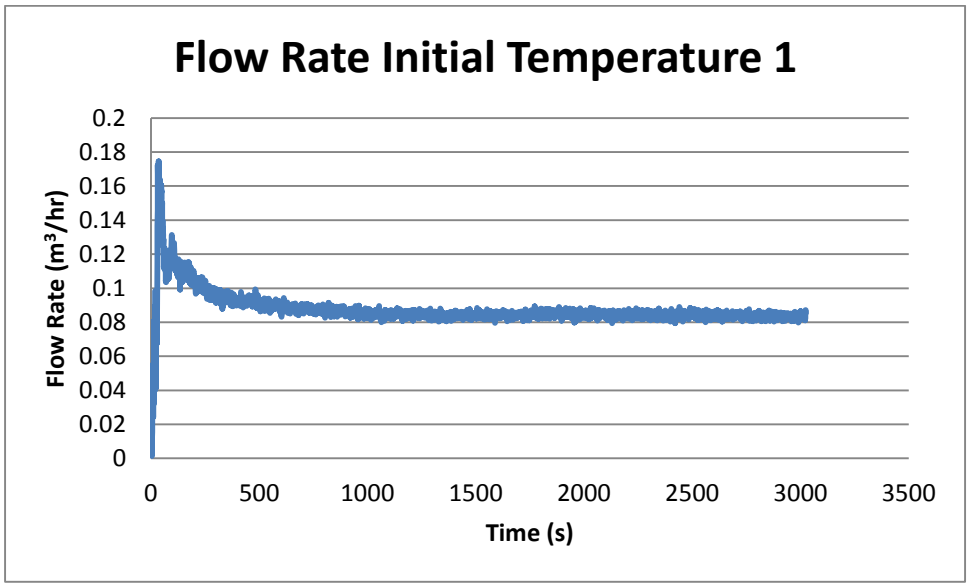

Figure B.37 Flow Rate from the 1st Initial Temperature Test

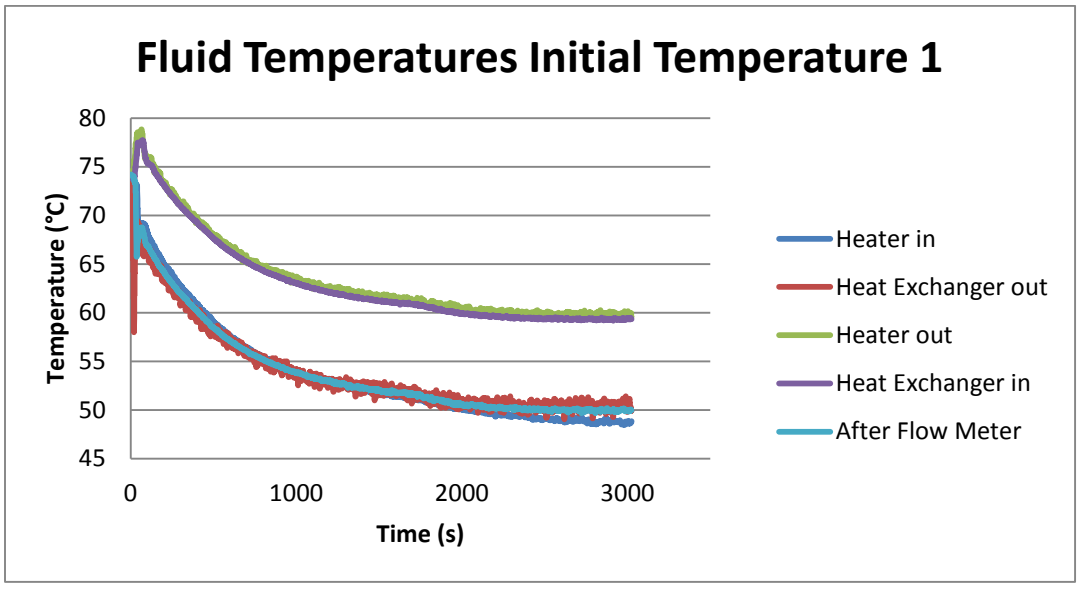

Figure B.38 Fluid Temperatures from the 1st Initial Temperature Test

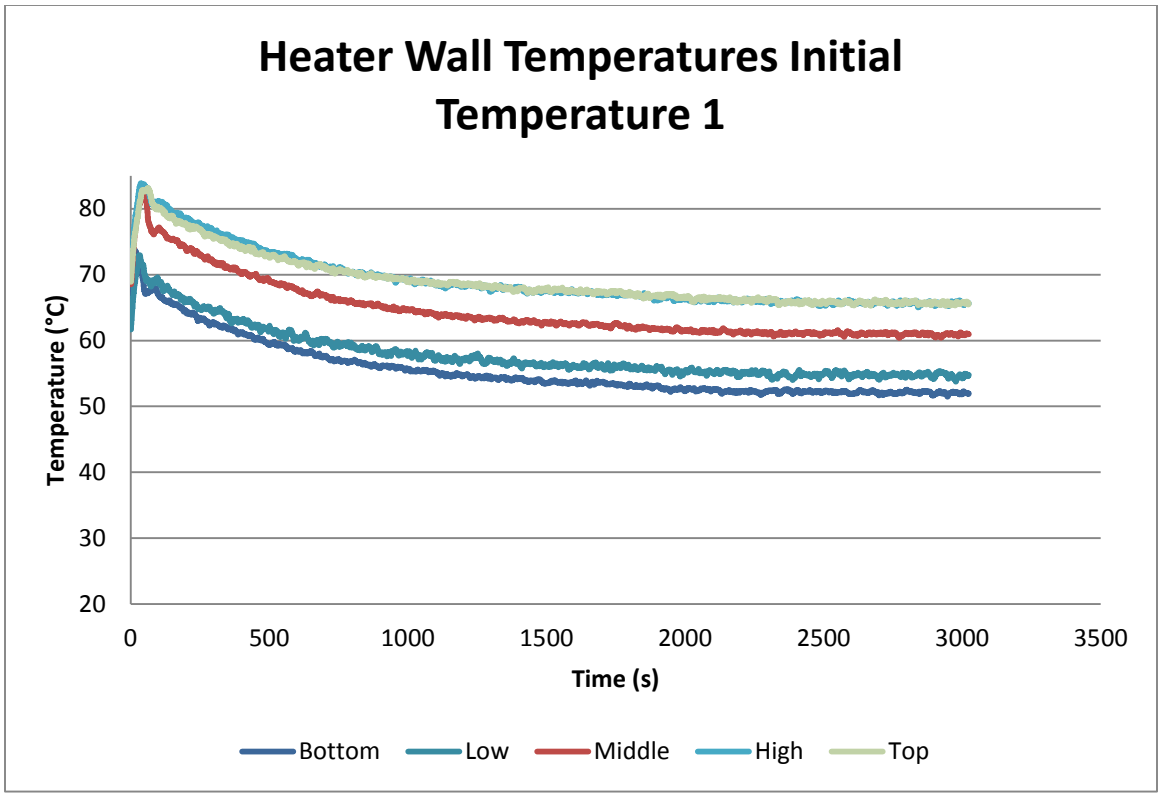

Figure B.39 Heater Wall Temperatures from the 1st Initial Temperature Test

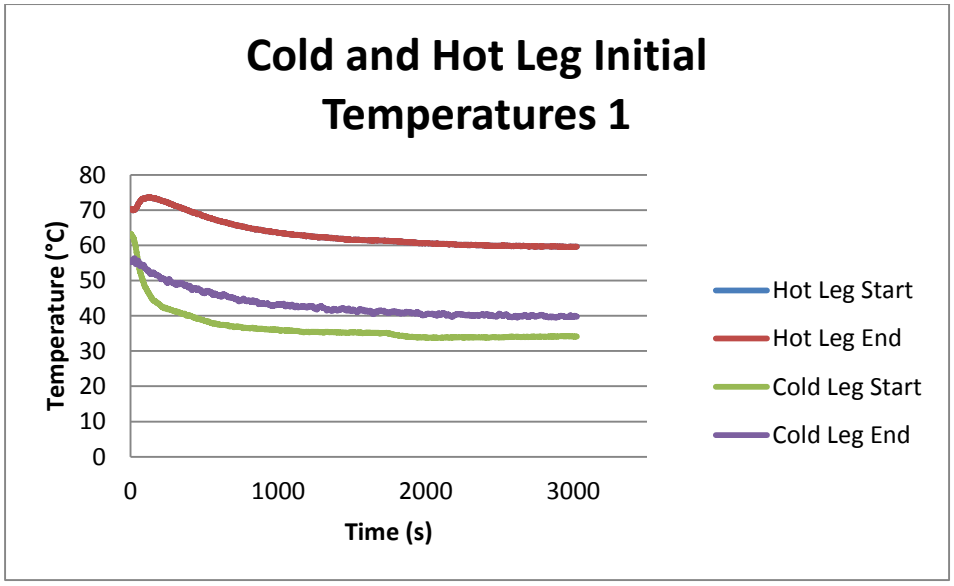

Figure B.40 Key Wall Temperatures from the 1st Initial Temperature Test

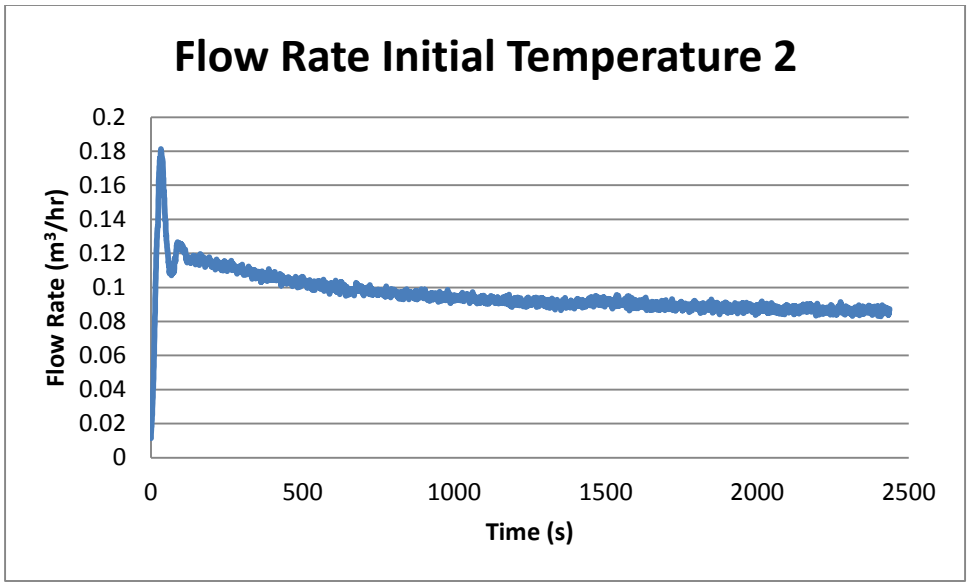

Figure B.41 Flow Rate from the 2nd Initial Temperature Test

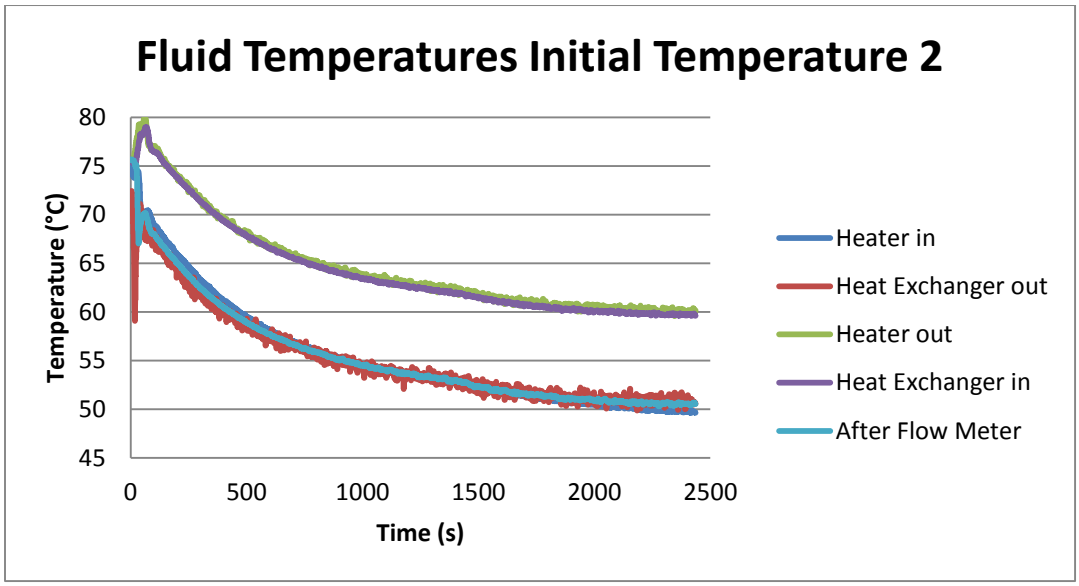

Figure B.42 Fluid Temperatures from the 2nd Initial Temperature Test

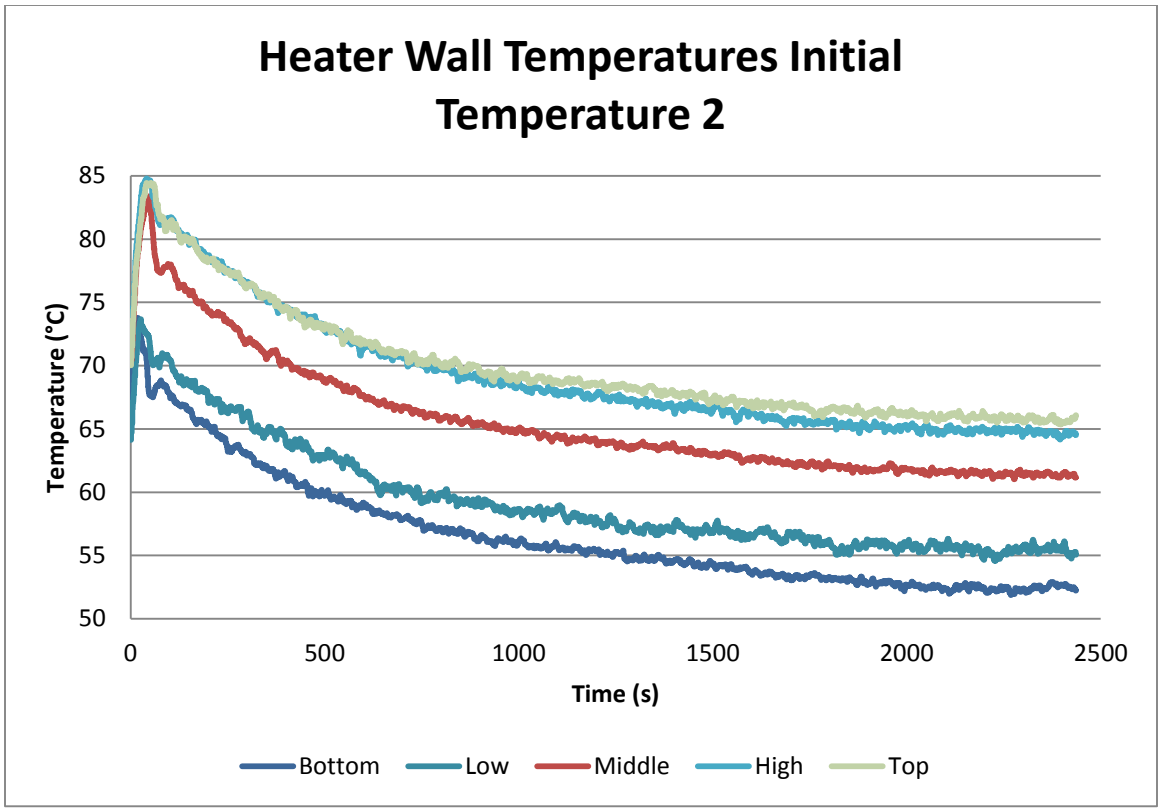

Figure B.43 Heater Wall Temperatures from the 2nd Initial Temperature Test

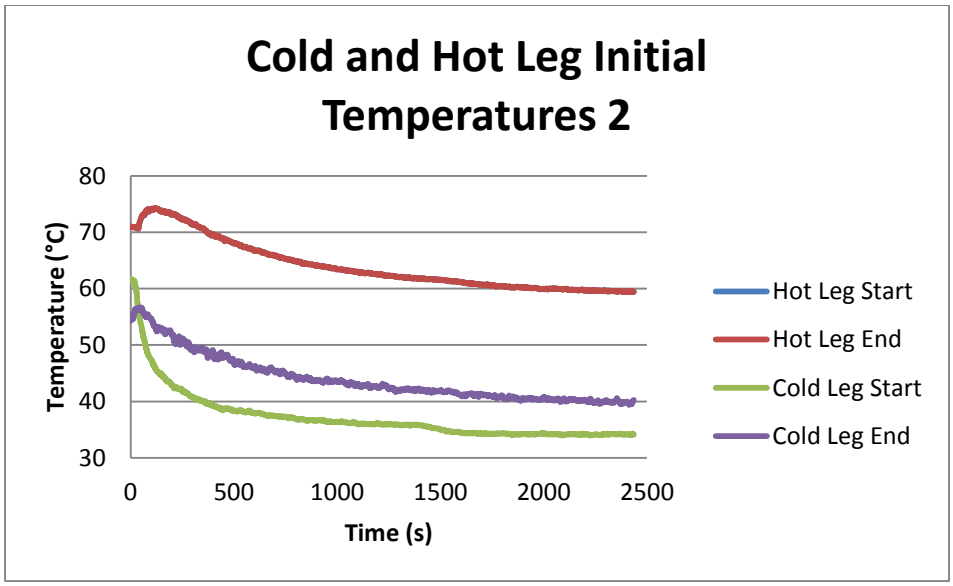

Figure B.44 Key Wall Temperatures from the 2nd Initial Temperature Test

For the last two experimental runs, the flow was started in the forward direction using a pump and then the pump was shut off and valves were switched to the natural circulation

mode configuration. The heat exchanger and heater were then quickly turned on. The results from the two tests are shown below.

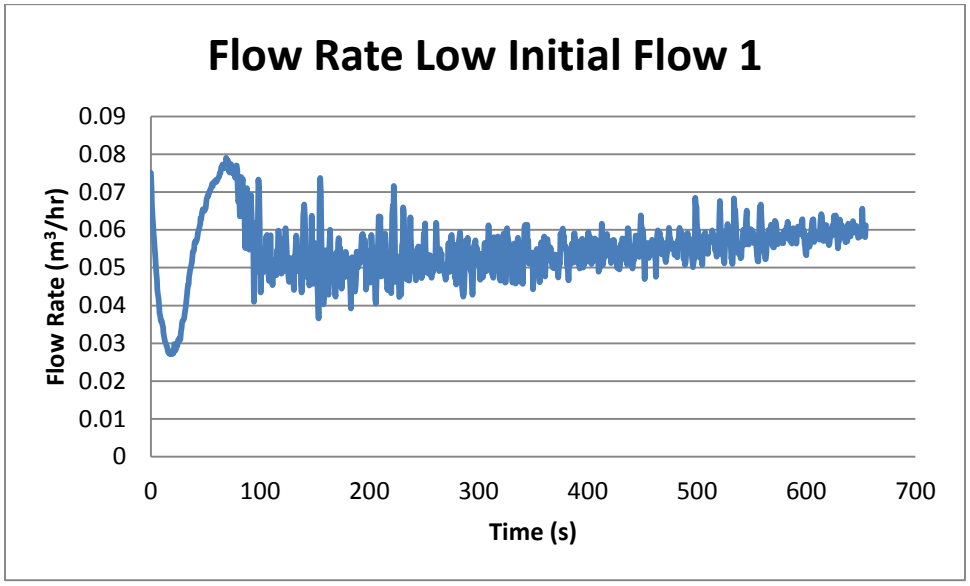

Figure B.45 Flow Rate from the 1st Initial Flow Test

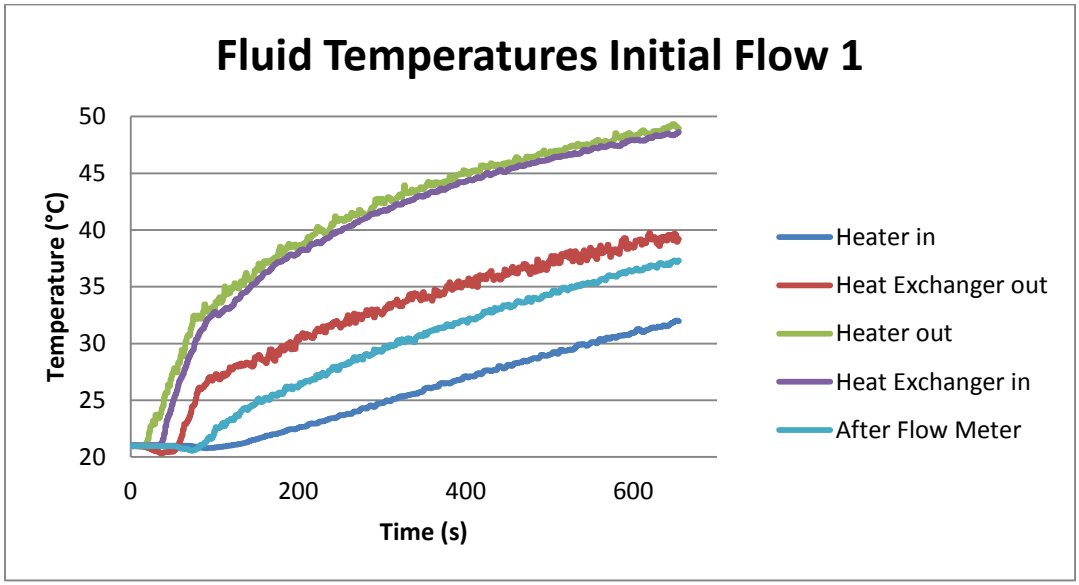

Figure B.46 Fluid Temperatures from the 1st Initial Flow Test

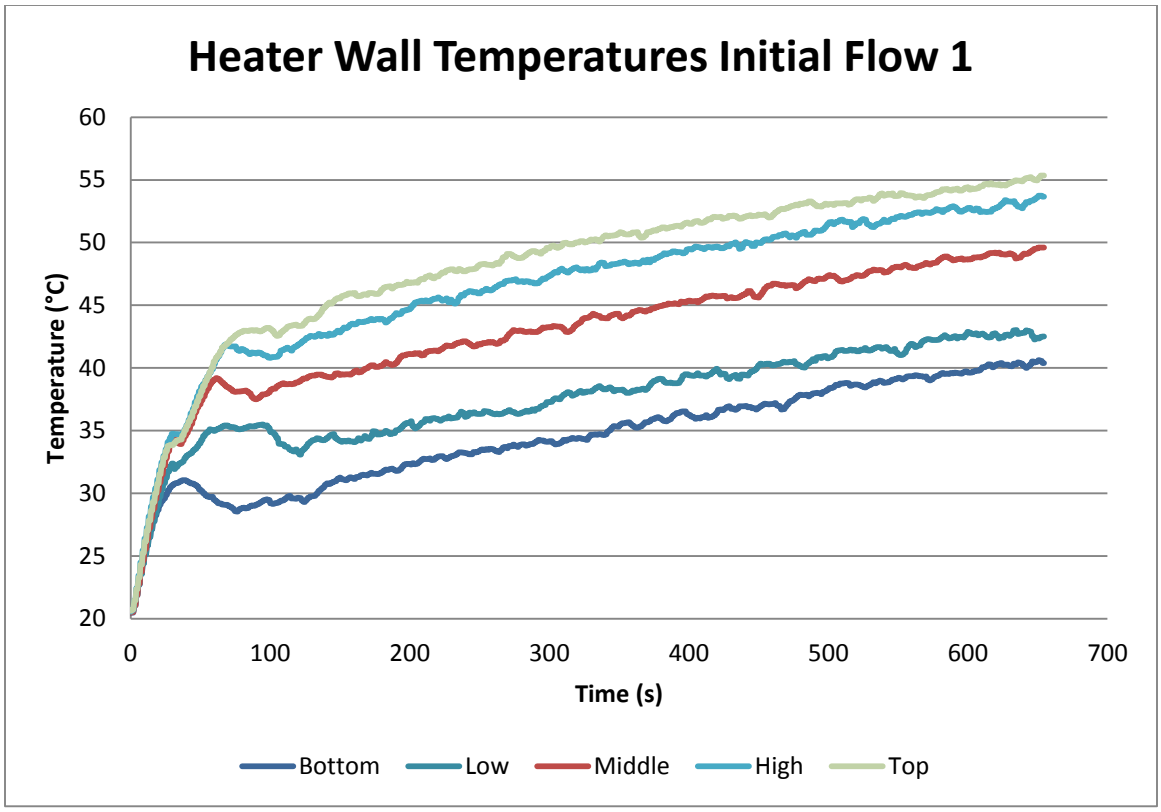

Figure B.47 Heater Wall Temperatures from the 1st Initial Flow Test

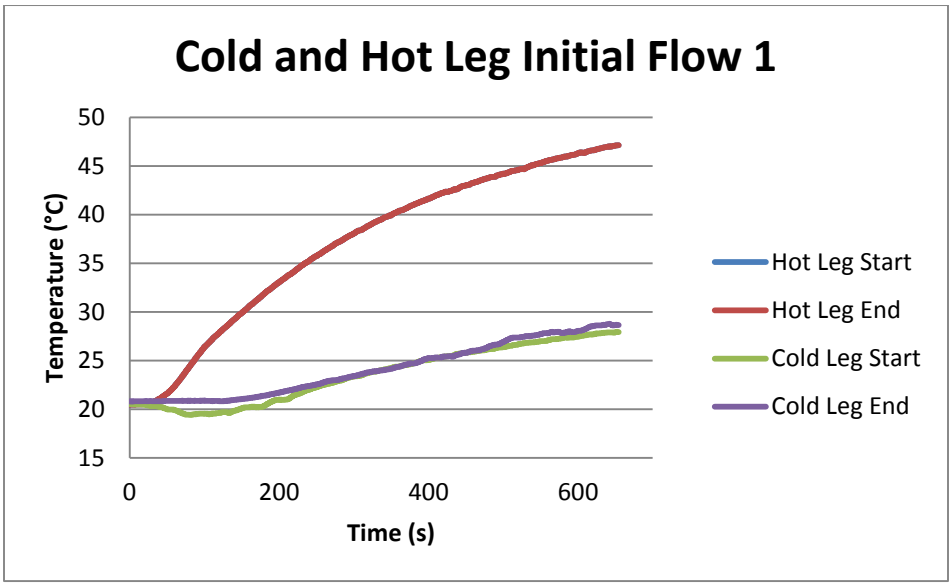

Figure B.48 Key Wall Temperatures from the 1st Initial Flow Test

The results from the second run with an initial flow rate are shown below.

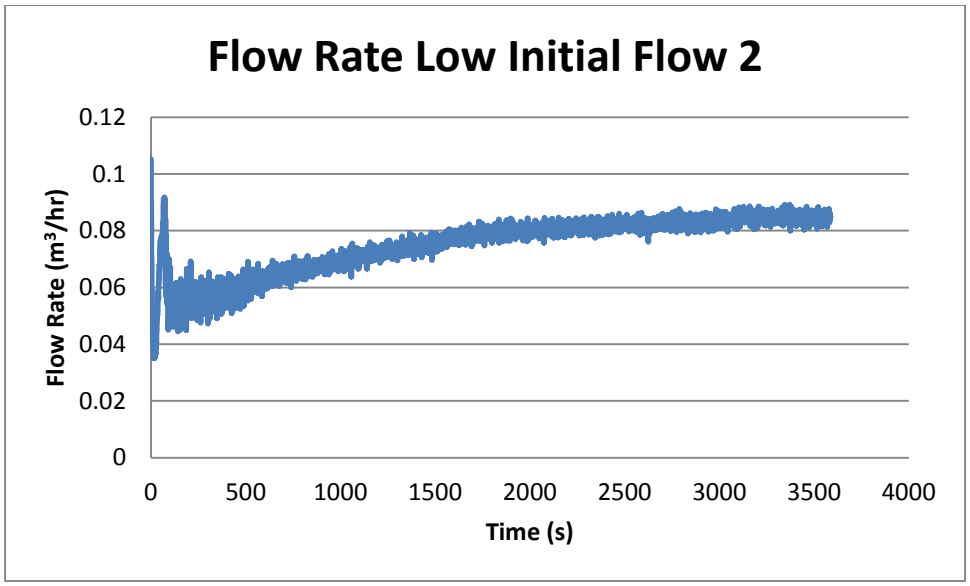

Figure B.49 Flow Rate from the 2nd Initial Flow Test

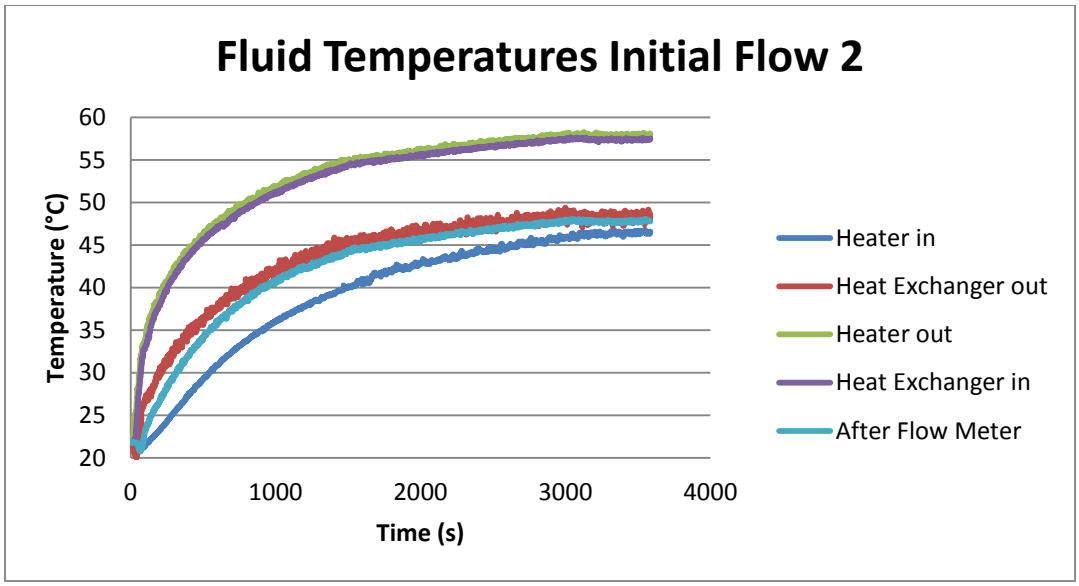

Figure B.50 Fluid Temperatures from the 2nd Initial Flow Test

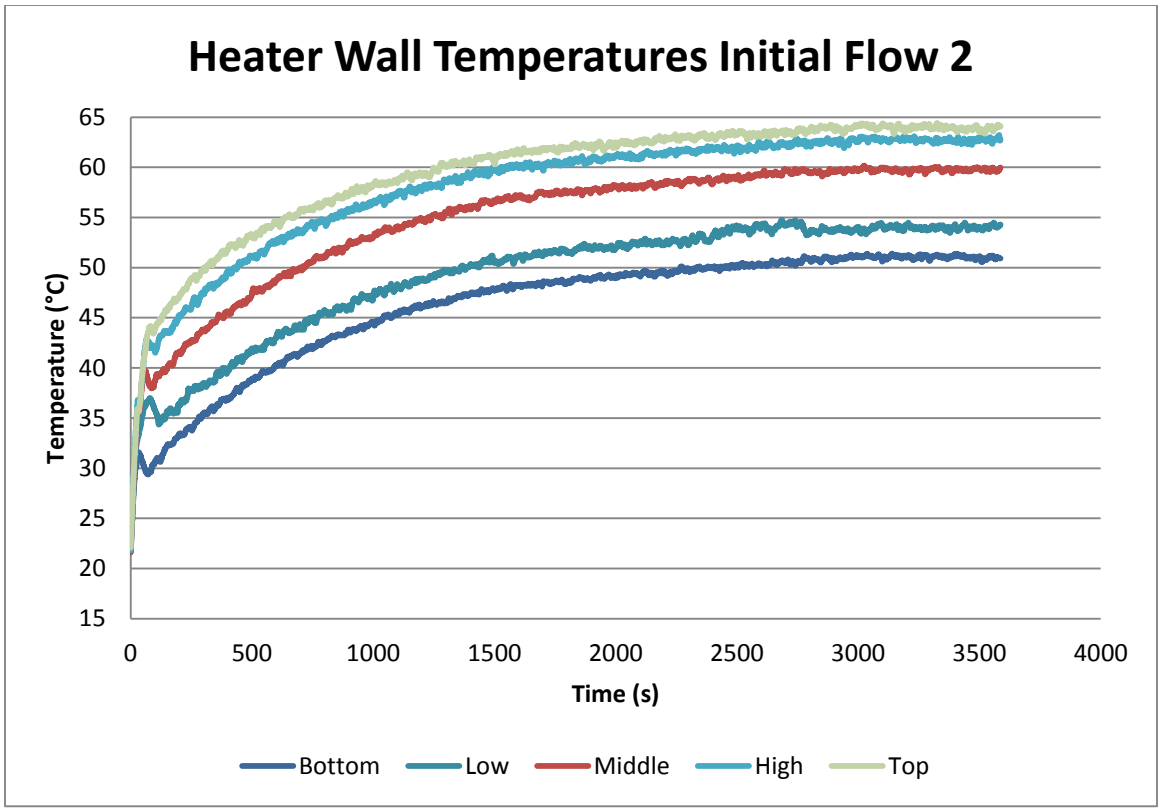

Figure B.51 Heater Wall Temperatures from the 2nd Initial Flow Test

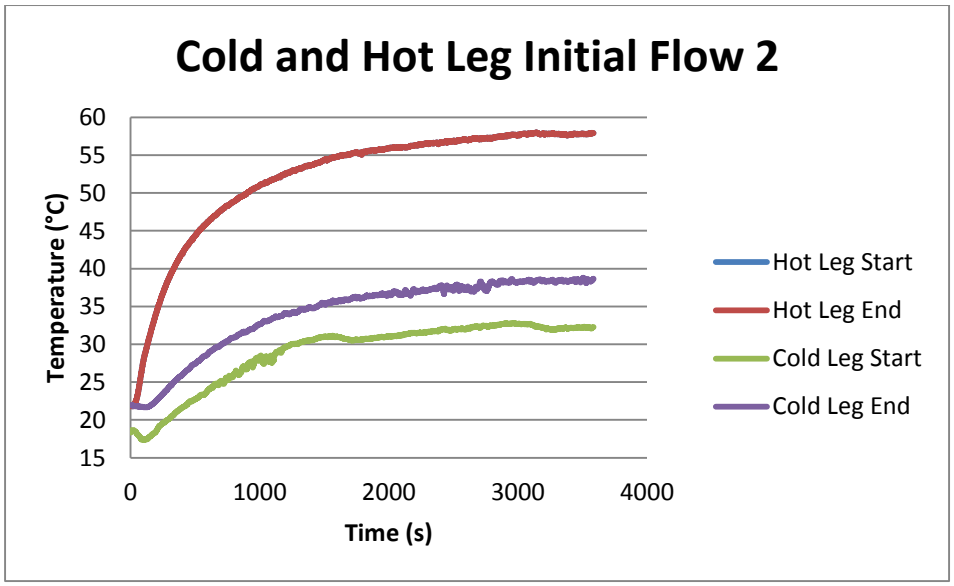

Figure B.52 Key Wall Temperatures from the 2nd Initial Flow Test

The results from the LOHS tests are shown below.

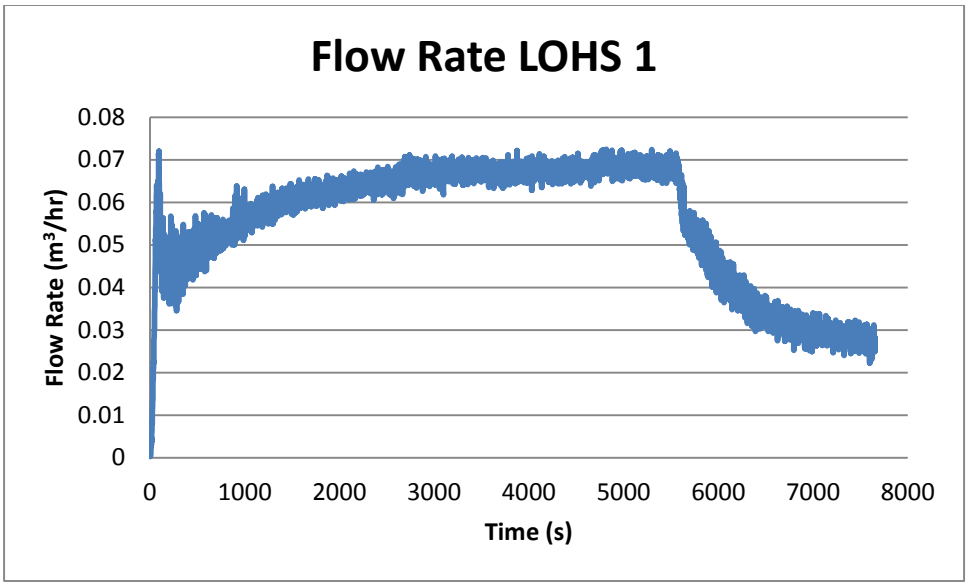

Figure B.53 Flow Rate from the 1st LOHS Test

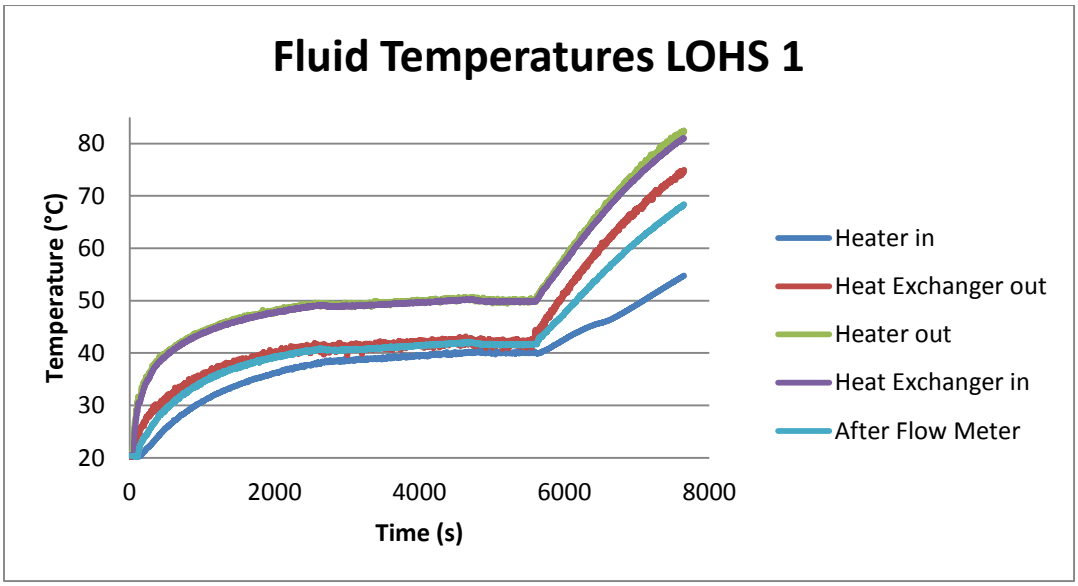

Figure B.54 Fluid Temperatures from the 1st LOHS Test

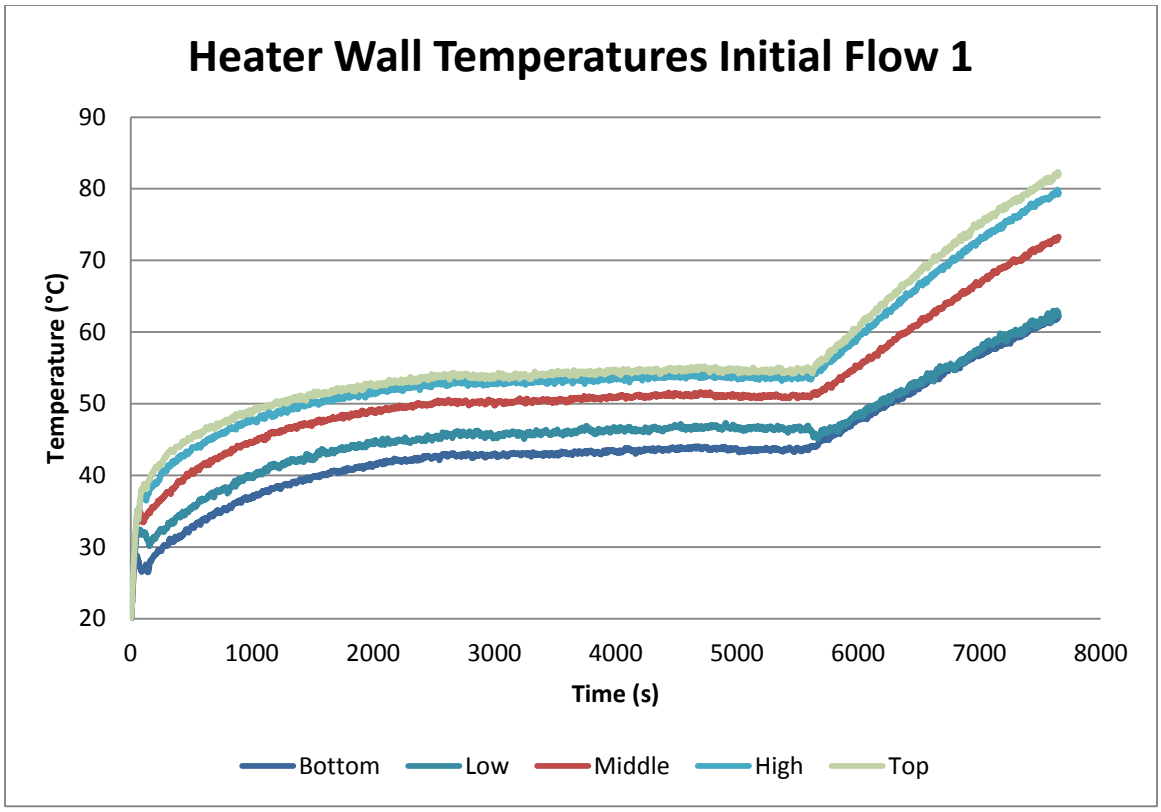

Figure B.55 Heater Wall Temperatures from the 1st LOHS Test

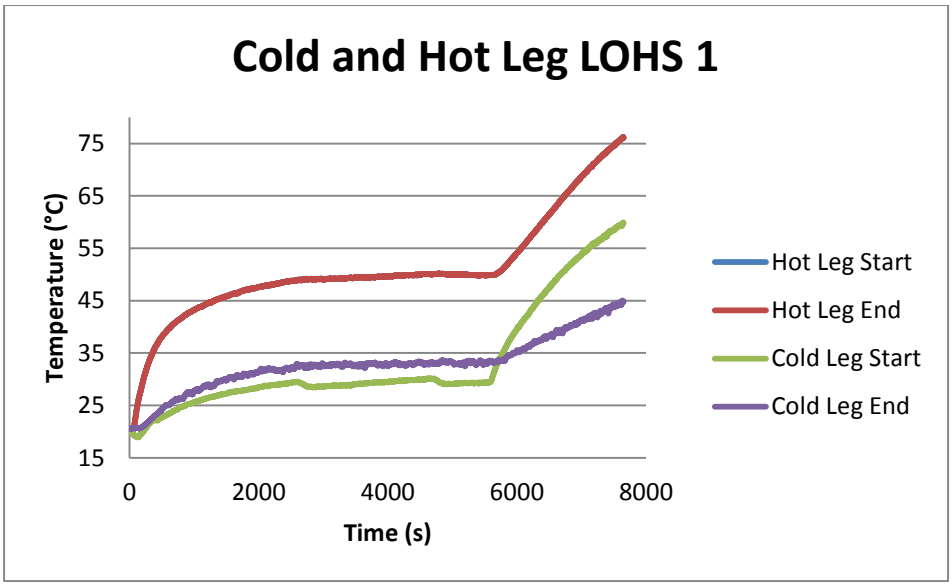

Figure B.56 Key Wall Temperatures from the 1st LOHS Test

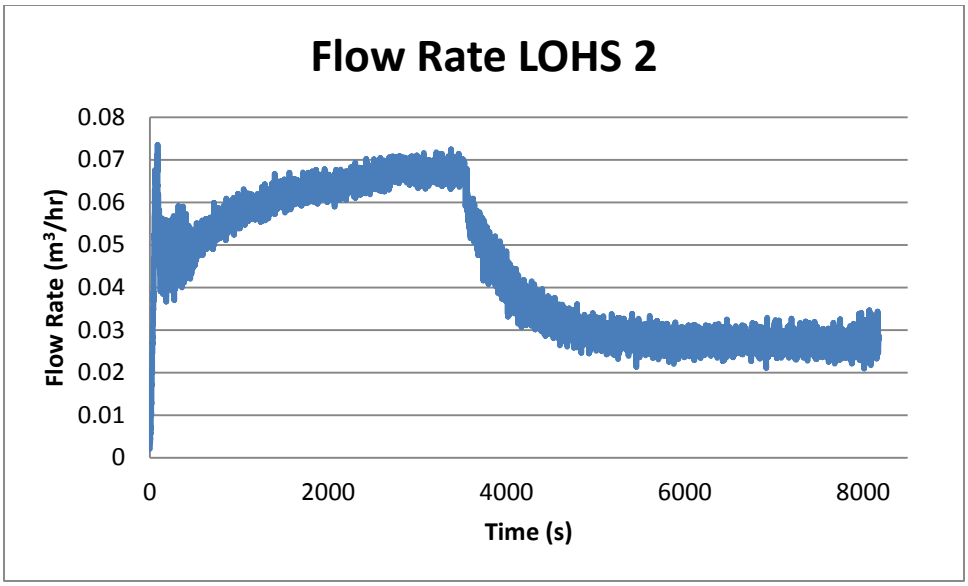

Figure B.57 Flow Rate from the 2nd LOHS Test

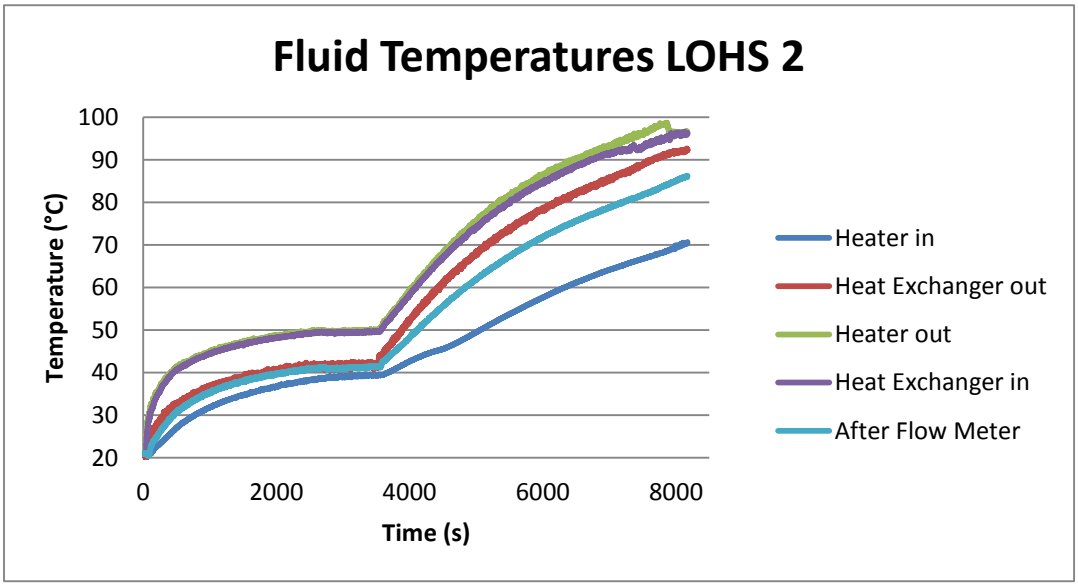

Figure B.58 Fluid Temperatures from the 2nd LOHS Test

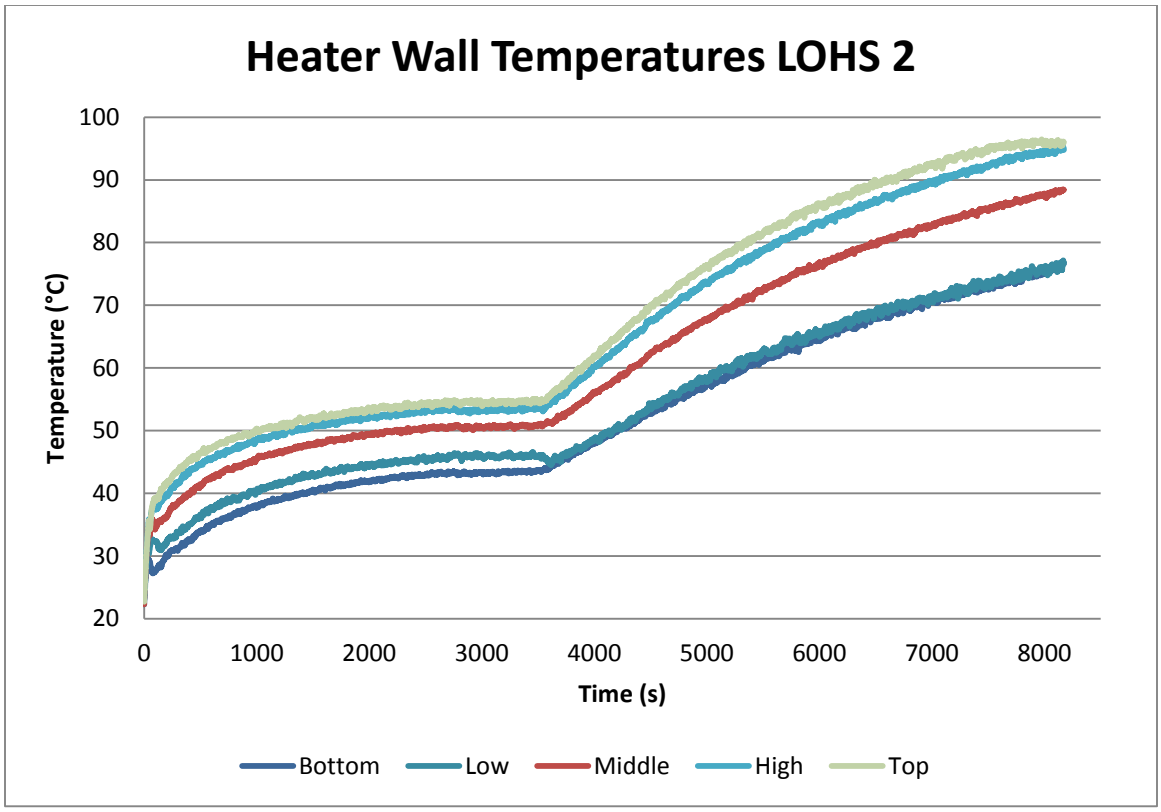

Figure B.59 Heater Wall Temperatures from the 2nd LOHS Test

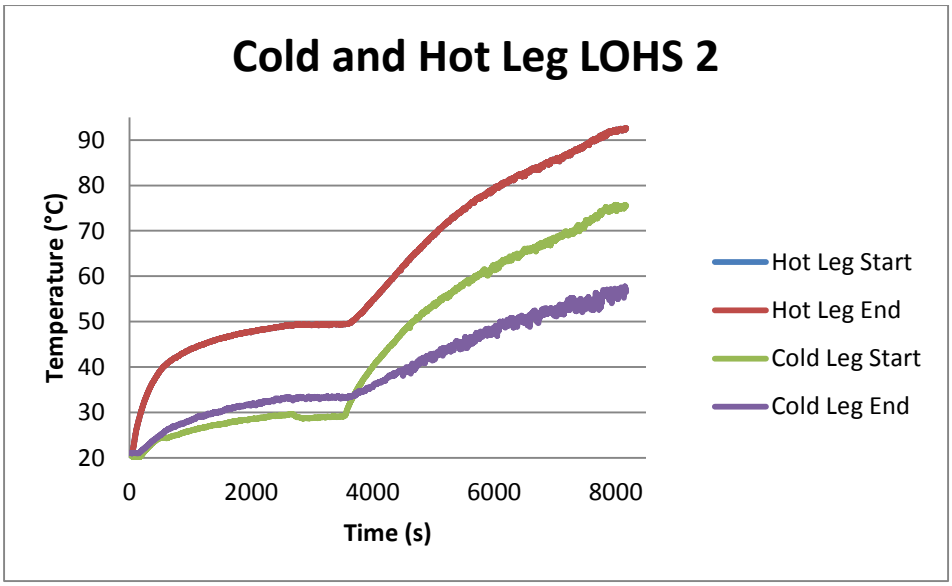

Figure B.60 Key Wall Temperatures from the 2nd LOHS Test